DOE/PC/92534--11

Selective Catalytic Reduction of Sulfur Dioxide to Elemental Sulfur

Final Report

June 1995

by

Wei Liu
Maria Flytzani-Stephanopoulos
Adel F. Sarofim

Department of Chemical Engineering
Massachusetts Institute of Technology
Cambridge, MA 02139

Prepared for

The U.S. Department of Energy
The Pittsburgh Energy Technology Center
Pittsburgh, Pennsylvania
DOE/Project Manager: Dr. Michael Baird (PETC)
Grant No.: DE-FG22-92PC92534

Executive Summary

Elemental sulfur recovery from SO_2-containing gas stream is highly attractive as it produces a salable product and no waste to dispose of. However, commercially available schemes are complex and involve multi-stage reactors, such as Claus plant. This project has investigated new metal oxide catalysts for the single stage selective reduction of SO_2 to elemental sulfur by a reductant, such as CO. Significant progress in catalyst development has been made during the course of the project. We have found that fluorite oxides, CeO_2 and ZrO_2, and rare earth zirconates such as $Gd_2Zr_2O_7$ are active and stable catalysts for reduction of SO_2 by CO. More than 95% sulfur yield was achieved at reaction temperatures about 450°C or higher with the feed gas of stoichiometric composition. Reaction of SO_2 and CO over these catalysts demonstrated a strong correlation of catalytic activity with the catalyst oxygen mobility. Furthermore, the catalytic activity and resistance to H_2O and CO_2 poisoning of these catalysts were significantly enhanced by adding small amounts of transition metals, such as Co, Ni, Co, etc. The resulting transition metal-fluorite oxide composite catalyst has superior activity and stability, and shows promise in long use for the development of a greatly simplified single-step sulfur recovery process to treat variable and dilute SO_2 concentration gas streams. Such a simple catalytic converter may offer the long-sought "Claus-alternative" for coal-fired power plant applications.

Among various active composite catalyst systems the Cu-CeO_2 system has been extensively studied. XRD, XPS, and STEM analyses of the used Cu-CeO_2 catalyst found that the fluorite crystal structure of ceria was stable at the present reaction conditions, small amounts of copper was dispersed and stabilized on the ceria matrix, and excess copper oxide particles formed copper sulfide crystals of little contribution to catalytic activity. A working catalyst consisted of partially sulfated cerium oxide surface and partially sulfided copper clusters. The overall reaction kinetics were approximately represented by a first order equation. The reaction mechanism was discussed within the Redox framework. The copper and cerium oxide in the composite catalyst play different roles: copper provides CO adsorption sites and cerium oxide provides oxygen vacancy sites. Thus, a synergism is realized.

The project objectives were extended to other oxidation reactions, CO oxidation and methane oxidation, to generalize the complete oxidation activity of the new catalysts. The catalytic properties for oxidation of CO and hydrocarbon are useful information to single-step sulfur recover process development, because practical reaction streams for SO_2 reduction by CO may contain certain amounts of oxygen and/or hydrocarbons. In addition, new complete oxidation catalysts would benefit technologies in (a) gas turbine exhaust cleanup and (b) vehicle exhaust emission control.

The Cu-CeO_2 and Cu-ZrO_2 composites were found to be active catalysts for complete oxidation of CO and methane. The Cu-CeO_2 catalyst showed a CO oxidation activity higher than any other base metal oxide catalysts reported in the literature, demonstrating a

strong synergism. The Au-CeO_2 was identified as an active and stable catalyst for low temperature CO oxidation. STEM microstructure analyses revealed that copper in the Cu-CeO_2 composite existed in the forms of isolated ions, clusters, and bulk CuO particles. Isolated ions and clusters were strongly bonded to the cerium oxide matrix. Cu^{+1} species was observed with all the Cu-CeO_2 catalysts by XPS. The oxidation rates of CO and methane over the Cu-CeO_2 catalysts were expressed by the following equation:

$$\frac{dP_{CO2}}{dt} = \frac{kK_R P_R P_O^n}{1 + K_R P_R}$$

where P_R denotes the partial pressure of CO or methane and P_O is the partial pressure of oxygen, and n is a small number close to zero. The activation energies of the surface reactions are 78-94kJ/mol for CO oxidation and 79kJ/mol for methane oxidation, respectively. The heat of adsorption derived from the kinetics is in the range of 28 to 62kJ/mol for CO and 14kJ/mol for methane, respectively. The Langmuir-Hinshelwood mechanism and synergistic reaction model were proposed for CO oxidation over the Cu-CeO_2 and Au-CeO_2 catalysts. In this model, copper clusters of Cu^{+1} species or gold particles provide sites for CO adsorption, cerium oxide provides the oxygen source, and the reaction proceeds at the interface of the two kinds of materials.

Acknowledgments

We would like to acknowledge our collaborators: Dr. Andreas Tschope, a BASF Postdoctoral Fellow, and Prof. Jackie Y. Ying at MIT Department of Chemical Engineering for preparation of nanocrystalline cerium oxide catalysts and chemisorption measurements; Mr. Robert Williams, B.S. '93, Ms. Farnaz Haghseta, B.S. '96, Mr. Cyrus Wadia, B.S. '96, undergraduate students at MIT, and Mr. Eric Mullins, a visiting student from Cumberland College under DOE/ORISE Program, for their assistance in catalyst preparation and activity tests.

We also wish to thank several staff members at MIT Materials Science and Engineering Center: Dr. Anthony Garratt-Reed for STEM analyses, Mr. Michael Frongillo for HRTEM analyses, Mr. Leonard Sudenfield for SEM analyses, Mr. John Martin and Ms. Elizabeth L. Shaw for their assistance in XPS analyses, and Dr. Joseph Adario for his assistance in XRD analyses. This work made use of the MRSEC Shared Facilities supported by the National Science Foundation under Award Number DMR-9400334.

Contents

List of Figures

List of Tables

Chapter 1

Introduction

1.1 Project Objective and Outline

This research aims to develop and study new catalyst materials of high activity and stability for the reduction of sulfur dioxide by carbon monoxide to elemental sulfur. Direct sulfur recovery from dilute sulfur dioxide streams is integrally related to the on-going and future generation of efficient and economical (a) flue gas desulfurization process and (b) hot coal gas cleanup technology.

The research objectives include (i) evaluation of CeO_2-based catalysts for direct reduction of SO_2 to S; (ii) conduction of detailed parametric studies with selected catalyst compositions; (iii) correlation of catalyst activity/selectivity with catalyst structural properties. The project objectives are extended to other catalysts to check the hypothesis of labile oxygen/vacancy mechanism and to other oxidation reactions to generalize the complete oxidation activity of the new catalysts.

This report consists of seven chapters. Chapter 1 gives detailed information of the project background, proposed new catalyst formula, and scientific discussion of the new catalyst system. The general description of experimental principles and procedure are covered in Chapter 2, while research results and discussions comprise the subsequent chapters. Chapter 3 discusses sulfur dioxide reduction by carbon monoxide over ceria-based catalysts with emphasis on correlation of catalytic activity with oxygen mobility. The structure and activity of novel transition metal-fluorite oxide composite catalysts are reported in Chapter 4. Chapters 5 and 6 include the results for total oxidation of carbon monoxide and methane: catalyst composition and activity in Chapter 5, catalyst structure and reaction kinetics in Chapter 6. Each of the Chapters 3-6 contains a brief introduction of research background and specific experimental methods as well as bibliography. Finally, the main conclusions drawn from this work and proposal for future study are summarized in Chapter 7.

1.2 Background

1.2.1 Old Problems and New Challenges—Flue Gas Desulfurization

Sulfur dioxide is a notorious environmental pollutant causing acid rain formation and various ecological damages. Sulfur dioxide is mainly generated from burning sulfur-containing fossil fuels. About 55% of the electric power in the U.S. is produced by coal-fired power plants. As a result, coal-fired power plants are the primary sources of SO_2 emission. The 1990 Clean Air Act amendments call for a reduction of about 50% in these

SO_2 emissions by the end of this century. Estimates for the costs of flue gas desulfurization (FGD) systems alone by that time are $6-8 billion for capital expenditures with additional operating expenses of $3 billion/year. The majority of commercial flue gas desulfurization (FGD) plants in use today are based on scrubbing processes (92 % wet scrubbers and 8 % dry scrubbers). Such schemes fix the sulfur dioxide by an oxide sorbent, typically limestone ($CaCO_3$) or lime (CaO). These scrubbers are fraught with problems, such as high costs, large space requirements, high energy consumption, consumption of calcium oxide, a huge amount of solid waste containing metal sulfite/sulfate. The disposal of the solid waste is becoming costly with decreasing landfills and increasing public concerns over environmental pollution.

On the other hand, the 1990 Clean Air Act amendments also require significant reduction of another major air pollutant – NOx in the flue gas emissions. Fulfillment of the Clean Air Act will require very large capital investment. Thus, it is imperative to develop highly efficient and inexpensive new FGD technologies. Recent new legislation opens up the large, lucrative market by offering the opportunity for utilities to buy and sell rights (allowances of SO_2 emission) on the Chicago Board of Trade *(1)*. This has certainly added another impetus to new technology development.

Regenerative Flue Gas Desulfurization. Several development efforts have emphasized the improvement of the scrubbing technology. Recently, emphasis is shifting toward regenerative processes coupled with simultaneous de-NOx process, with no throwaway waste *(2,3,4)*. Figure 1.1 shows the scheme of a typical dry regenerative FGD process, where sulfur dioxide and oxygen in a flue gas stream react with metal oxide sorbent to form metal sulfate at typical exhaust gas temperatures and then, the saturated oxide sorbent is regenerated by a reducing stream to oxide form for cyclic operation. The regenerative FGD process has the advantages of energy efficiency, low cost of sorbents and waste disposal. However, these advantages can be greatly offset by the treatment of the regenerator offgas containing a few percent of SO_2 and probably, some residual reductant.

Recovery of elemental sulfur from the regenerator offgas is an attractive approach, because the solid sulfur product can be easily stored or transported. The Claus plant is a dominant commercial process for elemental sulfur recovery. In this process, H_2S gas stream is combusted with air in a burner to produce a stoichiometric mixture of SO_2 and H_2S and then, those two compounds react over two or three catalyst beds to produce elemental sulfur. The Claus process is widely used in refineries to treat gases containing fairly high concentrations of H_2S. But, this process is not suitable for the treatment of low concentration level (<5%) SO_2-containing gases, because SO_2 has to be converted into H_2S and combustion of low concentration H_2S gas is not stable in the burner. Therefore, it would be more cost-effective to replace the complex Claus plant with a high-efficiency, single-stage catalytic converter (designated as SO_2-to-S) to reduce SO_2 directly to elemental sulfur by using a reductant, as shown in Figure 1.1.

Integrated Gasification Combined Cycle (IGCC). Another application area of the SO_2-to-S converter was explored by researchers at the Research Triangle Institute *(5,6)*

for IGCC power generating systems. The IGCC system has held high promise for efficient and clean utilization of coal in power generation. But, desulfurization of hot coal gas is still one of main technological challenges. As illustrated in Figure 1.1, H_2S in the hot coal gas is usually scrubbed by metal and/or metal oxide sorbent at high reaction temperatures and the resulting metal sulfide is regenerated by air calcination. A diluted SO_2 stream is discharged by the regeneration process. Thus, elemental sulfur can be recovered from this gas stream through the SO_2-to-S converter.

The regenerator offgas volume is typically about ten times less than the parent flue gas or coal gas flowrate. Therefore, the direct sulfur recovery will require significantly lower capital investment. In addition to the previous two application areas, the SO_2-to-S converter, in general, can be used to recover elemental sulfur from any SO_2-containing industrial streams as long as no excess oxidant exists.

1.2.2 Previous and Ongoing Studies of Catalytic Reduction of Sulfur Dioxide to Elemental Sulfur

Directly reducing SO_2 into elemental sulfur by a reductant gas has considerable historical background. A comprehensive review of early work is given in a 1975 proceeding *(7)*. The gaseous reducing agents studied so far include carbon monoxide, hydrogen, synthesis gas (H_2 + CO), natural gas, etc. The type and location of the primary operation (sulfur source) dictate the choice of the reductant. The Allied Corporation operated a commercial plant to reduce SO_2 with CH_4 to elemental sulfur over a bauxite catalyst in 1970, as the emission control system for a Canadian sulfide ore roasting facility *(7)*. The reduction of SO_2 with CH_4 over an activated alumina catalyst was recently investigated by Sarlis and Berk *(8)*. The maximum elemental sulfur yield achieved in the single reduction step was around 50%. Therefore, the residual gas comprising of SO_2, H_2S, and COS had to go through a downstream Claus plant in order to achieve high sulfur recovery. But, this technology was only suitable for gas streams containing more than 4% SO_2. Direct reaction of SO_2-rich streams (>10.0% SO_2) with coke at 850-900°C to produce elemental sulfur was also tested *(9)*. Reduction of SO_2 by natural gas was disclosed by Stiles in 1975 *(10)* involving a supported catalyst containing thorium oxide in combination with one or more oxides of Cr, Mn, Ba, Sr, Ca, Ta or mixed rare earth chromites.

Most previous studies of reduction of sulfur dioxide to elemental sulfur considered use of carbon monoxide as the reductant. Various catalyst systems have been reported. These include supported transition metal catalysts (Cu, Pd, Ag, Co, Fe, Ni, Cr, Mn, etc.) *(11,12)* and ABO_3 perovskite-type mixed oxide catalysts containing alkaline earth and rare earth elements as well as transition metal elements *(13,14,15)*. But, none of these catalysts reached commercial application. The major technical problems arising from reduction of sulfur dioxide by carbon monoxide are the formation of COS and low activity and low sulfur yield in the presence of water vapor.

Two research groups have recently reported high elemental sulfur recovery from sulfur dioxide. Agarwal et al. *(5,6)* have achieved 95% elemental sulfur yield over a proprietary catalyst with coal gas as reductant. To avoid water vapor effects, they operated the reactor at high pressures (400 psi). Chang et al. *(16)* have realized 90% sulfur yield over a γ-Al_2O_3-supported catalyst containing 0 to 8 wt. % Fe, Co, Ni, Cr, Mn, Cu, Mo, and Se at temperatures $\geq$ 400°C and space velocities $\leq$10,000 h^{-1} by using stoichiometric synthesis gas (H_2/CO=0.3 ~ 3) as a reducing agent.

1.3 Formulation of a Novel Catalyst System

1.3.1 Catalyst Formula

It is believed that unique catalytic properties can be derived from *appropriate combination of appropriate metal oxides*. In this work we have pioneered a new catalyst combination of fluorite oxide, alkaline earth and rare earth oxides, and transition metal oxides given in the following empirical formula *(17,18)*:

$$[(FO_2)_{1-n}(DO_\delta)_n]_{1-k}M_k \quad (1)$$

$$[Ln_xZr_{1-x}O_{2-0.5x}]_{1-k}M_k \quad (2)$$

where FO_2 is a fluorite oxide; DO_δ represents a dopant oxide consisting of alkaline earth and rare earth oxides; M is a transition metal; Ln is a lanthanide element from La to Tb; n is a number from 0 to 0.15; k is a number having a value from 0.0 to about 0.25; x is a number around 0.5. Fluorite oxides have a fluorite-type crystal structure (face-centered cubic lattice) shown in Figure 2.1 The large tetravalent (+4) cations have an eight-coordination of oxygen ions. An unit cell contains four cations occupying opposite four corners. Common fluorite oxides are CeO_2, ZrO_2, ThO_2, HfO_2. In a fluorite structure, tetravalent cations can be replaced by divalent cations (e.g., Mg^{+2}, Ca^{+2}, Sr^{+2}) or trivalent cations (e.g., Sc^{+3}, Y^{+3}, La^{+3}, Gd^{+3}). Oxygen vacancies are created by this substitution. High oxygen vacancy concentration and oxygen mobility are the most remarkable properties of these oxides. Thus, the fluorite oxides have been extensively studied as oxygen ionic conductors *(19,20)*. Solubility of various fluorite oxide-dopant oxide systems are listed in Table 1.1.

$Ln_{1-x}Zr_xO_{2-0.5x}$ compounds in formula Equation 2 are rare earth zirconates of Pyrochlore (P) structure around x=0.5. The P structure can be considered as an ordered defect fluorite structure. Pyrochlores, such as $Gd_2Zr_2O_7$, in contrast to fluorite-type oxides, are intrinsic anion conductors with substantial ionic conductivity as pure materials where there is no possibility of dopant-vacancy association *(20, 21)*. Therefore, bracketed materials in the above formula are essentially oxygen ion conductors.

These materials are ceramic materials of good physical and chemical stability and are best used as catalyst supports. Transition metals are added into the catalyst to improve the electronic and surface adsorption properties. Typically, the transition metals considered in the above catalyst formulations are copper, nickel, cobalt, chromium, manganese, iron, silver, and gold. Different from conventional transition metal catalysts, the transition metals are used in minor amounts, mainly as additives in the present composite catalyst.

1.3.2 Main Reactions Studied in This Project

$$SO_2 + 2\,CO \rightarrow S + 2\,CO_2 \quad (3)$$
$$CO + 1/2\,O_2 \rightarrow CO_2 \quad (4)$$
$$CH_4 + 2\,O_2 \rightarrow CO_2 + 2\,H_2O \quad (5)$$

The above reaction (3) is the main reaction in SO_2 reduction by CO. It is a typical redox reaction in which SO_2 is reduced into sulfur while CO is oxidized to CO_2. Along with SO_2 reduction by CO, total oxidation of CO and CH_4 were also studied in this project. The fundamental reason to include the three reactions is that all the three reactions involve oxygen transfer from one molecule to another molecule resulting stable end products, that is, complete oxidation. We tried to gain an understanding of the present new catalyst system from a point of view of generic oxidation catalysis. Practically, catalytic properties for CO and hydrocarbon oxidation will be useful information when the reaction streams for SO_2 reduction by CO contain certain amounts of oxygen and/or hydrocarbons. In addition, new complete oxidation catalysts would benefit technologies in (a) gas turbine exhaust cleanup and (b) vehicle exhaust emission control.

Carbon monoxide and hydrocarbons are partial combustion products of fossil fuels and are ubiquitous air pollutants. Methane was used in this work as a model hydrocarbon compound because of its refractory nature. However, methane itself is a potent greenhouse gas and may be regulated in the near future. To date, commercial catalysts for these purposes are predominantly supported precious metals (Pt, Pd). The high cost of precious metals and need for more active catalyst systems have driven further research in this area.

1.3.3 Scientific Rationale

Electronic Property. Ordinary metal oxides can be generally classified into the following two categories according to their electronic properties *(22)*:

p-type (electron excess) conductivity—
CoO, FeO, MnO, NiO, PdO, Ag_2O, Cu_2O, Mn_2O_3, Cr_2O_3, $(Co, Fe, Mg, Zn)Cr_2O_4$

n-type (hole excess) conductivity—
ZnO, CaO, MoO_3, WO_3, Fe_2O_3, V_2O_5, SnO_2, Pb_2O_3, $*TiO_2$, $*ThO_2$, $*SiO_2$, $*Al_2O_3$, $*ZrO_2$, $*CeO_2$, MnO_2

*materials with very low electronic conductivity.

P-type oxides favor the adsorption process involving electron transfer from the oxide to the probe molecule, e.g., $\text{oxide} - e + O_2 \rightarrow O_2^-$; vice versa, the n-type oxides favor the adsorption process involving electron transfer from the probe molecule to the oxide. Fluorite oxides are n-type oxides. More accurately, they are pure oxygen ionic conductors and have very low electronic conductivity. The transition metal oxides selected in the catalyst formula Equations 1-2 are p-type oxides. In the materials science field, previous

studies of fluorite oxides have mainly focused on improving ionic conductivity by alkaline earth and rare earth oxide dopants, while little information is available about doping the fluorite oxide with transition metals. In general, transition metals do not form solid solution with fluorite oxides. The preliminary studies by Pound 1994 *(23)* showed that the addition of CoO, NiO, and CuO improved the electronic conductivity of CeO_2. Therefore, the combination of the two types of materials will facilitate adsorption processes involving any kind of electron transfer. A great amount of effort has been devoted to develop a unitary electronic catalysis theory. Now, it is generally recognized that many different factors are involved in a catalytic process so that a single explanation is unlikely. This work will emphasize the surface chemistry aspects in the reaction mechanistic discussion.

Oxygen Mobility. Two general comments given by Satterfield *(24)* in reviewing practical oxidation catalysts are: (i) most of the metal oxides of interest are non-stoichiometric and the state of oxidation of the catalyst can be affected by reaction conditions; (ii) with oxide catalysts, chemisorbed surface oxygen and lattice oxygen as well as oxygen mobility may play a role. Iwamoto et al. *(25)* investigated the oxygen adsorption properties of sixteen oxides and classified them into three categories:

(A) No oxygen adsorption over the range 10 to 550°C—V_2O_5, MoO_3, Bi_2O_3, WO_3.
(B) Relatively large amounts of oxygen desorption—Cr_2O_3, MnO_2, Fe_2O_3, Co_3O_4, NiO, CuO.
(C) Pre-evacuation at high temperatures is required to observe oxygen desorption—TiO_2, ZnO, SnO_2, Al_2O_3, SiO_2.

Group A oxides are selective oxidation catalysts. Group B oxides mainly catalyze the complete oxidation of olefins. Group C oxides are in the intermediate situation. Such comparisons lead to the assumption that the adsorbed oxygen is related to complete oxidation while the lattice oxygen is more important for selective oxidation. Effect of different oxygen species and oxygen mobility on complete catalytic oxidation of volatile organic compounds was further discussed by Spivey *(26)*.

Perovskite-type mixed oxides, e.g., $LaCoO_3$, of both excellent electronic and ionic conductivity properties, have been extensively studied as oxidation catalysts and electrode materials in the metal oxide fuel cell *(27)*. Correlation of oxygen mobility with oxidation activity for perovskite-type mixed oxide catalysts has been actively pursued in the literature. Oxygen vacancy and mobility properties were also used to interpret the reaction mechanism for CO oxidation over the cerium oxide *(28,29)*. However, the oxygen ion conductors showed CO oxidation activity typically at much higher temperatures than the transition metal oxide catalysts. For reaction of SO_2 with CO over mixed metal oxide catalysts, a redox mechanism involving participation of catalyst surface oxygen/vacancy was proposed *(30-33)*. Although no direct correlation of catalyst activity with oxygen mobility has been established so far, the previous literature generally agrees that oxygen mobility is relevant to oxidation catalysis.

Therefore, we specifically chose oxygen ionic conducting materials as a starting point in pursuing the correlation of oxygen mobility with catalytic activity. In fact, this is one of the fundamental reasons why the above three oxidation reactions (Equations 3-5) were

included in this work. The three oxidation reactions all involve oxygen transfer from one molecule to another. We would like to examine in what way and extent the oxygen vacancy and mobility play a role in these oxidation reactions.

Synergistic Effect. There are a number of examples that an active catalyst can be obtained by combination of different components of low or no catalytic activity. One of well-known catalyst systems is Cu/ZnO that is active for hydrogenation of CO to methanol and the water-gas-shift (WGS) reaction. Regarding the fluorite oxides, composite materials of transition metal and fluorite oxides, such as Cu-Ce-O, Cu-Zr-O, Cu-Th-O, etc., have long been known as catalysts for hydrogenation of CO *(34)*. Frost's "junction effect theory" *(35)* offers a hypothesis that the crucial chemistry occurs entirely on the oxide phases and that the role of the metal component is simply to promote electronically the reactivity of the oxide. Baiker et al. *(36)* found that the (Cu, Ag, Au)/ZrO_2 system catalyzed the hydrogenation of CO_2 and the reverse WGS reaction. Crystallization of the amorphous ZrO_2 resulted in significantly lower activity, which was considered as evidence of the crucial role played by the interface between ZrO_2 and the group IB metal in determining catalytic activity. "Strong metal-support interaction" and reaction at interface concepts have been developed during studies of binary catalyst systems *(37,38)*.

In the environmental catalysis field, CeO_2 and/or ZrO_2 have been widely used in the automotive catalytic converter as additives. Comprehensive information on the role played by CeO_2 in this application was reported in *(39)*. A great amount of effort has been devoted to studying the "strong interaction" of precious metals (Pd, Pt, Rh) with ceria and its effect on catalytic activity. In contrast, oxidation properties of non-precious metals and fluorite oxide composites have rarely been studied. Two of such studies involve the Mn/Ce composite oxide for the low-temperature combustion of fats by Imamuru and Ando *(40)* and the Cu/YSZ (ytrria-stabilized zirconia) catalys for CO oxidation *(41)*.

1.4 Outline of Present Research Approach

Catalyst design is a long-sought objective in the catalysis field *(42)*. Chemical reaction engineering expertise can be used to optimize the catalyst preparation procedure, catalyst pore structure, and active phase distribution. But, truly designing of catalysts from the materials of point of view is still in its infancy. In this study we will apply two important catalysis concepts, metal-support interactions and reactions at interfaces, to metal−fluorite oxide composite catalyst development. The research will focus on identification of major catalyst compositions and structures and their correlation with steady-state catalytic activity.

Among various catalyst systems given by Equations 1-2, the Cu-Ce(D)-O system (D=dopant) was thoroughly studied, while the other systems were briefly examined. The reasons to emphasize the Cu-Ce(D)-O catalyst are: (i) CeO_2 has stable fluorite structure from room temperature to its melting point (2600°C); (ii) fundamental information on both cerium oxide and copper is well established; (iii) cerium and copper are inexpensive elements available in various precursors.

1.5 Literature Cited

1. Goldburg, C.B., and Lave, L.B., *Environ. Sci. Technol.* **26**(11), 2076-78 (1992).
2. Kwong, K.V., Meissner, R.E., and Hong, C.C., in "The Parsons FGC Process Simultaneous Removal of SO_X and NO_X" Presentation at the 1990 Annual Meeting of AIChE, Chicago, Illinois, November 11-16, Chicago, Illinois, **1990**.
3. Flytzani-Stephanopoulos, M., Z. Hu, C.S. Shin, Benedek, K., He, B., and Loftus, P., "Cross-Flow, Filter-Sorbent-Catalyst for Particulate, SO_2, and NOx Control", Final Report to U.S. Department of Energy, Contract No. 22-89PC89805, May 1994.
4. "PETC/Industry Partnership: the NOXSO Process", PETC Review, September, 1990.
5. Gangwal, S.K., and McMichael, W.J., "Bench-scale testing of sulfur recovery process" in Proceedings of the Tenth Annual Gasification and Gas Stream Cleanup Systems Contractors' Review Meeting, DOE/METC-90/6115, Vol.1, DE90009689, August, 1990.
6. Gangwal, S.K., and McMichael, W.J., Agarwal, S.K., Jang, B.L., Howe, G.B., Chen, D.H., and Hopper, J.R., "DSRP, Direct Sulfur Production" in Proceedings of the Thirteenth Annual Gasification and Gas Stream Cleanup Systems Contractors" Review Meeting, 424-43, Contract No. DE-AC21-90MC27224, 1993.
7. Rinckhoff, J.B., and Pfeiffer, J.B. (eds.), "Sulfur Removal and Recovery from Industrial Processes", Advances in Chemistry Series, No.139, American Chemical Society, **1975**.
8. Sarlis, J., and Berk, D., *Ind. Eng. Chem. Res.* **27**, 1951-1954 (1988).
9. Rush, R.E., and Edwards, R.A., "Operating Experience with Three 20 MW Prototype Flue Gas Desulfurization Processes at Gulf Power Company's Scholtz Electric Generating Station," Presented at EPA Flue Gas Desulfurization Symposium, Hollywood, Florida, November 8-11, **1977**.
10. Stiles, A. B., U.S. Patent 3 856 459, **1975**
11. Ryason, P.R., et al., U.S. Patent No. 3 454 355.
12. Haas, L.A., et al. U.S. Patent No. 3 888 970, **1975.**
13. Bajars, L., U.S. Patent 3 978 200, **1976.**
14. Whelan, J. M., U.S Patent 4 081 519, **1978.**
15. Hibbert, D.B., *Catal. Rev.- Sci. Eng.* **34**(4), 391-408 (1992).
16. Chang, S.G., Jin, Y., and Yu, Q.Q., "Catalysts for the Reduction of Sulfur Dioxide to Elemental Sulfur", Technical Report of Energy and Environmental Division, Lawrence Berkeley Laboratory.
17. Flytzani-Stephanopoulos, M., and Liu, W., "Elemental Sulfur Recovery", U.S. Patent No. 5 384 301, 1995.
18. Liu, W., and Flytzani-Stephanopoulos, M., "Composite Catalysts for Carbon Monoxide and Hydrocarbons Oxidation", U.S.Patent Application, serial No. 08/142, 519 (pending).
19. Hagenmuller, P., and Van Gool, W., Solid Electrolytes, Academic Press, New York, 1978.

20. Tuller, H.L., and Moon, P.K., *Materials Science and Engineering* B1 **20**, 171-191 (1988).
21. van Dijk, M.P., de Vries, K.J., and Burggraaf, A.J., *Solid State Ionics* **9&10**, 913-920 (1983).
22. Jose L.G. Fierro and Juan F. Garcia De La Banda., *Catal. Rev.-Sci. Eng.* **28**(2&3), 265-333 (1986).
23. Pound, B.G., Solid State Ionics **52**, 183-188 (1992).
24. Satterfield, C. N., Heterogeneous Catalysis in Industrial Practice, 2nd ed., McGraw-Hill, Inc., 1991.
25. Iwamoto, M., Yoda, Y., Yamazoe, N., and Seiyama, T., *J. Phys. Chem.* **82**, 2564 (1978).
26. Spivey, J.J., *Ind. Eng. Chem. Res.* **26**, 2065-2180 (1987).
27. Minh, N.Q., *J. Am. Ceram. Soc.* **76**(3), 563-88, (1993).
28. Breysse, M., Guenin, M., Claudel, B., Latreille, H., and Veron, J., *J. Catal.* **27**, 275-280 (1972).
29. Breysse, M., Guenin, M., Claudel, B., Latreille, H., and Veron, J., *J. Catal.* **28**, 54-62 (1972).
30. Happel, J., Hnatow, M.A., Bajars, L., and Kundrath, M., *Ind. Eng. Chem., Prod. Res. Dev.* **14**, No.3, 154-158 (1975).
31. Happel, J., Leon, A.L., Hnatow, M.A., and Bajars, L. ibid. **16**, No.2, 150-154 (1977).
32. Hibbert, D.B., and Campbell, R. H., *Appl. Catal.* **41**, 273-287 (1988).
33. Hibbert, D.B., and Campbell, R. H., *Appl. Catal.* **41**, 289-299 (1988).
34. Wallace, W.E., France, J., and Shamsi, A.; in "Rare Earth in Modern Science and Technology" Vol.3, Plenum, New York, 1982.
35. Frost, J.C., *Nature* **334**, 577 (1988).
36. Baiker, M.K, Maciejewski, M., Menzi, S., and Wokaun, A., in Guczi, L., Solymosi, F., and Tetenyi, P., (editors), New Frontiers in Catalysis, Proceedings of the 10th International Congress on Catalysis, Budapest, July, page 1257, 1992.
37. Baker, R.T.K., Tauster, S.J., and Dumesic, J.A., (Editors), "Strong Metal-Support Interactions", American Chemical Society, Washington, DC, 1986.
38. Stevenson, S.A., Dumesic, J.A., Baker, R.T.K., and Ruckenstein, E., (Editors), "Metal-Support Interactions in Catalysis, Sintering, and Redispersion", Van Nostrand Reinhold Company Inc., 1987.
39. Crucq, A., (editor), "Catalysis and Automotive Pollution Control II", Elsevier Science Publishers B.V., Amsterdam, 1991.
40. Imamuru, S., and Ando, M., *Ind. Eng. Res.* **28**, 1452-1456 (1989).
41. Dow, W.P., and Huang, T.J., *J. Catal.* **147**, 322-332 (1994).
42. Bell, A.T., in Hegedus, L.L., et al. (Editors), "Catalyst Design, Process and Perspectives", Wiley, New York, p103, 1987.

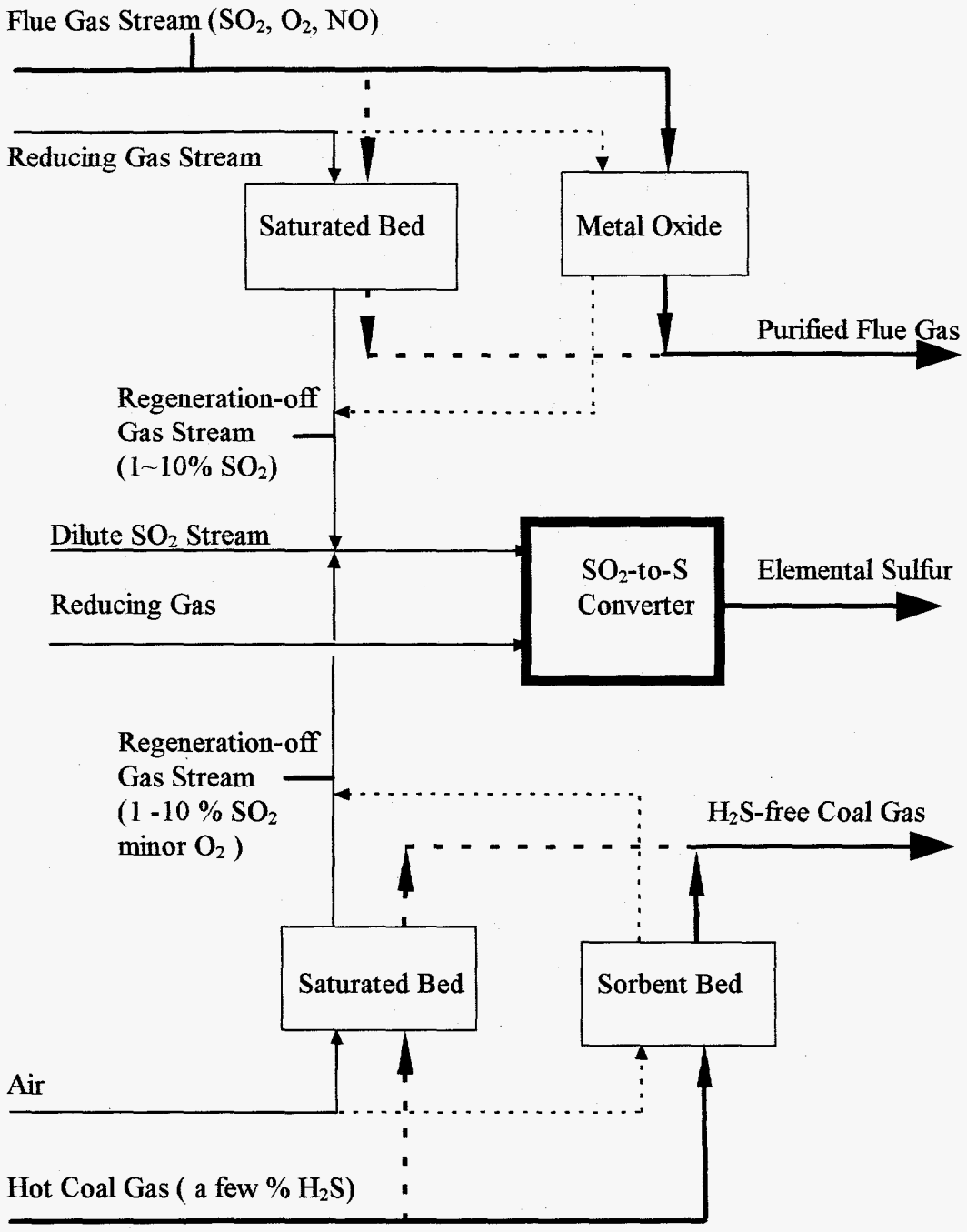

Figure 1.1 Elemental Sulfur Recovery from the Dry Regenerative Flue Gas and Hot Coal Gas Desulfurization Processes.

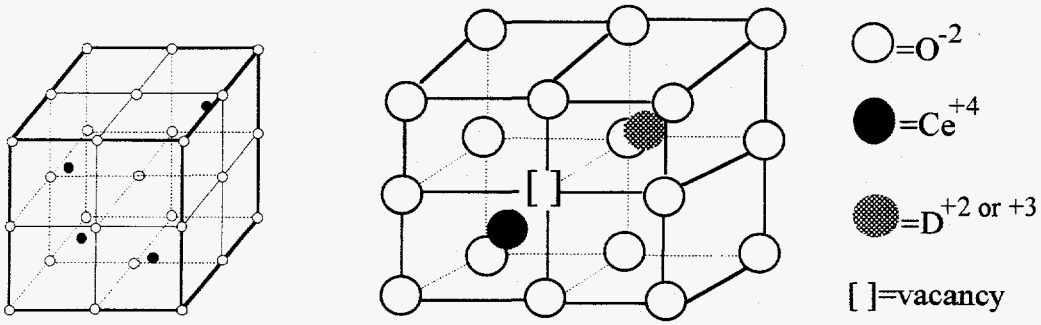

a unit cell

a half unit cell

Figure 1.2 Crystal Structure of Fluorite Oxide.

Table 1.1 Solubility of the common alkaline earth and rare earth oxides in three fluorite oxides (solubility in at. %, the temperature for preparing the solid solution ranged from 1000 to 1800°C).

Dopant Oxide	CeO_2	ZrO_2	ThO_2
MgO	2	6-21	-
CaO	23	14-20	10
SrO	9	-	4
Sc_2O_3	5	5-46	0.5
Y_2O_3	100	5	14
La_2O_3	44	6-32	32
Sm_2O_3	100	10-50	43
Yb_2O_3	33	7-46	5

(data from Kim, D.J., *J. Am. Ceram. Soc.* **72**(8), 1415-21 (1989)).

Chapter 2

Experimental

2.1 Catalyst Preparation

2.1.1 Precursors

Major chemicals and their sources used in this work are listed in Table 2.1. Low purity cerium nitrate containing about 1.5 wt. % La was used in regular catalyst synthesis. The cerium from this precursor was designated as Ce(La) in the catalyst formula throughout the report. High purity cerium nitrate (99.99%, Aldrich) was used to prepare the catalysts containing different dopant ions (Sr, Sc, La, Gd). Cerium acetate (99.9%, Aldrich), heated for 4 h at 750°C in air, was used as the primary precursor of La-free cerium oxide.

2.1.2 Complexation Method with Citric Acid

Courty and Marcilly *(1)* reviewed various preparation methods of bulk mixed oxide catalysts. The complexation method is supposed to permit production of an amorphous solid compound of homogeneous composition without phase segregation from the starting solution. This method was used in preparation of perovskite mixed oxide *(2)* and preparation of Zn-Ti-O binary oxide sorbents *(3)*. In the early stage of this research work, the complexation method was used to prepare cerium oxide catalysts doped with alkaline earth and rare earth elements. The procedure included: (i) Metal nitrates and citric acid of molar ratio one were dissolved in de-ionized water separately; (ii) The citric acid solution was added into the nitrate solution dropwise under constant magnetic stirring at room temperature; (iii) The resulting mixed solution was concentrated into a viscous fluid in a rotary evaporator at 70 - 80°C and the final volume of this fluid was carefully controlled to avoid sticking of the fluid to the glassware; (iv) The fluid was transferred on a glass dish, placed in a vacuum oven where a solid foam was formed during overnight drying at 70-80°C and 15 kPa; (v) The solid foam was calcined at 600°C in a muffle furnace under flowing air for a few hours; (vi) The resulting solid was crushed and sieved, and particles of 420-840 μm were saved for activity tests.

The catalysts prepared by this procedure are listed in Table 3.1 of the Chapter 3. This method indeed yielded high pore volume and large fraction of macropores (>1μm in diameter). But, the resulting catalyst was bulky and had a packing density of typically 0.1 g/cc so that a large reactor volume was required. Moreover, the preparation procedure was time-consuming, and phase segregation and foaming failure often occurred in the vacuum drying process. Therefore, the coprecipitation method was used in subsequent catalyst preparation.

2.1.3 Coprecipitation

The transition metal-fluorite oxide composite catalysts were mainly synthesized by a conventional coprecipitation method consisting of the following steps: (i) Mixing aqueous salt solutions of the metals; (ii) Precipitating the metal ions with carbonate agent with on-line pH monitoring; (iii) Filtering and washing the precipitate twice with de-ionized water at 50 to 70°C; (iv) Drying the filtered cake overnight in an oven at 100°C; (v) Crushing the dried lump into smaller particles and heating it in a muffle furnace at 600 to 700°C for a few hours. Precipitation in the above procedure was the key step in determining final catalyst composition, texture, and structure. Effects of some important parameters in this step are discussed below with Cu-Ce-O as an example.

(a) Precipitation agent. Both ammonium carbonate and sodium carbonate were used as precipitation agents. The advantage of using ammonium carbonate was that no impurity metal ions were introduced because any residual ammonium carbonate easily decomposed at high calcination temperatures. The disadvantage was the formation of metal-ammonia complex that enhanced solubility of transition metal ions (Ni^{+2}, Cu^{+2}, etc.) and often caused loss of transition metals. In contrast, sodium carbonate could induce the complete precipitation of metal ions, but introduces sodium impurity ions. Residual sodium ions sometimes remained on catalyst surface even after careful washing.

(b) Precipitation process and supersaturating. Different precipitation approaches were evaluated for the Cu-Ce-O system. These included (i) pouring stoichiometric amounts of carbonate solution into mixed metal ions solution or vice versa; (ii) gradually adding carbonate solution into the metal ions solution during vigorous stirring or in pH increasing; (iii) gradually adding metal ions solution into the carbonate solution or in pH decreasing. The pH increasing precipitation was found to be the best procedure. Figure 2.1 shows a typical pH profile during precipitation. One transition region in the pH profile was observed with the Cu-Ce-O system, suggesting coprecipitation of Cu^{+2} and Ce^{+3} ions. The addition of carbonate solution was typically stopped at pH~7, the equivalent point.

(c) Precipitation temperature. Solubility of metal carbonates in water increases with temperature. But, increasing precipitation temperature usually gave a catalyst of small, uniform crystal sizes and good copper dispersion. Therefore, most precipitations were carried out at 60 to 75°C.

The coprecipitation was easy to conduct, but very difficult to achieve reproducible results. The underlying fundamental problems are heterogeneity caused by selective precipitation, that is, two metal ions have different precipitation rates, and competitive nucleation and particle aggregation processes. Figure 2.2 shows the pore size distribution of $Cu_{0.15}[Ce(La)]_{0.85}O_x$ catalyst from three different batches. In batch No. 1, coprecipitation was conducted in ascending pH at 60-70°C and the resulting precipitate was immediately washed and dried. An average pore size of 206Å was achieved. In batch No. 2, carbonate solution was poured into the Cu^{+2}+Ce^{+3} solution and the resulting precipitate was left at room temperature for 12 h. A much smaller average pore size, 51Å, was obtained from this procedure. In batch No.3, the catalyst was prepared by following

exactly the same procedure as for the batch No.1. Yet, the resulting pore structure showed somewhat difference. Little theoretical analysis of particle growth during the aqueous phase precipitation has been reported in the literature. Therefore, the precipitation was carried out mostly based on the empirical rules.

The calcination procedure was the second important step in catalyst preparation. Metal carbonate completely decomposed into metal oxide at current calcination temperatures between 600 to 700°C. Most catalysts were calcined in air, while some catalysts were calcined in nitrogen. N_2 calcination was used to keep copper dispersed in the cerium oxide lattice. Since copper oxide and cerium oxide are immiscible, air calcination will promote the segregation of copper oxide from cerium oxide.

2.1.4 Catalyst Support and Impregnation

High surface area of cerium oxide is of general interest in catalysis. Fierro et al., 1985 *(4)* achieved 50-60 m^2/g surface area by carefully controlling the thermal decomposition of amorphous $Ce(OH)_4$. But, the surface area of this type of cerium oxide dramatically decreased at high sintering temperatures. Powell et el., 1988 *(5)* prepared cerium oxide powder by spray drying an aqueous solution of cerium nitrate, citric acid, and nitric acid. A BET surface area of 20 m^2/g was realized after heating for 4 h at 800°C. In this work cerium oxide of reasonable surface area and mesopore size distribution could be made from direct thermal decomposition of commercial cerium acetate (Aldrich). Figure 2.3 shows the pore size distribution of the cerium oxide prepared by 4-h thermal decomposition of cerium acetate at 750°C, while Table 2.2 lists its physical properties. This kind of cerium oxide was used in this work as bulk cerium oxide catalyst and support for various transition metals.

γ-Al_2O_3 support was supplied by LaRoche and its specification is given in Table 2.2. The supported catalysts were prepared by the conventional wet impregnation method using aqueous salt solutions of the metals. The slurry of the support and solution was degassed in vacuum so that the salt solution fully filled the pores of the support during impregnation. After excess solution was drained, the sample was dried for a few days at room temperature and then heated in air for 4 h at 650°C. The pore size distribution of the resulting 15 at.% $CuOx/CeO_2$ catalyst is shown in Figure 2.3. The impregnated catalyst basically kept the original pore structure and the BET surface area was slightly decreased.

2.1.5 Nanocrystalline Catalysts

Cerium oxide is generally considered to be versatile in its oxidation state ($Ce^{+4} \leftrightarrow Ce^{+3}$). The following reaction has appeared extensively in the literature.

$$CeO_2 + CO \text{ (or } H_2) \rightarrow CeO_{2-x} + CO_2 \text{ (or } H_2O) \quad (1)$$

In fact, bulk reduction of cerium oxide only occurs at 700 to 800°C and even surface reduction still requires a temperature around 500°C *(6)*. Bulk CeO_2 is a very stable compound. In contrast, no air-stable, non-stoichiometric cerium oxide has ever been synthesized, because reduced CeO_2 is immediately re-oxidized when exposed to air or

moisture. The catalytic properties of non-stoichiometric cerium oxide were first studied in this work through collaboration. Tschoepe and Ying 1994 *(7)* prepared non-stoichiometric cerium oxide powder in an ultrahigh vacuum (UHV) apparatus. In the UHV chamber, a metallic target was sputtered by magnetron, the metal vapor was rapidly thermalized and supersaturated in argon pressure, which led to homogeneous nucleation of nano-sized clusters in the inert gas phase, and the clusters were collected on the substrate cooled by liquid nitrogen. Then, oxygen was introduced into the chamber to oxidize the metallic clusters into oxide powder that was subsequently scraped off. Due to high operation cost and very small yield, only four catalysts were prepared by this method, i.e., pure CeO_{2-x}, 10 at. % La-doped CeO_{2-x}, 15 at. % Cu-doped CeO_{2-x}, and pure CuO. Detailed description of the preparation and characterization of this new type of catalyst materials was reported in *(7-9)*. The major finding was that non-stoichiometric cerium oxide prepared by this method is stable at atmospheric conditions and can keep certain non-stoichiometry properties even after air calcination at high temperature as illustrated by Figure 2.4. Catalytic activities of the non-stoichiometric cerium oxide catalysts will be reported for comparison with the bulk catalyst.

It should be noted that the same CeO_2 crystal size as prepared by the above procedure can be achieved by the regular precipitation technique followed by low calcination temperatures. The non-stoichiometry of the nanocrystalline cerium oxide probably resulted from the controlled oxidation of metallic clusters on the liquid nitrogen-cooled substrate rather than its crystal size. The cooling effect prevented metallic clusters from being fully oxidized so that intrinsic non-stoichiometry was generated in a cerium oxide particle.

2.2 Catalyst Characterization

2.2.1 Compositional Analysis

For bulk composition analysis, the catalyst powder was dissolved in concentrated hydrofluoric acid solution and then, diluted by de-ionized water, the resulting solution was analyzed by the Inductively Coupled Plasma (ICP) atomic emission spectrometry (Perkin Elmer Plasma 40). The catalyst surface composition was analyzed by X-ray Photoelectron Spectroscopy (XPS). Details of the analyses will be discussed below.

2.2.2 Surface Area, Pore Size, and Metal Dispersion

N_2 Adsorption/Desorption. Total BET surface area was routinely measured by single-point N_2 adsorption and desorption on a Micromeritics 2000 instrument. Selected catalysts were analyzed on a Micromeritics ASAP 2000 apparatus for multipoint BET surface area and pore size distribution measurements. The catalyst sample in the single-point measurement was pretreated by 30-minute heating in 30% N_2/He flow at 300°C and measurement typically run about ten minutes. In the multipoint measurement the catalyst was degassed in vacuum by heating for about five hours and one sample analysis took about ten hours. However, the single-point desorption gave satisfactory result of total BET surface area for the present catalysts.

Chemisorption and Metal Dispersion. The specific surface area of supported metal catalysts is usually measured by specific chemisorption. Characterization of alumina-supported precious metal catalysts (Pt, Pd, Rh) by chemisorption (H_2 or CO) is well established. In contrast, specific surface area of the non-precious metals on a mixed oxide catalyst is difficult to measure. In this work, an effort was made to measure the specific copper surface area in the Cu-Ce-O composite catalyst.

Both H_2 and CO adsorption were used in the literature to measure the metallic copper surface area *(10,11)*. Sinfelt et al. *(11)* found that at room temperature, the adsorption of hydrogen on copper is slow and not completed in times comparable to 1 h. By contrast, adsorption of CO is fast and essentially complete in about 15 minutes and approaches saturation at pressures below 10 cm. However, some literature even reported no irreversible H_2 adsorption on copper at room temperature. The problems with using CO chemisorption to count surface Cu atoms are the extensive physical adsorption, especially when a support of high surface area is used, and the unknown CO/Cu stoichiometry. H_2 adsorption was tried in this work for copper surface area measurement in the Cu-Ce-O catalyst. The Cu-Ce-O catalysts were pre-reduced by H_2 at 350°C for 2 h. But, the copper surface area calculated from the amount of irreversible adsorbed H_2 at room temperature was unreasonably small, which confirms little irreversible adsorption of H_2 on copper.

Recent advancements in specific copper surface area measurement have involved the use of N_2O to form a monolayer of chemisorbed O atoms on metallic Cu surface through the following reaction:

$$Cu + N_2O \rightarrow N_2 + [Cu\text{-}O\text{-}Cu] \qquad (2)$$

The decomposition temperature of N_2O is an important parameter to use this method. Scholten and Konvalinka *(12)* and Evans et al. *(13)* recommended 90-100°C adsorption temperature, because irreproducible results were obtained at lower temperatures and bulk oxidation was significant above 120°C. Both single- and multiple-pulse techniques were used to carry out the measurement. The application of a single-pulse of N_2O in excess of that required to oxidize all the surface copper and a temperature of 90°C has been shown to provide a reliable measurement of specific copper surface area. But, promotion of bulk oxidation of copper in catalysts containing oxides of chromium, zinc and aluminum can lead to an overestimate of the surface copper atoms. The frontal chromatography technique was developed by Chinchen et al. *(14)* to overcome the bulk oxidation problem. An improved method by Bond and Namijo *(15)* involves reacting Cu catalysts with pure N_2O under conditions expected to lead to the formation of a complete layer of O atoms having an O/Cu ratio of 0.5, but without oxidation of the bulk Cu, and the number of chemisorbed O atoms is then determined by TPR. In this work, a modified TPR experimental procedure was performed on a thermal gravitational analyzer (TGA) to measure copper surface area in the Cu-Ce-O catalyst. The procedure consisted of the following steps:

(i) Holding temperature at 30°C in ultra high purity He overnight

(ii) Reducing the copper oxide in the Cu-Ce-O catalyst to metallic copper at a heating rate of 5°C/min up to 350°C in ultra high purity 5% H_2/He and holding the temperature at 350°C for 25 min.
(iii) Lowering the temperature in He to 60°C
(iv) Passing ultra high purity N_2O flow through the sample at 60°C for 1.5 h
(v) Switching to He for 0.5 h and lowering temperature to 30°C
(vi) Reducing the catalyst at a heating rate of 5°C/min to 350°C in ultra high purity 5% H_2/He and holding at 350°C for 25 min.

The copper surface areas measured by this procedure are listed in Table 2.3. It can be seen that the copper surface areas were comparable to the total BET surface areas. As we will see from the STEM and XPS analyses, only a small fraction of the Cu-Ce-O catalyst area is counted for as copper and H_2-reduction does not yield better copper dispersion. The number in Table 2.3 was apparently overestimated. A plausible explanation for such a result is that both cerium oxide surface and copper oxide were reduced during the TPR by 5% H_2/He, and N_2O reacted with both metallic Cu surface and the reduced cerium oxide.

$$CeO_{2-x} + x\ N_2O \rightarrow CeO_2 + x\ N_2 \qquad (3)$$

No method was found in this work to allow a reliable measurement of the specific copper surface area in the Cu-Ce-O catalyst. Therefore, copper dispersion, specific surface activity per copper, and turn-over frequency are not reported in this.

2.2.3 X-ray Powder Diffraction (XRD)

XRD analysis has been routinely used in this work for crystal phase identification based on diffraction peak position and pattern. In addition, two specific uses of the XRD analyses are measurements of miscibility of two kinds of oxides and crystal particle size. According to Vegard's rule, if metal oxide B is soluble in metal oxide A, the lattice spacing change of the metal oxide A imparted by the metal oxide B is proportional to the concentration of the metal oxide B in the lattice.

$$\Delta d_{hkl} = const \cdot C_B \qquad (4)$$

Figure 2.5 shows that ceria lattice spacing monotonically declines with nominal copper content in the Cu-Ce(La)-O composite catalyst calcined in N_2, which suggests that some copper was dissolved in ceria lattice. However, the lattice spacing was changed after the catalyst was calcined in air at 750°C because of the intrinsic insolubility. Crystal particle size can be calculated according to XRD peak broadening *(16,17)*. The accurate calculation needs to correct the internal lattice strain by using two peaks and instrumental broadening. Only simple Sherrer's equation with one XRD peak at 2 theta less than 40° was used for the particle size calculation in this work. At such low 2 theta values, this estimate usually gives satisfactory results.

$$d_p = \frac{0.9\lambda}{B \cdot COS\theta} \qquad (5)$$

where d_p is the diameter of a crystal, λ is the wavelength of X-ray, θ is the X-ray reflection angle, B is the full width of peak at half maximum (FWHM) in radians and estimated by Warren's method:

$$B^2 = B_M^2 - B_S^2 \quad (6)$$

where B_M is the measured peak width, Bs is the instrumental broadening and was around 0.05° for the system used in this work.

XRD analyses in this work were all performed on a Rigaku 300 X-ray Diffractometer with a Rotating Anode Generators, monochromatic detector, and DEC VAX Station II computer for complete control and data recording as well as for data processing. Sample preparation consisted of grinding catalyst powder as fine as possible, well mixing the power with a resin solution, pouring the slurry on a glass square, and drying the sample in an oven. Copper Kα1 radiation was used with power setting of 50kV and 200mA. For crystal phase survey, typical operation parameters were divergence slit of 1°, scattering slit of 1°, receiving slit of 0.3°, and scan rate of 10°/min with 0.02° data interval. For lattice structural analysis, typical operation parameters were divergence slit of 1°, scattering slit of 1° receiving slit of 0.15°, and 0.02° data interval with 2 seconds acquisition time at each point.

2.2.4 Spectroscopic Studies

X-ray Photoelectron Spectroscopy (XPS). XPS is among the most frequently used techniques in catalysis *(18-20)*. It yields information on the elemental composition and the oxidation state of elements. All XPS analyses were performed on a Perkin Elmer 5100 system with 2 mm spatial resolution. This system was configured with an Argon plasma gun for catalyst surface etching and depth profiling, and a dual anode X-ray source (Mg Kα & Al Kα). However, this apparatus does not include a pre-treatment chamber that allows in-situ thermal treatment of samples and no cooling system inside the XPS vacuum chamber. All measurements were carried out at room temperature and without any sample pretreatment. A Mg Kα X-ray source was primarily used in this work and the incident photo energy, hν, is 1253.6eV. The X-ray generator power was typically set at 15kV and 20mA. Sample preparation consisted of attaching a small piece of adhesive tape on a square of tantalum foil and pressing catalyst powder on the tape. Since the materials studied in this work do not have good electronic conductivity, the electrostatic charging was pronounced so that an energy shift from 4 to 6eV was observed. Fortunately, C1s peak was found in all measurements resulting from hydrocarbon moiety in the sample, and was used as an internal standard. Therefore, all binding energies were adjusted relative to C1s at 284.6eV.

An approximate and general expression for calculation of the atomic fraction of any constituent in a sample is given by equation 12:

$$C_X = \frac{I_x/S_x}{\sum_i I_i/S_i} \quad (7)$$

where Cx is the atomic fraction of constituent, x; I is the peak area of a specific peak; S_x is the atomic sensitivity factor that is usually given in the instrument manual. The above equation is accurate when the sample is homogeneous and the sensitivity factor matrix, $\{S_i\}$, is independent for all materials. For a porous catalyst sample, interference from catalyst pores should be kept in mind. Application of equation 12 to the measurement of dispersion of supported particles should be cautious, because XPS has a 2-mm spatial resolution that a physical mixture of small particles (<<2mm, without any dispersion) can yield high atomic fraction. However, the surface composition given by XPS is a valuable number in comparison of catalysts of similar structure.

Electron Microscopy. Scanning electron microscopy (SEM) was performed on a Cambridge Stereoscan 240 MK.3 instrument. Catalyst morphology and composition can be easily obtained by SEM. Figure 2.6 shows two typical SEM micrographs. The top picture is for the $Ce(La)O_2$ catalyst prepared by complexation, while the bottom is for the $Cu_{0.5}[Ce(La)]_{0.5}O_x$ catalyst prepared by precipitation. Numerous macropores were observed with the complexation-made catalyst. The precipitated catalyst looked more dense and homogeneous. However, low magnification of SEM micrographs gave very limited information of catalyst microstructure (in tens of nm scale). Energy dispersive X-ray (EDX) analysis of SEM can give an accurate atomic composition as low as a few percent and the measured value was consistent with the ICP-AE analysis. But, the smallest dimension analyzed by the SEM/EDX was about 1μm. At such scale, most of catalysts appeared homogeneous. In summary, SEM/EDX analyses did not yield really useful information for the present catalyst system.

High resolution transmission electron microscopy (HRTEM) analyses were performed on Akashi EM002B system of the proved point-to-point resolution of 0.18nm. HRTEM is commonly used for studying supported catalysts, especially, precious metal catalysts. Figure 2.7 shows a HRTEM micrograph of the 15 at.% $CuOx/CeO_2$ catalyst. CuO particles cannot be distinguished from CeO_2 particles in the HRTEM picture, because cerium is much heavier than copper. This drawback rendered the HRTEM analysis not suitable for microstructure study of the present Cu-Ce-O catalyst.

Scanning transmission electron microscopy (STEM) combines high magnification and microanalysis capability. It turned out to be an effective tool for the present catalyst characterization and was extensively used in this work. A few STEM analyses were performed on a Vacuum Generators HB-5 system. Most of the analyses were performed on a state-of-the-art Vacuum Generators HB603 system that operates at 300kV and has a X-ray microprobe of 0.14nm optimum resolution. The STEM microprobe can be located at different positions of a small particle (ca.10nm) for elemental analysis and can also be used to simultaneously map several elements of a given region. Elemental mapping was carried out on a 128x128 and 256x256 data matrix. Higher data density gives better compositional resolution but requires longer acquisition time. Although optimum resolution of the microprobe is 0.14nm, the highest magnification achieved in the present STEM analyses was 1 $x10^6$. Image drifting with on-stream measurement time became severe at high magnification, which affected accurate elemental mapping. In addition, sample contamination and thickness also hindered microanalysis at atomic level.

Two methods, dusting and microtoming, were used for STEM sample preparation. The microtoming procedure is outlined as follows: very small amounts of catalyst powder as fine as possible was embedded in a resin matrix; the resin was ultramicrotomed to slices of 80 to 120nm; the slices were supported on a nickel grid and coated with carbon. Detailed procedure was described by Zhao in the STEM analyses of the Mo-Co-Ni/Al_2O_3 catalysts *(21)*. This procedure was time-consuming. Later, it was found that simply dusting catalyst powder on a nickel grid coated by a carbon film can give satisfactory results. It is noted that the sample preparation for HRTEM analysis was the same as for the STEM except for the use of a copper grid instead of the nickel grid.

2.3 Apparatus and Procedure

The schematic of reaction apparatus is shown in Figure 2.8. All catalysts were tested in a laboratory-scale, quartz tube packed bed reactor with a porous quartz frit placed at the middle for supporting the catalyst. The 0.6 cm I.D x 50 cm long reactor was used in regular catalyst test, while a 1.0 cm I.D. reactor was used for high volume of catalyst loading. The reactor tube was heated by a Lindberg furnace. The reaction temperature was monitored by a quartz tube-sheathed K-type thermocouple placed at the top of the packed bed and controlled by a Wizard temperature controller. The reacting gases, all certified calibration gas mixtures with helium(Matheson), were measured with rotameters or mass flow controllers mixed prior to the reactor inlet. The resulting gas mixture flowed downward through the packed bed. Water vapor was introduced with helium bubbling through a heated water bath. The pressure drop of gas flowing through the assembly was small. Thus, experiments were carried out at nearly atmospheric pressure. Elemental sulfur produced by SO_2 and CO reaction was condensed out in a cold trap installed at the outlet of the reactor. A filter was installed at the entrance of GC gas sample loop to remove particulate. Product gas was analyzed by a HP5880A Gas Chromatograph (GC) with a Thermal Conductivity Detector (TCD). A typical 0.5 ml gas was injected into GC column by an automatic sampling valve. Helium was used as the GC carrier and reference gas, each at 30cc/min.

A 1/4" O.D. x 6' long packed column of Chromosil 310(from SUPELCO) operated at 60°C provided base-base separation of CO, CO_2, COS, H_2S, CS_2, and SO_2. This column was primarily used in reaction of SO_2 and CO. CO_2 concentration was analyzed by this column in oxidation of CO and methane by air. But, two additional SS(stainless steel) columns, 10 ft x1/8" packed by 80/100 carbosphere and 5ft x1/8" packed by 80/100 Hayesep T, both from ALTECH, were occasionally used to check carbon balance in oxidation of CO and methane. The Carbosphere column at a temperature program from 30°C to 225°C at 25°C/min separated N_2, CO, CH_4, CO_2, C_2H_4, C_2H_4, C_2H_6. The Hayesep T column at constant temperature 32°C separated air, CH_4, CO_2, C_2H_2, C_2H_4, C_2H_6. No C_2 and CO species were detected in methane oxidation and no hydrocarbon compounds were found in CO oxidation in the presence of water vapor. Thus, carbon balance was easily achieved in oxidation of CO and CH_4. Because Carbosphere and Hayesep T columns required long analysis time, regular gas analysis was performed with the

Chromosil 310 column. The TCD showed linear response to all the compounds mentioned above and a detection limit of less than 100 ppm by volume.

2.4 Literature Cited

1. Courty, P., and Marcilly, C., "A Scientific Approach to the Preparation of Bulk Mixed Oxide Catalysts" In *Preparation of Catalysts III;* Poncelet, G.; Grange, P.; Jacobs, P.A.; Ed.; Elsevier Science Publishers: Amsterdam, The Netherlands, pp485-519, 1983.
2. Baythoun, M.S.G., and Sale, F.R. *J. of Mater. Sci.* **17**, 2757-2769 (1982).
3. Lew, S., Ph.D. Thesis, Massachusetts Institute of Technology, 1991.
4. Fierro, J.L.G., Mendioroz, S., and Olivan, A.M. *J. of Colloid and Interface Science* **107**(1), 60-69 (1985).
5. Powell, B. R., Bloink, R. L., and Eickel, C. C., "Preparation of Cerium Oxide Powders for Catalyst Supports", *J. Am. Ceram. Soc.* **71**(2), C-104-C-106 (1988).
6. Yao, H.C., and Yu Yao, Y.F., *J. Catal.* **86**, 254 (1984).
7. Tschöpe, A. and Ying, J.Y, *J. Nanostr. Mater.* **4**[5], 617 (1994).
8. Tschope, A., Ying, J.Y., Amonlirdviman, K., and Trudeau, M.L., in Mater. Res. Soc. Symp. Proc., "Molecularly Designed Ultrafine/Nanostructured Materials", Materials Research Society, Pittsburgh, PA, in press.
9. Trudeau, M.L., Tschope, A., and Ying, J.Y., *Surf. Interf. Anal.,* in press (1995).
10. Emmett, P.H., and Skau, N., *J. Amer. Chem. Soc.* **65**, 1029 (1943).
11. Sinfelt, J.H., Taylor, W.F., and Yates, D.J.C., *J. Phys. Chem.* **69**, 95 (1965).
12. Scholten, J.J.F., and Konvalinka, J.A., *Trans. Faraday Soc.* **65**, 2465 (1965).
13. Evans, J.W., Wainwright, M.S., Bridgwater, A.J., and Young, D.J., *Appl. Catal.* **7**, 75 (1983).
14. Chinchen, G.C., Waugh, K.C., and Whan, D.A., *Appl. Catal.* **25**, 101 (1986).
15. Bond, G.C., and Namijo, S.N., *J. Catal.* **118**, 507-510 (1989).
16. Cullity, B.D., Elements of X-ray Diffraction, Addison-Wesley Pub. Co., Reading, Massachusetts, 1978.
17. Matyl, R.J., Schwartz, L.H., and Butt, J.B., "Particle Size, Particle Size Distribution, and Related Measurements of Supported Metal Catalysts", *Catal. Rev. - Sci. Eng.*, **29**(1), 41-99 (1987).
18. Niemantsverdriet, J.W., Spectroscopy in Catalysis-An Introduction, VCH, 1993
19. Briggs, D., and Seah, M.P., (Eds.), Practical Surface Analysis by Auger and X-ray Photoelectron Spectroscopy, Wiley, New York, 1983.
20. Wagner, C.D., Riggs, W.M., Davis, L.E., Moulder, J.F., and Muilenburg, G.E., Handbook of X-ray Photoelectron Spectroscopy, Perkin Elmer, Eden Prairie, Minnesota, 1979.
21. Zhao, X., Sc.D. Thesis, Massachusetts Institute of Technology, 1992.

Table 2.1 Materials Inventory for Catalyst Preparation.

Elements	Precursors	Sources
Au	chloroauric acid ($HAuCl_4$)	Aldrich
Ce	cerium nitrate hexahydrate (99 %), containing ca. 1.5 wt. % Lanthanum	Aldrich
Ce	cerium acetate hydrate, 99.9%	Aldrich
Ce	cerium nitrate hexahydrate, 99.99 %	Aldrich
CO_3^{-2}	sodium carbonate, A.C.S. grade	Fisher Scientific
CO_3^{-2}	ammonium carbonate, A.C.S. grade	Fisher Scientific
Cr	chromium(III) nitrate, 98.5%	Johnson Matthey
Co	cobalt(II) nitrate hydrate, 99.99%	Aldrich
Cu	copper(II) nitrate, A.C.S. grade	Johnson Matthey
Gd	gadolinium nitrate, 99.9%	Johnson Matthey
Mn	manganese(II) nitrate tetrahydrate, 98%	Fluka
Ni	nickel nitrate, A.C.S. grade	Fisher Scientific
Pt	hydrogen hexachloroplatinate(IV) hydrate, A.C.S. grade	Aldrich
Tb	terbium(III) nitrate pentahydrate, 99.9%	Aldrich
Y	yttrium nitrate pentahydrate, 99.9%	Aldrich
Zr	zirconium dichloride oxide hydrate, 99.9%	Johnson Matthey

Table 2.2 Properties of Catalyst Supports.

Items	γ-Al_2O_3	CeO_2
source	LaRoche	cerium acetate
Properties:		
particle size, μm	72	100
surface area, m^2/g	300	24
pore volume, cc/g	ca. 1.0	ca. 0.5
packing density, g/cc	0.6	1.0

Table 2.3 Results of N_2O Adsorption Measurement for Specific Copper Area.

samples	initial sample weight (mg)	BET surface area (m^2/g)	adsorbed oxygen mmole	copper surface area (m^2/g)*
15 at. % $CuO+CeO_2$	26.9	18	5.6×10^{-3}	17
15 at. % $CuOx/CeO_2$	31.1	21	4.4×10^{-3}	12
$Cu_{0.15}[Ce(La)]_{0..85}O_x$	19.3	45	1.0×10^{-2}	42
14 at. % CuO/Al_2O_3	17.4	137	1.1×10^{-2}	51

*assuming Cu/O_{ad} =2/1 and copper surface area of 1.47×10^{19} atoms/m^2 or 6.8×10^{-20} m^2/atom.

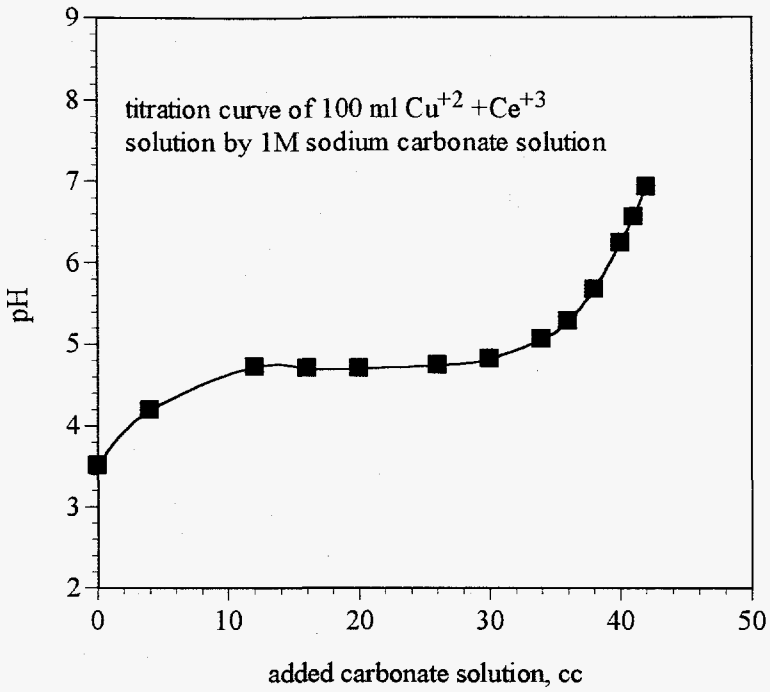

Figure 2.1 A Typical pH Profile During Titration of Cu^{+2} + Ce^{+3} Solution by Carbonate Solution.

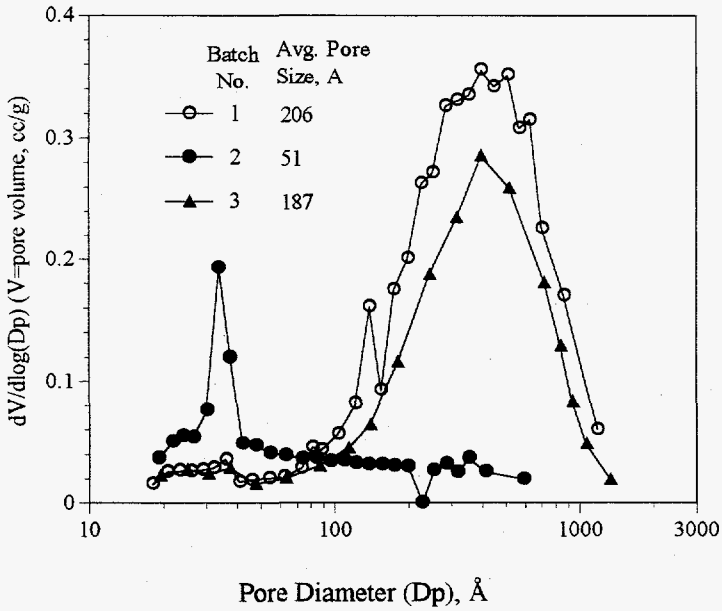

Figure 2.2 dV/dlog(D_p) Desorption Pore Volume Plots for $Cu_{0.15}[Ce(La)]_{0.85}O_x$ Catalysts.

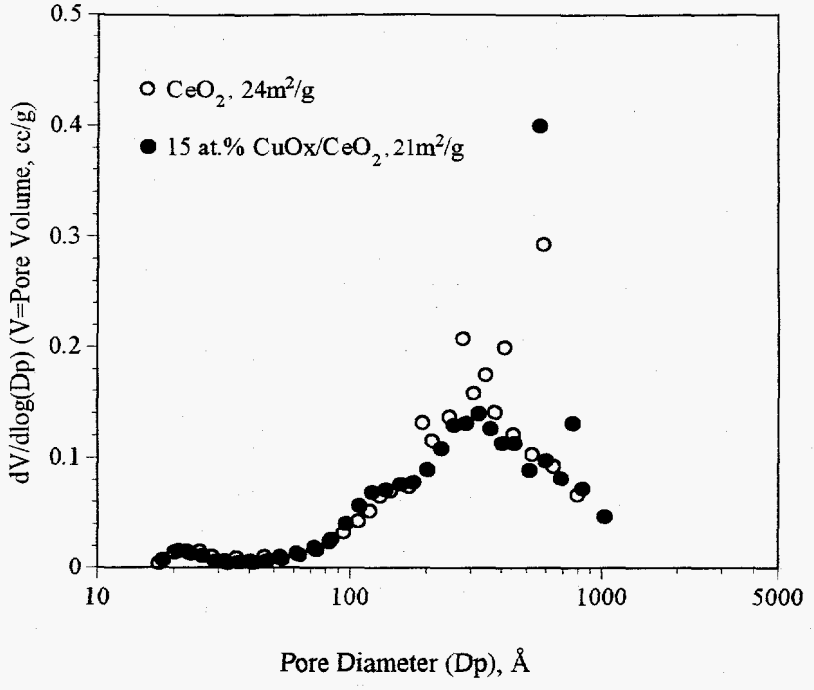

Figure 2.3 dV/dlog(D_p) Desorption Pore Volume Plots For CeO_2 Support and 15 at.% CuOx/CeO_2.

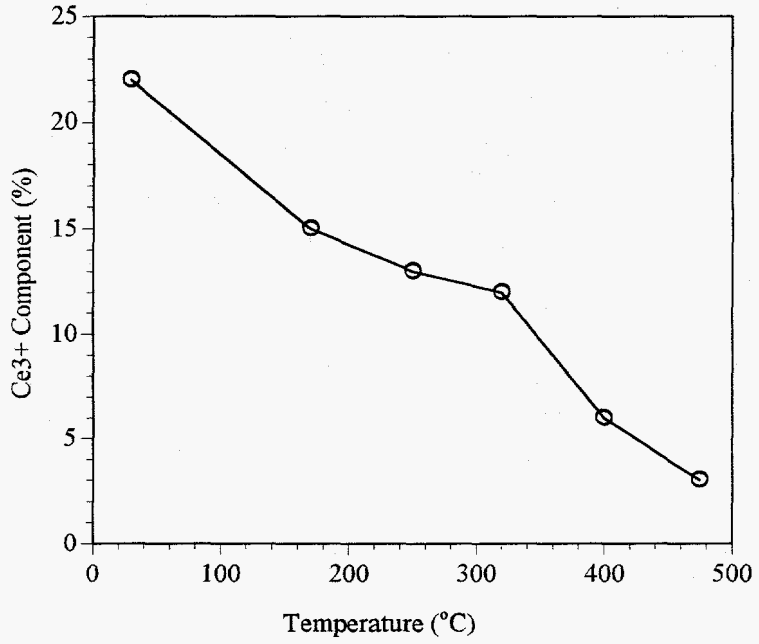

Figure 2.4 Percentage of Ce^{3+}-Component in CeO_{2-x} Determined by Deconvolution of The Ce-3d Core Level XPS Spectrum after Annealing in 1 Kpa Of 1% CO_2/He at the Temperatures Indicated *(8)*.

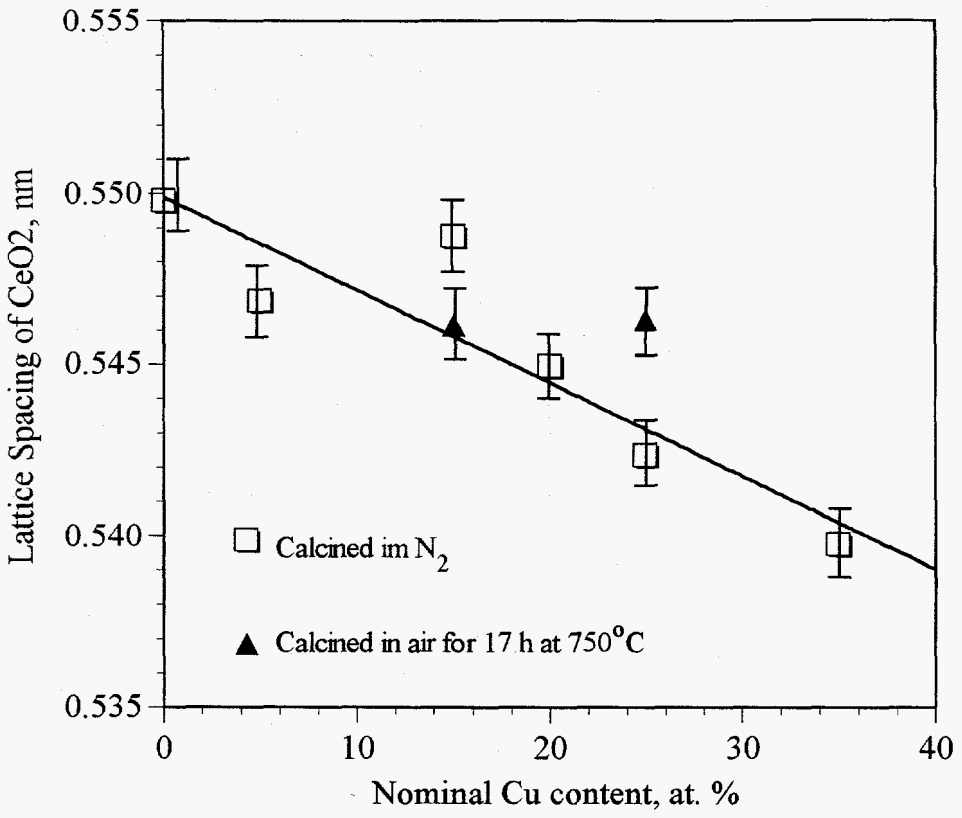

Figure 2.5 Lattice Spacing of Ceria in Cu-Ce(La)-O Composite Catalysts Prepared by Coprecipitation and Calcined in N_2 at 600°C.

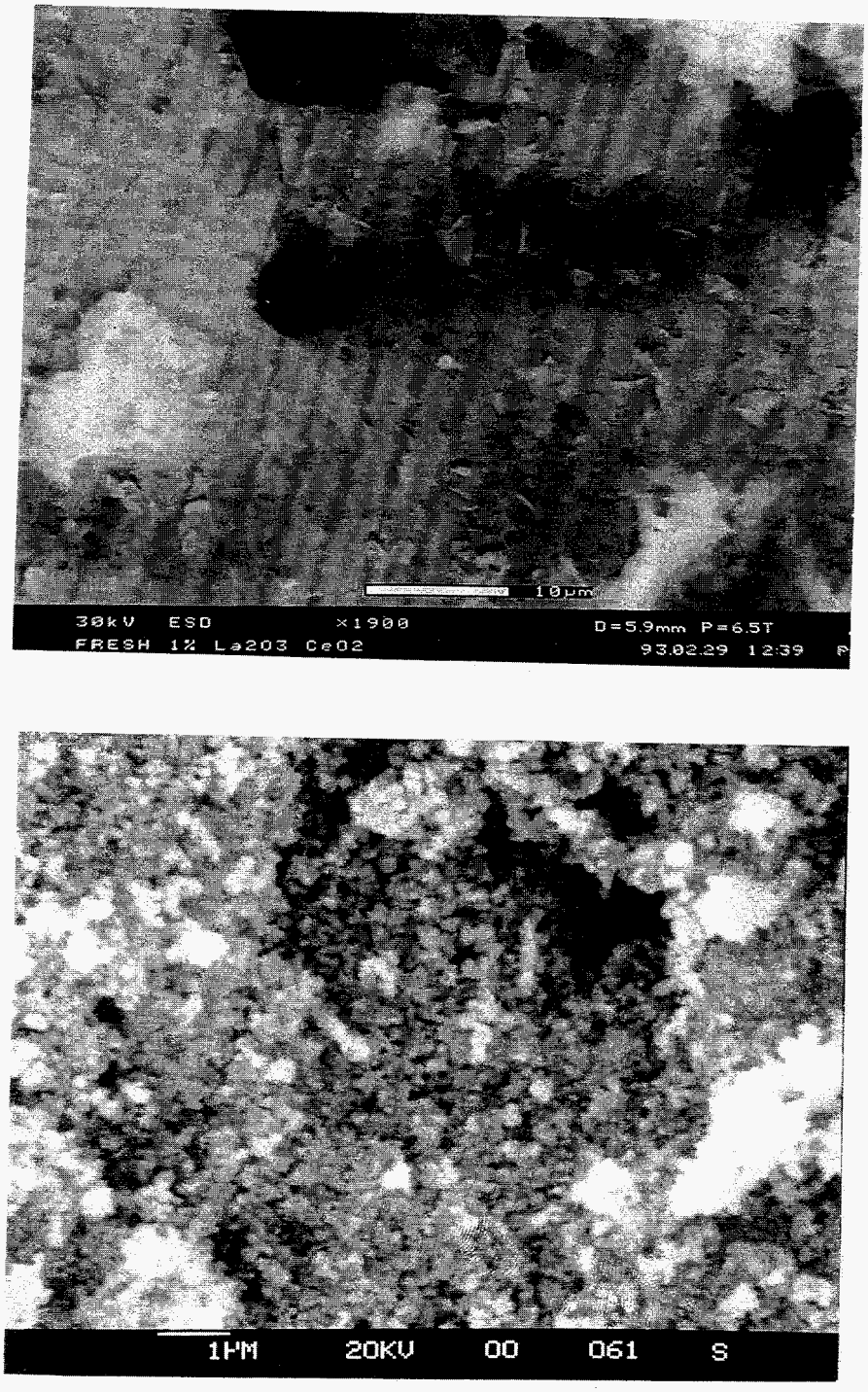

Figure 2.6 SEM Micrographs. Top: $Ce(La)O_2$ prepared by complexation; Bottom: $Cu_{0.5}[Ce(La)]_{0.5}O_x$ prepared by coprecipitation.

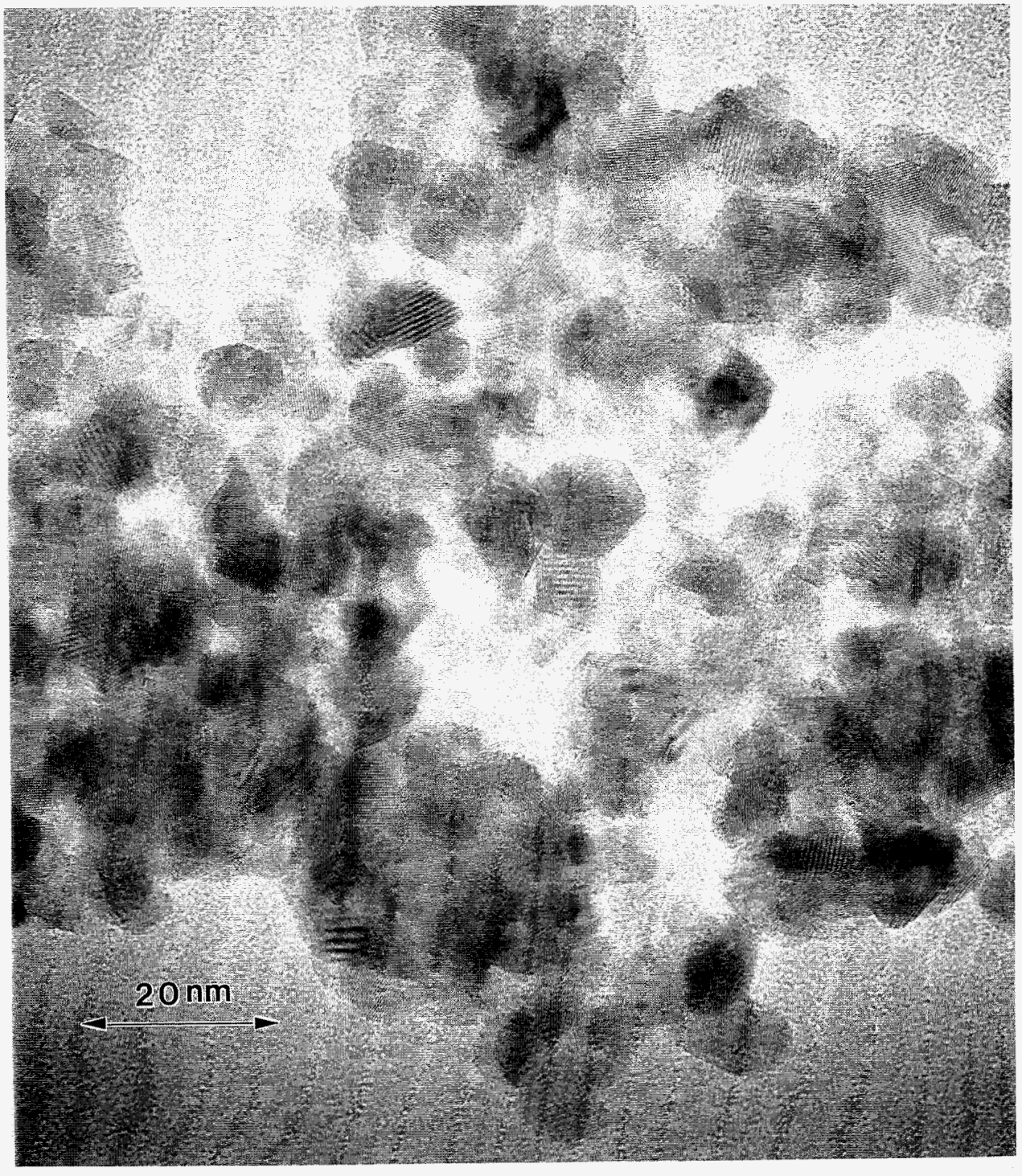

Figure 2.7 TEM Micrograph of 15 at.% $CuOx/CeO_2$ Catalyst.

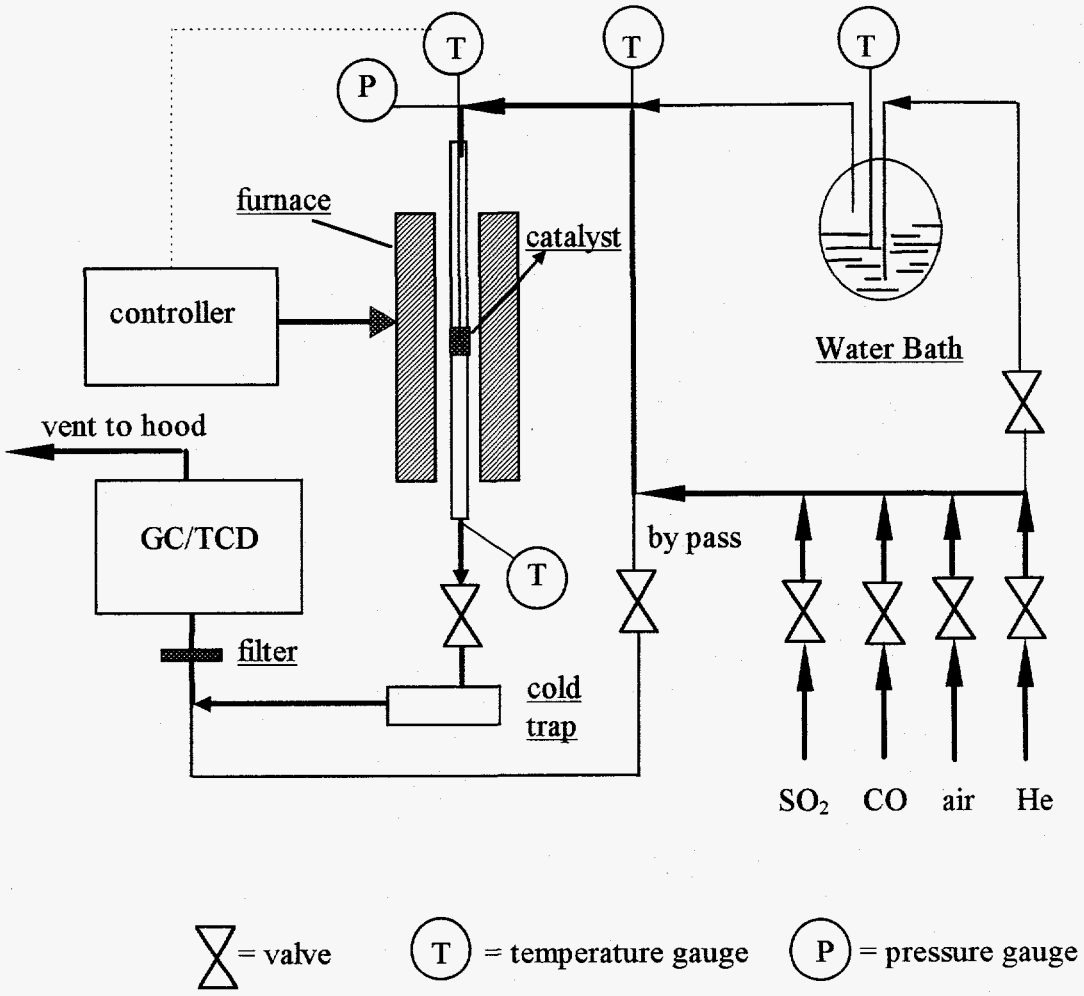

Figure 2.8 Schematic of Reactor Apparatus.

Chapter 3

Reduction of SO_2 by CO to Elemental Sulfur over Ceria Catalysts

3.1 Introduction

The direct reduction of SO_2 by CO to elemental sulfur is thermodynamically favorable but it proceeds very slowly in the absence of a catalyst. A secondary undesirable reaction can occur between CO and elemental sulfur forming COS, which may also reduce SO_2 to elemental sulfur through reaction 3. COS is more toxic than SO_2 and its production should be minimized in a sulfur recovery process.

$$SO_2 + 2\ CO \rightarrow 2\ CO_2 + 1/x\ S_x \quad (1)$$

$$CO + 1/x\ S_x \rightarrow COS \quad (2)$$

$$2\ COS + SO_2 \rightarrow 2\ CO_2 + 3/x\ S_x \quad (3)$$

The redox reaction mechanism has been proposed for the SO_2 reduction by CO *(1-3)*. According to this mechanism, the reductant removes oxygen from the catalyst surface while the oxidant gives up its oxygen to the catalyst, so that the catalyst surface is constantly reduced/oxidized during the course of the reaction. Bulk cerium oxide has been identified as an active catalyst for the SO_2 reduction in our previous work *(4)*. It is well known that CeO_2 has high oxygen vacancy concentration, and these properties can be further enhanced by doping other metal ions into its fluorite-type crystal lattice. The present studies attempt to test if the catalytic activity of CeO_2 can be improved by incorporating dopant ions into its lattice, and to explore other CeO_2-containing catalysts.

3.2 Experimental

All bulk catalysts tested here were prepared by the well-known amorphous citrate method and are listed in Table 3.1. This method provides well dispersed mixed oxides or mixed oxide compounds. The resulting catalyst has large fraction of macropores(>1 mm in diameter) which facilitates pore diffusion. The detailed preparation procedure was gave in Chapter 2. Particles between 20 to 35 mesh (420-840μm) were typically used in the tests. All activity tests were carried out in a laboratory-scale, packed bed flow reactor, which consists of a 1.0 cm I.D. x 50 cm long quartz tube with a porous quartz frit placed at the middle for supporting the catalyst. The detailed description of the reactor apparatus was presented in Chapter 2. The fresh and used catalysts were typically activated by heating

for one hour in 10% CO/He at 600°C. After activation, the reacting gases were introduced and the reaction temperature was raised to about 650°C. When a steady-state reaction was reached, the temperature was lowered in steps of about 50°C until the reaction was quenched. In catalysts evaluation test, the inlet gases of 1 % SO_2 and 2 % CO were used, while the total flow rate was kept at 200 sccm. The packed height of catalyst bed was around 7 mm and the contact time was 0.01 to 0.05 g·s/cc(STP). The elemental sulfur yield, i.e., the fraction of inlet SO_2 converted into elemental sulfur, was derived from the material balance of carbon and sulfur, and occasionally checked by titration of the sulfur collected in the cold trap.

3.3 Results and Discussion

3.3.1 CeO_2 Catalyst

Figure 3.1 shows the experimental results of SO_2 reduction by CO on the bulk CeO_2 catalyst prepared in this work (Table 3.1). When a feed gas of lower CO content than the stoichiometric was used, any SO_2 reacted was converted into elemental sulfur. When the CO content exceeded the stoichiometric amount, 100% SO_2 conversion was achieved at lower reaction temperature, but COS became a major product. For example, when the CO to SO_2 ratio was 3, the SO_2 conversion was 100 % with 36 - 62 % yield of elemental sulfur over the temperature range of 530 to 700°C and corresponding 64 - 38 % of COS yield. The elemental sulfur yield increased with the reaction temperature.

In the following discussion and figures, only the elemental sulfur yield will be presented. Because a feed gas of nearly stoichiometric composition was used and the COS formation was always negligible in these studies, the elemental sulfur yield corresponds with the SO_2 conversion.

3.3.2 Doped CeO_2 Catalysts

It is well known that the oxygen vacancy concentration of CeO_2 can be enhanced by introducing di- or tri-valent metal ions into its lattice. Y_2O_3 was studied as a dopant by Wang et al. *(5)*. Some of their results are listed in Table 3.2. Both the oxygen ion conductivity and activation enthalpy varied with the Y_2O_3 dopant concentration. 1% Y_2O_3 dopant generated the highest oxygen conductivity and the lowest activation enthalpy. Y_2O_3-doped cerium oxide catalysts (Table 3.1) were prepared and tested in this work. Figure 3.2 shows the effect of the Y_2O_3 dopant on the catalyst activity. The 1% Y_2O_3 doped ceria catalyst (CeO_2(Y)) showed higher activity than either the pure CeO_2 or a 10% Y_2O_3-doped ceria (CeO_2(10Y)). Thus, more than 95% elemental sulfur yield was obtained over the CeO_2(Y) at 600°C, that is, at 50°C lower temperature than for the other two catalysts.

When two tri-valent metal ions are introduced in the CeO_2 crystal structure, one oxygen vacancy is created,

$$V_O + 2D \leftrightarrow D \cdots V_O \cdots D$$

where V_O and D denote the oxygen vacancy and trivalent dopant cation, respectively. The dopant ion and the created oxygen vacancies form associated pairs as denoted by $D \cdots V_O \cdots D$. Different dopants will bring about different crystal structure change and interaction of vacancy-ion pair, thus resulting in different oxygen mobility. Table 3.3 lists some experimental results from the studies by Gerhardt-Anderson and Nowick *(6)*, together with the calculated association enthalpy by Butler et al. *(7)*. The 1% Sc_2O_3 dopant in CeO_2 generated the strongest vacancy-ion association and had the lowest oxygen conductivity among trivalent ion-doped ceria. The CeO_2(La) had comparable oxygen conductivity to CeO_2(Y) at low temperature, but had a little lower association enthalpy than the CeO_2(Y). The experimental results of SO_2 reduction by CO on the bulk cerium oxide catalyst doped with these elements are compared in Figure 3.3 on the same total surface area basis. More than 95% sulfur yield was obtained at 600°C for all three catalysts. When the reaction temperature was lowered, the sulfur yields on the CeO_2(Sc) and CeO_2(La) catalysts fell off steeply at about 600°C and 560°C, respectively, while the sulfur yield on the CeO_2(Y) catalyst decreased gradually from 600°C. The CeO_2(La) catalyst showed the highest activity.

Figure 3.4 shows the light-off behavior of the reaction of SO_2 with CO over different catalysts. For this study, we started with the fresh catalyst without any pretreatment by a reducing agent and raised the reaction temperature from 500 to 700°C in a 50°C-step, holding at each temperature for half an hour. The reaction was lighted off at the same temperature(around 650°C) over all the La_2O_3-doped ceria catalysts, independent of dopant content and the amount of catalyst used. But, the reaction did not light-off on the CeO_2(Sc) catalyst even at temperatures as high as 690°C. After one-hour heating under the reaction atmosphere at 690°C, the CeO_2(Sc) catalyst still appeared pale yellow (as fresh ceria), while an activated(reduced) catalyst had a dark blue color. This experiment indicated that the La_2O_3-doped catalyst can be used without activation by a reductant gas, but, higher reaction temperature is needed to initiate the reaction.

The effect of La_2O_3 dopant concentration on the fall-off behavior is shown in Figure 3.5. Increasing the dopant concentration from 1 % to 35 at.% did not improve the catalyst performance. On the other hand, incorporation of 5 at.% MgO into the 1% La_2O_3-doped ceria greatly decreased the catalytic activity. The fall-off temperature over CeO_2(5Mg+La) catalyst is about 50°C higher than that on the CeO_2(La). XRD analysis revealed the existence of only the fluorite ceria crystal phase in these oxide compounds. The vacancy association energy in MgO-doped ceria is 1.23eV, much higher than that in the La_2O_3-doped ceria, 0.26eV, as shown in Table 3.3. This strong association stabilized

the oxygen vacancy and thus capped outside oxygen on the CeO_2(5Mg+La) catalyst surface. Higher temperature would be needed to remove the more strongly bonded surface capped oxygen to maintain the reduction/oxidation cycle. This issue will be further addressed later. The CeO_2(La) catalyst was used in further studies because of its superior performance.

3.3.3 CeO_2(La) Catalyst

Figure 3.6 shows the effect of contact time on the elemental sulfur yield over the CeO_2(La) catalyst. The contact time did not change the product selectivity. More than 95% sulfur yield was always achieved under complete SO_2 conversion. The elemental sulfur yield curve fell off at a lower temperature when a longer contact time was used. However, above a value of 0.02 g·s/cc(STP) contact time, the fall-off temperature stays at about 500°C. This is the temperature associated with the reduction of surface capping oxygen of ceria according to Yao and Yao's studies *(8)*. Therefore, when the reaction temperature is below 500°C, CO cannot reduce the catalyst surface to provide the active sites for SO_2 reduction. The catalyst showed good stability as indicated by Figure 3.7. No deactivation was observed during a 11-hour steady-state run at 532°C. As stated before, only a small amount of COS was formed with the dry feed gas of nearly stoichiometric composition.

For the same contact time, 0.02g·s/cc(STP), the fall-off temperature over the CeO_2(La) catalyst shown in Figure 3.5 is about 50°C higher than that in Figure 3.6. The feed gas used in the studies shown in Figure 3.5 was contaminated by a small amount of water vapor (~400 ppm). This indicated that the catalyst may be poisoned by water vapor.

3.3.4 Water Vapor Effects

The introduction of water vapor in the reacting atmosphere may affect the catalytic activity by adsorption on the catalyst surface, and change the product distribution through the following reactions:

$$COS + H_2O \rightarrow H_2S + CO_2 \quad (4)$$

$$CO + H_2O \rightarrow H_2 + CO_2 \quad (5)$$

$$H_2 + [S] \rightarrow H_2S \quad (6)$$

$$3/x\ S_x + 2\ H_2O \rightarrow 2\ H_2S + SO_2 \quad (7)$$

The [S] in reaction 6 indicates any kind of sulfur source, such as metal sulfide and adsorbed surface sulfur. The reactions 4-7 listed above are thermodynamically feasible under present conditions.

The effects of water vapor on the SO_2 reduction by CO are illustrated in Figure 3.8. Upon the addition of 3% H_2O, three small peaks of CO_2, H_2S, and SO_2, appeared simultaneously. The CO_2 peak may result from the reaction of H_2O with adsorbed CO on

the catalyst surface, and the H_2S and SO_2 peaks may be produced by the reverse Claus reaction of adsorbed surface sulfur and H_2O. In the presence of 3% H_2O, sulfur compounds in the product stream consisted of H_2S, SO_2 and elemental sulfur, while COS was negligible. The ratio of H_2S to SO_2 was approximately stoichiometric, because in the feed gas the stoichiometric ratio of $[CO]/[SO_2]=2$ was used. When the reaction temperature was lowered from 660 to 617°C, no apparent product distribution change was seen. When the temperature was lowered to 580°C, the H_2S decreased a little while the SO_2 increased a little. The catalyst quickly deactivated when the temperature was further lowered to 540°C, while no deactivation was observed for the dry feed gas at this temperature(see Figure 3.6). Li et al. *(9,10)* in their studies of CO adsorption on ceria found that surface OH groups inhibit CO adsorption and that CO adsorption depends on the degree of surface dehydroxylation. Apparently, then, in the present study the water vapor lowered the catalyst activity for SO_2 and CO reaction by taking up the active surface sites for CO chemisorption. The overall effect of water vapor is displayed as partial poisoning of the catalyst and promotion of H_2S formation.

The variation of product gas distribution with the $[CO]/[SO_2]$ ratio is shown in Figure 3.9. The H_2S formation increased with the $[CO]/[SO_2]$ ratio; conversely, the SO_2 concentration decreased with the $[CO]/[SO_2]$. The maximum elemental sulfur yield was obtained around the stoichiometric $[CO]/[SO_2]$ ratio. In the region of $[CO]/[SO_2]>2$, H_2S may be produced by hydrolysis of COS and the reaction of the adsorbed sulfur on the catalyst surface with hydrogen from the WGS reaction. In the region of $[CO]/[SO_2] < 2$, COS formation is negligible and thus, the H_2S may come mainly from the reaction of surface sulfur with hydrogen. Because more reductant gas was consumed to produce H_2S than elemental sulfur, there was not enough reductant left for the reduction of SO_2 so that some of the inlet SO_2 was not reduced. This became more obvious when less CO was used in the feed gas. Although the reverse Claus reaction 7 is thermodynamically feasible at high temperature, this reaction would give a simultaneous production of H_2S and SO_2. This is not the case as shown in Figure 3.9. Further testing showed that at a given temperature the H_2S formation increased with the water vapor content. In a practical application, since the H_2S and SO_2 in the product stream are in stoichiometric amount when the $[CO]/[SO_2]$ is around 2, a downstream Claus reactor may be directly used to convert the H_2S and SO_2 into elemental sulfur. Alternatively, for a dry regenerative flue gas desulfurization process, the product gas from the sulfur recovery unit can be recycled to the burner after condensation and collection of sulfur.

3.3.5 CeO_2(La) is an Active Catalyst for Claus Reaction and COS Hydrolysis

Catalytic activity of CeO_2(La) for Claus reaction and the water vapor effect are illustrated by Figure 3.10. More than 80% inlet SO_2 was converted into elemental sulfur

around 230°C in the absence of H_2O. Upon addition of 13% H_2O, SO_2 increased by 65% of its inlet concentration while 90% of the inlet H_2S disappeared. The excess SO_2 is postulated to come from the following reactions:

$$H_2S_{ads} + 2\ H_2O \rightarrow SO_2 + 3\ H_2 \quad (8)$$

$$S_{ads} + 2\ H_2O \rightarrow SO_2 + 2\ H_2 \quad (9)$$

where S_{ads} was the sulfur produced by the previous Claus reaction and deposited on the catalyst. The catalyst lost its activity immediately when exposed to H_2O. Its activity cannot be recovered by stopping H_2O. The catalyst became activated only when the temperature was raised over 500°C. There was a burst of SO_2 around 500°C during temperature rise, where twice the inlet SO_2 was released with consumption of 78% of the inlet H_2S. This may be explained by oxidization of H_2S by adsorbed H_2O. It seems that the previously adsorbed H_2O on the catalyst desorbs only at high temperatures (>500°C). The catalyst was completely re-activated after removal of the adsorbed H_2O. Figure 3.11 shows that complete conversion of COS to H_2S was achieved at temperatures above 270°C.

3.4 Mechanistic Consideration

Two reaction mechanisms have been proposed for the reduction of SO_2 by CO, namely the redox mechanism *(1,2)* and the COS intermediate mechanism *(11-13)*. According to the latter, CO first forms a COS intermediate with the sulfided catalyst, and then COS reduces SO_2 to elemental sulfur. The evidence used to argue in favor of this mechanism is (i) XRD-detected metal sulfide in the used catalyst, and (ii) COS formation upon passing CO gas through the catalyst bed. In the present study, only the ceria (CeO_2) crystal phase was found in the fresh and used ceria catalyst by XRD analysis. In another test, when the steady-state reaction over the CeO_2(La) catalyst was reached at 650°C, the feed gas was switched to He, and after a ten-minute flush, CO was allowed to scavenge the catalyst surface for half a hour. No COS was detected in the exit gas stream. The same results were obtained at 600°C and 550°C. Furthermore, a significant amount of CO_2 was released during the regeneration of a spent ceria catalyst with CO, while no COS was observed. These results argue against the COS intermediate mechanism for SO_2 reduction by CO over ceria catalysts. However, our tests have shown that CeO_2(La) is also a good catalyst for the reduction of SO_2 by COS, with more than 96% SO_2 converted to elemental sulfur over the temperature range from 390 to 650°C.

We propose that the SO_2 reduction by CO on ceria proceeds via the redox mechanism:

$$\text{Cat-O} + \text{CO} \rightarrow \text{Cat-[ ]} + \text{CO}_2$$

$$\text{Cat-[ ]} + \text{SO}_2 \rightarrow \text{Cat-O} + \text{SO}$$

$$\text{Cat-[ ]} + \text{SO} \rightarrow \text{Cat-O} + \text{S}$$

We found that the catalyst had to be pre-reduced to initiate the reduction/oxidation cycle at low temperature. This is evidenced by the catalyst color change. The fresh CeO_2 was pale yellow and had no activity. The activated catalyst appeared dark blue, which is the characteristic color of partially reduced CeO_2. The reaction proceeds easily on the catalyst pretreated by a reducing agent, such as CO. In contrast, the reaction is difficult to start in the reacting atmosphere due to the presence of both a reductant(CO) and an oxidant(SO_2), and may need high temperature (Figure 3.4). As one oxygen vacancy is created by the release of one CO_2 molecule, the SO_2 donates its oxygen to that vacancy to form a SO group. The SO is mobile on the surface until it finds another vacancy to donate its oxygen or a vacancy may migrate to a neighboring site to accept its oxygen. High oxygen mobility in the catalyst will facilitate the oxygen transfer from one site to another on the surface or from the bulk to the surface. However, the oxygen vacancy can be taken up by other molecules existing in the reacting gas phase, such as H_2O and O_2. The more strongly these impurity oxygen atoms attach to the vacancy, the more severe a poisoning effect they will bring about. The creation of oxygen vacancies on the surface is, then, a key step.

Incorporation of dopant ions into ceria lattice enhances the oxygen vacancy concentration and mobility. But, the vacancies created by the dopant on a fresh catalyst surface are always capped by the oxygen atoms from ambient oxygen or water. Therefore, the capping oxygen has to be removed to activate the catalyst. The oxygen vacancy and the dopant ion are associated in pairs by a certain energy. The stronger this association, the lower the vacancy energy state is and the more strongly the vacancy is capped by an outside oxygen. In other words, strong association increases the difficulty of removing the capping oxygen. The CeO_2(La) material of lower association energy than the CeO_2(Y), showed higher activity, although these two catalysts have the same oxygen ion conductivity(Table 3.3 and Figure 3.3). The CeO_2(Sc) has the highest vacancy-ion association energy among tri-valent ion-doped ceria so that the reaction cannot proceed(Figure 3.4) without removing the strongly capped surface oxygen in a highly reducing atmosphere. As discussed earlier, the vacancy association energy in the MgO doped ceria is 1.23eV (Table 3.3), even greater than that of the CeO_2(Sc), 0.67eV. Apparently, the addition of 5 at.% MgO into the CeO_2(La) greatly stabilized the oxygen vacancy and decreased the catalytic activity(Figure 3.5). Table 3.3 indicates that the association energy increases with dopant content. Therefore, increasing the dopant concentration does not necessarily enhance the catalytic activity. This is evidenced by the data shown in Figure 3.5, where increasing La_2O_3 dopant from 1 to 35 at.% had no effect on the catalyst performance. For a catalyst, surface adsorption/desorption processes are always important in addition to these oxygen vacancy and mobility properties. Because MgO is a more basic oxide than La_2O_3 and La_2O_3 is more basic than CeO_2, the present results indicate that the acid/base properties of the catalyst play little role in the reduction of SO_2 by CO.

3.5 Conclusions

Cerium oxide is an active catalyst for SO_2 reduction by CO and its activity can be enhanced by doping La_2O_3 into its lattice. More than 95% elemental sulfur recovery can be achieved on CeO_2-based catalysts at reaction temperatures about 500°C or higher when the feed gas has the stoichiometric composition. The reaction of SO_2 with CO on the catalyst appears to proceed according to the redox mechanism. The results of our work demonstrate a correlation of the catalytic activity with the oxygen vacancy mobility and energetics in a doped ceria catalyst. Water vapor partially poisons the ceria catalysts and promotes the production of H_2S. The elemental sulfur yield is lowered in the presence of water. Further work with transition metal modified cerium oxide catalysts will be reported in the next chapter.

3.6 Literature Cited

1. Happel, J.; Leon, A.L.; Hnatow, M.A.; Bajars, L. *Ind. Eng. Chem., Prod. Res. Dev.* **16**, 150-154 (1977).
2. Hibbert, D.B.; Campbell, R.H. *Appl. Catal.* **41**, 289-299 (1988).
3. Hibbert, D.B.; Campbell, R.H. *Appl. Catal.* **41**, 273-287 (1988).
4. Flytzani-Stephanopoulos, M.; Hu, Z. U.S. Patent 5 242 673, 1993.
5. Wang, D.Y.; Park, D.S.; Griffith, J.; Nowick, A.S. *Solid State Ionics* **2**, 95-105 (1981).
6. Gerhardt-Anderson, R.; Nowick, A.S. *Solid State Ionics* **5**, 547-550 (1981).
7. Butler, V.; Catlow, C.R.A.; Fender, B.E.F.; Harding, J.H. *Solid State Ionics* **8**, 109-113 (1983).
8. Yao, H.C.; Yao, Y.F.Y. *J. Catal.* **86**, 254-265 (1984).
9. Li, C.; Sakata, Y.; Arai, T.; Domen, K.; Maruya, K.; Onishi, T. *J. Chem. Soc., Faraday Trans. 1*, **85**, 929-943 (1989).
10. Li, C.; Sakata, Y.; Arai, T.; Domen, K.; Maruya, K.; Onishi, T. *J. Chem. Soc., Faraday Trans. 1*, **85**, 1451-1461 (1989).
11. Haas, L.A.; Khalafalla, S.E. *J. Catal.* **29**, 264-269 (1973).
12. Haas, L.A.; Khalafalla, S.E. *J. Catal.* **30**, 451-459 (1973).
13. Baglio, J.A. *Ind. Eng. Chem. Prod. Res. Dev.* **21**, 38-41 (1982).

Table 3.1 Catalysts Tested in This Study.

No.	Catalyst	Composition[a]	Surface Area (m^2/g)	
			fresh[b]	used[c]
1.	CeO_2	CeO_2	34.0	29.0
2.	CeO_2(Y)	1 at. %Y	27/23[d]	9.5/20[d]
3.	CeO_2(10Y)	10 at. %Y	19.8[d]	19.3[d]
4.	CeO_2(Sc)	1 at. % Sc	47/30[d]	30/27[d]
5.	CeO_2(La)	1 at. % La	34.0	19.5
6.	CeO_2(6La)	6 at. % La	32.6	22.8
7.	CeO_2(20La)	20 at. % La	37.5	19.4
8.	CeO_2(35La)	35 at. % La	28.8	17.2
9.	CeO_2(5Mg+La)	5 at. % Mg + 1 at. % La	30.2	22.4

a. "at. %" denotes the corresponding metal atomic percentage.
b. Measured before use.
c. Measured after about 6-hour reaction time on-stream.
d. Fresh catalysts were further calcined for 15 h at 750°C after 3-h calcination at 600°C.

Table 3.2 Variation of Oxygen Conductivity and Activation Enthalpy With Composition of CeO_2:Y_2O_3 (data from Wang et al. *(5)*).

mole % Y_2O_3	H_σ (ev)[a] at 180°C	σ (S/cm) at 180°C	σ (S/cm) at 580°C
0.0 %	0.92	3×10^{-8}	2×10^{-4}
1 %	0.79	1.8×10^{-6}	8×10^{-3}
10 %	1.15	1.5×10^{-7}	4.5×10^{-3}

a. H_σ related to σ by $\sigma T \propto \exp(-H_\sigma/RT)$.

Table 3.3 Association Enthalpy h_A and Conductivity for Solid Solutions of Different Dopants in CeO_2 (data from Gerhart-Anderson and Nowick *(6)*).

Dopant	Ionic radius (Å)	h_A (ev)[a] 1 % D_2O_3	h_A (ev)[a] 6 % D_2O_3	σ (S/cm) at 400°C for 1% D_2O_3
La^{+3}	1.18	0.14/0.26[b]	0.18	3.3×10^{-4}
Gd^{+3}	1.06	0.12/0.17[b]	0.16	5.3×10^{-4}
Y^{+3}	1.01	0.21/0.38[b]	0.26	3.3×10^{-4}
Sc^{+2}	0.87	0.67/0.62[b]	—	4.4×10^{-7}
Mg^{+2}	0.89	1.23[b]	—	—
Ca^{+2}	1.12	1.12[b]	—	—

a. h_A is related to σ by $\sigma T \propto \exp(-(h_A + h_m)/RT)$

b. data were calculated by Butler et al. *(7)*.

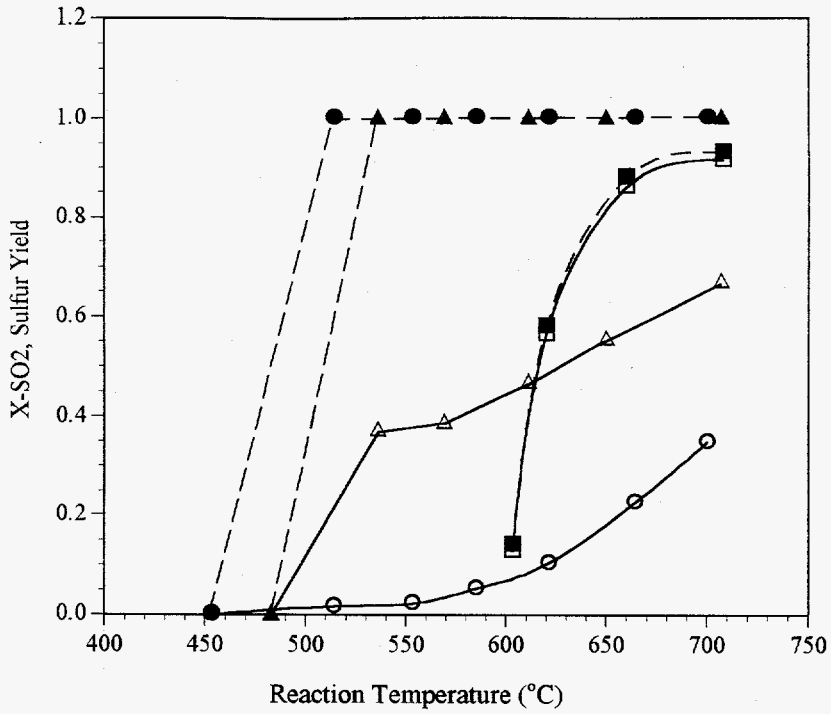

Figure 3.1 Elemental Sulfur Yield and SO_2 Conversion on Bulk CeO_2 Catalyst (R_{CO}=[CO]/[SO_2]; 1% SO_2, 0.017s·g/cc(STP)). R_{CO} = 4: O ●; R_{CO} = 3: ▲ △; R_{CO} = 1.9: ■ □ (filled symbols for SO_2 conversion, unfilled ones for sulfur yield).

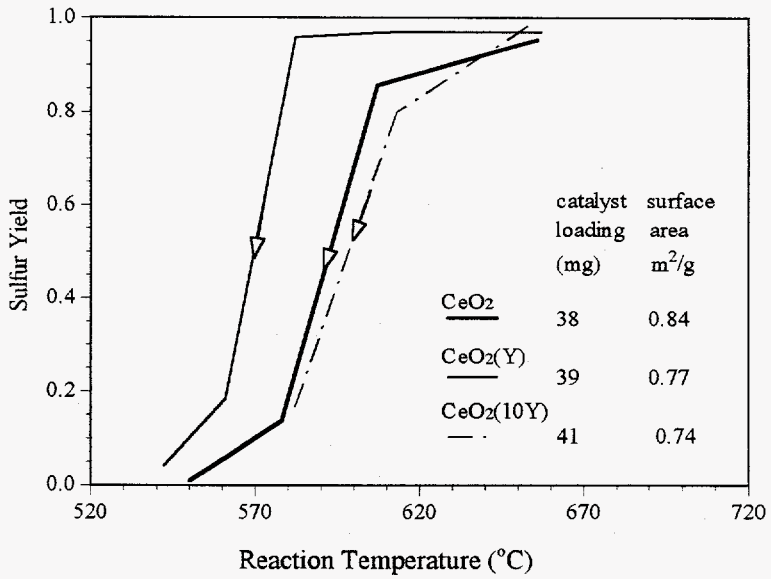

Figure 3.2 Effect of Y_2O_3 Dopant Content in Ceria on Catalyst Activity ([CO]/[SO_2]=2; 1% SO_2, 0.012 s·g/cc(STP)).

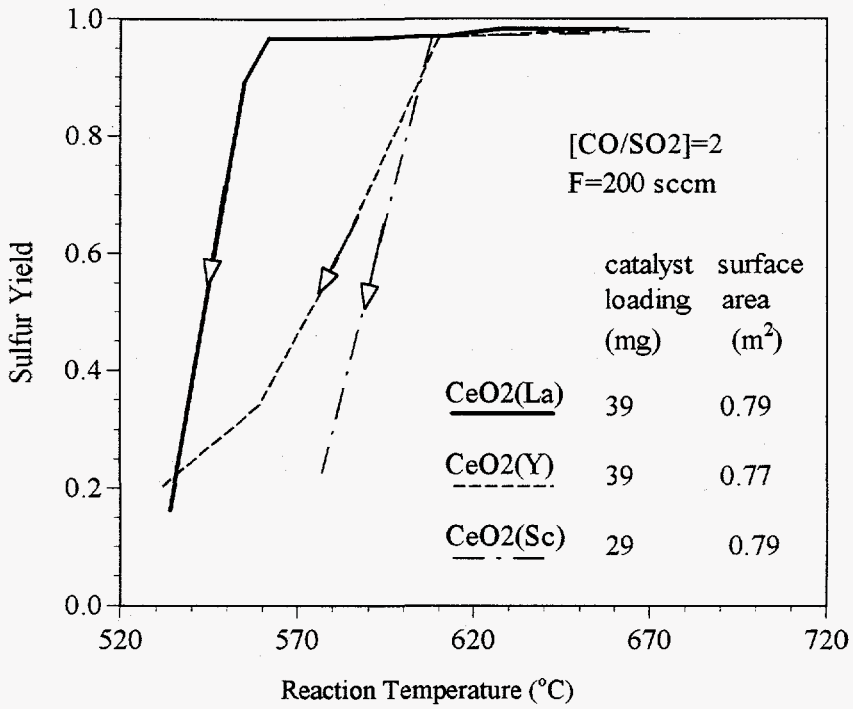

Figure 3.3 Effect of Different Dopants in Ceria on Catalyst Activity.

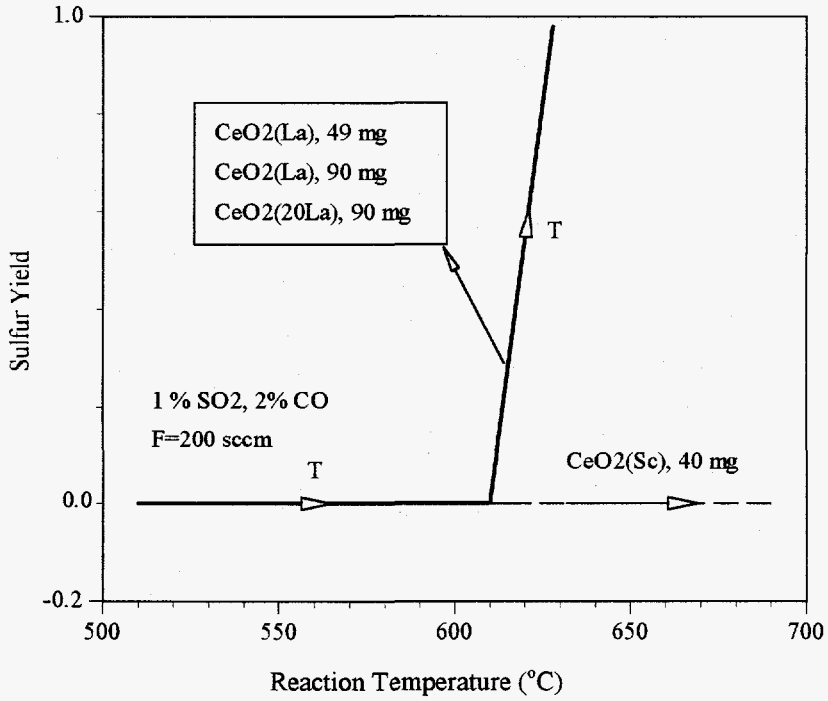

Figure 3.4 Light-off Behavior over Doped Ceria Catalysts in the Absence of Activation.

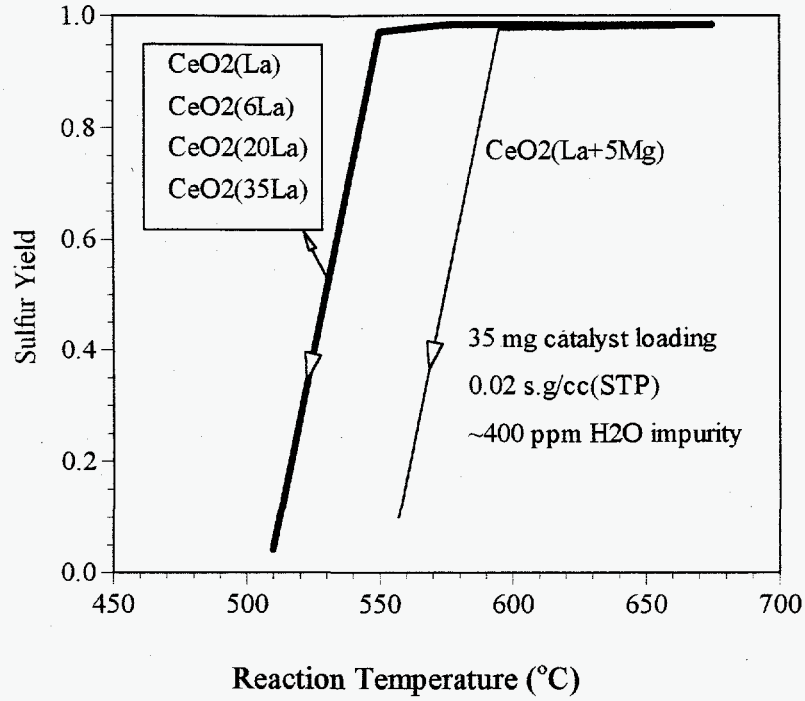

Figure 3.5 Effects of La_2O_3 Dopant Content and MgO Dopant on Catalyst Activity.

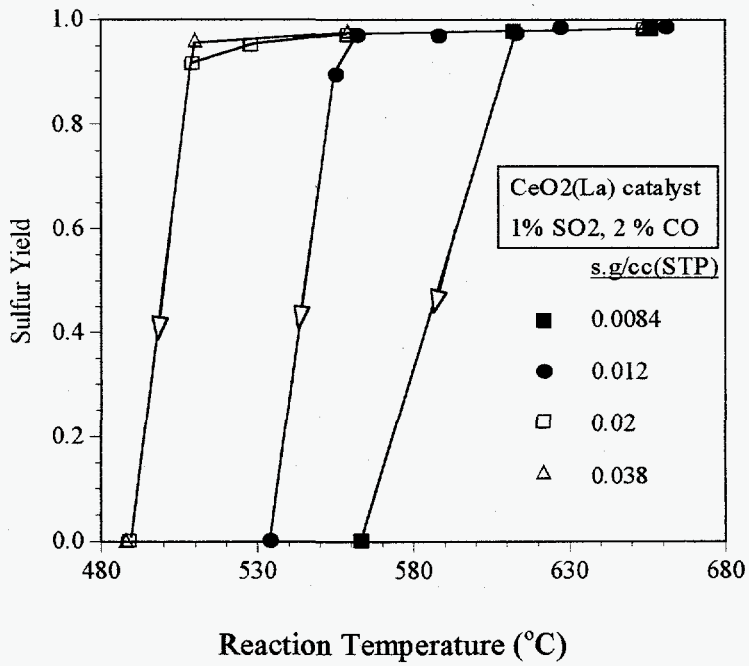

Figure 3.6 Effect of Contact Time on Sulfur Yield over the CeO_2(La) Catalyst.

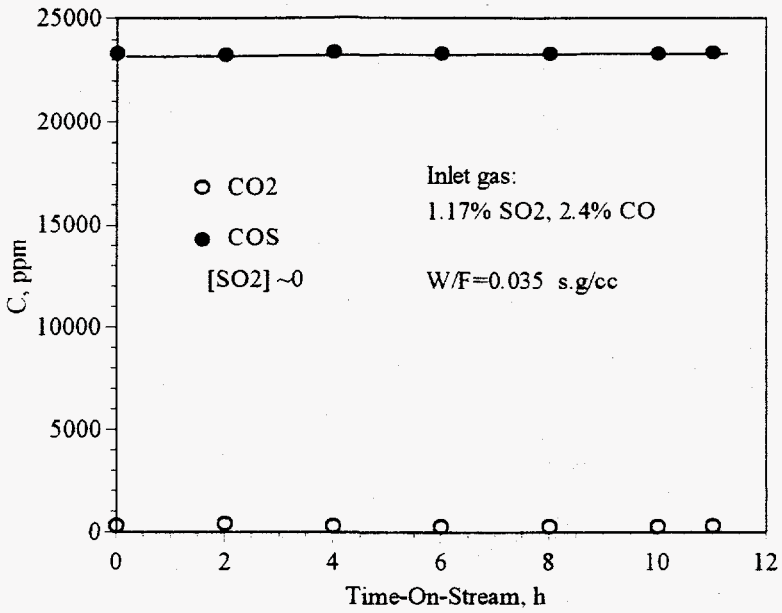

Figure 3.7 Long-term Activity of CeO_2(La) Catalyst at T=532°C.

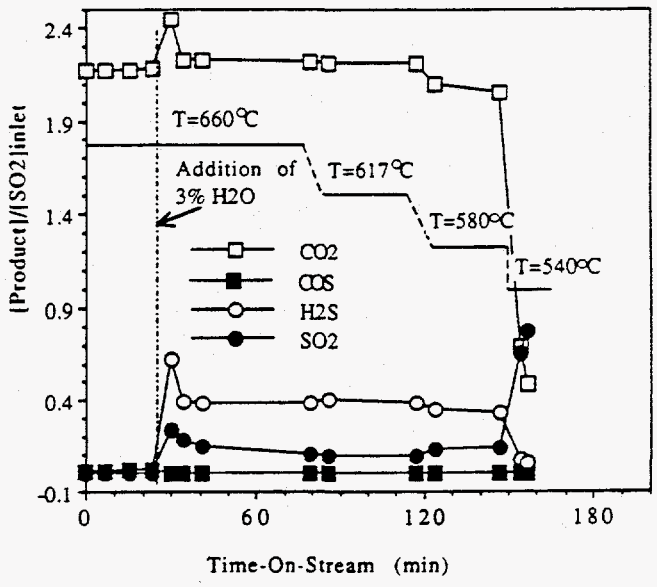

Figure 3.8 Product Distribution with Temperature on CeO_2(La) Catalyst in the Presence of Water Vapor (1.07% SO_2, 2.2% CO, 3% H_2O; 0.043s·g/cc).

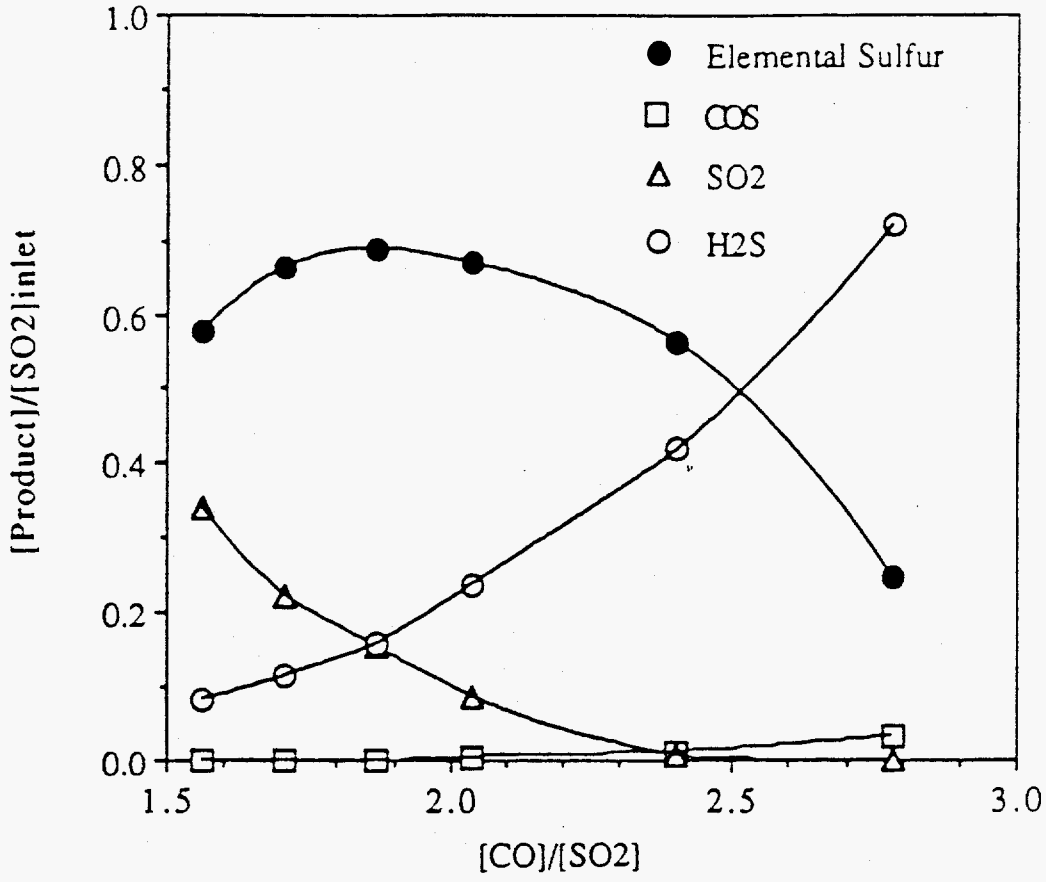

Figure 3.9 Product Distribution with the [CO]/[SO_2] Ratio on CeO_2(La) Catalyst in the Presence of Water Vapor at 610°C (1% SO_2, 1.5% H_2O; 0.043s·g/cc).

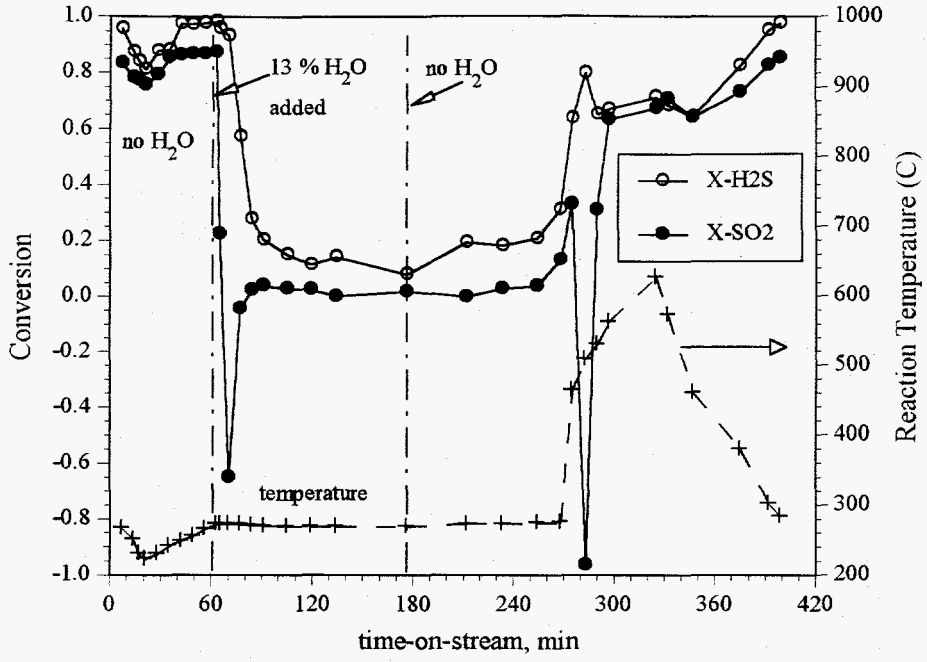

Figure 3.10 Claus Reaction over CeO_2(La) Catalyst (0.52 % SO_2, 0.94 % H_2S, 1200 v/v/h).

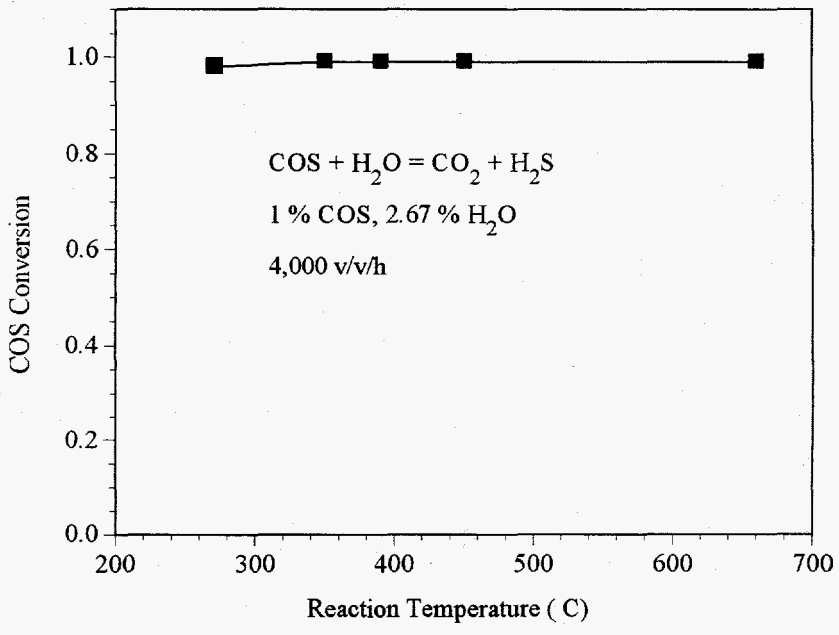

Figure 3.11 Hydrolysis of COS over CeO_2(La) Catalyst.

Chapter 4

Reduction of SO_2 by CO to Elemental Sulfur over Composite Oxide Catalysts

4.1 Introduction

The overall reactions involved in direct reduction of SO_2 by CO to elemental sulfur are as follows:

$$SO_2 + 2\ CO \rightarrow 2\ CO_2 + 1/x\ S_x \quad (1)$$

$$CO + 1/x\ S_x \rightarrow COS \quad (2)$$

$$2\ COS + SO_2 \rightarrow 2\ CO_2 + 3/x\ S_x \quad (3)$$

where x=2-8 or higher. At high temperatures, predominantly gaseous elemental sulfur, S_2, is produced through equation 1. The presence of water vapor in the feed gas may have a major effect on both the catalytic activity and product selectivity by poisoning the catalyst and/or promoting the following reactions:

$$CO + H_2O \rightarrow H_2 + CO_2 \quad (4)$$

$$COS + H_2O \rightarrow H_2S + CO_2 \quad (5)$$

$$H_2 + [S] \rightarrow H_2S \quad (6)$$

$$3/x\ S_x + 2\ H_2O \rightarrow 2\ H_2S + SO_2 \quad (7)$$

Reactions 1-7 have favorable thermodynamics at the conditions of interest to this work(atmospheric pressure, 300 to 700°C). The challenge to realize the one-stage elemental sulfur recovery scheme is to develop a catalyst which is not poisoned by water or other gas impurities and to maximize the yield of elemental sulfur. In the previous chapter we reported that cerium oxide, a fluorite oxide well known for its high oxygen vacancy concentration and mobility, is an active catalyst and its activity can be further enhanced by doping it with lanthanum oxide. However, alkaline earth and rare earth oxide dopants did not improve the resistance of ceria towards water poisoning. In the present study, we have modified the ceria with transition metals, examined other oxygen ion conducting materials as potential catalysts, evaluated catalyst activity and selectivity as a function of catalyst type and operating conditions, including the effect of water vapor, extensively characterized the Cu-Ce-O catalyst system, and studied the reaction kinetics.

4.2 Experimental

Apparatus and Procedure. All catalysts were tested in a 0.6cm I.D. x 50cm quartz tube packed bed flow reactor apparatus described in Chapter 2. A fresh catalyst was evaluated by a two-step test procedure. In the first step, the reactant gas mixture was introduced into the reactor at about 500°C and the reaction temperature was raised by about 50°C-increments after a steady-state reaction was reached at each temperature. The reaction light-off temperature was thus identified, at which the reaction occurred with SO_2 conversion exceeding 90%. In the second step, the reaction temperature was lowered in steps of about 50°C from a high temperature until conversion was significantly decreased. Hysteresis effects between the light-off and fall-off branches were followed in this sequence of steps. The effect of water on the catalyst activity and selectivity was examined by adding about 2% water vapor into the reactant gas mixture. Unless specifically noted, catalyst tests were typically performed with 150 mg catalyst loaded in the reactor, gas flow rate set at 100 sccm and comprising 1 % SO_2, 2 % CO by volume, and balance helium. The contact time was 0.09 g·s/cc(STP). Each catalyst has different packing density so that the space velocity varied with the individual catalyst tested. Sulfur dioxide conversion, X-SO_2, elemental sulfur yield, Y-sulfur, and R_{CO} ratio are defined by following equations:

$$X\text{-}SO_2=\{[SO_2]_o-[SO_2]\}/[SO_2]_o$$
$$Y\text{-sulfur}=[S]/[SO_2]_o$$
$$R_{CO}=[CO]_o/[SO_2]_o$$

where $[SO_2]_o$ and $[CO]_o$ are the inlet sulfur dioxide and carbon monoxide concentrations, respectively, while $[SO_2]$ and [S] are the outlet sulfur dioxide and elemental sulfur concentrations, respectively. Sulfur product was calculated from the material balance of carbon and sulfur, and occasionally checked by titration of the sulfur collected in the cold trap.

Kinetic measurements were also conducted in a fixed bed microreactor of 6mm I.D. SO_2 conversion was controlled by catalyst loading and gas flow rate. The catalyst loading varied from 6 to 300 mg, while the flow rate varied from 100 to 400sccm. Separate experiments confirmed that inter- and intra-particle mass transfer under the present conditions were eliminated. Blank test also showed that SO_2 conversion in the absence of catalyst was less than 2% at temperatures below 650°C. The small amounts of catalyst were usually diluted by quartz particles so that a packed height about 5mm was achieved. For all kinetics measurements, the catalyst was pre-conditioned for 2 h at 650°C in 1 % SO_2 and 2 % CO mixture. The steady-state reaction conversion was recorded. Generally, no apparent conversion decline within 30 min was considered as steady state. The steady state was easily achieved at high reaction temperatures. At low temperatures, a longer time varied from a few hours to one day was needed to reach a steady state when the reaction condition was changed.

Catalyst. Both bulk composite and impregnated oxide catalysts were prepared in this study. The composite catalysts were prepared by coprecipitating aqueous salt solutions of the metals with ammonium carbonate. The precipitates were washed twice with hot de-ionized water and then dried for about 12 h at 110°C. The dried samples were further heated for a few hours in stagnant air at 650°C. The particle sizes used for activity tests were -35+100 mesh (420 - 149 μm) except for tests with zirconia catalysts where -250 mesh (<63μm) particles were used. For kinetics measurements, particles of a average size of 100μm were used. The supported catalysts were prepared by conventional wet impregnation of the support with aqueous salt solutions of the metals. The slurry of the support and solution was degassed in vacuum so that the salt solution fully filled the pores of the support during impregnation. Then, the excess solution was filtered. The wetted samples were dried for two days at room temperature and then heated for four hours at 650-700°C in a muffle furnace. The $Cu/\gamma\text{-}Al_2O_3$ catalyst was prepared by reduction of $CuO/\gamma\text{-}Al_2O_3$ with 10 % CO/He at 300°C.

Microstructure of the used catalyst was analyzed by Scanning transmission electron microscopy (STEM) on a Vacuum Generators HB603 instrument. The catalyst surface properties were characterized by X-ray photoelectron spectroscopy (XPS) on a Perkin Elmer 5100 instrument. The catalyst reducibility was investigated on a Cahn TG 121 thermogravimetric analyzer with a MKS quadrupole mass spectrometer attached for gas analysis.

4.3 Results

4.3.1 Transition Metal-Impregnated Ceria Catalysts

Figure 4.1 shows the light-off curves of sulfur dioxide reaction with carbon monoxide over the transition metal-impregnated ceria catalysts. The light-off temperatures are 500°C on the Cu/CeO_2 and Ni/CeO_2 catalysts, 550°C on the Pt/CeO_2, and 600°C on the Co/CeO_2 and Mn/CeO_2. A light-off temperature higher than 600°C was found for unmodified ceria and for Cr/CeO_2 catalysts. Thus, addition of transition metals significantly lowered the light-off temperature of ceria. The fall-off behavior on these catalysts as well as water vapor effects are plotted in Figure 4.2. In these tests, ceria and Cr/CeO_2 were activated by reduction with 10% CO/He at 600°C. The reaction starts to fall off around 550°C on ceria and below 500°C on the other catalysts. The Cr/CeO_2 shows a low fall-off temperature, although it was difficult to activate it in the reaction mixture(Figure 4.1). However, this catalyst completely deactivated upon addition of water at 550°C as did ceria. The other catalysts were still active in the presence of water. The sulfur yield at 510°C was higher on the Cu, Co, Ni-impregnated ceria catalysts(~0.7) than on the Mn, Pt-impregnated ceria (0.4-0.6). Table 4.1 lists the numeric values of sulfur yield and SO_2 conversion in tests with the dry and wet reactant gas mixtures shown in Figures 4.1-2. It is seen that in the dry gas almost all the sulfur dioxide was converted to

elemental sulfur. However, the elemental sulfur yield decreased from a typical 0.96 (dry gas) to 0.4-0.7(wet gas) due to the formation of hydrogen sulfide.

Figure 4.3 shows the variation of gaseous product distribution with time-on-stream on the Cu/CeO_2 catalyst at 510°C in the presence of water. Formation of H_2S according to reactions (4) and (6) consumed some reductant CO, resulting in sub-stoichiometric amount for the reduction of SO_2. The ratio of H_2S to SO_2 concentration in the product gas was around stoichiometric, which means that nearly complete conversion of the inlet CO took place. Figure 4.3 also indicates that the Cu/CeO_2 catalyst is stable under the reacting conditions, since no apparent deactivation was observed during a 25-hour run. This promising catalyst system was used for detailed studies of the SO_2 reaction with CO.

4.3.2 Effect of Copper Content on the Catalyst Activity and Selectivity of the Cu-Ce-O System

Two series of Cu-Ce-O catalysts, listed in Table 4.2, were prepared by coprecipitation and impregnation methods, respectively, to evaluate the effect of copper content on the catalyst activity and selectivity. The La-doped ceria and alumina-supported copper catalysts are also included in Table 4.2 for comparison. The bulk Cu-Ce-O composite catalyst typically has a surface area around 30 m^2/g, while the impregnated ceria catalyst has a surface area slightly lower than the CeO_2 support (24 m^2/g). The Cu/Al_2O_3 catalysts have much higher surface area(~130 m^2/g) due to the γ-alumina support. Since the SO_2 conversion increases very fast with the reaction temperature, only experimental results at relatively low temperatures are included in Table 4.2 to compare the activity and selectivity. The light-off temperature on all the Cu-Ce-O catalysts was approximately 500°C, while the light-off temperatures on the Cu/Al_2O_3 catalysts and La-doped ceria were 560°C and 610°C, respectively.

The impregnated and bulk Cu-Ce-O catalysts show similar overall behavior and the catalyst activity is not sensitive to the copper content in the catalyst. However, there is a trend for the selectivity toward elemental sulfur to decrease as the copper content increases. In the presence of 2 % water, hydrogen sulfide instead of carbonyl sulfide becomes a major byproduct over the Cu-Ce-O catalyst. The elemental sulfur yield drops from a typical 95% in the dry gas to about 70% in the wet gas. The $Cu/\gamma\text{-}Al_2O_3$ catalyst has a little higher activity than the $CuO/\gamma\text{-}Al_2O_3$, but, both catalysts are much less active than the Cu-Ce-O catalysts. Also, in contrast to the Cu-Ce-O, the copper/alumina catalyst favors the formation of COS in the presence of water as has been reported in the literature *(1)* and verified in this work.

4.3.3 Zirconate and Zirconia Catalysts

Zirconium oxide has the fluorite type structure of ceria and is similar to ceria in many physical properties, such as high oxygen mobility and oxygen ion vacancy concentration,

but, zirconia is much more difficult to be reduced than ceria. Yttrium-stabilized zirconia is a well known oxygen ion conductor *(2)*. Mixed oxides of lanthanide elements and zirconium were reported by Bajars *(3)* as catalysts for sulfur dioxide reduction by CO. In addition, $Zr_2Ln_2O_7$-type zirconates (Ln= lanthanide element from La to Tb) of pyrochlore structure, notably, $Gd_2Zr_2O_7$, are known as another class of oxygen ion conductors *(4)*.

Several zirconates(Ce, Tb, Gd) and zirconia-based oxides were prepared and tested in this work under the same conditions as the ceria-based catalysts. The results are summarized in Table 4.3. The zirconates have surface areas from about 30 to 50 m^2/g. Y-doped zirconia has much higher surface area than the Cu-doped zirconia, which may reflect the known stabilization effect yttrium imparts to the zirconia crystal structure. The zirconia-based catalysts consist largely of mesopores(tens Å in dia.). Therefore, small particles, less than 63 μm, were used in the tests of the ZrO_2-based catalysts to overcome pore diffusion resistance. The light-off temperature over the Ce, Tb and Gd-zirconates was around 700°C, higher than that for ceria. After the reaction was initiated at high temperature, however, the zirconate catalyst could maintain its high activity as the reaction temperature was lowered to 470°C. The performance of the $Gd_2Zr_2O_7$ catalyst system is illustrated in Figure 4.4. More than 95% elemental sulfur yield was obtained over the temperature range 470 to 700°C in the dry gas. After the addition of 2 % water into the reactant gas at 560°C, the $Ce_2Zr_2O_7$ and $Tb_2Zr_2O_7$ catalysts were quickly deactivated; only the $Gd_2Zr_2O_7$ catalyst remained active. As the temperature was decreased to 510°C, this catalyst was also deactivated in the presence of water(Figure 4.4). Therefore, $Gd_2Zr_2O_7$ is the most active among the three zirconate catalysts tested. The activity of this catalyst can be promoted by copper as indicated by the data of Table 4.3.

The yttria-doped zirconia catalyst, $Zr_{0.9}Y_{0.1}O_x$, has a 610°C light-off temperature, same as the La-doped ceria. The light-off temperature was lowered to 510°C by the addition of copper. The slightly lower SO_2 conversion observed on the Cu-Zr(Y)-O catalyst(Table 4.3) compared to Cu-Ce(La)-O at the same reaction temperature(Table 4.3) may be due to pore diffusion limitation in the former catalyst system. Overall, zirconia is similar to ceria in its catalytic properties for the reduction of sulfur dioxide by carbon monoxide.

4.3.4 Effect of Carbon Dioxide on Catalyst Activity and Selectivity

Carbon dioxide is produced by the present reaction and may also be present in the feed gas stream. Thus, its effect on catalyst activity and selectivity was briefly checked in this work. As shown in Figure 4.5, addition of about 3 % carbon dioxide into the reactant gas mixture at 510°C almost completely suppressed the reaction on the $Ce_{0.9}La_{0.1}O_x$ catalyst. The SO_2 conversion dropped from about 1.0 to 0.1, while the sulfur yield decreased from 0.96 to trace amounts. The catalyst activity was restored in the presence

of carbon dioxide only when the temperature was raised to 600°C. However, the elemental sulfur yield was decreased to 0.81 because CO_2 lowered the SO_2 conversion and promoted the production of carbonyl sulfide(Figure 4.5). In contrast, addition of CO_2 at 510°C did not suppress the reaction on the 7.8 wt. % Cu/CeO_2 catalyst. This catalyst can maintain its activity even at the lower temperature of 465°C. Sulfur yield was decreased by a few percent as a result of promoted COS production and lower SO_2 conversion. These results show that copper can enhance the resistance of the ceria catalyst to carbon dioxide poisoning.

4.3.5 Bulk $Cu_{0.15}[Ce(La)]_{0.85}O_X$ Catalyst

The $Cu_{0.15}[Ce(La)]_{0.85}O_X$ catalyst was chosen for further studies. This catalyst showed no apparent deactivation during a 35-h run in the presence of 2 % water at 470°C. The variation of surface area with temperature is shown in Table 4.4.

Light-off over $Cu_{0.15}[Ce(La)]_{0.85}O_x$ Catalyst. Light-off and fall-off behavior of various catalysts were reported above as major reaction characteristics. The light-off behavior of the Cu-Ce-O catalyst was carefully examined with the $Cu_{0.15}[Ce(La)]_{0.85}O_x$ as a model catalyst. Figure 4.6 shows light-off curves of the $Cu_{0.15}[Ce(La)]_{0.85}O_x$ catalyst under various reaction conditions. The light-off over this catalyst occurred at the temperature range from 440 to 465°C irrespective of initial SO_2 concentration and contact times. This confirmed that the light-off temperature was determined by the intrinsic kinetics property of the catalyst and not caused by heat release effect in this exothermic reaction. Thus, the light-off temperature can be used as a crude criterion in the catalyst activity ranking. It is noted that the same SO_2 conversion was achieved at a temperature indicated by the thermocouple placed on the top of the catalyst bed or inserted inside the catalyst bed. The temperature gradient in the packed bed was diminished by the small reactor tube (6mm) and shallow catalyst bed (<10mm). Although the light-off temperature is not affected by the reaction conditions, the lowest light-off temperature was observed with a catalyst pre-reduced by CO. This effect is further illustrated by the activation profiles in Figure 4.7 where nano-$Cu_{0.15}Ce_{0.85}O_x$ catalyst, prepared by inert gas phase condensation and controlled oxidation to non-stoichiometric cerium oxide, shows an activation process more rapid than the corresponding bulk catalyst and comparable to the pre-reduced bulk catalyst.

SO_2 Conversion. Effect of $[CO]/[SO_2]$ ratio in the feed gas, R_{CO}, on product distribution over the $Cu_{0.15}[Ce(La)]_{0.85}O_x$ catalyst is shown in Figure 4.8. Under constant contact time and reaction temperature, SO_2 conversion rapidly increased with R_{CO}. COS formation over the $Cu_{0.15}[Ce(La)]_{0.85}O_x$ catalyst was minor at low SO_2 conversions but became significant at high SO_2 conversions if R_{CO} greater than 2. Variation of conversion with contact time at different temperatures is plotted in Figure 4.9. The conversion starts to decline from 0.99 at contact times shorter than about 0.045g·s/cc(STP) at 510°C. No effect of contact time on selectivity was observed. Considering these results, reaction

kinetics over the $Cu_{0.15}[Ce(La)]_{0.85}O_x$ catalyst was investigated by varying SO_2 concentration with R_{CO} being fixed at 2. Under such reaction composition, selectivity to sulfur was always about 95%. Therefore, only SO_2 conversion is reported in the following results. Figure 4.10 shows typical plots of SO_2 conversion at 510°C versus contact time for different inlet SO_2 concentration. These data were fitted by the same first-order equation. Resulting rate constant was a weak function of $[SO_2]_{inlet}$.

Water Vapor Effect on the $Cu_{0.15}[Ce(La)]_{0.85}O_x$ Catalyst. The effect of temperature on product distribution in the presence of 2% H_2O is shown in Figure 4.11. The difference between SO_2 conversion and sulfur yield in Figure 4.11 mainly comprised of H_2S. The temperature showed no effect on sulfur yield from 560 to 450°C over which SO_2 conversion kept constant. Sulfur yield declined with SO_2 conversion when temperature was decreased from 450 to 435°C. Effect of contact time on sulfur yield is illustrated in Figure 4.12. For all three temperatures tested (470°C, 510°C, and 560°C), difference between SO_2 conversion and sulfur yield was not affected as the contact time decreased from 0.09 to 0.022s·g/cc. These results indicate that production of H_2S occurs simultaneously with SO_2 conversion. Sulfur yield cannot be optimized by modifying operation conditions, temperature, contact time.

Although only three SO_2 conversion data points are available in Figure 4.12, its variation still nicely fell into the first order conversion line. Effect of water vapor content on sulfur yield is shown in Figure 4.13. Sulfur yield sharply decreased from ca. 0.76 to ca. 0.53 as water vapor was raised from 2 % to 4 %. However, further increasing water vapor content did not cause a major change in sulfur yield. Sulfur yield was maintained at 0.45 level in the presence of 8 or 13 % H_2O. It is noted again that difference between SO_2 conversion and sulfur yield was mainly due to production of H_2S. COS formation was always minor in the presence of water vapor. Because stoichiometric feed gas was employed, the produced H_2S relative to un-reacted SO_2 was always kept at the stoichiometric ratio as long as complete CO conversion occurred. Figure 4.13 shows that SO_2 conversion and sulfur yield levels were flat at high temperatures. The higher the water vapor content in the feed gas, the more rapidly did SO_2 conversion and sulfur yield fall off as temperature was lowered. Therefore, water vapor also had some inhibition effect on catalyst activity.

4.3.6 Catalyst Characterization

The comprehensive information on fresh catalyst structure will be presented in Chapter 6. The catalyst structure and composition usually changed after use for SO_2 and CO reaction due to the introduction of sulfur. XRD analyses of the fresh composite Cu-Ce-O catalysts identified two crystal phases, fluorite-type and copper oxide, in catalysts containing over 15 at.% copper, and only the fluorite structure in the composites containing less than 15 at.% Cu. Also in the Y-doped and Cu-doped zirconia catalysts, only the fluorite-type structure was found. Two small copper oxide peaks were found in the fresh 7.8 wt.% CuO_x/CeO_2 catalyst as shown in Figure 4.14, but, these two peaks disappeared in the used catalyst. The distinct fluorite-type diffraction pattern was found in

both the used and fresh Cu-Ce-O catalysts, which indicates that the fluorite oxide was stable in the present reaction conditions.

Elemental distributions (S, Cu, Ce, O) in the used Cu-Ce-O catalysts were extensively studied with STEM X-ray microprobe. Figure 4.15a shows the elemental maps for the $Cu_{0.02}[Ce(La)]_{0.98}O_x$ catalyst after 2-day test. No bulk copper oxide or sulfide particles were observed with this catalyst. Copper remained well dispersed in cerium oxide matrix after use. The existence of small amounts of sulfur was revealed. But, the sulfur content was too low for its distribution map to be unambiguously discriminated against background noise. Figures 4.15b-c show typical elemental distributions in a used $Cu_{0.15}[Ce(La)]_{0.85}O_x$ catalyst. Three major structural characteristics are: (i) bulk copper particles formed segregated copper sulfide crystals; (ii) copper and sulfur extensively distributed on cerium oxide matrix; (iii) cerium oxide was the backbone of the catalyst structure.

Catalyst surface composition and property were analyzed by XPS. Tables 4.5-6 list the surface compositions of the used $Cu_{0.02}[Ce(La)]_{0.98}O_x$ and $Cu_{0.15}[Ce(La)]_{0.85}O_x$ catalysts, respectively. The surface composition of the top portion of the $Cu_{0.02}[Ce(La)]_{0.98}O_x$ catalyst bed is similar to that of the bottom portion and the catalyst tested for 6 h has similar composition to the one used for a much longer time. Two O1s peaks were found in all three $Cu_{0.02}[Ce(La)]_{0.98}O_x$ samples that suggest two kinds of oxygen species in the catalyst. The nature of the oxygen species will be discussed later. Copper content was close to the XPS detection limit. But, it is clear that there is more sulfur than that needed for copper sulfide formation. Carbon species were found in all the XPS measurements and it came from carbonaceous compound deposition. A simple calculation found that there is more oxygen detected on the catalyst surface than the stoichiometric amount of metal oxide (assume $Ce=CeO_2$ and $Cu=CuO$). The excess oxygen may be associated with sulfur element. Recall the light-off curves in Figure 4.6 where the $Cu_{0.15}[Ce(La)]_{0.85}O_x$ catalyst showed no activity at 433°C but became completely activated at high temperatures, such as 510°C. The surface composition listed in Table 4.6 shows that the un-activated catalyst contained more sulfur and oxygen but less cerium than the activated one.

Figures 4.16a-d show the XP spectra of Ce3d, Cu2p, O1s, and S2p core electrons. The binding energy of Ce3d5/2 is usually not affected by cerium oxidation state. Different cerium species are distinguished by their spectra pattern. The Ce3d spectra in Figure 4.16a for the un-activated $Cu_{0.15}[Ce(La)]_{0.85}O_x$ catalyst look the same as the cerium sulfate measured by Loof et al., 1991 *(5)*. The Ce3d spectra for the activated $Cu_{0.02}[Ce(La)]_{0.98}O_x$ looks more like cerium oxide, while the activated $Cu_{0.15}[Ce(La)]_{0.85}O_x$ catalysts contains some sulfate component. The presence of Ce^{+3} cannot be identified by the XPS because of its low intensity. Cu_2S cannot be discriminated from Cu_2O because both of them have the same binding energy and L_3VV Auger kinetic energy *(6)*. The Cu2p3/2 peak at 935.6eV is assigned to copper sulfate. The O1s spectra indicate two kinds of oxygen species. In accordance with the literature data, the components at ca. 529.4eV and ca. 532eV are assigned to metal oxides and metal sulfates, respectively. Similarly, the S2p components at 167.0 to 168.9eV and at 162.1 to 162.6eV are assigned to metal sulfate and metal sulfide, respectively. Based on the present results, it is postulated that in a working catalyst some

of copper is associated with copper sulfide, while some of cerium is associated with sulfate. An activated catalyst usually comprised of both metal sulfate and sulfide, while the un-activated 15 at. % catalyst surface was totally covered by sulfate.

The surface was enriched in copper after use. Table 4.8 shows that the Cu/Ce and S/Cu ratios measured by XPS for a $Cu_{0.15}[Ce(La)]_{0.85}O_x$ catalyst after two-day test decreased by argon ion sputtering of the surface, but the S/Cu did not reach a zero value because of interference from the catalyst pores.

4.3.7 Reducibility of the $Cu_{0.15}[Ce(La)]_{0.85}O_x$ Catalyst

Reducibility of the $Cu_{0.15}[Ce(La)]_{0.85}O_x$ catalyst by CO was investigated on a thermogravimetric analyzer coupled with a mass spectrometer. Figure 4.17 shows a typical temperature-programmed reduction profile of the catalyst in 3.5 % CO/N_2. The reduction started at ca. 80°C. The doublet peak appeared around 120°C and 145°C, respectively. There was no peak found around 500°C that is usually observed with bulk CeO_2 and caused by reduction of surface capping oxygen according to Yao and Yao *(7)*. The continuous weight loss was accompanied with the evolution of CO_2 as measured by mass spectrometry. TPR studies of bulk CuO materials *(8,9)* found that the reduction peaks appeared between 200 to 300°C. Therefore, the presence of cerium oxide significantly lowered copper oxide reduction temperature. This profile looks the same as the one found for precious metal (Pt, Rh)/CeO_2 system (10), suggesting strong synergism between copper and cerium oxide. The initial reduction rates, defined by the following equation, were measured under constant temperatures for the following kinetic analysis:

$$R_w = -\frac{dW}{W_o dt}\Big|t = 0 \qquad (8)$$

This rate is plotted versus reduction temperature over the range of 100 to 600°C in Figure 4.18 in an Arrhenius form. The resulting activation energy, 12kJ/mol, is a very small number. SO_2 sorption on the $Cu_{0.15}[Ce(La)]_{0.85}O_x$ catalyst and reducibility of the sulfated catalyst were investigated as follows: flushing the reactor system with N_2, achieving a stable baseline, introducing 1 % SO_2/N_2 into the reactor, about half a hour later, switching the SO_2 stream to 2 % CO/N_2. Although no oxygen was fed, the catalyst showed rapid weight gain upon introduction of SO_2. This indicates that SO_2 reacted with catalyst surface oxygen, because cerium oxide has high oxygen storage ability. Even in the presence of oxygen, Hedges and Yeh *(11)* found that SO_2 uptake rate on the CeO_2/Al_2O_2 sorbent was independent of P_{O2}. Therefore, the cerium oxide surface oxygen is active for sulfate formation. Reducibility of the catalysts after sulfation was dramatically decreased. No apparent reduction was observed below 450°C, as opposed to the significant and rapid reduction with the fresh sample below this temperature. The Arrhenius plot of the initial reduction rate of the sulfated catalyst is shown in Figure 4.19. Clearly, two reduction regions exist. Below 550°C, reduction rate steeply increases with temperature, resulting in an activation energy of 239kJ/mol. Above 550°C, the activation energy is only 9.8 kJ/mol comparable to that for fresh catalysts.

4.4 Discussion

Previous studies have suggested that the reduction of sulfur dioxide by carbon monoxide proceeds via a redox mechanism.

$$\text{Cat-[ ]} + SO_2 \rightarrow \text{Cat-O} + SO \quad (9)$$

$$\text{Cat-O} + CO \rightarrow \text{Cat-[ ]} + CO_2 \quad (10)$$

$$\text{Cat-[ ]} + SO \rightarrow \text{Cat-O} + S \quad (11)$$

Accordingly, the reaction is initiated by the creation of an oxygen vacancy. As an oxygen vacancy is created, SO_2 donates one oxygen to that vacancy to form a SO group. The SO may be mobile on the surface until it finds another vacancy to donate its oxygen or a vacancy may migrate to a neighboring site to accept its oxygen. High oxygen mobility in the catalyst would facilitate the oxygen transfer on the surface or from the bulk to the surface. Therefore, oxygen vacancy and mobility seem to be important properties for an active catalyst. The active catalysts previously reported *(12-15)*, La-Ti-O and La-Co-O perovskite mixed oxides, generally possess such properties. Ceria and zirconia studied in this work are well known for their oxygen vacancy and mobility properties. Ceria has a very stable fluorite-type structure, while the fluorite structure of zirconia can be stabilized by the use of oxide dopants. The oxygen vacancy in a fluorite oxide is created by replacing the metal ion (Ce^{+4} or Zr^{+4}) in the lattice with other di or tri-valent metal ions. Rare earth zirconates ($Ln_2Zr_2O_7$) having oxygen mobility properties were also found to be active catalysts in this work. All these results support the present mechanistic argument.

However, the oxygen vacancy can be taken up by other oxygen-containing molecules, such as CO_2 or H_2O. The stronger the association of these impurity oxidants with the vacancy, the more they will inhibit the reaction. Thus, creation of oxygen vacancies on the surface is a key step. Incorporation of alkaline and rare earth dopant oxides into the ceria lattice enhances the oxygen vacancy concentration and mobility. But, the created vacancies are usually capped by an outside oxygen and the strong vacancy-dopant ion association stabilizes the capping oxygen. The capping oxygen has to be removed to bring about oxygen vacancy and initiate the redox reaction. For ceria, temperature-programmed reduction by hydrogen *(7)* has found that the surface capping oxygen can be removed at about 500°C. Higher reduction temperature may be needed in the presence of SO_2 due to its strong bonding to the surface. It is also known that CO adsorption on ceria is inhibited by water *(16,17)*. The introduction of transition metals may provide surface sites for CO adsorption and facilitate the reduction of the fluorite oxide surface through strong metal-support interaction as found in the Pt-CeO_2 system *(8,10)*:

$$\text{Cat-M}\cdots CO + \text{Cat-O} \rightarrow \text{Cat-M} + \text{Cat-[ ]} + CO_2 \quad (12)$$

In the above equation, "Cat-" represents the catalyst surface and "M" is a metal site. The produced oxygen vacancy through Equation 11,Cat-[ ], can further react according to the redox reaction scheme (8)-(10). This assumption was validated by the fact that the catalytic activity of ceria or zirconia and resistance to water or carbon dioxide poisoning

were significantly enhanced by the addition of transition metals, such as copper. XPS studies showed that copper in the Cu-Ce-O catalyst tends to be stabilized in a reduced oxidation state (Cu^{+1}) instead of CuO, while it is well known that CO strongly adsorbs on Cu^{+1} sites. Preliminary temperature-programmed reduction experiments indicated that addition of copper can initiate the reduction of surface capping oxygen of ceria at low temperatures. These data suggest that there is a strong interaction between copper (oxide) and ceria. For the Cu-Ce-O system, both coprecipitation and impregnation preparation methods gave rise to an active catalyst. The catalyst activity was not sensitive to the copper content, but the selectivity tended to decrease with the copper content. XRD analysis identified the CuO phase when the copper content was over 15 at. %. STEM analysis revealed bimodal size distribution of copper on ceria. Only small amounts of copper are needed to promote the catalytic properties of ceria, and the excess copper (oxide) can form aggregates.

As reported in the literature *(14,18)*, the transition metal will likely be sulfided by the elemental sulfur product:

$$\text{Cat-M} + S_X \rightarrow \text{Cat-MS}_X \tag{13}$$

Copper sulfide was found on a used Cu-Ce-O catalyst by XPS surface compositional analysis, but was not detected by XRD analysis, possibly because it is dispersed in ceria in amorphous form or because copper sulfide crystals did not grow on the stable ceria surface. The fluorite oxide showed high stability in the present study. For example, ceria kept its fluorite-type crystal structure after a 48 h test run. STEM elemental mapping showed that the sulfur on the catalyst was extensively associated with copper. The formation of copper sulfide extracted copper from the bulk so that the surface was enriched in copper on the used catalyst. Copper sulfide may play a similar role to copper in promoting the reducibility of the fluorite oxide. But, the deposited sulfur may react with CO to form COS through following equation:

$$\text{Cat-MS}_X + \text{CO} \rightarrow \text{Cat-M} + \text{COS} \tag{14}$$

Therefore, an adsorbed CO molecule can pick up oxygen through equation (10) and sulfur through equation (14). We believe that COS formation is the result of these two competitive processes and it prevails in the following two cases: (i) when excess CO exists and the oxidant is not sufficient to oxidize it, the extra CO reacts with sulfur to form COS; (ii) when the surface oxygen is more strongly bound than sulfur, the adsorbed CO picks up sulfur to form COS. The reaction of CO and the deposited sulfur is further illustrated by Figure 4.20, where COS evolution profiles are shown for 2% CO/He scavenging of the used catalysts following a helium flush. A simple exponential decay of COS(t) predicted by assuming a formation rate $r_{COS}=k_S[S]_{surf.}P_{CO}$ fits well the data of Figure 4.20.

In addition to reactions 10-11, SO_2 can also react with the surface capping oxygen to form surface sulfate:

$$SO_2 + 2O_{cat} \xrightarrow{\text{strong}} SO_{4,cat} \tag{15}$$

The surface sulfate is strongly bonded to the catalyst surface. In the presence of CO, the sulfate may be reduced by CO back to SO_2 through the following reaction:

$$SO_{4,cat} + 2CO \xrightarrow{slow} SO_2 + 2CO_2 + 2V_{O,cat} \quad (16)$$

But, the reaction (26) is a very slow step. Based on the present results and literature information, we think that surface capping oxygen in the above reactions is supplied from cerium oxide. Cerium oxide has high oxygen storage capacity and its surface oxygen cannot be flushed away by an inert gas stream such as helium. The formation of surface sulfate on cerium oxide does not require the presence of gaseous oxygen. A working catalyst comprises partially reduced cerium oxide surface and sulfated surface. Because the cerium oxide is immediately capped by sulfate species upon the introduction of the reacting gas mixture at low temperatures, a hysteresis effect was observed with this reaction and the light-off temperature essentially represents a temperature at which the catalyst surface could be regenerated. The light-off temperature around 450°C is consistent with the TPR result that apparent reduction of the sulfated surface starts to occur around 450°C.

The above mechanistic discussion is strongly confirmed by the experimental results with non-stoichiometric cerium oxide *(19)*, CeO_{2-x}. Figure 4.21 compares light-off and fall-off temperatures of nanocrystalline CeO_{2-x} catalysts with those of precipitated catalysts. CeO_{2-x} catalysts have partially reduced surface and high concentration of oxygen vacancies and quasi-free electrons. Accordingly, light-off temperature on the CeO_{2-x} catalyst was decreased by ca. 100°C. A little hysteresis effect was observed with the bare CeO_{2-x} catalyst and negligible hysteresis effect with the La-doped CeO_{2-x} catalyst. The bare CeO_{2-x} and La-doped CeO_{2-x} catalysts showed even better performance than Cu-promoted CeO_2 prepared by precipitation. The significantly reduced light-off temperature and hysteresis effect of the CeO_{2-x} catalysts clearly demonstrate the importance of partially reduced cerium oxide surface in maintaining the redox reaction cycle.

The role copper played in the Cu-Ce-O catalyst probably is to promote the reducibility of cerium oxide and provide surface sites for CO adsorption. The promotion effect of copper to the surface reduction of fresh catalysts is clearly demonstrated by the TPR result. The Cu^{+1} species were observed by XPS with the fresh catalyst. But, the catalyst surface became complex in the $CO+SO_2$ reacting atmosphere. CuO particles formed copper sulfide crystals that have overall small surface area and little contribution to the catalytic activity. It is not known at the present time how copper ions and clusters in the cerium oxide matrix are affected by sulfur compounds. According to a recent study by Badley et al. *(20)* on SO_2 and CO adsorption on Cu/Al_2O_3, SO_2 can block CO adsorption on Cu^{+2} sites but not Cu^{+1} sites, while the pre-adsorption of CO does not prevent SO_2 adsorption. Therefore, copper may still provide strong sites such as Cu^{+1} for CO adsorption even in the presence of SO_2.

Water vapor does not poison the Cu-Ce(La)-O catalyst but can react with CO to produce hydrogen, that is, the water-gas-shift (WGS) reaction can proceed over the Cu-Ce(La)-O catalyst. This secondary reaction reduces amount of CO available for SO_2

reduction. In addition, produced hydrogen can react with the surface sulfur to produce H_2S.

$$CO_{ad} + H_2O_{ad} \rightarrow CO_2 + H_{2ad} \quad (17)$$

$$H_{2,ad} + [S]_{ad} \rightarrow H_2S_{ad} \quad (18)$$

The present parametric studies suggest that all the above reactions occur on the surface. The bulk reaction process is negligible. Therefore, sulfur yield is controlled by the surface reactions and could not be maximized by varying the reactor operation conditions. It is known that the WGS reaction proceeds on metal oxide catalysts through a redox mechanism *(21)*. Similar to the reaction scheme for SO_2 reduction by CO, the creation of surface oxygen vacancy by CO reduction is considered to be the rate-determining step. Therefore, the WGS reaction inevitably occurs on the present catalyst. The H_2O molecule will compete with SO_2 to donate its oxygen to the vacancy. As a result, H_2 production or H_2S production increases rapidly with partial pressure of water vapor. But, further increasing water vapor content beyond 8% did not cause significant change of product distribution. This information suggests that the WGS reaction may involve adsorbed H_2O. Because of the high redox activity of the Cu-Ce(La)-O catalyst, complete CO conversion was still achieved in the presence of water vapor. As long as stoichiometric SO_2 and CO composition is used, the produced H_2S and un-reacted SO_2 in the reactor effluent stream will also be in stoichiometric ratio. Therefore, high sulfur recovery may be achieved by using a down stream Claus reactor.

4.5 Conclusion

In this work, we have found that fluorite type oxides, ceria and zirconia, are active catalysts for reduction of SO_2 by CO with high selectivity to elemental sulfur over carbonyl sulfide. The activity of these oxides may result from their high oxygen vacancy concentration and mobility properties that are needed for a redox reaction mechanism. Addition of active transition metals such as copper to the fluorite oxide significantly lowered the reaction light-off temperature and enhanced the catalyst resistance toward water vapor and carbon dioxide poisoning. Sulfur yield over the Cu-Ce-O catalysts was a strong function of R_{CO}. More than 95% selectivity to sulfur was achieved on both catalysts with a reacting gas mixture of $R_{CO} \leq 2$. Analyses of the Cu-Ce-O system showed that the fluorite crystal structure of ceria is stable at the present reaction conditions and copper dispersion is stabilized by the ceria matrix. An active Cu-Ce-O catalyst can be prepared by either coprecipitation or impregnation. The catalyst activity is not sensitive to the copper content.

The reaction mechanism was discussed within the redox framework with the surface reduction as an initiation step. SO_2 participated the redox reaction and also formed surface sulfate with the surface capping oxygen. Bulk CuO particles in the catalyst formed metal sulfide crystals that were active for COS production. But, copper was considerably dispersed in the cerium oxide matrix after reaction. A working catalyst consisted of partially sulfated cerium oxide surface and partially sulfided copper. Copper and cerium oxide are considered to provide CO adsorption sites and oxygen vacancy sites,

respectively. Combination of copper and cerium oxide significantly enhanced reducibility of both copper oxide and cerium oxide. In the presence of water vapor, H_2O molecules competed with SO_2 to donate oxygen to the vacancy site favoring the water-gas-shift (WGS) reaction. Hydrogen produced from the WGS reaction promoted H_2S production. Sulfur yield was determined by the reaction stoichiometry and could not be optimized by changing the reactor operation conditions.

4.6 Literature Cited

1. Querido, R., and Short, W.L., *Ind. Eng. Chem., Process Des. Develop.* **12,** 10-18 (1973).
2. Hagemuller, P., and Van Gool, W., Solid Electrolytes, Academic Press, New York, 1978.
3. Bajars, L., U.S. Patent 3 978 200, 1976.
4. Tuller, H.L., and Moon, P.K., *Materials Science and Engineering* B1, 171-201 (1988).
5. Loof, P., Kasemo, B., Bjomkvist, L., Andersson, S., and Frestad, A., in Crucq, A. (editor), Catalysis and Automotive Pollution Control II, 1991 Elsevier Science Publishers B.V., Amsterdam, pp153-273.
6. Wagner, C.D., Rigg, W.M., Davis, L.E., Moulder, J.F., and Muilenberg, G.E., Handbook of X-ray Photoelectron Spectroscopy, Perkin-Elmer, 1978.
7. Yao, H.C., and Yao, Y.F.Y., *J. Catal.* **86**, 254-265 (1984).
8. Fierro, G., Jacono, M. L., Inversi, M., Porta, P., Lavecchia, R., and Cioci, F., "A study of anomalous temperature-programmed reduction profiles of Cu_2O, CuO, and CuO-ZnO", *J. Catal.* **148**, 709-721 (1994).
9. Boyce, A. L., Graville, S. R., Sermon, P. A., and Vong, M.S.W., "Reduction of CuO-containing catalysts, CuO: I &II, XRD and XPS", *React. Kinet. Catal. Lett.* **434**(1), 1-18 (1991).
10. Nunan, J.G., Silver, R..G., and Bradley, S.A., in Silver, R.G., Sawyer, J.E., and Summers, J.C., (Eds.) Catalytic Control of Air Pollution, ACS Symposium Series 495, American Chemical Society, Washington, DC 1992, Chapter 17.
11. Hedges, S.W., and Yeh, J.T., *Environmental Progress* **11**(2), 98-103 (1992).
12. Whelan, J.M., U.S.Patent 4 081 520, 1977.
13. Hibbert, D.B., and Campbell, R.H., *Appl. Catal.* **41**, 273-287 (1988).
14. Hibbert, D.B., and Campbell, R.H., *Appl. Catal.* **41,** 289-299 (1988).
15. Hibbert, D.B., *Catal. Rev. - Sci. Eng.* **34,** 391-408 (1992).
16. Li, C., Sakata, Y., Arai, T., Domen, K., Maruya, K., and Onishi, T., *J. Chem. Soc., Faraday Trans.* 1 **85,** 929-943 (1989).
17. Li, C., Sakata, Y., Arai, T., Domen, K., Maruya, K., and Onishi, T., *J. Chem. Soc., Faraday Trans.* 1 **85,** 1451-1461 (1989).
18. Baglio, J.A., *Ind. Eng. Chem. Prod. Res. Dev.* **21,** 38-41 (1982).

19. Tschöpe, A., Liu, W., Flytzani-Stephanopoulos, M., and Ying, J.Y., *J. Catal.* 1995, in press.
20. Badley, M.B., Rochester, C.H., Hutchings, G.J., and King, F., "FTIR Spectroscopic Study of Thiophene, SO_2, and CO Adsorption on Cu/Al_2O_3 Catalysts" *J. Catal.* **148**, 438-452 (1994).
21. Kung, H., "Transition Metal Oxide: Surface Chemistry and Catalysis" in Delmon, B. and Yates, J.T., (Editors), Studies in Surface Science and Catalysis, Vol. 45, p245, Elsevier, 1989.

Table 4.1 Transition Metal-Impregnated Ceria Catalysts.

Catalyst		Light-off	Y-sulfur/X-SO_2[f] at 510°C	
Composition	surface area (m^2/g)	$T_{90\%}$[c](°C)	dry gas[d]	wet gas[e]
CeO_2	24	>600	0.04/0.12	0.0/0.0
Cu/CeO_2[a]	21.4	500	0.97/0.99	0.73/0.91
Ni/CeO_2[a]	22.7	500	0.97/0.98	0.69/0.78
Pt/CeO_2[b]	22.9	550	0.66/0.68	0.42/0.44
Mn/CeO_2[a]	20.8	600	0.95/0.97	0.60/0.66
Co/CeO_2[a]	22.5	600	0.96/0.98	0.73/0.88
Cr/CeO_2[a]	16.3	>600	0.96/0.97	0.0/0.0

a. CeO_2 was impregnated with 0.5M metal nitrate solution. The atomic transition metal content in the resulting catalyst ($n_M/(n_M+n_{Ce})$x100 %) is about 13 %.
b. CeO_2 was impregnated with 10 mg Pt/cc hydrogen hexachloroplatinate(IV) hydrate solution.
c. reaction temperature at which 90% conversion occurred during temperature-rise test.
d. reacting gas mixture consisted of 1% SO_2, 2% CO, balance helium.
e. 2% H_2O was added into reacting gas mixture.
f. sulfur yield/SO_2 conversion; see text.

Table 4.2 Variation of Catalyst Activity and Selectivity with Catalyst Composition in the Cu-Ce-O System.

Catalyst		Y-sulfur/X-SO_2[f]			
Composition	surface area m^2/g	dry gas[d] 465°C	dry gas[d] 510°C	wet gas[e] 470°C	wet gas[e] 510°C
Composite Catalyst[a]					
$La_{0.1}Ce_{0.9}O_x$	28.5	0.06/0.20	0.97/1.00	—	0.0/0.0
$Cu_{0.01}[Ce(La)]_{0.99}O_x$	57.0	0.97/1.00	0.97/1.00	0.65/0.81	0.66/0.90
$Cu_{0.05}[Ce(La)]_{0.95}O_x$	57.0	0.83/0.92	0.95/0.98	0.53/0.71	0.61/0.87
$Cu_{0.15}[Ce(La)]_{0.85}O_x$	30.7	0.97/0.99	0.97/1.00	0.69/0.90	—
$Cu_{0.20}[Ce(La)]_{0.80}O_x$	37.1	0.86/0.89	0.93/0.96	0.72/0.89	0.73/0.91
$Cu_{0.25}[Ce(La)]_{0.75}O_x$	30.2	0.93/0.97	0.94/1.00	0.64/0.84	0.69/0.92
$Cu_{0.35}[Ce(La)]_{0.65}O_x$	33.8	0.93/0.98	0.94/1.00	0.67/0.88	—
Impregnated Catalyst[b]					
CeO_2 support	24.0	0/0.0	0.04/0.12	—	0.0/0.0
3.5 wt.% CuOx/CeO_2	22.0	0.93/0.97	0.94/1.00	0.60/0.77	0.73/0.93
7.8 wt.% CuOx/CeO_2	21.0	0.84/0.92	0.95/0.99	0.56/0.73	0.68/0.91
21 wt.% CuO/γ-Al_2O_3	137	0.38/0.42	0.56/0.57	—	—
Cu/γ-Al_2O_3[c]	137	—	0.77/0.81	—	0.38/0.61

a. catalysts were prepared by coprecipitation. (La) denotes that the cerium nitrate precursor used contained about 1.38 wt.% lanthanum.
b. catalysts were prepared by impregnation. wt. % denotes the weight percent of copper.
c. prepared by reducing the 21 wt.% CuO/γ-Al_2O_3 with 10 % CO/He at 300°C.
d. reacting gas mixture consisted of 1% SO_2, 2 % CO, balance helium.
e. 2% H_2O was added into reacting gas mixture.
f. sulfur yield/SO_2 conversion; see text.

Table 4.3 Reduction of Sulfur Dioxide by Carbon Monoxide over Zirconate and Zirconia Catalysts.

Catalyst		Light-off	Y-sulfur/X-SO_2[d] (510°C)	
Composition[a]	surface area(m^2/g)	$T_{90\%}$ (°C)	dry gas[b]	wet gas[c]
$Gd_2Zr_2O_7$	37.8	700	0.95/0.99	0.0/0.0
$Tb_2Zr_2O_7$	50.8	700	0.97/0.99	—
$Ce_2Zr_2O_7$	37.0	700	0.96/1.00	—
$(Gd_2Zr_2)_{0.85}Cu_{0.15}O_x$	28.2	510	0.97/0.99	0.59/0.81
$Zr_{0.9}Y_{0.1}O_x$	41.7	610	0.54/0.58	—
$[Zr_{0.9}Y_{0.1}]_{0.85}Cu_{0.15}O_x$	65.0	510	0.87/0.90	—
$Zr_{0.8}Cu_{0.2}O_x$	17.8	510	0.92/0.96	0.70/0.87

a. catalysts were prepared by coprecipitation.
b. reacting gas mixture consisted of 1 % SO_2, 2 % CO, balance helium.
c. 2% H_2O was added into reacting gas mixture.
d. sulfur yield/SO_2 conversion; see text.

Table 4.4 Variation of the Surface Area of $Cu_{0.15}[Ce(La)]_{0.85}O_X$ Catalyst with Thermal Treatment.

	fresh catalyst	tested 12 h in dry gas[a] at ~500°C	tested 37 h in wet gas[b] at ~500°C	tested 18 h in dry gas[a] at ~750°C	calcined 17 h in air at ~750°C
S_g(m^2/g)	30.7	26.4	26.8	22.8	22.6

a. dry reactant gas mixture consisted of 1 % SO_2, 2 % CO, balance helium.
b. 2% H_2O was added into the dry reactant gas mixture.

Table 4.5 Surface composition of used $Cu_{0.02}[Ce(La)]_{0.98}O_x$ catalysts.

elements	Used for 6 h at 440°C		Used for two days at different temperatures
	top portion	bottom portion	
Ce3d	23.2	22.4	25.2
Cu2p3	2.6	3.2	5.3
S2p	5.9	8.3	5.6
O1s	68.2	66.1	63.9
–fraction of 529.6eV	57%	61 %	55 %
–fraction of 532.1eV	43%	39 %	45 %

Table 4.6 Surface composition of used $Cu_{0.15}[Ce(La)]_{0.85}O_x$ catalysts.

elements	tested for 2 h at 433°C	tested for 2 h at 510°C
Ce3d	9.9	23.1
Cu2p3	7.3	9.2
S2p	13.7	6.8
O1s	69.1	60.8
–fraction of 529.6eV	0 %	46 %
–fraction of 532.1eV	100 %	54 %

Table 4.7 XPS binding energies of the Cu-Ce-O catalysts.

Catalysts	Cu2p3		O1s		S2p	
$Cu_{0.15}[Ce(La)]_{0.85}O_x$						
tested for long term	932.2	–	529.2	531.6	168.0	162.6
tested at 510°C	932.9	934.5	529.6	532.1	168.8	162.1
tested at 433°C	–	933.8/935.6	–	532.1	167.0	–
$Cu_{0.02}[Ce(La)]_{0.98}O_x$						
tested for long term	–	–	529.4	532.0	168.9	–
tested at 440°C (bot.)	933.1*	933.1	529.4	531.8	168.2	162.5
tested at 440°C (top)	–	–	529.5	531.9	168.5	162.5
assignment	Cu^{+1}	Cu^{+2}	metal oxide	sulfate	metal sulfate	metal sulfide

*also contains 930.0eV component—isolated Cu ions.

Table 4.8 Surface Compositional Analysis of $Cu_{0.15}[Ce(La)]_{0.85}O_x$ Catalyst by XPS after tested for two days.

Atomic ratio	Cu/Ce	S/Cu
bulk material[a]	0.176	0
fresh catalyst	0.133	0
used catalyst	0.364	1.59
1-min Ar^+ sputtering	0.206	1.36
7-min Ar^+ sputtering	0.151	1.15

a. based on stoichiometry.

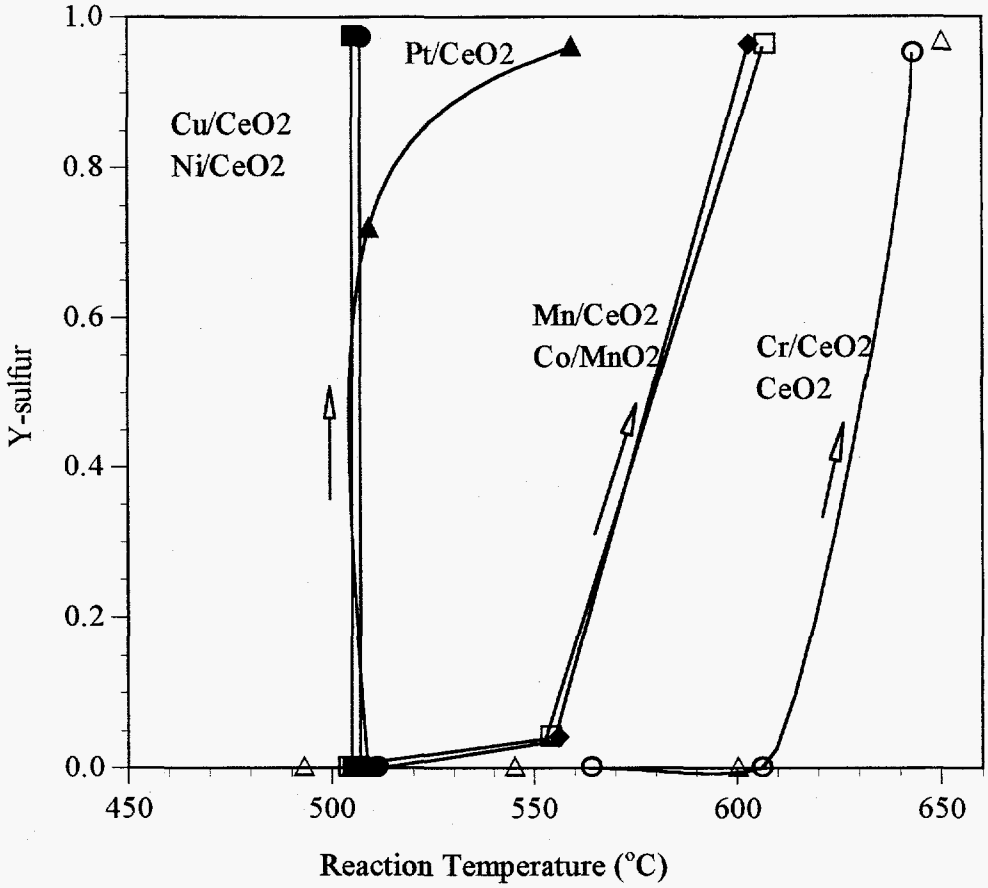

Figure 4.1 Light-off Behavior on the Transition Metal-Impregnated Ceria Catalysts (1% SO_2, 2% CO, 97% He).

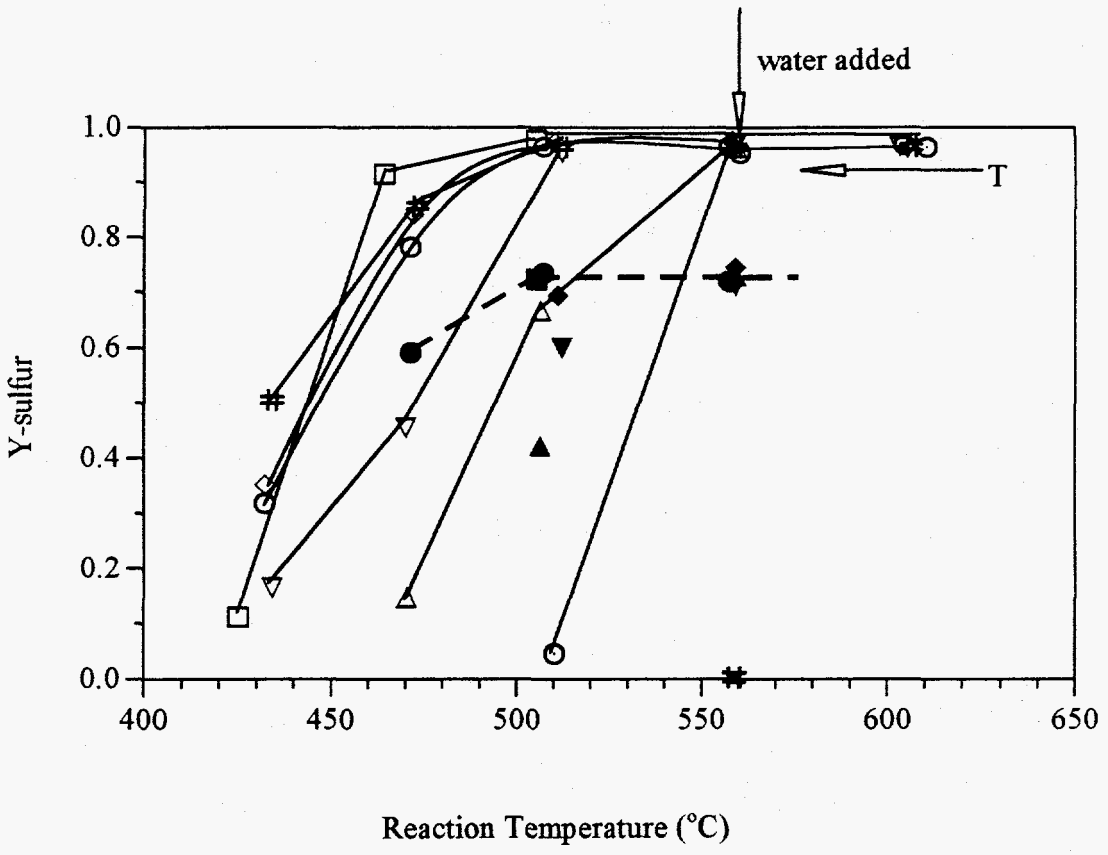

Figure 4.2 Fall-off Behavior and Water Vapor Effect on the Transition Metal-Impregnated Ceria Catalysts. □ = Cu/CeO_2, ◇ = Ni/CeO_2, △ = Pt/CeO_2, ▽ = Mn/CeO_2, ○ = Co/CeO_2, # = Cr/CeO_2, ⊙ = CeO_2. Unfilled symbols for dry gas (1 % SO_2, 2 % CO, 97 % He), The filled ones for wet gas (1% SO_2, 2 % CO, 2 % H_2O, 95 % He).

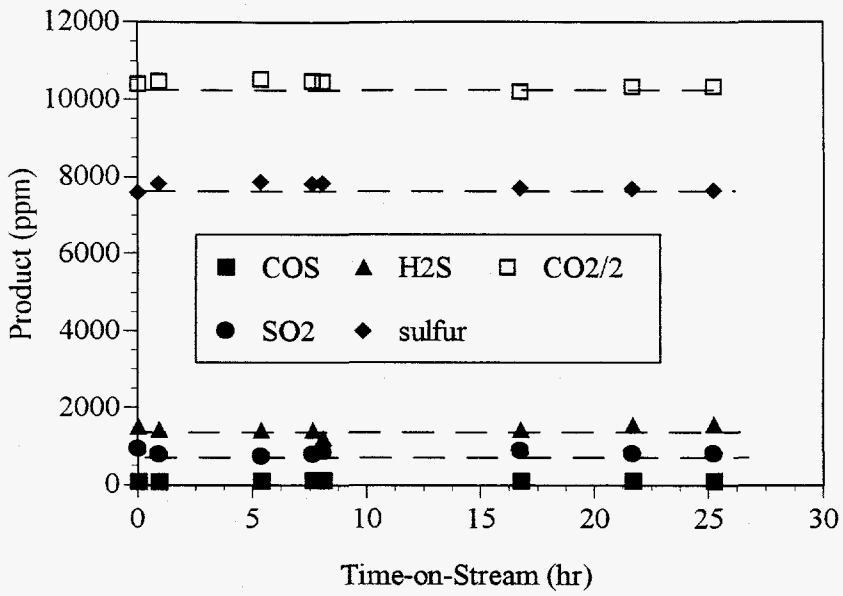

Figure 4.3 Long-term Test of Cu/CeO_2 Catalyst in Wet Gas (1% SO_2, 2.1 % CO, 2% H_2O, 95 % He; 100 sccm, 505°C, 307mg catalyst loading).

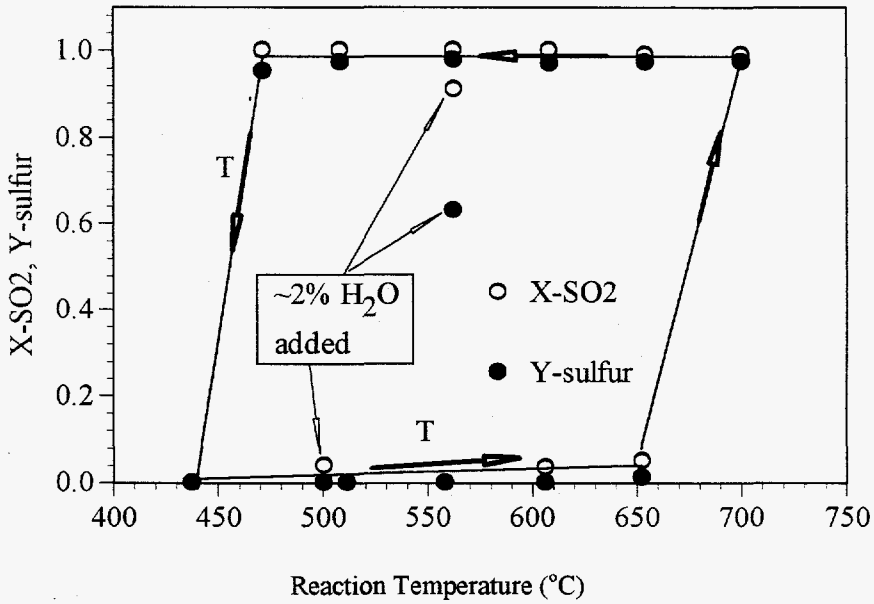

Figure 4.4 SO_2 Reduction by CO over the $Gd_2Zr_2O_7$ Catalyst (1% SO_2, 2% CO).

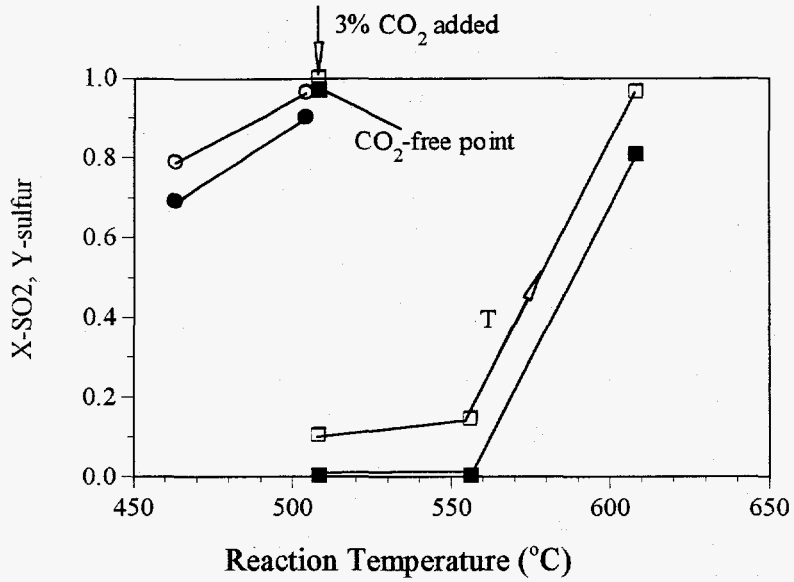

Figure 4.5 Effect of CO_2 on Catalyst Activity and Selectivity(1% SO_2, 2% CO, 3% CO_2, 94% He). □ = $La_{0.1}Ce_{0.9}O_{1.95}$, O = Cu/CeO_2. Unfilled symbols for X-SO_2 and the filled ones for Y-sulfur (■, ●).

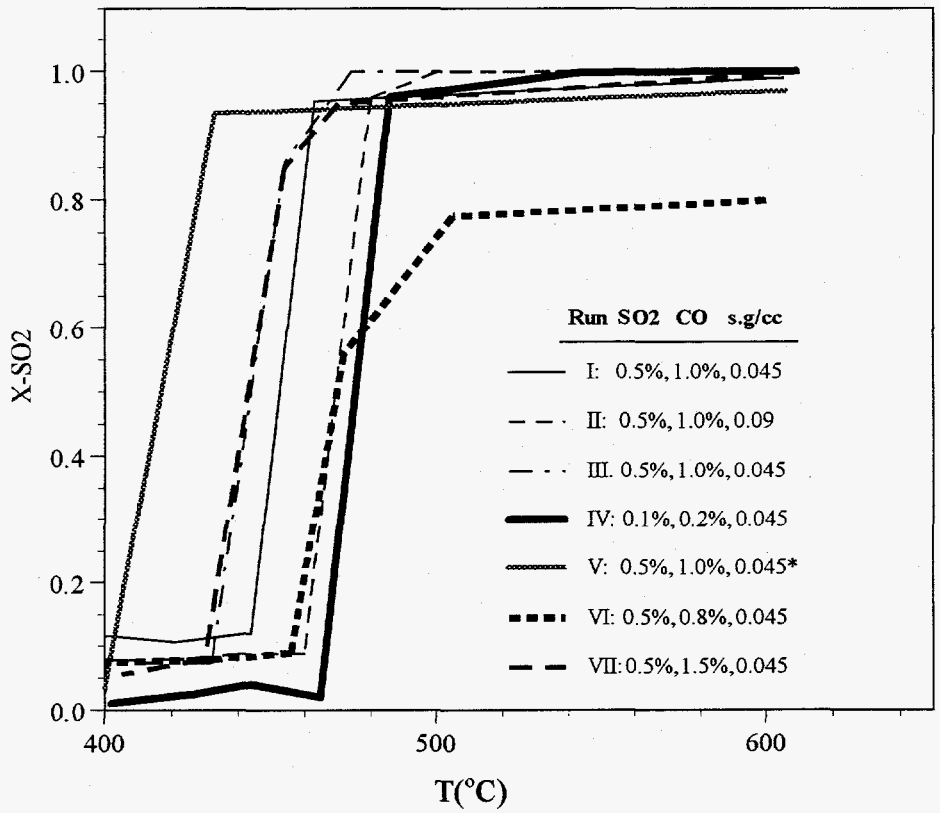

Figure 4.6 Effect of experimental conditions on light-off temperature of $Cu_{0.15}[Ce(La)]_{0.85}O_x$ catalyst (*pre-reduced in 2% CO/He for 1 h at 400°C).

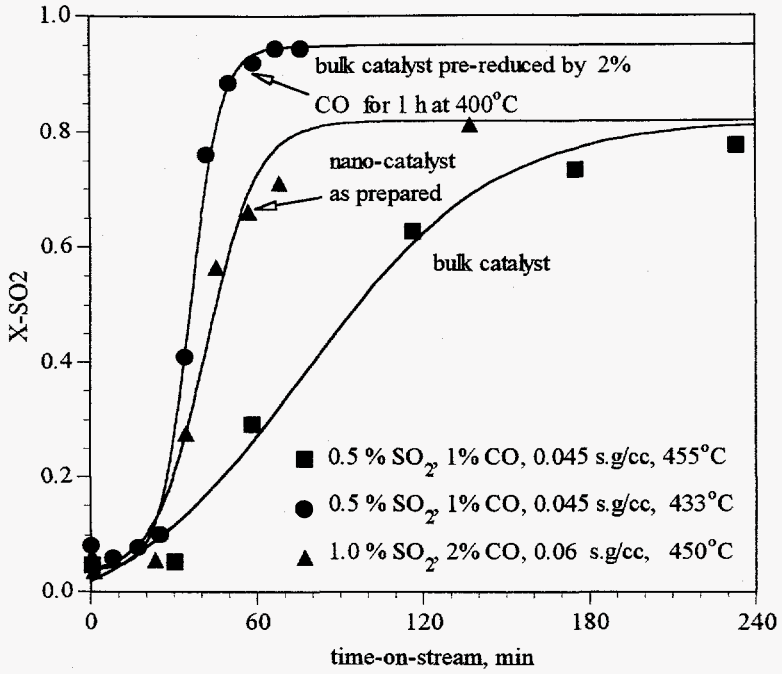

Figure 4.7 Activation profiles of 15 at.% Cu-containing Cu-Ce-O catalyst in the reacting gas mixture.

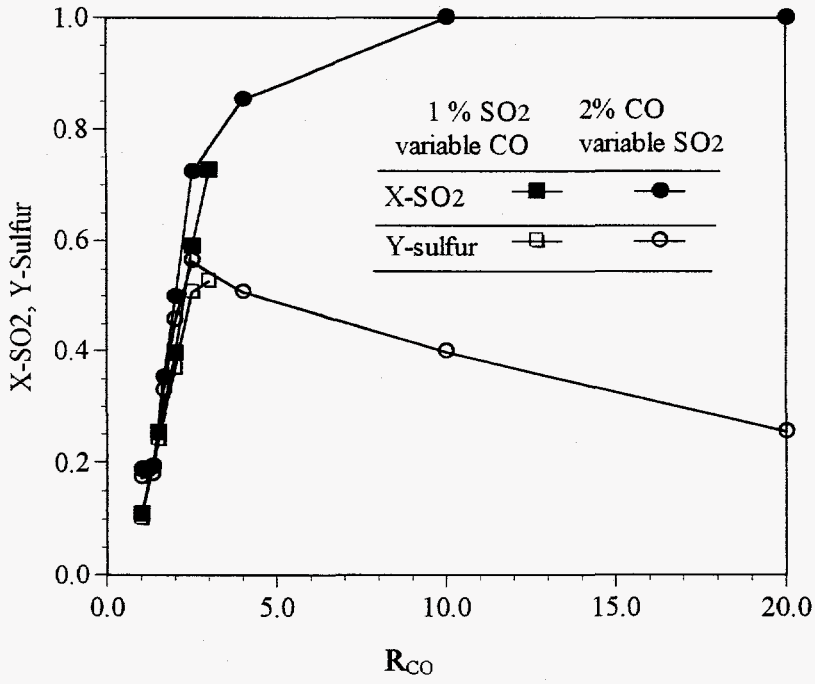

Figure 4.8 Product distribution over $Cu_{0.15}[Ce(La)]_{0.85}O_x$ catalyst versus R_{CO} (0.0113 s·g/cc, 470°C).

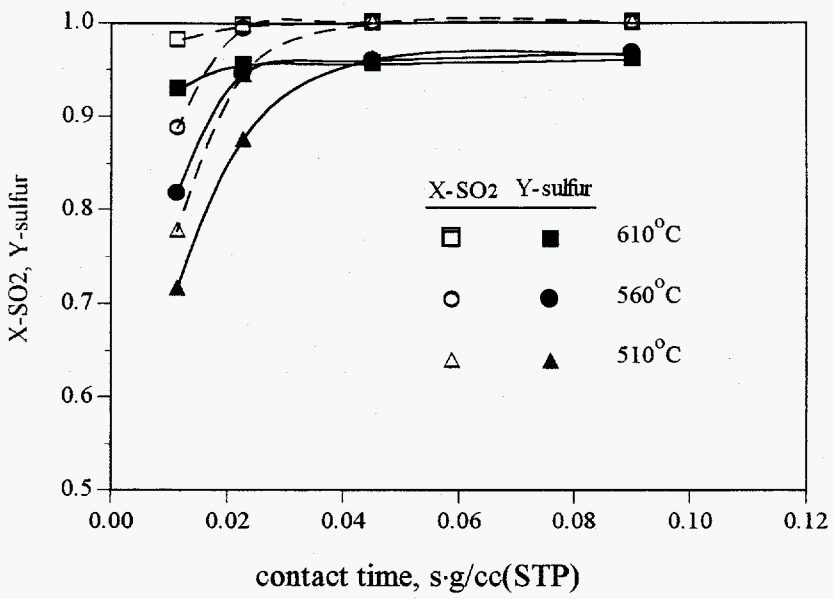

Figure 4.9 Effect of Contact Time on SO_2 Conversion at Various Temperatures (1% SO_2, 2% CO, 97% He; $Cu_{0.15}[Ce(La)]_{0.85}O_x$ Catalyst).

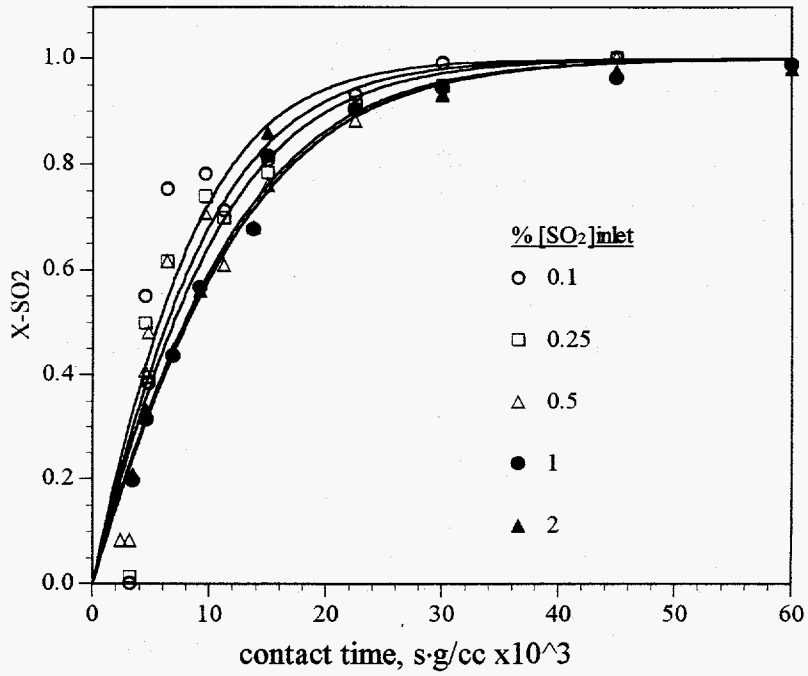

Figure 4.10 Variation of SO_2 conversion with contact time and inlet SO_2 concentration over $Cu_{0.15}[Ce(La)]_{0.85}O_x$ catalyst (R_{CO}=2, 510°C).

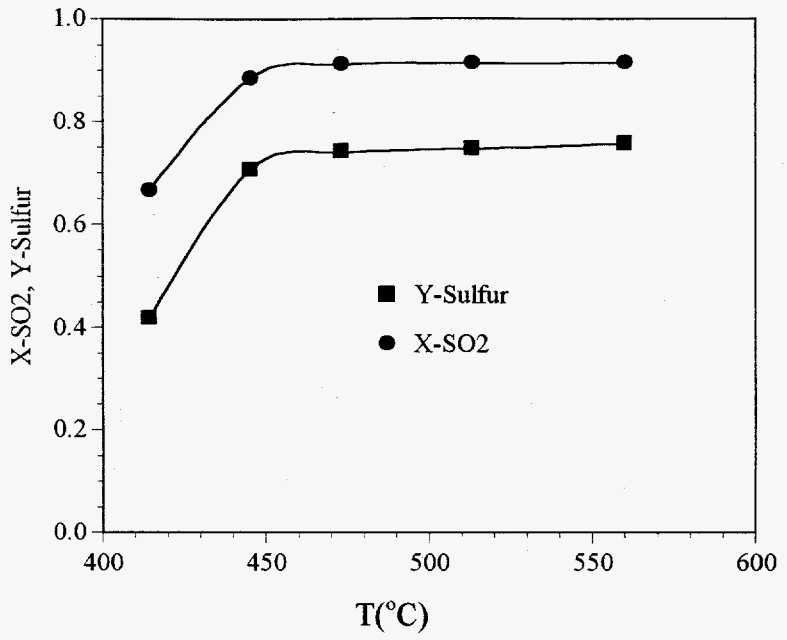

Figure 4.11 Variation of sulfur yield on $Cu_{0.15}[Ce(La)]_{0.85}O_x$ catalyst with reaction temperature in the presence of 2% H_2O (0.09s·g/cc, 1.15% SO_2, 2.4% CO).

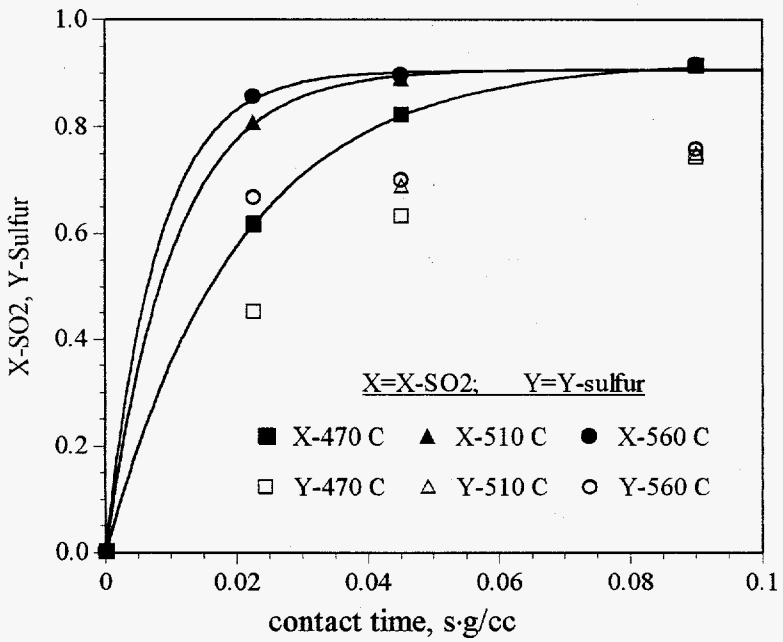

Figure 4.12 Variation of sulfur yield in the presence of 2% H_2O with contact time (0.09s·g/cc, 1.15% SO_2, 2.4% CO, $Cu_{0.15}[Ce(La)]_{0.85}O_x$ catalyst).

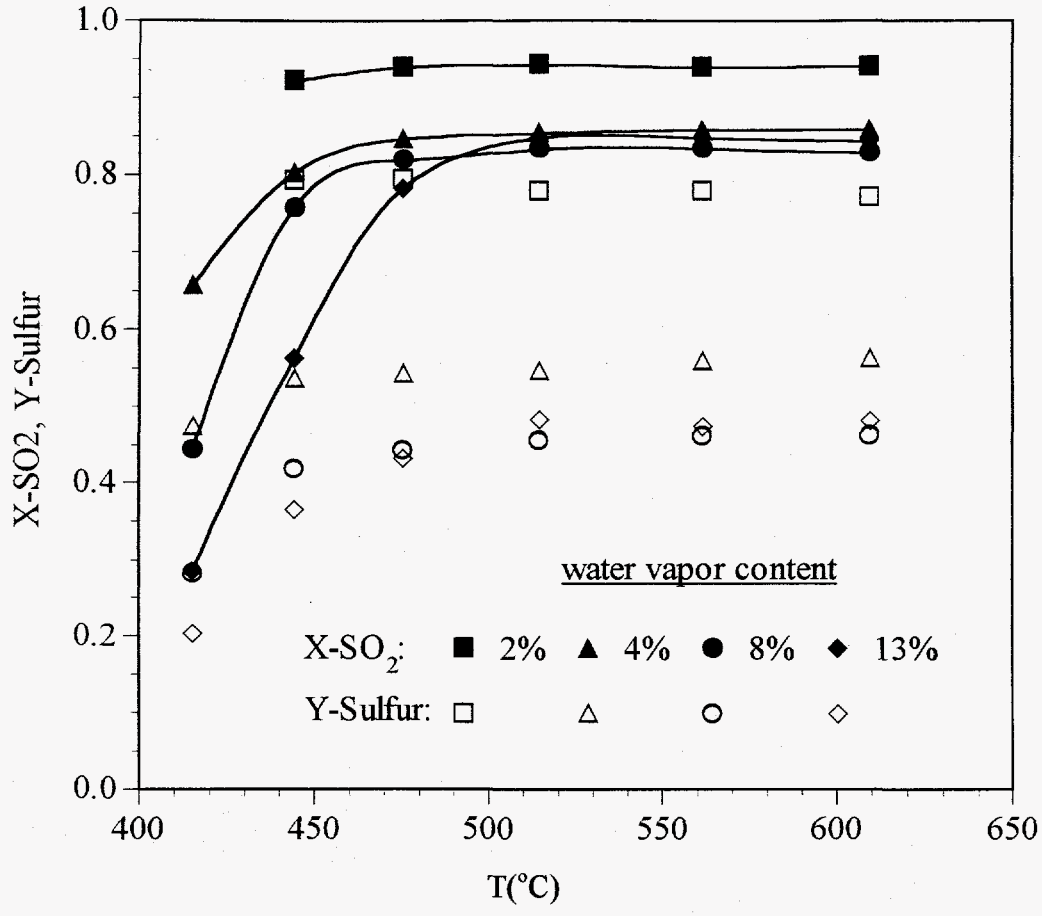

Figure 4.13 Variations of sulfur yield with temperature and water vapor content (0.09s·g/cc, 1 % SO_2, 2 % CO, $Cu_{0.15}[Ce(La)]_{0.85}O_x$ catalyst).

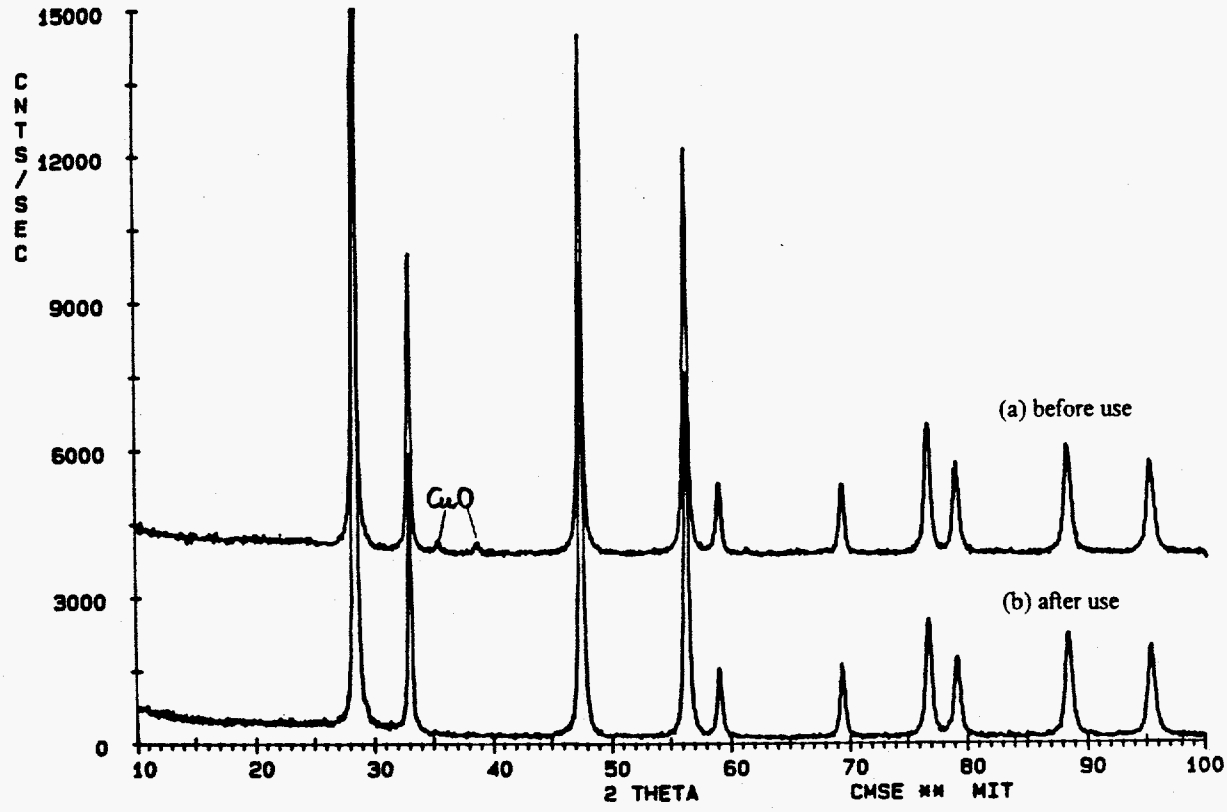

Figure 4.14 X-ray Diffractogram of the 7.8 wt.% CuOx/CeO_2 Catalyst (a) before use (b) after use.

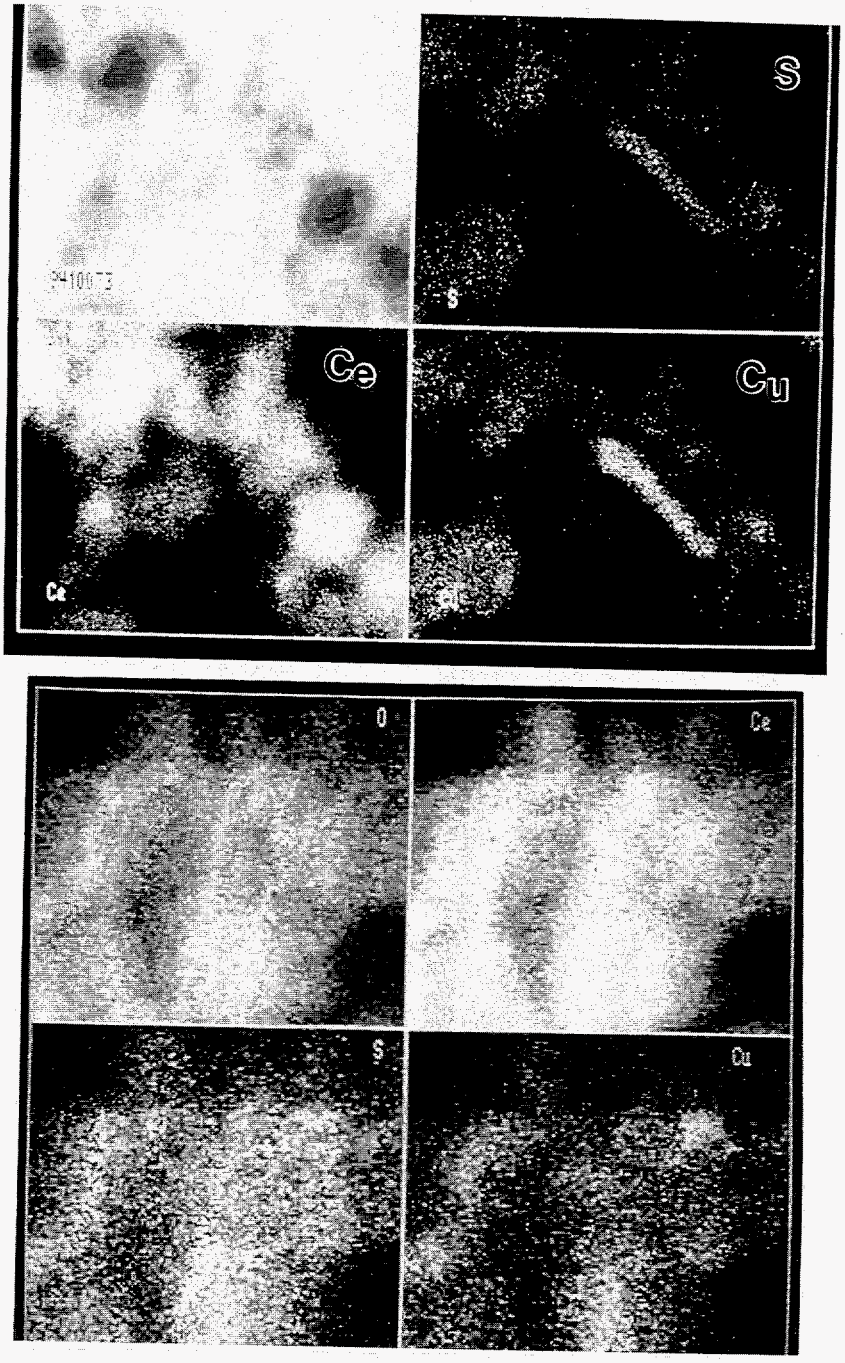

(a) $Cu_{0.15}[Ce(La)]_{0.85}O_x$

Figure 4.15 STEM elemental maps of the Cu-Ce(La)-O catalyst used for SO_2 and CO reaction.

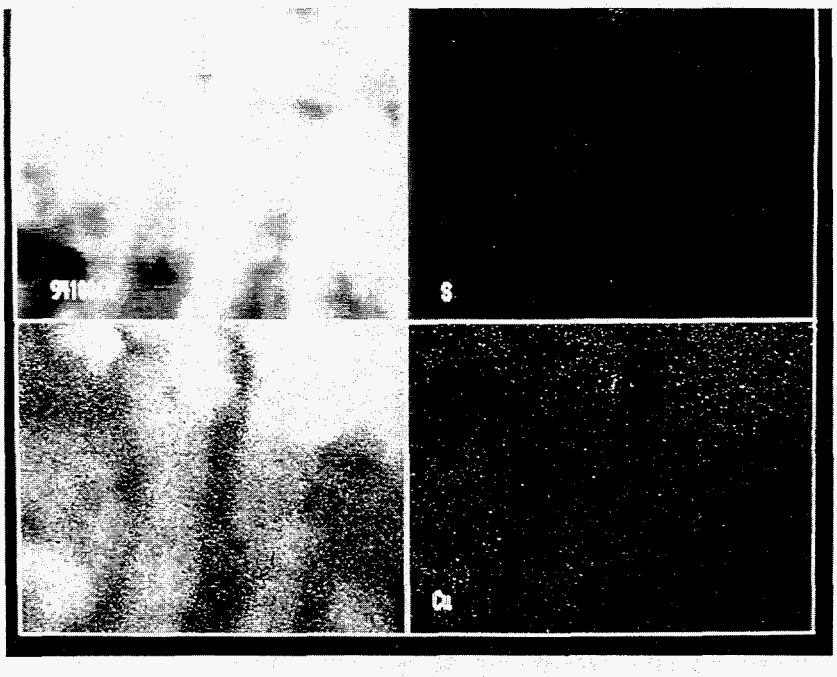

Image	S
Ce	Cu

100nm

(b) $Cu_{0.02}[Ce(La)]_{0.98}O_x$

Figure 4.15 STEM elemental maps of the Cu-Ce(La)-O catalyst used for SO_2 and CO reaction.

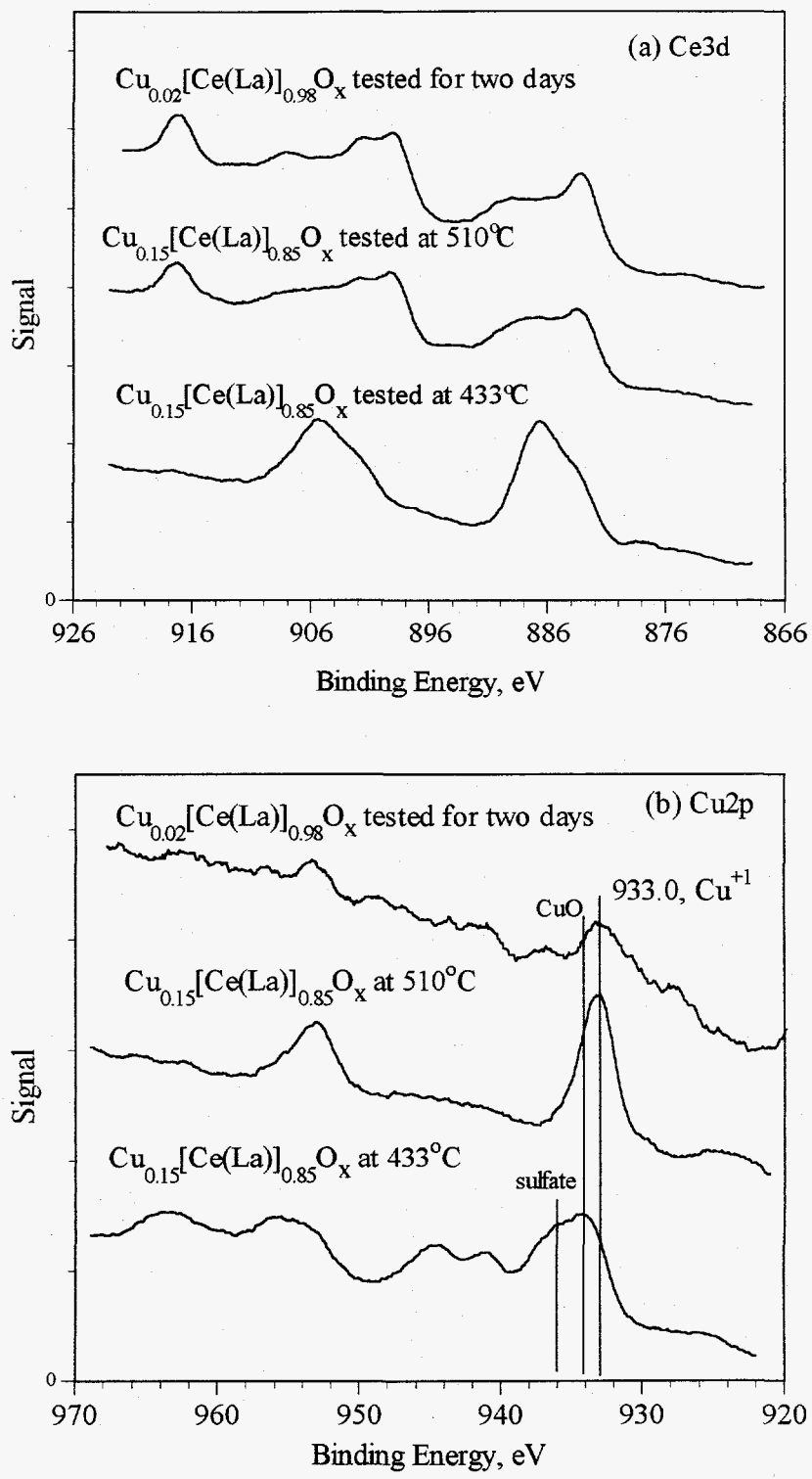

Figure 4.16 XPS of the Cu-Ce(La)-O catalyst used for SO_2 and CO reaction.

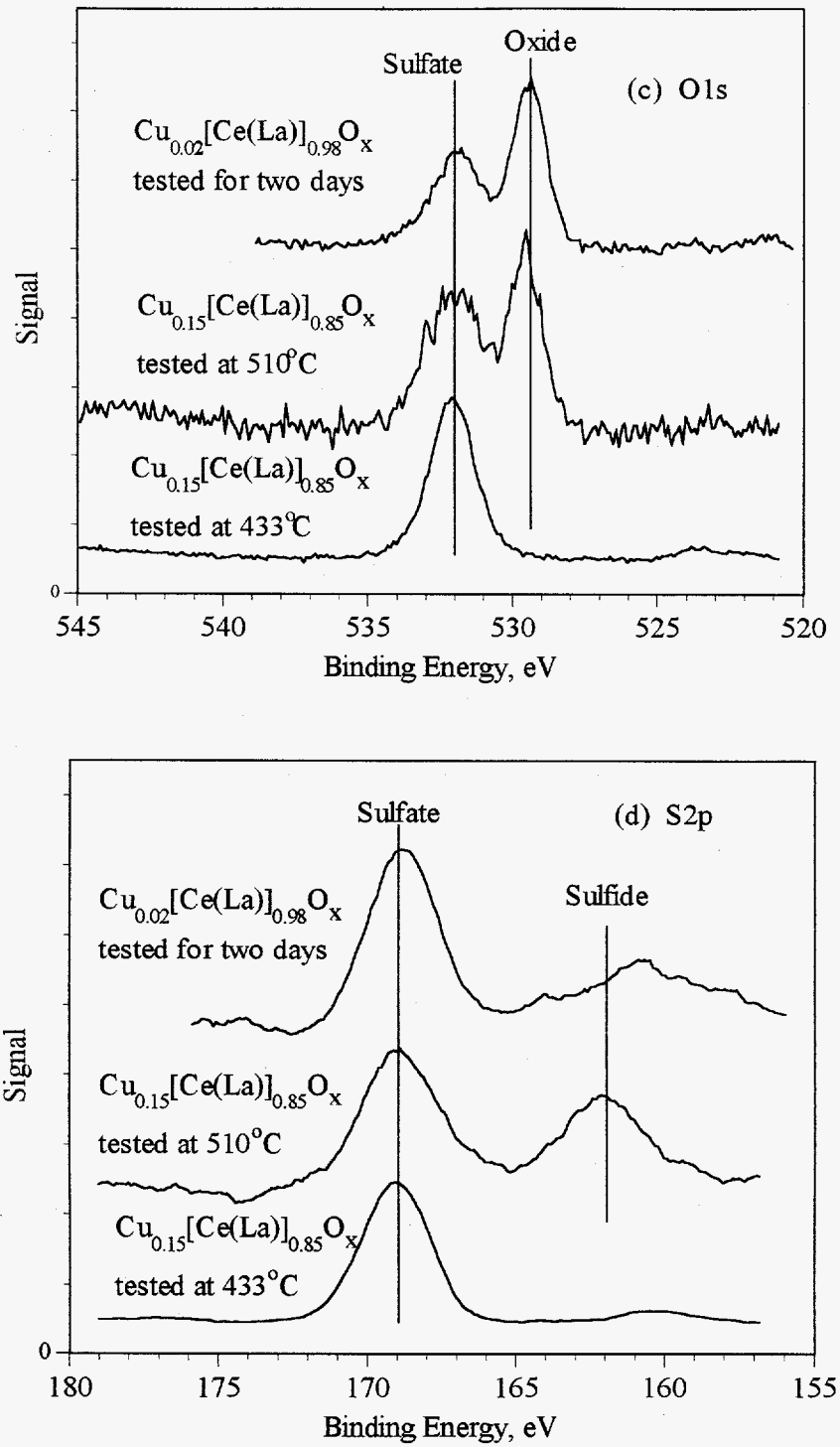

Figure 4.16 XPS of the Cu-Ce(La)-O catalyst used for SO_2 and CO reaction.

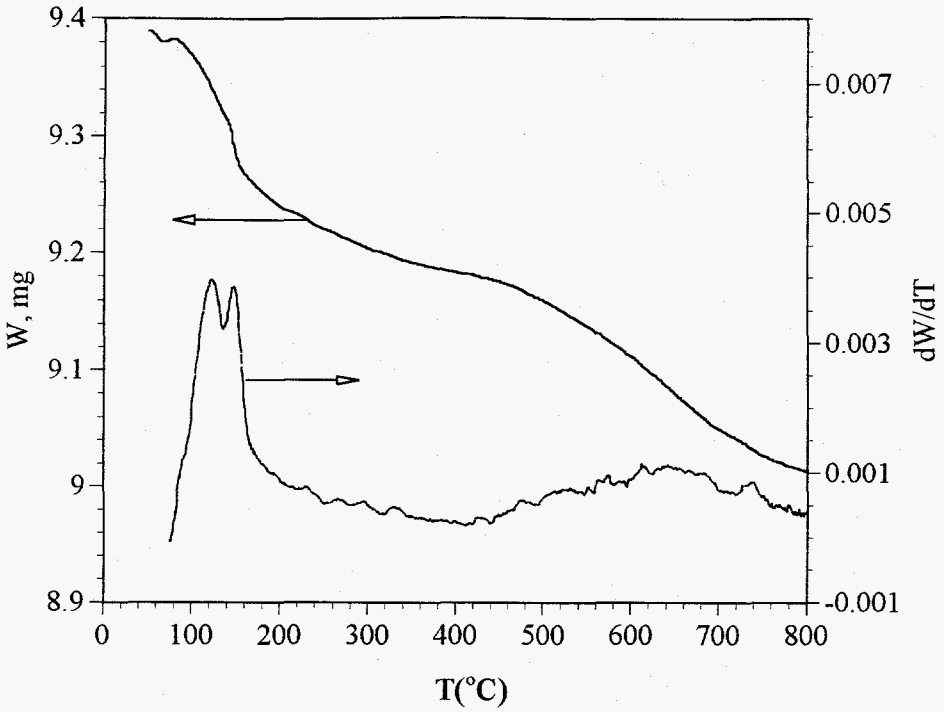

Figure 4.17 Temperature-programmed reduction profile of $Cu_{0.15}[Ce(La)]_{0.85}O_x$ catalyst by 3.5% CO/N_2.

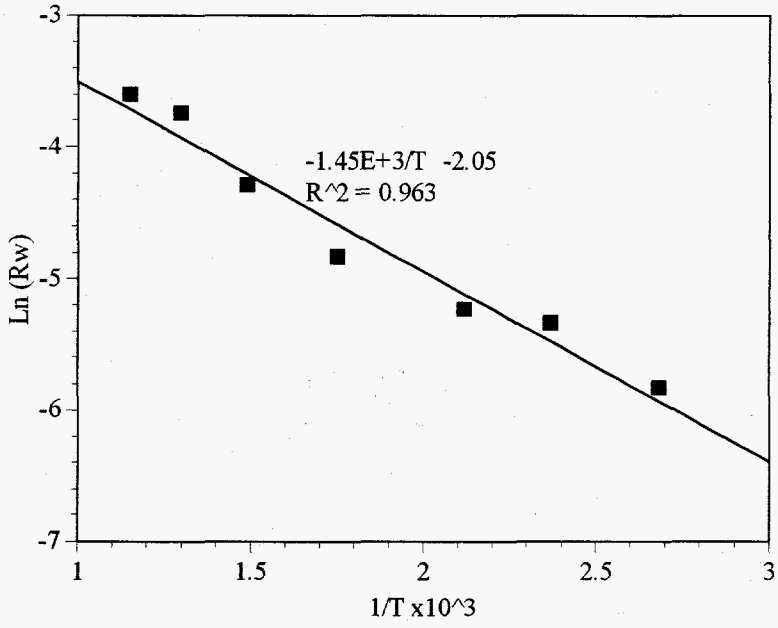

Figure 4.18 Arrhenius plot of the initial reduction rate of $Cu_{0.15}[Ce(La)]_{0.85}O_x$ catalyst by 0.5% CO/N_2.

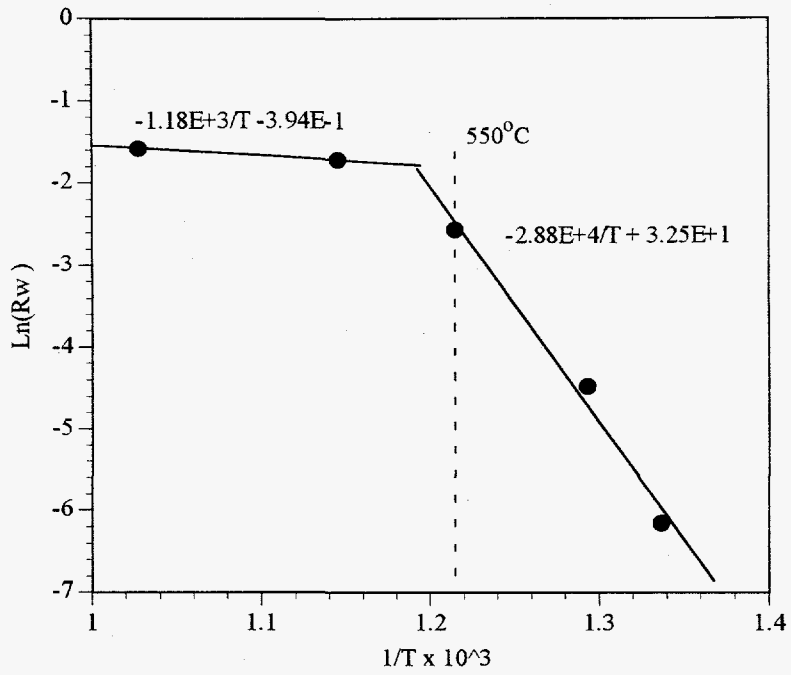

Figure 4.19 Arrhenius plot of the initial reduction rate of $Cu_{0.15}[Ce(La)]_{0.85}O_x$ catalyst pre-sulfated by 1% SO_2 for 2 h (reducing gas: 2% CO/N_2).

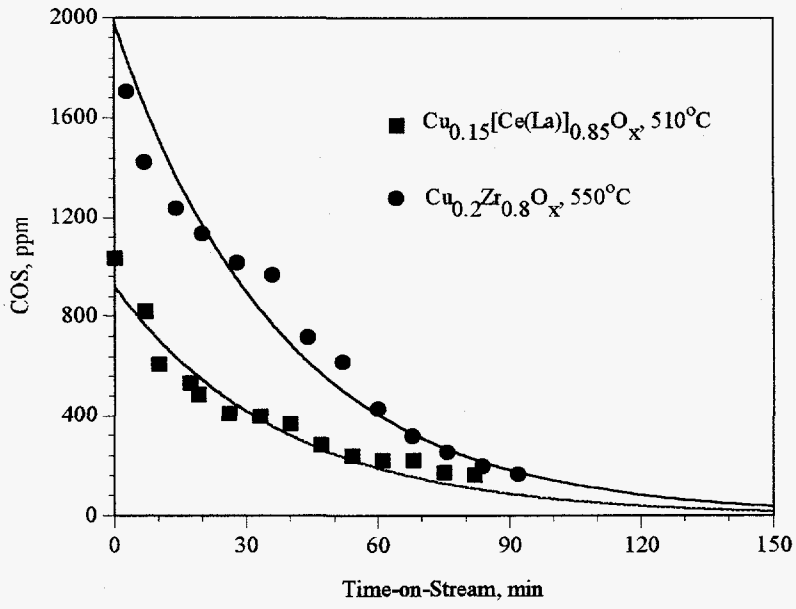

Figure 4.20 COS Evolution Profile During 2% CO/He Scavenging of Spent Catalysts.

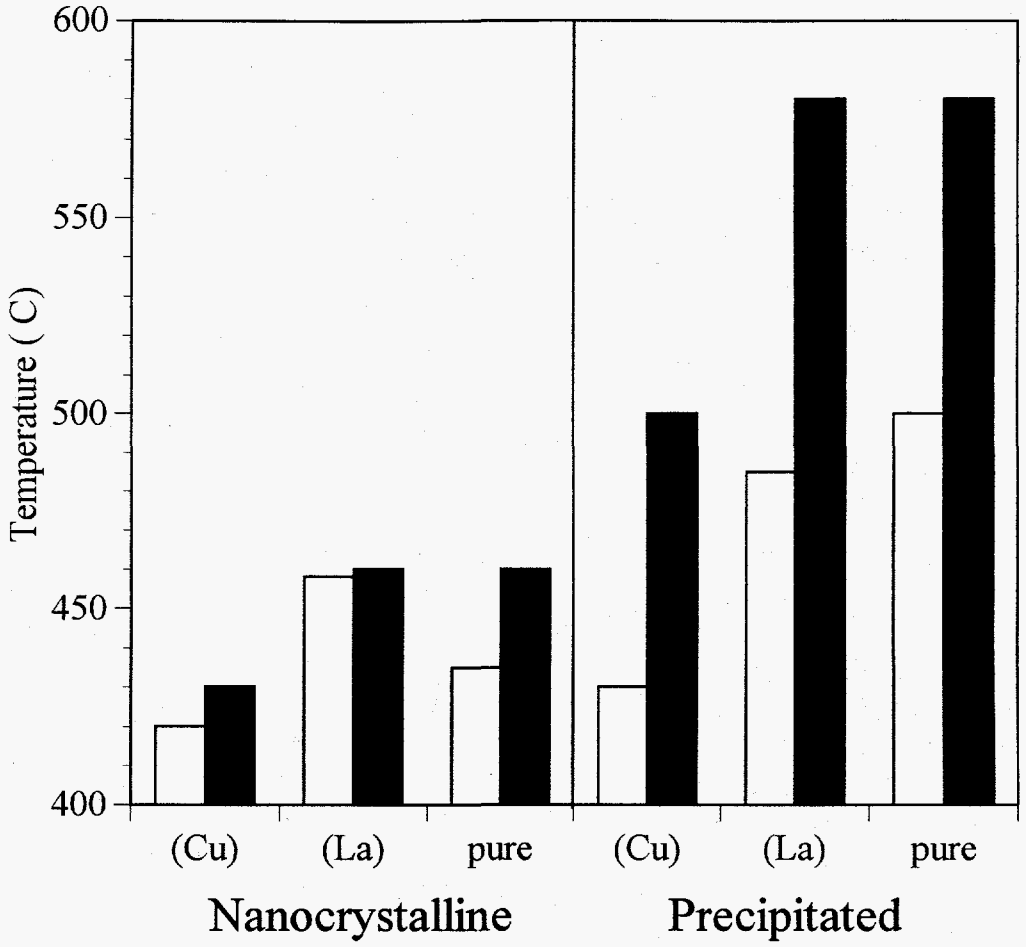

Figure 4.21 Light-off (filled bars) and fall-off (open bars) temperatures of precipitated and non-stoichiometric cerium oxide catalysts for SO_2 reduction by CO (1% SO_2, 2% CO, 0.09s·g/cc).

Chapter 5

Complete Oxidation of Carbon Monoxide and Methane over Transition Metal-Fluorite Oxide Composite Catalysts
I. Catalyst Composition and Activity

5.1 Introduction

Carbon monoxide and gaseous hydrocarbons are ubiquitous air pollutants emitted by many sources. Complete oxidation of these pollutants to carbon dioxide and water over active catalysts is used to meet continually changing environmental regulations in an economic way. Precious metals (Pt, Pd) are well known complete oxidation catalysts with high activity and stability, and are widely used for exhaust gas emission control. The high cost of precious metals and their sensitivity to sulfur poisoning have long motivated the search for substitute catalysts. A variety of transition metal oxides and mixed metal oxides have been examined. However, base metal oxide catalysts are generally less active and stable in the presence of water vapor and sulfur compounds than the precious metal catalysts. Methane is the most refractory hydrocarbon and thus, is often used as a model hydrocarbon compound for activity tests. In addition, methane itself is a potent greenhouse gas and the emission control of unburned methane from exhaust gases may be regulated in the future.

The fluorite-type oxides, such as ceria, zirconia, thoria, etc., have face-centered-cubic (FCC) crystal structure in which each tetravalent metal ion is surrounded by eight equivalent nearest O^{-2} ions forming the vertices of a cube. Oxygen vacancies are created when a fluorite oxide is doped by divalent or trivalent impurity ions. Thus, the fluorite oxides have been extensively studied as oxygen ion conducting materials *(1,2)* due to their high oxygen vacancy concentration and mobility properties. In the catalysis field, the fluorite oxides have been occasionally explored as catalysts for oxidation of carbon monoxide and methane. CeO_2-La_2O_3, CeO_2-ThO_2, and UO_2-ThO_2 oxides were tested as carbon monoxide oxidation catalysts long time ago *(3-6)*. A redox mechanism involving lattice oxygen/oxygen vacancy participation was proposed for carbon monoxide oxidation on cerium oxide *(7,8)*. A recent atomic simulation of carbon monoxide oxidation mechanism on cerium oxide *(9)* suggested that the surface oxygen of cerium oxide is more active than the bulk oxygen. Cerium oxide or zirconium oxide modified with other base metal oxides was tested for the oxidative coupling of methane *(10,11)*. For example, Ba-

doped CeO_2 was found to be an active catalyst with high selectivity to C_2 species *(11)*. Some other oxygen solid electrolytes including Zr-Y-O were examined for the complete oxidation of carbon monoxide and methane from an electronic point of view *(12)*. Typically, the fluorite-type oxides showed catalytic oxidation activity at high temperatures.

It is generally agreed that oxidation of carbon monoxide and hydrocarbons over oxide catalysts involves surface oxygen/oxygen vacancy participation *(7,10,11,13,14)* and the oxygen mobility of metal oxide catalysts has something to do with catalytic activity. In our previous studies of the reduction of sulfur dioxide by carbon monoxide to elemental sulfur *(15,16)*, or, alternatively, the oxidation of carbon monoxide by sulfur dioxide, we found that cerium oxide and zirconium oxide are active catalysts. The oxidation of carbon monoxide by sulfur dioxide is considered to proceed via a redox mechanism involving the surface oxygen/oxygen vacancy participation. The activity of cerium oxide for this reaction was enhanced by addition of small amounts of rare earth oxide dopants *(15)*. Further activity enhancement and catalyst resistance to water vapor and carbon dioxide poisoning were achieved by doping the fluorite oxide with transition metals, such as copper, cobalt, nickel, etc. *(16)*. Thus, we postulated that a general oxidation catalyst may be achieved by promoting fluorite oxides with active transition metals such as copper. In such a catalyst configuration, the transition metals are used in minor amounts and stabilized in the fluorite oxide matrix, while the fluorite oxide is the essential and major catalyst component and not an inert support. We have found that this type of catalyst was highly active for the complete oxidation of carbon monoxide and methane in a preliminary study *(17)*.

Cerium oxide has been widely used in the automotive three-way catalytic converter as an oxygen storage medium and thermal stabilizer. The interaction of ceria with precious metals (Pd, Pt, Rh) and its effect on the catalytic activity have been intensively studied *(18,19)*. By contrast, little information is available to date on the interaction of fluorite oxides with base metal catalysts and their application to complete oxidation of carbon monoxide and methane. A recent paper *(20)* studied the effect of oxygen vacancies in yttria-stabilized zirconia (YSZ) support on the properties of copper catalyst for carbon monoxide oxidation. Several binary mixtures of transition metals and fluorite oxides have been proposed in the literature as methanol synthesis catalysts *(21)*. However, an active catalyst for this application generally comprises the transition metal as the major component. From a materials point of view, alkaline earth and rare earth oxides have considerable solubility in fluorite oxides *(22)*, while transition metal oxides have little or no solubility *(23)*.

In the present study, we systematically examined the Cu-Ce-O composite oxide for carbon monoxide oxidation and the complete oxidation of methane, and briefly surveyed some other transition metal-fluorite oxide systems. The reasons for more emphasis on the Cu-Ce-O system are: (i) CeO_2 has a stable fluorite-type crystal structure from room temperature up to its melting point(2600°C); (ii) copper is known as an active oxidation catalyst; (iii) both cerium and copper oxide precursors are readily available commercially.

5.2 Experimental

5.2.1 Catalyst Preparation

The bulk composite catalysts were prepared by coprecipitating aqueous salt solutions of the metals with ammonium carbonate or sodium carbonate. The ammonium carbonate was a good precipitation agent and did not introduce impurity metal ions, but the formation of metal-ammonia complex often caused some slippage of transition metals. If sodium carbonate was used, the precipitate had to be carefully washed to remove residual sodium. The precipitates were washed twice with hot deionized water and then dried for about 12 hours at 110°C. The dried samples were typically heated for about 4 h at 650°C in air, unless specifically noted. Low purity (99%, Aldrich) cerium nitrate containing about 1.5 wt % lanthanum, corresponding to an atomic ratio of La to (La+Ce) of about 0.045, was used in the typical catalyst preparation. The cerium from this precursor was designated as Ce(La) in the catalyst formula throughout the paper. High purity (99.99%, Aldrich) cerium nitrate was used to prepare the catalysts containing different dopant ions (Sr, Sc, La, Gd). Cerium acetate(99.9%, Aldrich), heated for 4 h at 750°C in air, was used as the primary precursor of La-free cerium oxide. Chloroauric acid($HAuCl_4$), hydrogen hexachloroplatinate(IV) hydrate, and zirconium dichloride oxide hydrate were used as Au, Pt, and Zr precursors, respectively, while the AR grade metal nitrates were used for all other metals.

γ-Al_2O_3 was supplied by LaRoche. Bulk CuO was prepared by thermal decomposition of copper carbonate in air (4 h at 650°C). The supported catalysts were prepared by the conventional wet impregnation method using aqueous salt solutions of the metals. The slurry of the support and solution was degassed in vacuum so that the salt solution fully filled the pores of the support during impregnation. After excess solution was drained, the sample was dried for a few days at room temperature and then heated in air for 4 h at 650°C. The physical mixture of ceria and copper oxide, $CuO+CeO_2$, was prepared by blending the CuO and CeO_2 powders with water in an ultrasonic water bath for 10 minutes and followed by drying at 300°C for 1 h. For bulk composition analysis, the catalyst powder was dissolved in hydrofluoric acid and diluted by deionized water, the resulting solution was analyzed by the Inductively Coupled Plasma(ICP) atomic emission spectrometry(Perkin Elmer Plasma 40). Catalyst surface composition was analyzed by X-ray Photoelectron Spectroscopy(XPS) on a Perkin Elmer XPS 5100 system. The catalyst characterization was performed by single-point desorption of nitrogen on a Micromeritics Flow Sorb II 2300 apparatus for BET surface area measurement and X-ray powder diffraction(XRD) on a Rigaku 300 X-ray Diffractometer for crystalline phase identification. Throughout this paper, the at % denotes the ratio of a specific metal ion to the total metal ions in a given catalyst(x100%). The catalysts prepared by the coprecipitation and impregnation methods were denoted by $Cu_x[Ce(La)]_{1-x}O_{2-x}$ and CuO_x/CeO_2, respectively.

5.2.2 Apparatus and Procedure

Typically, catalysts were tested in a laboratory-scale packed bed flow reactor consisting of a 0.6 cm I.D. x 50 cm long quartz tube with a porous quartz frit placed at the middle for supporting the catalyst. Occasionally, a 1.0 cm I.D tube reactor was used when large catalyst volume was needed. The reactor tube was heated by a Lindberg furnace. Flowing air was used to cool the outside surface of the reactor tube when the test was conducted at low temperatures (<100°C). The reaction temperature was monitored by a quartz-sheathed K-type thermocouple placed at the top of the packed catalyst bed and controlled by a Wizard temperature controller. CO and CH_4 reacting gases were certified calibration gas mixtures balanced by helium(from Matheson). Air and helium(all from AIRCO) were used as oxidizing gas and diluent, respectively. The gas streams were measured with rotameters and mixed prior to the reactor inlet. The resulting gas mixture without further purification flowed downward through the packed catalyst bed. Water vapor was introduced with helium bubbling through a heated water bath. The pressure drop of gas flowing through the assembly was small. Thus, experiments were carried out at nearly atmospheric pressure. The product gas stream was analyzed by a HP5880A Gas Chromatography(GC) with a Thermal Conductivity Detector(TCD). The carbon balance was checked by simultaneous measurement of the reactant and products. Unless specifically noted, the catalyst loading was 150 mg which resulted in a packed bed height of typically 5 mm for CeO_2-based catalysts and 2-3 mm for ZrO_2-based catalysts in the 0.6 cm I.D. reactor. The total gas flow rate was set at 100 sccm consisting of 2 % CO or 2% CH_4, 16% O_2, and balance He and N_2. Thus, the contact time was 0.09 g·s/cc(STP) and the space velocity was typically 42,000 h^{-1} for the CeO_2-based catalysts. The prepared catalysts were directly tested without any pre-treatment unless specifically noted. The activity measurement was conducted in an ascending temperature manner so that the light-off behavior was recorded. No hysteresis effect was observed in these tests. The catalyst activity was ranked based on the light-off temperature at which 50% conversion occurred. The specific reaction rate was measured in a differential reactor mode with conversion not exceeding 10 % by choosing appropriate catalyst loading and flow rate. The SiC powder was used as an inert mixer to keep approximately the same packing height when small amounts of the catalyst tested.

5.3 Results and Discussion

5.3.1 Carbon Monoxide Oxidation

5.3.1.1 CeO_2 and $Zr_{0.9}Y_{0.1}O_{1.9}$ Catalysts

Figure 5.1 shows the light-off curves of CO oxidation over various CeO_2 catalysts containing different dopants as well as the $Zr_{0.9}Y_{0.1}O_{1.9}$ ($0.05Y_2O_3$-$0.9ZrO_2$)catalyst. The undoped CeO_2 had an activity similar to the La- and Sr-doped catalysts, but higher activity than the Sc or Gd-doped catalysts. The $Zr_{0.9}Y_{0.1}O_{1.9}$ catalyst had activity comparable to the CeO_2 catalysts at low temperatures and lower at high temperatures. In summary, all these catalysts showed relatively low activity with light-off temperatures(50% conversion) over

the range of 360 to 440°C. According to the oxygen vacancy formation theory *(24)*, one oxygen vacancy is created when one divalent(D^{2+}) or two trivalent (D^{3+})dopant ions are introduced into fluorite crystal lattices. The resulting oxygen vacancy and the parent dopant ions are energetically associated pairs. The higher the association energy the lower the oxygen vacancy mobility. The association energies in CeO_2 doped with various alkaline or rare earth oxides were experimentally measured and calculated *(24,25)*. The association energy increases in the order Gd<La<Sc<Sr. The oxygen mobility in the doped CeO_2 catalysts was found to correlate well with the catalytic activity for the reduction of sulfur dioxide by CO *(15)*. But, the present activity results show that the activity of the doped CeO_2 catalysts for CO oxidation did not correlate with either the bulk oxygen vacancy concentration or oxygen mobility. In contrast to the alkaline earth and rare earth oxide dopants, 1 at. % Cu dopant significantly increased the catalytic activity of $[Ce(La)]O_2$ and lowered the light-off temperature to 135°C (Figure 5.1). Thus, this catalyst was chosen for further study.

5.3.1.2 $Cu_{0.01}[Ce(La)]_{0.99}O_x$ Catalyst.

The fresh $Cu_{0.01}[Ce(La)]_{0.99}O_x$ catalyst shown in Figure 5.1 was prepared by 4 h calcination at 600°C in N_2. This different calcination procedure was used in an attempt to keep copper ions inside the cerium oxide lattice, because copper oxide is immiscible with cerium oxide. However, further calcination of this catalyst in flowing air turned out to be beneficial to the catalyst activity. Figure 5.2 shows the light-off curve shifted to lower temperature after the catalyst was treated at higher temperature (660°C, 760°C, 860°C). But, the light-off curves converge at high conversions. Table 5.1 lists the catalyst surface area and surface composition after different thermal treatments. The catalyst surface was significantly enriched in copper as the heating temperature increased, while La was slightly enriched on the surface. The surface area decreased from the fresh value of 57 to 27.3m^2/g after the catalyst was heated for 3 h at 860°C, while the light-off temperature(50% conversion) decreased from 150 to 80°C. These results show that copper oxide is not soluble in CeO_2, since calcining the catalyst in air drove the copper from the bulk to the surface, and the copper enrichment of the catalyst surface may have contributed to the activity increase. In contrast, the solubility of lanthanum oxide in cerium oxide was confirmed.

5.3.1.3 $Cu_x[Ce(La)]_{1-x}O_{2-x}$ Catalyst

Figure 5.3 shows the light-off curves over various bulk $Cu_x[Ce(La)]_{1-x}O_{2-x}$ catalysts prepared by coprecipitation. The experimental data for the catalysts with different bulk copper levels from 2 to 50 at.% are approximately represented by a single light-off curve, that is, the catalytic activity was not affected by the bulk copper content. The light-off temperatures were typically 80°C. Figure 5.4 shows the XRD patterns of these catalysts. At low copper content, there were no visible peaks due to the CuO crystal phase. As the copper content increased, the CuO peaks became apparent. We also see that the CuO peak width is generally narrower than that of CeO_2 peak, although the intensity of the

CuO peak is smaller. The crystal particle sizes of CuO and CeO_2 were estimated by peak broadening *(26)* with the Scherrer's equation and listed in Table 5.2. Table 5.2 also lists the surface composition determined by XPS. It is interesting that at low bulk copper content the surface copper content was higher than the bulk average, but the surface copper no longer increased for bulk copper content higher than ca. 15 at. %. It appears that copper is finely dispersed in CeO_2 at low copper contents, and when saturation is reached at higher copper contents, the excess copper formed bulk CuO particles that do not contribute to the XPS signal(or "invisible" to XPS).

On the basis of the activity results, we propose that the catalyst activity derives primarily from the combination of finely dispersed copper-cerium oxide system, while the CuO particles have negligible contribution. This hypothesis was confirmed by the following experiment. Bulk CuO can be easily dissolved in nitric acid. Thus, the bulk CuO particles in the $Cu_x[Ce(La)]_{1-x}O_{2-x}$ catalyst were removed by immersing the sample in nitric acid for 14 h and followed by filtering, washing with de-ionized water and drying at 650°C for 1 h. The catalyst compositions after this treatment are shown in Table 5.2. The higher the initial bulk copper content the more copper was removed by this process resulting in similar bulk composition(as determined by ICP) for three copper-containing catalysts: 15, 25 and 50 at. % in spite of large initial composition difference. XRD analyses of the nitric acid-treated catalysts revealed absence of the CuO phase as shown in Figure 5.4. The surface composition of the treated 50 at.% Cu catalyst is similar to the 2 at. % Cu catalyst. Figure 5.3 shows negligible difference in the catalytic activities between the fresh and the nitric acid-treated catalysts. Thus, we conclude that copper clusters, invisible by XRD and stabilized by strong interaction with CeO_2, mainly contribute to the catalytic activity. Only a small amount of copper(a few percent) is needed to promote the CO oxidation activity of CeO_2, and excess copper forms bulk CuO particles having little contribution to catalyst activity. The bulk copper content needed for uniform surface coverage of a CeO_2 catalyst with 30 m^2/g surface area was calculated to be 8.5 at.% by assuming monolayer Cu^{+2} ions of radius equal to 0.087nm. This fact and the surface composition listed in Tables 1 and 2 suggest that only small fraction of copper in the Cu-Ce-O catalyst of high level copper content is dispersed on cerium oxide surface. Further details of catalyst microstructure are given in Part II of this paper *(27)*.

5.3.1.4 Effect of Dopant Oxides on the Catalytic Activity of $Cu_{0.15}Ce_{0.85}O_x$ Catalyst

The effect of 1 at.% alkaline earth or rare earth dopant oxide on the CO oxidation activity of the $Cu_{0.15}Ce_{0.85}O_x$ catalyst is shown in Figure 5.5. The light-off curves on all the catalysts virtually overlapped. It seems that 1 at.% dopant(La, Sr, Gd, La) had little effect on the CO oxidation activity of the $Cu_{0.15}Ce_{0.85}O_x$ catalyst, similar to the case of the bulk CeO_2 catalyst (Figure 5.1). The effect of La dopant content on the $Cu_{0.15}Ce_{0.85}O_x$ catalyst activity is shown in Figure 5.6. La dopant had a negative effect on the catalytic activity when its doping level reached 10 at.%. The surface La content of this catalyst was about 18 at %. Thus, the activity decrease may be due to excessive La-enrichment of the catalyst surface. The variation of the activity at low La doping level was probably caused by some

variability in catalyst preparation. Typically, the activity measurement showed good reproducibility, while the catalyst preparation by coprecipitation had fair reproducibility with about ±10°C variation in the light-off temperature. It is also noted that Na impurity introduced in the coprecipitation with sodium carbonate had a detrimental effect on the catalytic activity. However, the catalysts prepared with ammonium carbonate and sodium carbonate showed similar activity as long as the Na ions were carefully washed away.

5.3.1.5 Activity Enhancement by the Concerted Effect of CuO and CeO_2

The experimental results presented so far have indicated that the Cu-Ce-O type mixed oxide is a highly active catalyst for CO oxidation, as full conversion to CO_2 over this catalyst occurred around 100°C. The catalyst activity is due to the synergistic effect between CuO and CeO_2 as illustrated by Figure 5.7. Bulk CeO_2 catalyst had low activity at low temperatures, while bulk CuO is known as an active catalyst for CO oxidation with a light-off temperature(50% conversion) around 140°C as measured in this work. When the same bulk CuO powder was mixed with the CeO_2 powder according to the procedure described earlier with an atomic ratio of 15:85, the light-off curve shifted to low temperatures by about 80°C. The 15 at.% Cu-containing bulk catalyst $Cu_{0.15}[Ce(La)]_{0.85}O_x$ and the impregnated 15 at.% CuO_x/CeO_2 catalysts showed only slightly higher activity than the physical mixture.

The bulk CuO had much lower surface area than the Cu-Ce-O catalyst. To clarify that the activity enhancement effect was due to the interaction of CuO and CeO_2, additional tests were run as shown in Figure 5.8. The light-off curves on the $Cu_{0.15}[Ce(La)]_{0.85}O_x$ and bulk CuO catalysts in Figure 5.8 were measured on the same total BET surface area basis. The light-off temperature on the $Cu_{0.15}[Ce(La)]_{0.85}O_x$ catalyst was still about 70°C lower than that on the bulk CuO. Compared to Figure 5.7, the light-off curve on the bulk CuO catalyst was not affected as the CuO loading increased from 150 to 1000mg. The 14 at.% CuO/γ-Al_2O_3 catalyst had significantly lower activity than the bulk CuO, but comparable activity to the literature data. This may be explained by the known formation of copper aluminate in alumina-supported copper oxide catalyst. The specific copper surface area of this catalyst measured by N_2O decomposition was about 50 m^2/g. The copper dispersion effect was also examined in Figure 5.8 with 3.2 at.% Cu-ZSM-5 and 3.1 at.% Ce plus 1 at.% Cu, Ce-Cu-ZSM-5 catalysts. Compared to the 2 at.% Cu-containing Cu-Ce(La)-O catalysts (Figure 5.3), these ion-exchanged zeolite catalysts had very low activity at temperatures lower than 250°C. Copper dispersion in these two catalysts, however, is high, because copper ions are associated with Al ions in the ZSM-5 frame work *(28)*. The results in Figures 7 and 8 clearly indicate that the Cu-Ce-O catalyst has much higher activity than other copper-based catalysts on the basis of either unit catalyst weight or total surface area. While good metal dispersion is, in general, necessary to obtain an active catalyst, high copper dispersion alone is not sufficient to achieve an active CO oxidation catalyst; the enhanced activity of the Cu-Ce-O composite catalyst must result from the interaction of copper and CeO_2 or a "concerted effect" between these two kinds of materials.

The reaction rate on the $Cu_{0.15}[Ce(La)]_{0.85}O_x$ catalyst is compared with those on some well-known CO oxidation catalysts reported in the literature *(29,30, 31)* in Table 5.3. Manganese-based mixed oxides have long been known as low temperature CO oxidation catalysts. Copper oxide is also one of the most studied oxidation catalysts. The reaction rate on the $Cu_{0.15}[Ce(La)]_{0.85}O_x$ is a few times higher than that on the Mn-based catalysts and 300 times higher than the Cu/δ-alumina catalyst. Recently, Rajadurai and Carberry *(31)* reported the perovskite-type mixed oxide, $La_{0.8}Sr_{0.2}CrO_{3-\delta}$, as an active CO oxidation catalyst rivaling the platinum catalysts. Table 5.3 shows that the $Cu_{0.15}[Ce(La)]_{0.85}O_x$ has a reaction rate per unit catalyst weight comparable to the Pt/alumina catalyst and much higher than $La_{0.8}Sr_{0.2}CrO_{3-\delta}$. The conventional N_2O decomposition method *(32)* was tried to measure the specific copper surface area in the Cu-Ce(La)-O catalyst. However, we were not able to get a reliable measurement due to the strong interaction between Cu and $[Ce(La)]O_2$. The specific copper surface area in the $Cu_{0.15}[Ce(La)]_{0.85}O_x$ catalyst was roughly estimated by multiplying the BET surface area by the surface atomic fraction of copper in Table 5.2. Table 5.3 shows that the specific reaction rate on the $Cu_{0.15}[Ce(La)]_{0.85}O_x$ is comparable to the Pt/alumina and the $La_{0.8}Sr_{0.2}CrO_{3-\delta}$. Therefore, the Cu-Ce-O system has both low light-off temperatures and high intrinsic activity for CO oxidation.

5.3.1.6 Activities of Other Transition Metal-Fluorite Oxide Catalysts

So far we have considered the Cu-Ce(D)-O system where D denotes a dopant element. Next, the CO oxidation over other transition metal-fluorite oxide systems will be briefly discussed. Several light-off curves are shown in Figure 5.9. The $Au_{0.05}[Ce(La)]_{0.95}O_x$ catalyst prepared by calcination in air for 1 h at 500°C followed by 1 h at 600°C exhibited the highest activity. Complete CO oxidation over this catalyst occurred at room temperature (26°C). Pt-Ce(La)-O, Cu-Zr-O, and Cu-Zr(Y)-O catalysts showed comparable activity, slightly higher than the Co-Ce(La)-O catalyst. But, all these catalysts except for the Au-Ce(La)-O were less active than the Cu-Ce(La)-O catalyst. Fine gold particles supported on Co_3O_4, α-Fe_2O_3, and TiO_2 were found to be excellent low temperature CO oxidation catalysts by Haruta *(33)*. The high activity was considered due to active catalytic sites formed at the boundary of gold particle and metal oxide where CO adsorbed on gold reacted with the oxygen adsorbed on the metal oxide. The activity of the present $Au_{0.05}[Ce(La)]_{0.95}O_x$ catalyst was compared with the Au/α-Fe_2O_3 in Table 5.4. The activity of the $Au_{0.05}[Ce(La)]_{0.95}O_x$ catalyst was slightly lower than that of the Au/α-Fe_2O_3, which may be due to the bigger gold particle size in the $Au_{0.05}[Ce(La)]_{0.95}O_x$ catalyst. In contrast to the Cu-Ce(La)-O system where finely dispersed copper cannot be dissolved in nitric or hydrochloric acid due to the strong interaction with cerium oxide, the gold particles in the $Au_{0.05}[Ce(La)]_{0.95}O_x$ catalyst can be dissolved in hydrochloric acid, while bulk gold is insoluble. This implies that the small gold particles in the $[Ce(La)]O_2$ matrix indeed have some particular properties. It is noteworthy that the $Au_{0.05}[Ce(La)]_{0.95}O_x$ catalyst showed good stability. The catalyst maintained its high activity after being subjected to a 3-h treatment at 650°C either in flowing air or 25% H_2/He. No deactivation was observed in a 4-day run at room temperature with the

reacting gas saturated with water vapor. The water vapor effect on the other catalysts is addressed in the following section.

5.3.1.7 Effect of Water Vapor on Catalyst Activity

Water vapor generally inhibits or poisons the oxidation activity of base metal oxide catalysts and imposes a second challenge beyond that of boosting the activity of the non-precious metal oxide catalysts. The extensive search of base metal catalysts as alternatives to precious metals for exhaust gas treatment in the 1960s identified copper oxide, mixed with chromium oxide and/or rare earth oxides, to be an active catalyst *(34,35)*. However, the copper catalyst was severely deactivated upon addition of water vapor due to changes in the nature of surface copper *(36)*. Perovskite-like compounds $RE_{1-x}Pb_xMnO_3$ and $RECoO_3$ (RE=La, Pr or Nd) were pioneered as oxidation catalysts for the automotive exhaust treatment in the early 1970s *(37)*. Although these mixed oxides later showed lower activity than the precious metal catalyst and propensity to water vapor poisoning *(38,39)*, they have indeed stimulated intensive studies of this type catalyst.

The water vapor effect on the present catalysts was examined and typical results are shown in Figure 5.10. Water vapor effects on the bulk CuO and the 14 at.% $CuO/\gamma\text{-}Al_2O_3$ catalysts are also included in Figure 5.10 for comparison. The water vapor content in exhaust gas streams is usually around 15 %. Excess water vapor, 32%, was used in our tests to study its effect. In Figure 5.10, the CO conversion on the bulk CuO catalyst decreased to 0.1 from 0.99 within about 2 h after the addition of water vapor at 340°C. The conversion recovered to only 0.35 2 h later after the reacting gas was switched back to the dry feed gas. The conversion over the $CuO/\gamma\text{-}Al_2O_3$ catalyst also decreased monotonically at a rate of about 0.03/h in the presence of water vapor. In contrast, no deactivation was observed over the Cu-Ce(La)-O, Co-Ce(La)-O and Cu-Zr(Y)-O catalysts under the same experimental conditions. It is noted that the preceding calcination process during catalyst preparation had a strong effect on the Cu-Ce(La)-O catalyst activity in the presence of water vapor as illustrated by Figure 5.11. On the $Cu_{0.01}[Ce(La)]_{0.99}O_x$ and $Cu_{0.5}[Ce(La)]_{0.5}O_x$ catalysts prepared by 4 h-calcination at 600°C in N_2, the conversion declined monotonically at a rate of about 0.09/h and 0.012/h, respectively. However, these two catalysts maintained stable activity in the presence of water vapor after they were further heated for 3 h at 650°C in flowing air.

In conclusion, the transition metal-fluorite oxide composite catalyst exhibits significant enhancement for carbon monoxide oxidation in both catalytic activity and stability in the presence of water vapor, and the enhancement stems from the strong interaction of the two kinds of materials.

5.3.2 Methane Oxidation

Screening tests for complete methane oxidation were performed over several transition metal-fluorite oxide catalysts at a contact time of 0.09g·s/cc(STP). ZrO_2-based catalysts prepared in this work had much higher packing density than the CeO_2-based catalysts. The space velocity for the ZrO_2-based catalyst was about 100,000 h^{-1}, while the space velocity

for the CeO_2-based catalysts was typically 42,000 h^{-1}. In Figure 5.12, the $Cu_{0.2}Zr_{0.8}O_x$ catalyst showed high activity for methane oxidation with a light-off temperature(50% conversion) of 450°C. The $Cu_{0.5}Zr_{0.5}O_x$ catalyst had a light-off temperature of 510°C, which suggests that an excessive amount of copper in the Cu-Zr-O catalyst system may have a negative effect on catalytic activity. Bulk CeO_2 had the lowest activity among the catalysts tested. However, the light-off temperature over CeO_2 was lowered from 650 to 540°C in the presence of 4.5 at.% La dopant and further to 490°C by the addition of 8 at.% Cu. The 50 at.% Cu-containing Cu-Ce(La)-O catalyst showed similar activity to the one containing 8 at.% Cu.

The 15 at.% Cu-containing Cu-Ce(D)-O catalysts with different dopant(D) were examined and the results are shown in Figure 5.13. The 1 at.% Sc-doped $Cu_{0.15}Ce_{0.85}O_x$ catalyst had slightly higher activity than the undoped one, while the 1 at.% La-doped or 1 at.% Sr-doped catalyst had significantly higher activity than the undoped. The 4.5 at.% La-doped catalyst, $Cu_{0.15}[Ce(La)]_{0.85}O_x$, had the highest activity. But, further increasing the La dopant level to 10 at.% decreased the catalytic activity, which was similar to the case of CO oxidation. 50% and 95% methane conversion to carbon dioxide over the $Cu_{0.15}[Ce(La)]_{0.85}O_x$ took place at 450°C and 520°C, respectively. The $Cu_{0.15}[Ce(La)]_{0.85}O_x$ showed comparable activity to the $Cu_{0.2}Zr_{0.8}O_x$ catalyst in Figure 5.12 and higher activity than the $Cu_{0.08}[Ce(La)]_{0.92}O_x$ or $Cu_{0.5}[Ce(La)]_{0.5}O_x$ in Figure 5.12. The activity of the $Cu_{0.15}[Ce(La)]_{0.85}O_x$ catalyst was stable as no conversion decline was observed during a 15 h-run at 600°C with 99% methane conversion. Therefore, the dopant oxide in the CeO_2-based catalyst played a more important role in methane oxidation than in CO oxidation. However, the activity enhancement cannot be explained simply on the basis of oxygen vacancy and energetics. SrO and La_2O_3 are more basic oxides than Sc_2O_3. It is plausible to assume that the catalyst surface acidic/basic sites are important for methane oxidation. This assumption is illustrated by the following reaction scheme where cat denotes the catalyst; M^{n+} is an acidic site, and O^- is a basic site.

$$M_{cat}^{n+} - CH_3^{\delta-} \cdots\cdots H^{\delta+} - O_{cat}^{-} \xrightarrow{slow} M_{cat}^{n+} - CH_3^{-} + HO_{cat}$$

It is generally agreed that the most difficult step in activating methane is to break the C-H bond *(10, 40)*. As one hydrogen atom is abstracted from the methane molecule by a surface oxygen(basic site), the negatively charged residual is stabilized by a surface acidic site. The resulting intermediate can become a methyl radical by giving back its electron to the catalyst and the methyl radical may subsequently form the precursors of a variety of chemical products. These intermediate species are easily oxidized into carbon dioxide and water. Both surface basic and acidic sites with suitable strength and geometry are needed to form a transition state and lower the activation energy in the C-H bond breakage. The present results indicate that copper-fluorite oxide composites are active catalysts for methane oxidation and more importantly, the activity is tunable by using different dopant oxides in suitable amounts.

It is noted that methane oxidation is much slower than carbon monoxide oxidation, and the light-off curves shown in Figures 5.12 and 5.13 are in the kinetic regime; that is,

the light-off curve will be shifted to lower temperatures by increasing the contact time. Table 5.5 briefly compares the activity of the $Cu_{0.15}[Ce(La)]_{0.85}O_x$ catalyst with some active perovskite mixed oxide catalysts reported in the literature *(41,42,43)*. Per unit catalyst weight, the $Cu_{0.15}[Ce(La)]_{0.85}O_x$ catalyst had an activity a few times higher than the other catalysts. Per unit surface area, the activity of the $Cu_{0.15}[Ce(La)]_{0.85}O_x$ catalyst was comparable to the $LaCoO_3$ catalyst, an extensively studied perovskite system. Formation of the perovskite compound needs high temperature so that it is difficult to prepare with high surface area. The preparation of the present transition metal-fluorite oxide composite catalyst mostly requires good dispersion of the transition metals in the fluorite matrix and thus, a high catalyst surface area can be obtained by using appropriate low temperature synthesis methods. In conclusion, the present composite oxide catalyst is a promising, new catalyst system showing high activity for the complete oxidation of methane.

5.3.3 Simultaneous Oxidation of CO and CH_4 over the $Cu_{0.15}[Ce(La)]_{0.85}O_x$ Catalyst

Figure 5.14 shows the light-off curves of carbon monoxide and methane oxidation over the $Cu_{0.15}[Ce(La)]_{0.85}O_x$ catalyst in two different reacting gas mixtures. The oxidizing gas(II) consisted of 0.228 % CH_4, 0.1% CO, and 1.0% O_2. The reducing gas composition(III) consisted of 0.228% CH_4, 0.1% CO, and 0.35% O_2. The light-off curves under the oxidizing and reducing conditions overlapped. Also, the light-off curves of methane oxidation in the presence of CO were similar to light-off in the absence of CO. 95% conversion of CO and methane occurred at about 100°C and 550°C, respectively. The oxidation behavior of the present catalyst is very different from that on precious metal catalysts (Pd, Pt, Rh) reported in the literature *(44)*. On the precious metal catalysts, the light-off curves of both CO oxidation and CH_4 oxidation were strongly affected by the reacting atmosphere. Under reducing conditions, methane oxidation produced substantial amounts of CO and H_2 at high temperatures *(44)*, while no partial oxidation products(CO, H_2) were observed over the present catalyst. This was confirmed by separate studies under various space velocities. The CO and H_2 oxidation on the metal-fluorite oxide composite catalysts appear to proceed very fast, as previously noted. This is an advantage of the present catalyst over the precious metal catalysts, because CO is a more harmful pollutant than methane.

5.4 Summary

Transition metal-fluorite oxide composite catalysts were studied in this work for the complete oxidation of carbon monoxide and methane. A variety of highly active oxidation catalysts can be prepared from this family of catalysts. The transition metal or metal oxide is usually insoluble in the fluorite oxide, while alkaline earth and rare earth oxides have solubility over a wide concentration range. Therefore, transition metals can be well dispersed in the fluorite oxide matrix without worrying about the adverse effect of solid solution formation, and alkaline and rare earth oxide can be used to tune the physical and chemical properties of the fluorite oxides. The good transition metal dispersion and, more

importantly, the strong interaction between the transition metal and the fluorite oxide results in high catalyst activity and stability. The transition metal dispersion and display of this "strong interaction" are not sensitive to catalyst preparation process. Some specific conclusions were drawn from this work as follows:

Carbon Monoxide Oxidation

(1)The Cu-Ce-O composite showed higher CO oxidation activity than any other of the base metal oxide catalysts reported in the literature. The catalytic activity was not affected by small amounts of alkaline earth and rare earth dopants or impurities(ca. 1 at.%). Only a small amount of copper(ca. 2 at.% or 0.7 wt.%) was needed to promote the catalytic activity of CeO_2, while excess copper formed bulk CuO particles of little contribution to the catalyst activity. These catalysts showed excellent resistance to water vapor poisoning.

(2) The $Au_{0.05}[Ce(La)]_{0.95}O_x$ is an active and stable catalyst for low temperature CO oxidation(room temperature).

(3) The activity of the Cu-Ce-O system was superior to Co-Ce-O and Cu-Zr-O, but all these catalyst systems showed improved resistance to water vapor poisoning.

Methane Oxidation

(4) The Cu-Ce-O and Cu-Zr-O composites are active catalysts for the complete methane oxidation. The Cu-Ce-O catalyst activity can be tuned by using alkaline earth and rare earth oxide dopants in suitable amounts. Both La and Sr dopants provided significant promotion effect.

(5) No partial oxidation products, such as CO, H_2, etc., were observed during methane oxidation over the Cu-Ce(La)-O and Cu-Zr-O catalysts under reducing conditions.

Further characterization of the Cu-Ce(La)-O catalyst and CO and methane oxidation kinetics will be presented in Part II of this paper *(27)*.

5.5 Literature Cited

1. Tuller, H.L., and Moon, P.K., *Mater. Sci. & Eng.* B1, 171-191 (1988).
2. Hagenmuller, P., and Van Gool, W., Solid Electrolytes, Academic Press, New York, 1978.
3. RienAcker, G., *Z. Anorg. Allg. Chem.* **59**, 280 (1949).
4. RienAcker, G., and Wu, Y., *Z.Anorg. Allg. Chem.* **315,** 121 (1962).
5. RienAcker, G., and Birckenstaedt, M., *Z. Anorg. Allg. Chem.* **262**, 81 (1950).
6. Claudel, B.M., and Brau, G.G., *J. Catal.* **14**, 322 (1969).
7. Breysse, M., Guenin, M., Claudel, B., Latreille, H., and Veron, J., *J. Catal.* **27**, 275-280 (1972).
8. Breysse, M., Guenin, M., Claudel, B., Latreille, H., and Veron, J., *J. Catal.* **28**, 54-62 (1972).
9. Sayle, T. X.T., Parker, S.C., and Catlow, C.R.A., *J. Chem. Soc., Chem. Commun.* 977-978 (1992).
10. Maitra, A.M., *Appl. Catal. A*: General, **104**, 11-59 (1993).
11. Otsuka, K., Komatsu, T., and Shimizu, Y., in Inui, T., (Editor), Successful Design of Catalysts, Elsevier Science Publishers B.V., Amsterdam, pp43-50, 1988.
12. Doshi, R., Alcock, C.B., Gunasekaran, N., and Carberry, J.J., *J. Catal.* **140**, 557-563 (1993).
13. Spivey, J. J., *Ind. Eng. Chem. Res.* **26**, 2165-80 (1987).
14. Satterfield, C. N., Heterogeneous Catalysis in Industrial Practice, 2nd ed., McGraw-Hill, Inc., 1991.
15. Liu, W., and Flytzani-Stephanopoulos, M., in Armor, J.N., (Editor), Environmental Catalysis(ACS Symposium Series 552), American Chemical Society, Washington, DC, pp373-392, 1994.
16. Liu, W., Sarofim, A. L., and Flytzani-Stephanopoulos, M., 1994, *Appl. Catal.* B, **4**,167-186 (1994).
17. Liu, W., Sarofim, A. L., and Flytzani-Stephanopoulos, M., in Materials and Processes for Environmental Protection, 1994 MRS Spring Meeting, Paper No. I3.9, San Francisco, CA.
18. Yao, H.C., and Yao, Y.F.Y., *J. Catal.* **86**, 254-265 (1984).
19. Crucq, A., (editor), Catalysis and Automotive Pollution Control II, Elsevier Science Publishers B.V., Amsterdam, 1991.
20. Dow, W.P., and Huang, T.J., *J. Catal.* **147**, 322-332 (1994).
21. Frost, J.C., *Nature* **334**, 577-580 (1988).
22. Kim, D.J., *J.Am. Ceram. Soc.* **72**, 1415-1421 (1989).
23. Levine, E.M., Robbins, C.R., and McMurdie, H.F., (Editors), Phase Diagrams for Ceramists, American Ceramic Society Inc. Publisher, 1969.
24. Gerhardt-Anderson, R., and Nowick, A.S., Solid State Ionics **5**, 547-550 (1981).
25. Butler, V., Catlow, C.R.A., Fender, B.E.F., and Harding, J.H., *Solid Sate Ionics* **8**, 109-113 (1988).
26. Cullity, B.D., Elements of X-ray Diffraction, Addison-Wesley Pub. Co., Reading, Massachusetts, 1978.

27. Liu, W., and Flytzani-Stephanopoulos, M., *J. Catal.* **153**(2), May 1995.
28. Zhang, Y.P., Tao, S., Sarofim, A. F., and Flytzani-Stephanopoulos, M., in Agarwal, S.K., Marcelin, G.M., Ozkan, U.S., (editors), NOx Reduction(ACS Symposium Series ---), American Chemical Society, Washington, DC ,1995, in press.
29. Wright, P.A., Natarajan, S., Thomas, J.M., and Gai-Boyes, P.L., *Chem.Mater.* **4**, 1053-1065 (1992).
30. Choi, K.I., and Vannice, M.A., *J. Catal.* **131**, 22-35 (1991).
31. Rajadurai, S., and Carberry, J.J., *J. Catal.* **147**, 594-597 (1994).
32. Bond, G.C., and Namijo, S.N., *J. Catal.* **118**, 507-510 (1989).
33. Haruta, M., Tsubota, S., Kobayashi, T., Kageyma, H., Genet, M. J., and Delmon, B., *J. Catal.* **144**, 175-192 (1993).
34. Stephens, R.E., Hirschler, D.A., Jr., and Lamb, F.W., U.S. Patent No. 3 226 340, 1965.
35. Stiles, A.B., U.S.Patent No. 3 230 034, 1966.
36. Agudo, A.L., Palacios, J.M., Fierro, J.L.G., Laine, J., and Severio, F., *Appl. Catal.* A: General **91**, 43-55 (1992).
37. Voorhoeve, R.J.H., Remeika, J.P., Freeland, P.E., and Matthias, B.T., *Science* **177**, 353-354 (1972).
38. Schlatter, J.C., Klimisch, R.L., and Taylor, K.C., *Science* **179**, 798-800 (1973).
39. Voorhoeve, R.J.H., Johnson, D.W., Jr., Remeika, J.P., and Gallagher, P.K., *Science* **195**, 827-833 (1977).
40. Zwinkels, M. F.M., Jaras, S. G., and Menon, P. G., *Catal. Rev.-Sci. Eng.* **35**, 319-358 (1993).
41. Baiker, A., Marti, P.E., Keusch, P., Fritsch, E., and Reller, A., *J. Catal.* **146**, 268-276 (1994).
42. Klvana, D., Vaillancourt, J., Kirchnerova, J., and Chaouki, J., *Appl. Catal.* A: General **109**, 181-193 (1994).
43. Arai, H., Yamada, T., Eguchi, K., and Seiyama, T., *Appl. Catal.* **26**, 265-276 (1986).
44. Oh, S. H., Mitchell, P.J., and Siewert, R.M., *J. Catal.* **132**, 287-301 (1991).

Table 5.1 Variation of the $Cu_{0.01}[Ce(La)]_{0.99}O_x$ Catalyst Surface Area and Surface Composition With Thermal Treatment in Air.

treatment	Surface Area	Composition(%)[b]		
	(m^2/g)	Cu	Ce	La
fresh[a]	57.0	4.97	89.0	6.02
+3 h in flowing air at 650°C	52.4	8.10	86.5	5.37
+3 h in flowing air at 760°C	44.5	9.08	84.7	6.19
+3 h in flowing air at 860°C	27.3	11.9	81.4	6.74

a. as prepared by 4-h calcination at 600°C in N_2.
b. determined by XPS with a standard deviation of ±1%, but not calibrated.

Table 5.2 Particle Size and Surface Composition of Cu-Ce(La)-O Catalysts.

Catalyst	Particle Size(nm)[c]		Surface Composition(%)[d]		
Cu/(Cu+Ce) x100%	CeO_2	CuO	La	Cu	Ce
2[a]	10	-	5.9	11.7	82.4
8(6)[b]	10	-	5.97	16.2	77.8
15(10.5)[b]	7.6	-	3.42	24.8	71.7
25(8.4)[b]	13	29	5.91	18.7	75.4
50(8.8)[b]	14(14)[b]	29	5.8(6.9)[b]	18.9(11.4)[b]	75.3(81.7)[b]

a. prepared by 4-hour calcination at 650°C and 3-h calcination at 860°C both in air.
b. the sample was immersed in nitric acid for 14 h at room temperature, filtered, washed with de-ionized water, and dried for 1 h at 650°C.
c. CeO_2 and CuO particle sizes were determined by XRD from the (111) and ($\bar{1}$11) peak widths at half maximum of CeO_2 and CuO, respectively.
d. determined by XPS with a standard deviation of ±1%, but not calibrated.

Table 5.3 Catalyst Activity for CO Oxidation.

Catalyst and Reaction Conditions	Surface Area (m^2/g)	Rate ($\mu mol/gcat \cdot s$)[d]	Rate ($\mu mol/m^2 \cdot s$)[e]
I. P_{CO}=0.01 bar, 130°C			
$Cu_{0.15}[Ce(La)]_{0.85}O_x$[a]	30	85	2.8
amorphous $CuMnO_x$ (28)[b]	39	10	0.27
II. P_{CO}=0.01 bar, 80°C			
$Cu_{0.15}[Ce(La)]_{0.85}O_x$[a]	30	19	0.63
spinel $CoCuMnO_4$ (28)[b]	113	9.4	0.083
III. P_{CO}=0.035 bar, 130°C			
$Cu_{0.15}[Ce(La)]_{0.85}O_x$[a]	30	195	6.5
12 wt.% Cu/δ-alumina *(30)*[a]	138	0.64	0.005
IV. P_{CO}=0.01 bar, 110°C			
$Cu_{0.15}[Ce(La)]_{0.85}O_x$[a]	30	32	1.1(4.3)[f]
0.5 wt.% Pt/alumina *(31)*[c]	247	25	0.10(5.5)[f]
$La_{0.8}Sr_{0.2}CrO_{3-\delta}$ (31)[c]	0.33	1.8	5.5

a. partial pressure of oxygen, P_O, is 0.17 bar.
b. P_O = 0.2 bar.
c. 1% CO, 99% O_2, unknown total pressure.
d. specific rate based on unit catalyst weight.
e. specific rate based on unit BET surface area.
f. specific rate based on specific copper or platinum surface area. The specific copper surface area was estimated by BET area x surface copper fraction(Cu/(Cu+La+Ce)).

Table 5.4 Gold-Metal Oxide Composite Catalyst Activity for CO Oxidation.

Catalyst	Surface Area (m^2/g)	Au particle size (nm)	rate at 31°C ($\mu mol/gcat \cdot s$)[a]
$Au_{0.05}[Ce(La)]_{0.95}O_x$	34.2	8.0	1.2
5 at. % Au/α-Fe_2O_3 *(33)*	72.0	4.0	1.9

a. rate calculated based on formation of CO_2 under the conditions of 1% CO, 1% O_2.

Table 5.5 Catalyst Activity for Methane Oxidation.

Catalyst and Reaction Condition	Surface Area (m^2/g)	Rate[c] ($\mu mol/gcat \cdot s$)	Rate[c] ($\mu mol/m^2 \cdot s$)
I. P_{CH4}=0.01bar, P_O=0.04 bar, 557°C			
$Cu_{0.15}[Ce(La)]_{0.85}O_x$[a]	30	11	0.36
$LaCoO_3$ *(41)*	3.5	1.3	0.36
II. P_{CH4}=0.04 bar, 550°C			
$Cu_{0.15}[Ce(La)]_{0.85}O_x$[a]	30	48	1.6
$La_{0.66}Sr_{0.34}Ni_{0.3}Co_{0.7}O_3$ *(42)*[b]	19	11	0.60
$La_{0.8}Sr_{0.2}MnO_3$ *(43)*[b]	-	6.6	-

a. partial pressure of oxygen, P_O, is 0.12 bar.
b. P_O=0.2 bar.
c. rate calculated based on CO_2 formation.

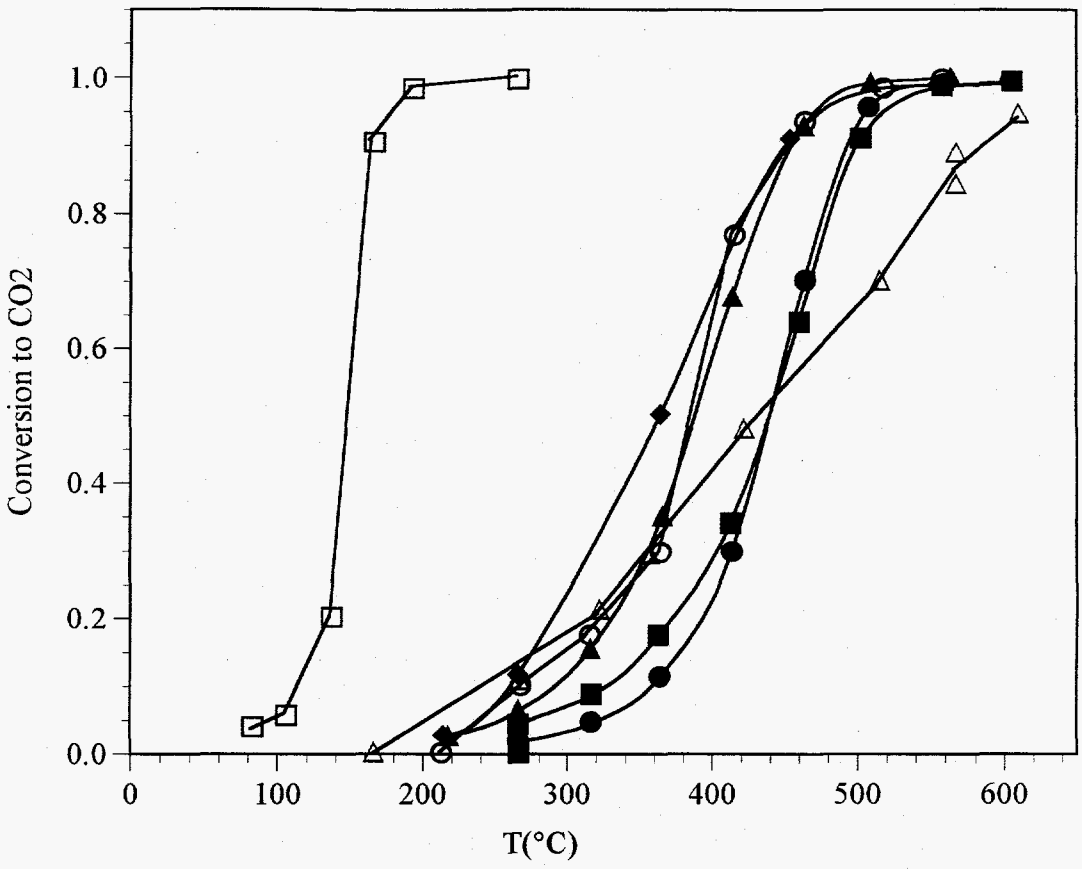

Figure 5.1 Light-off of CO Oxidation over Various 1 at.% Doped Ceria Catalysts and $Zr_{0.9}Y_{0.1}O_{1.9}$ Catalyst (100 sccm: 2% CO, 16% O_2; surface areas: $Zr_{0.9}Y_{0.1}O_{1.9}$ =42 m^2/g, 1 at.% Cu= 57 m^2/g, others ≅28 m^2/g). □ Cu-[Ce(La)]O_2 prepared by 4-h heating in N_2 at 600°C, ◆ La, ▲ Sr, O no dopant, ■ Sc, ● Gd, △ $Zr_{0.9}Y_{0.1}O_{1.9}$.

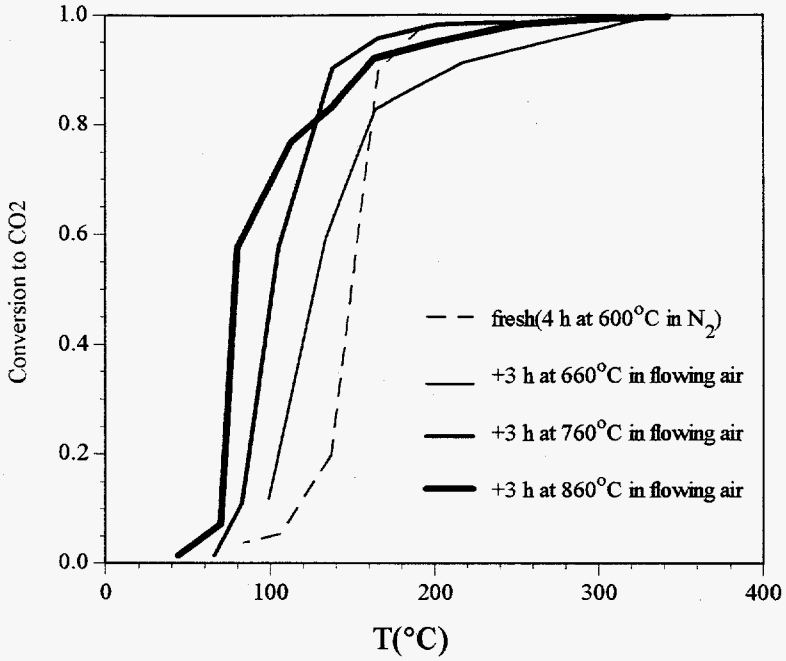

Figure 5.2 Effect of Thermal Treatment on the $Cu_{0.01}[Ce(La)]_{0.99}O_x$ Catalyst Activity for CO Oxidation (100 sccm: 2% CO, 16% O_2).

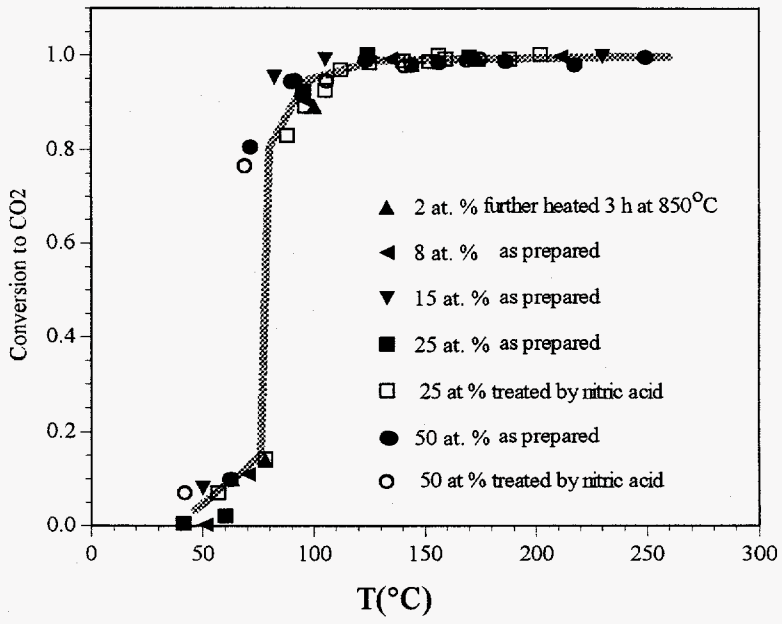

Figure 5.3 Effect of Bulk Copper Content in $Cu_X[Ce(La)]_{1-X}O_{2-X}$ Catalyst on CO Oxidation Activity (100 sccm: 2 % CO, 16 % O_2; surface areas ≅30 m^2/g).

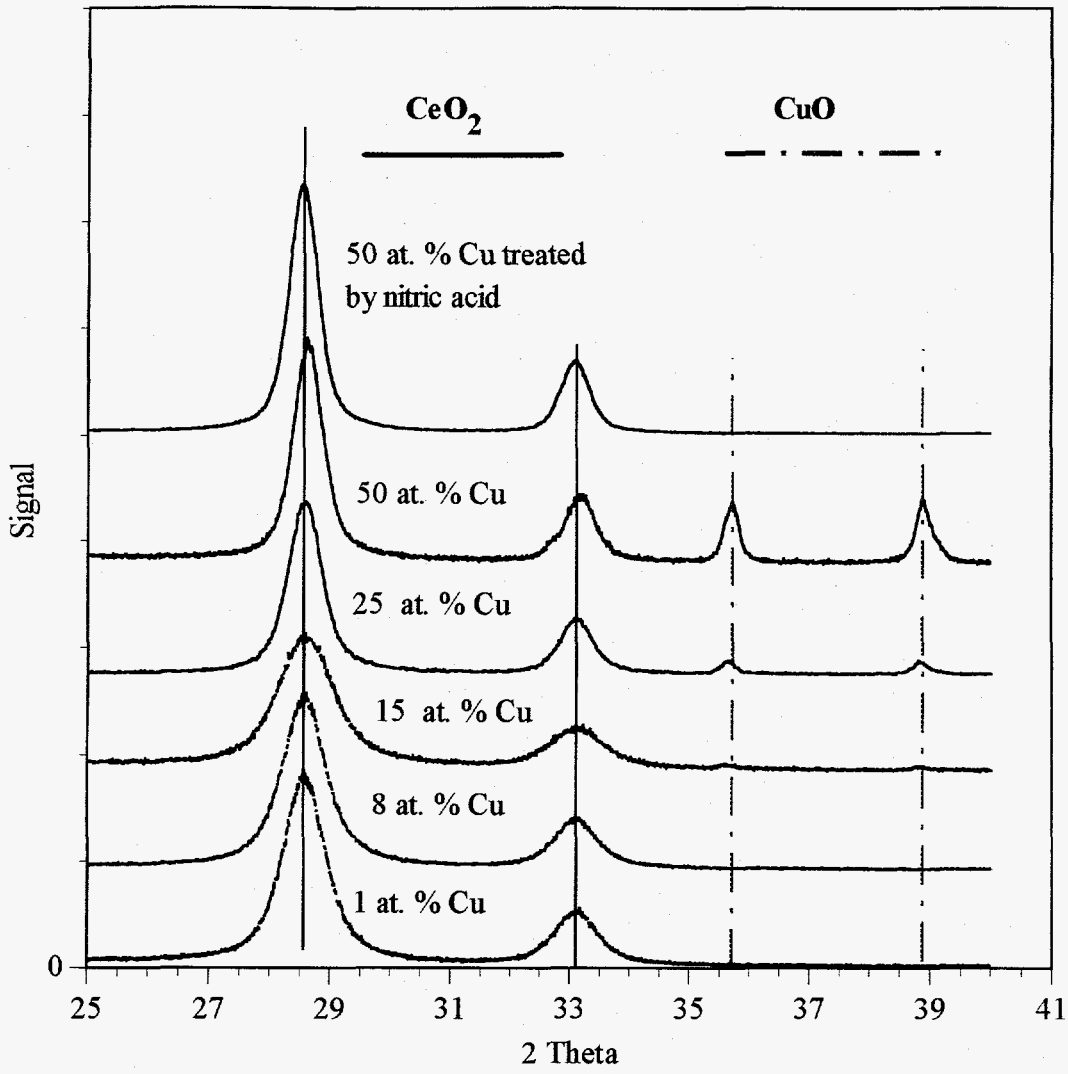

Figure 5.4 XRD Pattern of the Cu-Ce(La)-O Catalysts (Kα1 copper radiation, 50 kV, 200 mA, scan rate 1°/min).

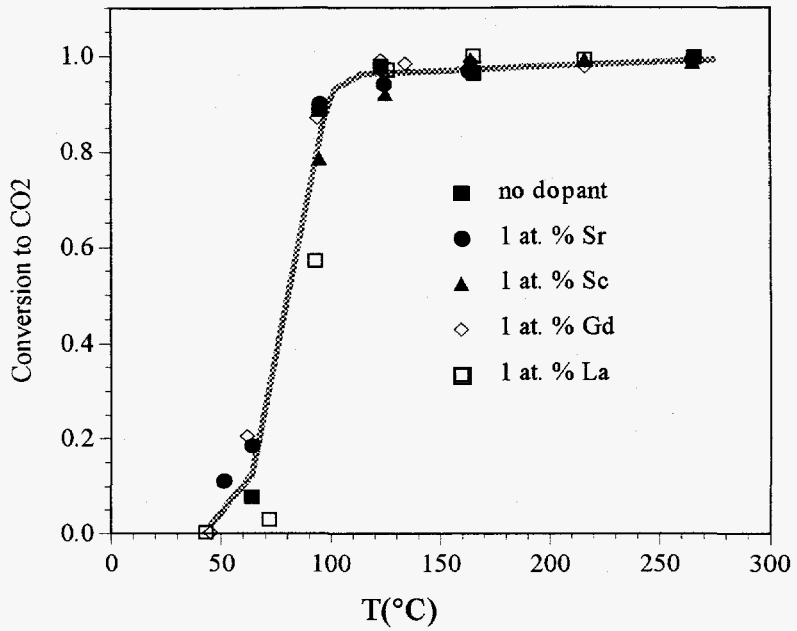

Figure 5.5 Effect of 1 at.% Dopant on the CO Oxidation Activity of $Cu_{0.15}Ce_{0.85}O_x$ Catalyst (100 sccm: 2% CO, 16% O_2; surface areas ≅30 m^2/g).

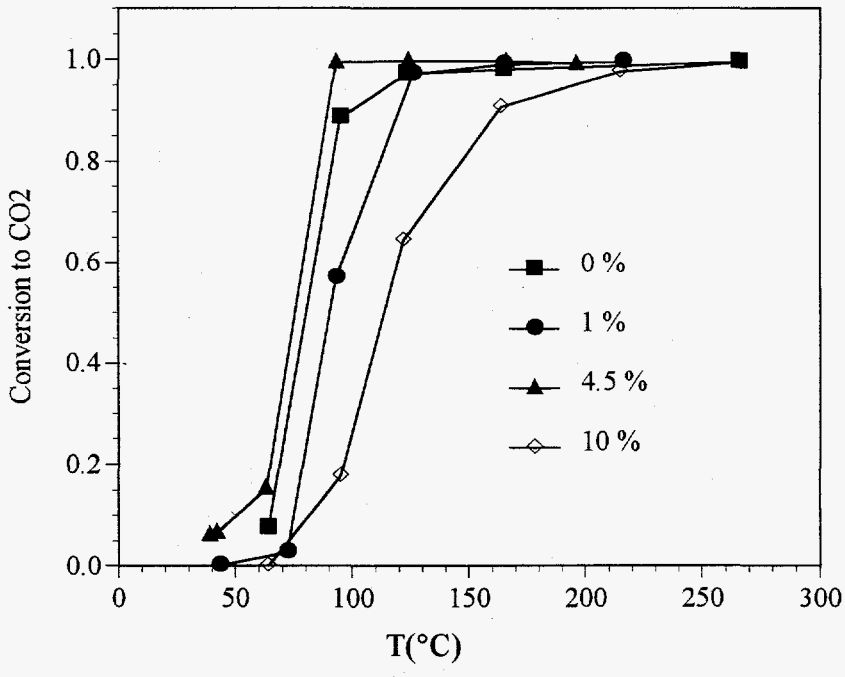

Figure 5.6 Effect of La Dopant Content on the CO Oxidation Activity of $Cu_{0.15}Ce_{0.85}O_x$ Catalyst (100 sccm: 2 % CO, 16 % O_2; surface areas ≅30 m^2/g).

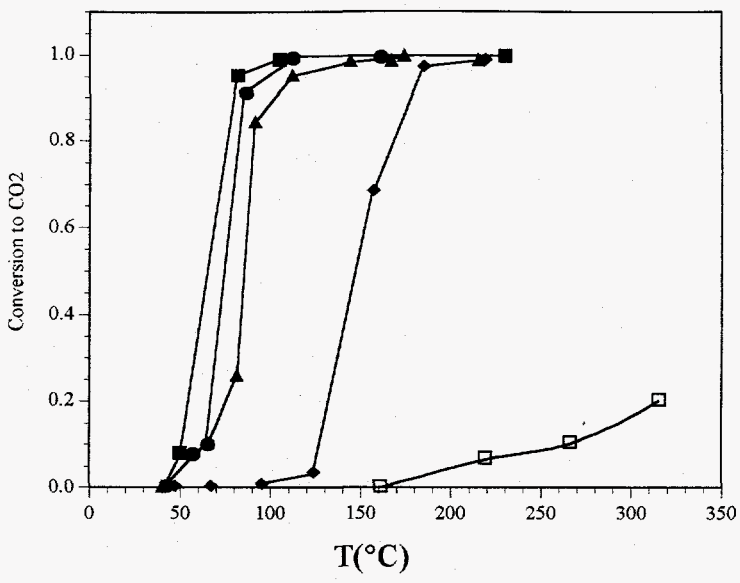

Figure 5.7 Activity Enhancement for CO Oxidation from Combination of CeO_2 and CuO (100 sccm: 2 % CO, 16 % O_2). ■ $Cu_{0.15}[Ce(La)]_{0.85}O_x$, 30 m^2/g, ● 15 at % CuO_x/CeO_2, 22.4 m^2/g, ▲ 15 at.% $CuO+CeO_2$ prepared by 1 h heating in air at 300°C, 18.6 m^2/g, ◆ bulk CuO, 1.64 m^2/g, □ CeO_2, 28m^2/g.

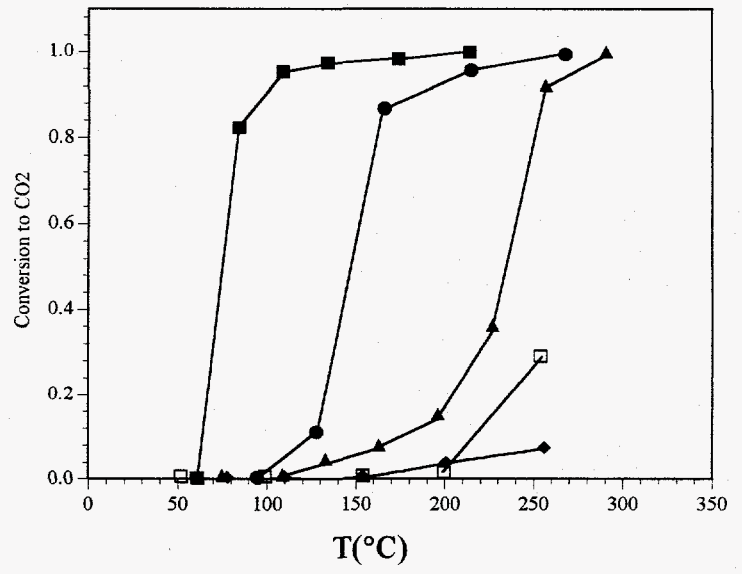

Figure 5.8 Effect of Copper Dispersion on CO Oxidation Activity (100 sccm: 2% CO, 16% O_2). ■ $Cu_{0.15}[Ce(La)]_{0.85}O_x$, 50 mg, 30 m^2/g ● CuO, 1000 mg, 1.64 m^2/g ▲ 14 at.% CuO/γ-alumina, 150 mg, 137 m^2/g ◆ 3.2 at.% Cu-ZSM-5, 150 mg, 400 m^2/g □ 3.1 at.% Ce, 1 at.% Cu, Ce-Cu-ZSM-5, 150mg, 400 m^2/g.

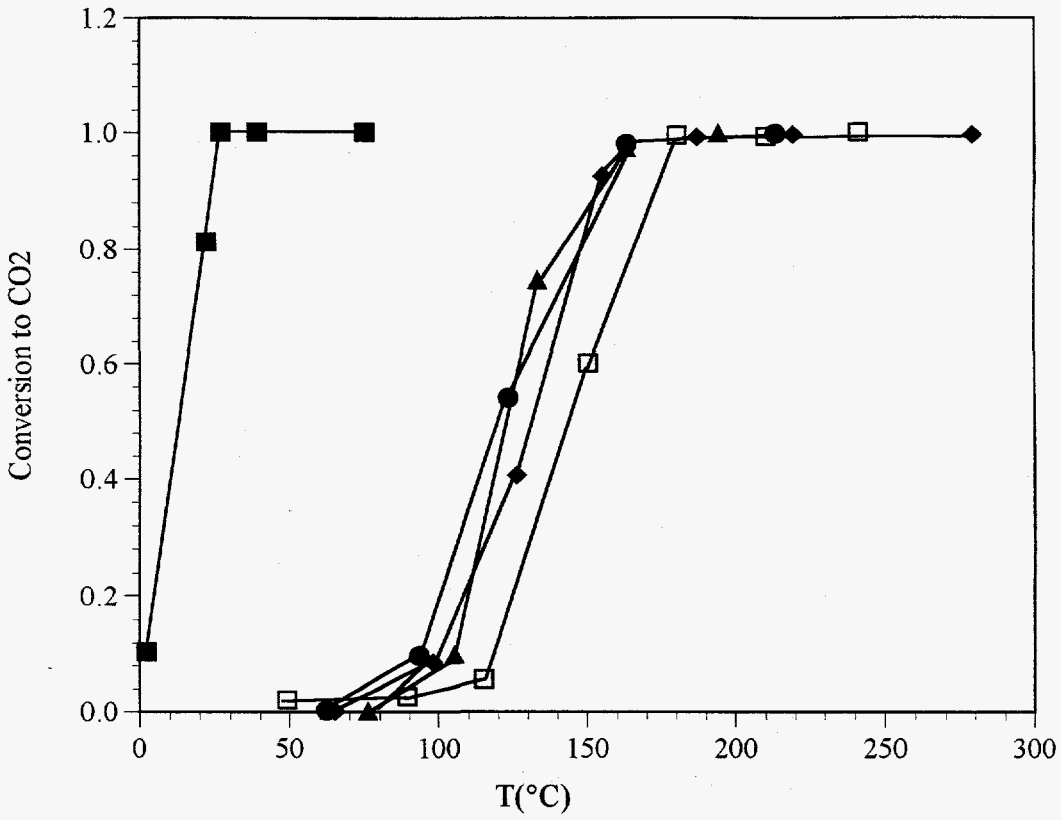

Figure 5.9 CO Oxidation over Various Composite Catalysts(150 mg catalyst loading; 100 sccm: 2 % CO, 16 % O_2). ■ $Au_{0.05}[Ce(La)]_{0.95}O_x$ prepared by air calcination for 1 h at 500°C + 1 h at 600°C, 34.2 m^2/g, ● $Pt_{0.03}[Ce(La)]_{0.97}O_x$, 28.1 m^2/g ▲ $Cu_{0.2}Zr_{0.8}O_x$, 17.8 m^2/g, ◆ $Cu_{0.15}[Zr_{0.9}Y_{0.1}]_{0.85}O_x$, 65 m^2/g, □ $Co_{0.2}[Ce(La)]_{0.8}O_x$, 30 m^2/g.

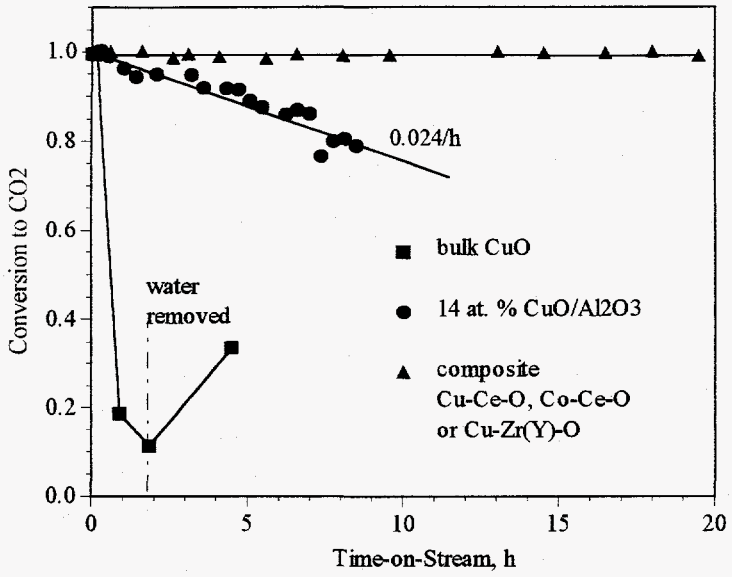

Figure 5.10 Effect of Water Vapor on CO Oxidation Activity over the Catalysts Prepared by 4 h Calcination at 650°C in Air (catalyst loading: 1000 mg for CuO catalyst, 150 mg for others; 340°C reaction temperature; 47 sccm H_2O + 100 sccm dry gas containing 2% CO and 16% O_2).

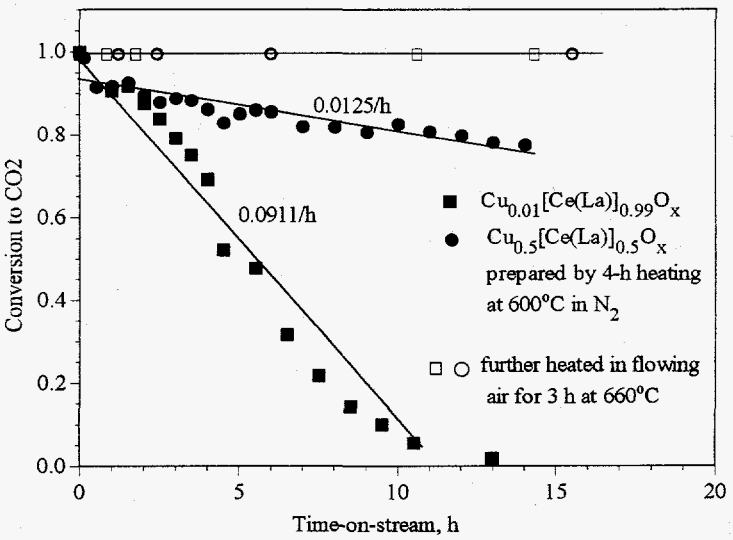

Figure 5.11 Effect of Catalyst Thermal Treatment on the CO Oxidation Activity in the Presence of Water Vapor (150 mg catalyst loading; 340°C reaction temperature; 47 sccm H_2O + 100 sccm dry gas containing 2% CO and 16% O_2).

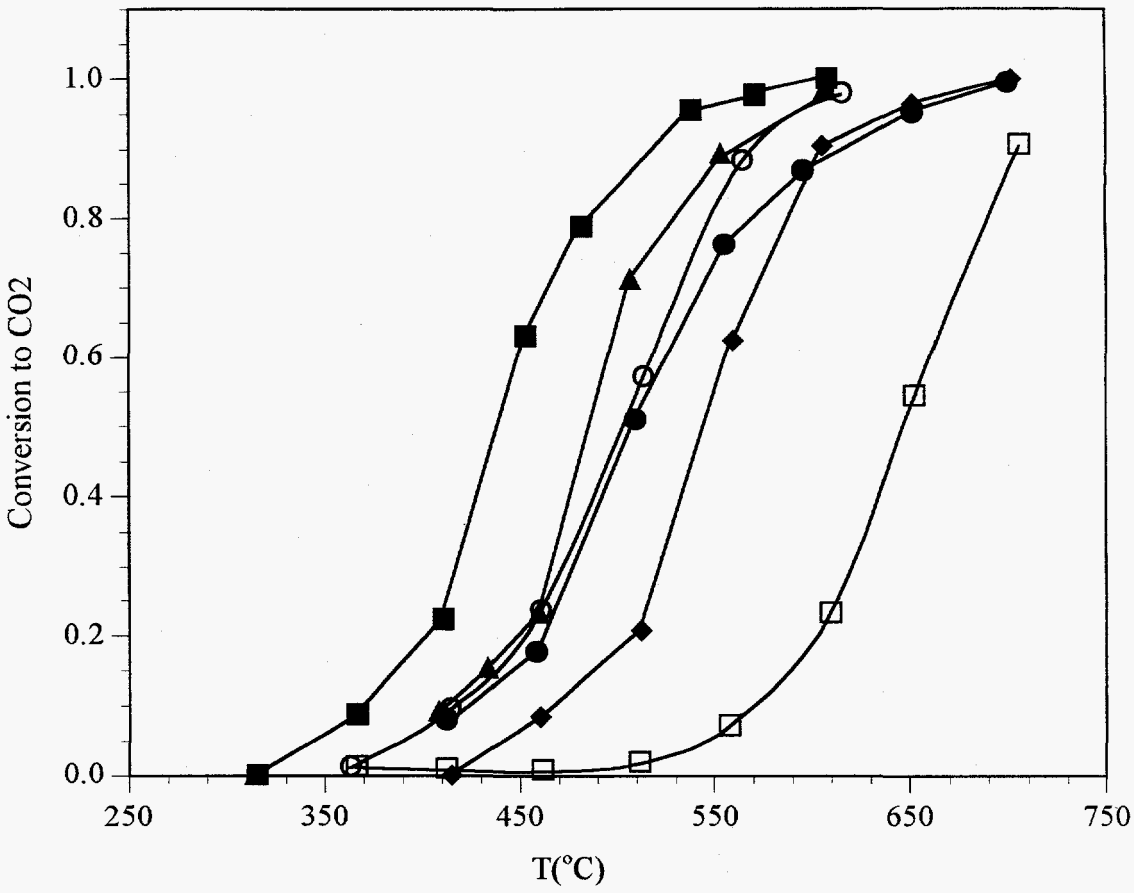

Figure 5.12 Methane Oxidation over Various Composite Catalysts (150 mg catalyst loading; 100 sccm: 2% CH_4, 16% O_2). ■ $Cu_{0.2}Zr_{0.8}O_x$, 17.8m^2/g ▲ $Cu_{0.08}[Ce(La)]_{0.92}O_x$, 43 m^2/g, ○ $Cu_{0.5}[Ce(La)]_{0.5}O_x$, 27.8 m^2/g ● $Cu_{0.5}Zr_{0.5}O_x$, 50.0 m^2/g ◆ $[Ce(La)]O_2$, 30 m^2/g □ CeO_2, 28 m^2/g.

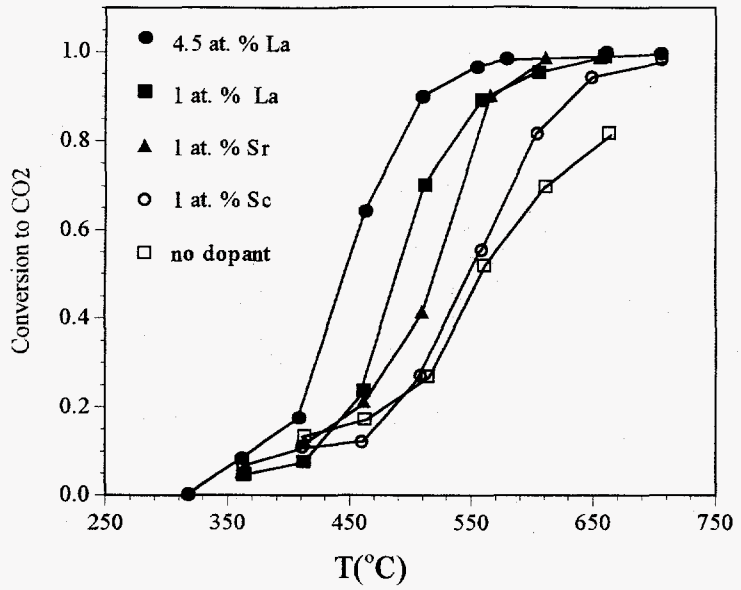

Figure 5.13 Effect of Dopant in the $Cu_{0.15}Ce_{0.85}O_x$ Catalyst on Methane Oxidation Activity (0.09s·g/cc, 2 % CH_4, 16 % O_2; catalyst surface area≅30 m^2/g;).

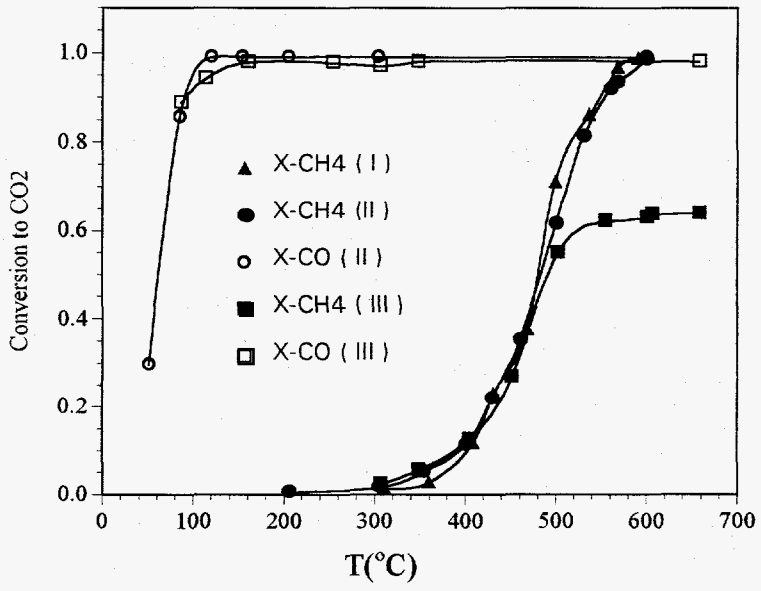

Figure 5.14 Simultaneous Oxidation of Methane and CO over the $Cu_{0.15}[Ce(La)]_{0.85}O_x$ Catalyst. I: in 0.228 % CH_4, 1% O_2. II: in oxidizing gas containing 0.228% CH_4, 0.1% CO, 1% O_2. III: in reducing gas containing 0.228% CH_4, 0.1% CO, 0.35 % O_2.

Chapter 6

Complete Oxidation of Carbon Monoxide and Methane over Transition Metal-Fluorite Oxide Composite Catalysts
II. Catalyst Characterization and Reaction Kinetics

6.1 Introduction

Transition metal-fluorite oxide composite catalysts were evaluated for the complete oxidation of CO and methane in the preceding paper *(1)*. The Cu-Ce-O system was identified as one of the most active catalyst systems. The significant enhancement of catalytic activity and resistance to water vapor for CO oxidation observed with this catalyst cannot be explained on the basis of copper dispersion alone. Thus, a strong interaction between these two kinds of materials was proposed. Strong interaction between a metal particle and its oxide support has long been a fascinating catalysis subject *(2-7)*. Moreover, another concept involving new active sites created at the interface between metal-support has been proposed *(6,7)*.

Although a mechanistic understanding of the correlation between catalyst properties and metal-support interactions is still limited, looking at the oxide support not simply as an inert carrier has given many insights for new catalyst development. For example, Frost *(8)* predicted the existence and properties of new methanol synthesis catalysts by using the minute Schottky junction theory at the interface between metals and oxides. In studies of CO hydrogenation, the precious metals-TiO_2 strong interaction has been one classic system in this field. "Strong interaction" between precious metals and cerium oxide has been another active area *(9)* in environmental catalysis because of the widespread use of cerium oxide in the precious metal-based automotive catalytic converter. The enhanced CO oxidation activity and stability of precious metal catalysts by yttria-stabilized zirconia(YSZ) support was recently reported and explained in terms of interfacial reactions *(10)*. A reaction mechanism based on the metal-support interface was also proposed for some low temperature CO oxidation catalysts, such as Pt/SnO_2 *(11)*, Pd/SnO_2 *(12,13)*, Au/α-Fe_2O_3 or TiO_2 *(14)*, etc. In a recent study of non-precious metal-fluorite oxide system for CO oxidation, a geometric interfacial interaction in Cu/YSZ involving surface oxygen vacancy was proposed *(15)*.

In this work we characterized the Au-Ce-O and Cu-Ce-O catalyst systems by X-ray Photoelectron Spectroscopy (XPS) and Scanning Transmission Electron

Microscopy(STEM) aided by X-ray microprobe analysis, and measured the reaction kinetics in order to elucidate the "strong interaction" between copper and cerium oxide and its effect on the catalytic activity. The Au-Ce-O catalyst clearly demonstrated a synergistic effect on catalytic activity and best served as a reference.

6.2 Experimental

6.2.1 Catalyst Preparation and Characterization

Bulk composite catalysts were prepared by coprecipitating the aqueous salt solutions of the metals with ammonium carbonate or sodium carbonate. CeO_2 support was prepared by thermal decomposition of cerium acetate hydrate(99.9%, Aldrich). The supported catalysts were prepared by conventional wet impregnation using the aqueous salt solution of the metal. The mixture of cerium oxide and copper oxide was prepared by mixing the CuO and CeO_2 powder with water and drying it for 1 h at 300°C. The details of the preparation procedure were described in the preceding paper *(1)*. The cerium precursor used for coprecipitation was low purity(99%) cerium nitrates(from Aldrich) containing 1.5 wt.% lanthanum. This type of cerium is designated as Ce(La) in the catalyst formula throughout this paper. The catalyst characterization was performed by nitrogen adsorption/desorption on a Micromeritics ASAP 2000 apparatus for BET surface area and pore size measurement and by X-ray powder diffraction(XRD) on a Rigaku 300 X-ray Diffractometer for crystalline identification. The catalyst typically had an average pore size of 20 nm and a BET surface area from 20 to 57 m^2/g. For the XRD analysis, copper Kα1 radiation was used with power setting of 50 kV and 200 mA. The divergence slit, scattering slit, and receiving slit were 1°, 1°, and 0.15°, respectively. The data was acquired at a 2 theta interval of 0.02°. The catalyst microstructure analysis was performed on a state-of-the-art Vacuum Generators HB603 Scanning Transmission Electron Microscope(STEM) equipped with a X-ray microprobe of 0.14 nm optimum resolution. For STEM analysis, the catalyst powder was dispersed on a nickel grid coated by a carbon film and the elemental maps were acquired on a 128 x 128 data matrix. The catalyst surface composition was determined by X-ray Photoelectron Spectroscopy(XPS) with a Perkin Elmer 5100 system. For XPS analysis, the catalyst powder was pressed on a tantalum foil and placed into the vacuum chamber without any pre-treatment. A Mg electron source was used with power setting of 15kV and 300W. The binding energy was adjusted to the C1s peak at 284.6eV which existed in all measurements. The Auger kinetic energy was calculated by 1253.6 - $(BE)_A$, where $(BE)_A$ is the measured binding energy of the Auger L_3VV line.

6.2.2 Apparatus and Procedure

The reactor was a 0.6cm I.D. x 50cm long quartz tube heated by a Lindberg furnace. The reaction temperature was monitored by a quartz glass-sheathed K-type thermocouple placed at the top of the packed catalyst bed. CO and CH_4 reacting gases were certified calibration gas mixtures balanced by helium(from Matheson). Air and helium(all from AIRCO)were used as oxidizing gas and diluent, respectively. The gas streams were

measured with mass flow controllers and mixed prior to the reactor inlet. The resulting gas mixture without further purification flowed downward through the packed bed. For kinetic measurements, the reactor was operated in a differential mode with the conversion not exceeding 10% so that the temperature was nearly uniform in the packed catalyst bed. Separate experimental tests showed that bulk mass transfer and intraparticle mass transfer resistance could be eliminated by using a gas flowrate greater than 200sccm and catalyst particles size less than 150 μm. Therefore, total gas flowrate of 400sccm and average catalyst particle size of 100 μm were used for the kinetics study. The reaction conversion was controlled by the catalyst loading, while the catalyst was diluted by silicon carbide to about 10 mm packed height. The partial pressure of the reacting gas species was varied over the range of 0.001 to 0.09 bar. CO oxidation over the Au-Ce-O catalyst was measured over the temperature range of 10 to 50°C. CO oxidation and methane oxidation over the Cu-Ce-O catalysts were conducted at temperatures from 40 to 200°C and from 400 to 550°C, respectively. Before any kinetic measurement, the catalyst was always treated for 1 h in the reaction gas mixture at 300°C for CO oxidation and 600°C for methane oxidation. Carbon dioxide concentration in the product gas stream was analyzed by a HP5880A Gas Chromatograph(GC) with a Thermal Conductivity Detector(TCD). The production of CO_2 was used to calculate the reaction rate:

$$Rate = N_t \cdot X_{CO2} / W_{CAT} \quad (1)$$

where N_t is the total molar gas flowrate in mol/s, X_{CO2} is the molar fraction of CO_2 in the product gas stream, and W_{CAT} is the catalyst weight in grams.

6.3 Results

6.3.1 Catalyst Characterization

6.3.1.1 Characterization of $Au_{0.05}[Ce(La)]_{0.95}O_x$ Catalyst

Only the 5 at.% Au-containing Au-Ce-O catalyst, $Au_{0.05}[Ce(La)]_{0.95}O_x$, was extensively characterized, because this catalyst showed better activity than the other Au-Ce-O catalysts of lower or higher gold content. Figures 6.1a-c show the XRD pattern, XPS spectra, and STEM elemental maps for the $Au_{0.05}[Ce(La)]_{0.95}O_x$ catalyst. The XRD pattern in Figure 6.1a consisted of CeO_2 and metallic gold crystal phases. The gold particle size calculated from the peak broadening is about 8nm. The binding energy of Au4f7/2 in the XPS was close to that of metallic gold given in the literature *(16)*. The gold particles were difficult to be visualized by electron microscopy because of the interference from cerium. However, clear images were obtained by elemental mapping with the STEM X-ray microprobe. STEM analysis indicated uniform distribution of small gold particles in the cerium oxide matrix. The gold particle sizes varied from 1 nm to tens of nm. There was no evidence of epitaxial growth of the gold particles on cerium oxide or spill-over of gold onto cerium oxide. The gold particle image in Figure 6.1c shows that the well-rounded gold particle was in intimate contact with cerium oxide. These results indicate that in the $Au_{0.05}[Ce(La)]_{0.95}O_x$ catalyst small metallic gold particles of an average size of

8nm were evenly distributed in the cerium oxide matrix and in intimate contact with the cerium oxide.

6.3.1.2 XRD and STEM Analyses of Cu-Ce-O Catalyst System

A few XRD analyses of the Cu-Ce-O catalysts prepared by coprecipitation were reported in the preceding paper *(1)*. For up to 15 at.% copper content, no CuO peaks were found by XRD. Figure 6.2 shows the XRD pattern of Cu-Ce-O catalysts containing 15 at.% or higher copper prepared by coprecipitation, impregnation, and physical mixing methods. The major peaks were due to the CeO_2 crystal phase. CuO appeared in smaller peaks and increased with copper content. No Cu_2O phase was found by XRD. Among three Cu-Ce-O catalysts containing 15 at.% Cu, the coprecipitated catalyst showed the lowest CuO phase intensity and the mixed oxide showed the highest CuO phase. We tried to correlate the variation of CeO_2 lattice space with copper content and catalyst preparation. But, the results were inconclusive. Overall, limited information was obtained from the XRD study.

The microstructure of the Cu-Ce-O system was first analyzed by high resolution transmission electron microscopy (HRTEM). Unlike alumina-supported precious metals, copper in the Cu-Ce-O catalyst could not be distinguished from cerium under electron microscopy because it is lighter than cerium. STEM having both high magnification and elemental analysis functions was found effective for the Cu-Ce-O catalyst characterization. The Cu-Ce-O catalyst was extensively analyzed by STEM. A few typical elemental maps are presented in Figure 6.3. The Cu map in Figure 6.3a for the $Cu_{0.15}[Ce(La)]_{0.85}O_x$ catalyst consists of a big CuO particle(17 nm) and a number of tiny copper spots distributed in the cerium oxide matrix. These copper domains could not be definitely differentiated from the solid solution as distinguishable fine copper particles due to the lighter copper atomic weight relative to cerium and the instrumental limitation itself. Few fine copper oxide crystals(nm) were found in the $Cu_{0.15}[Ce(La)]_{0.85}O_x$ catalyst by HRTEM. Taking into account the immiscibility of copper oxide in cerium oxide and further characterization evidence from other Cu-Ce-O catalysts as given below, we attribute these tiny copper domains to copper clusters invisible by XRD. Figures 3b and 3c show the elemental maps of the impregnated catalyst, 15 at.% CuO_x/CeO_2, and the physical mixture, 15 at.%$CuO+CeO_2$, respectively. Impregnation did not result in uniform deposition of copper on cerium oxide. But, the physical mixing generated not only mechanical mixture but also spillover of copper onto the cerium oxide. In the $CuO+CeO_2$ catalyst, a number of bulk copper oxide particles were found, but, copper clusters also existed in the cerium oxide matrix.. Qualitatively, a higher number of bulk copper oxide particles was found with the CuO_x/CeO_2 and $CuO+CeO_2$ catalysts than the $Cu_{0.15}[Ce(La)]_{0.85}O_x$. In contrast, more clusters were observed with the $Cu_{0.15}[Ce(La)]_{0.85}O_x$ than the other two 15 at.% copper-containing catalysts. These results are consistent with the smaller CuO peaks in the XRD pattern of the $Cu_{0.15}[Ce(La)]_{0.85}O_x$. In the preceding paper we reported that only bulk CuO in the Cu-Ce-O system could be removed by nitric acid. This conclusion is evidenced by the elemental map in Figure 6.3d for the $Cu_{0.15}[Ce(La)]_{0.85}O_x$ catalyst after it was immersed in nitric acid for 14 h, filtered, and washed with de-ionized water. Very few

bulk CuO particles remained in this nitric acid-treated catalyst, compared to the fresh one. However, the copper clusters remained intact.

Figures 6.3e-f show the elemental maps of the $Cu_{0.5}[Ce(La)]_{0.5}O_x$ catalyst. A large number of copper agglomerates were observed with this higher copper-containing material. It is interesting to notice that the bulk CuO particles were typically covered by smaller cerium oxide particles. This finding is illustrated by Figure 6.3e in which a big CuO agglomerate(ca. 300nm) was almost fully covered by smaller cerium oxide particles. But, when we look at a group of cerium oxide particles not associated with bulk CuO, a number of copper clusters are still dispersed in the cerium oxide matrix as shown in Figure 6.3f. Their existence was confirmed by electron-excited X-ray emission spectra in Figure 6.3g. The spectra also indicates that the amount of these copper clusters relative to cerium is indeed small and they did not appear in Figure 6.3e because of very low intensity relative to bulk CuO particles.

Figure 6.3h shows the elemental map of the $Cu_{0.01}[Ce(La)]_{0.99}O_x$ catalyst prepared by coprecipitation and 4 h calcination at 600°C in N_2. As expected, copper in this catalyst was well dispersed in the cerium oxide and its distribution pattern exactly matched cerium, which suggests the formation of solid solution. Notice that the high copper dispersion area in Figure 6.3h represents uniform copper distribution rather than high copper content. Heating the $Cu_{0.01}[Ce(La)]_{0.99}O_x$ catalyst in flowing air at 860°C drove the copper from bulk to surface and copper atoms aggregating into clusters. Resulting elemental maps as illustrated by Figure 6.3i looked similar to that of the nitric acid-treated $Cu_{0.15}[Ce(La)]_{0.85}O_x$ catalyst but less dense copper cluster population.

Since the coprecipitated catalysts contained lanthanum impurity, the X-probe was also used to check for La distribution. The analyses indicated atomic level mixing of lanthanum with cerium oxide or formation of solid solution. No lanthanum association with copper was found. The overall STEM analysis results are now summarized as: (i) copper in small amounts (a few percent) has strong tendency to associate with cerium oxide irrespective to the catalyst preparation method; (ii) excess copper forms bulk CuO particles that were covered by smaller CeO_2 particles; (iii) heating the catalyst of atomic copper dispersion caused segregation of copper and formation of copper clusters.

6.3.1.3 XPS Analyses of Cu-Ce-O Catalyst System

In the preceding paper *(1)* we reported the catalyst surface composition as measured by XPS. Here, the detail XP spectra are presented. We found that the XP spectra of the Cu-Ce(La)-O sample were unstable in the high vacuum chamber(ca. 7×10^{-8} torr) during the initial period of measurement. Once the sample was introduced into the XPS chamber, the relative intensity of the Cu2p3/2 shake-up peak at 943eV slightly decreased with on-stream measurement time while the Cu2p3/2 peak position shifted toward lower binding energy from 934.0eV. However, the XP spectra became stable after about thirty minutes. The shake-up peak and higher Cu2p3/2 binding energy are two major XPS characteristics of CuO, while the lower Cu2p3/2 binding energy and absence of the shake-up peak are characteristic of reduced copper species *(16)*. It is known that supported-copper oxide can

be reduced by the X-ray beam during XPS analysis. Although the beam effect could not be eliminated in the present XPS apparatus, further work confirmed that the initial instability of the Cu-Ce(La)-O sample was not suppressed by decreasing the X-ray power and was likely caused by the desorption of weakly-bound surface oxygen under high vacuum. Figures 4a-c show the XPS analyses of the 15, 25, and 50 at.% Cu-Ce(La)-O catalysts prepared by coprecipitation. These data were acquired in the Multiplex mode with about 1-h total acquisition time. Bulk CuO was prepared by thermal decomposition of copper carbonate and used as reference.

In Figure 6.4a, the bulk CuO showed a strong shake-up peak, and the shake-up peak intensity of the Cu-Ce(La)-O catalysts increased with the copper content and disappeared after the catalyst was treated by nitric acid using the procedure described previously. The Cu2p3/2 peak of the bulk CuO centered at 934.0eV, while the same peaks of the Cu-Ce(La)-O catalysts centered at about 933.1eV. The present observations suggest both CuO and reduced copper species existing in these Cu-Ce(La)-O catalysts. We could deconvolute the Cu2p3/2 peak to find the relative proportion of CuO in the Cu-Ce(La)-O catalysts. But, this peak did not show an apparent doublet shape, that made it hard to obtain a reliable value from this mathematical process. In addition, the weak shake-up peak did not allow us to use the shake-up peak/peak ratio for a reliable estimation either. Therefore, our discussion of the XPS results will be qualitative.

The two possible reduced copper forms, namely: metallic copper and Cu_2O, have similar binding energies but different Auger parameters *(16-20)*. Figure 6.4b shows the kinetic energy spectra of the Auger L_3VV electron. The doublet peaks for the Cu-Ce(La)-O samples also suggest the presence of two copper species. The 918.4eV and 915.7eV peaks in the Auger kinetic spectra correspond to bulk CuO and Cu^{+1} species, respectively. In agreement with the literature data we then assign the Cu2p3/2 peak at higher binding energy (934.0eV) to CuO and the Cu2p3/2 peak at the lower binding energy(933.1 eV) to the Cu^{+1} species(Figure 6.4a). Figure 6.4c shows the Ce3d XP spectra for the four catalyst samples under study. The four spectra look basically the same and similar to bulk CeO_2 reported in the literature *(16)*. The binding energies for bulk CeO_2 and reduced cerium oxide are the same. But, small spikes or peaks are usually found in the reduced cerium oxide at the D and D' positions *(21,22)*.

Figures 6.5a-b show the Cu2p XP spectra and L_3VV kinetic energies of the $Cu_{0.01}[Ce(La)]_{0.99}O_x$ and $Cu_{0.02}[Ce(La)]_{0.98}O_x$ catalysts. No shake-up peak was observed in Figure 6.5a, while the Cu2p3/2 peak was deconvoluted into two components: one at 933.1eV and another one at 930.0eV. The first one was assigned to Cu^{+1} species. The second component was difficult to be assigned since no copper species of such a low binding energy has been reported in the literature. We postulate that this component is due to isolated Cu^{+2} ions in the cerium oxide lattice. The existence of isolated copper ions and ion pairs in the Cu-Ce-O system was reported by Abou Kais, et al. *(23, 24)* and Sorial, et al.*(25)*, both using the electron paramagnetic resonance technique. The fraction of Cu^{+1} species in Figure 6.5a increased with heating temperature, while the fraction of isolated Cu^{+2} ions decreased. The STEM analyses indicated that heating the $Cu_{0.01}[Ce(La)]_{0.99}O_x$ catalyst in air drove the isolated copper ions to form copper clusters. Two components

seem to exist in the kinetic energy spectra of the Auger L_3VV electron in Figure 6.5b. It is noted that the isolated copper component at 930.1eV also appeared in the XP spectra for the nitric acid-treated 50 at.% copper-containing sample shown in Figure 6.4a. This was probably due to the copper ions remaining on the cerium oxide surface after the sample had been immersed in nitric acid for 14 h.

The XRD, STEM, and XPS analysis results for the Cu-Ce-O catalysts are briefly summarized as follows: (i) copper clusters undetectable by XRD exist in all the Cu-Ce-O catalysts and its relative amount depends on catalyst preparation, composition, and thermal treatment; (ii) the Cu^{+1} species result from the strong interaction of the copper clusters with cerium oxide.

6.3.2 Kinetic Results

6.3.2.1 CO Oxidation Kinetics over the $Au_{0.05}[Ce(La)]_{0.95}O_x$ Catalyst

Figure 6.6 shows the variation of CO oxidation rate on the $Au_{0.05}[Ce(La)]_{0.95}O_x$ catalyst with the partial of pressure of CO (P_{CO}) and oxygen (P_O). The experimental data were best fitted by a power order equation (2), with m=0.30 and n=0.18.

$$R_{CO} = kP_{CO}^{m}P_{O}^{n} \tag{2}$$

The R^2(R=correlation coefficient) values given in Figure 6.6 indicate that the plots of the rate versus P_{CO} under constant P_O were generally better fitted than the plots of the rate versus P_O. This is because of the lower reaction order in P_O. Although difficult to regress, this function is not important because of its small contribution to the overall rate process. The Arrhenius plot of the rate constant, k, is shown in Figure 6.9. The apparent activation energy was 53.7kJ/mol. The reaction orders and activation energy are compared to the literature data for other gold-metal oxide catalysts in Table 6.1. The $Au_{0.05}[Ce(La)]_{0.95}O_x$ catalyst showed similar kinetics to the other gold catalysts but higher activation energy and a stronger dependence on P_{CO}.

6.3.2.2 CO Oxidation Kinetics over the Cu-Ce-O Catalysts

The $Cu_{0.15}[Ce(La)]_{0.85}O_x$ catalyst and the $Cu_{0.01}[Ce(La)]_{0.99}O_x$ catalyst subjected to different thermal treatment were chosen for the kinetic study to also examine the composition effect. Figures 6.7 and 6.8 show the variation of the CO oxidation rates on the $Cu_{0.15}[Ce(La)]_{0.85}O_x$ at different reaction temperatures with P_{CO} and P_O, respectively. Under constant P_O, the rate increased with P_{CO}. The reaction order in P_{CO} seems to decrease from one to zero as P_{CO} increases. In Figure 6.8 the rate slowly increased with P_O under constant P_{CO}. Various rate equations derived from different reaction mechanism as well as the empirical power order equation *(2)* were evaluated to regress the experimental data. It was found that the experimental data were best represented by the following equations:

$$R_{CO} = \frac{k_{CO}K_{CO}P_{CO}P_{O}^{n}}{1+K_{CO}P_{CO}} \tag{3}$$

$$k_{CO} = A\exp(-Ea/RT) \quad (4)$$
$$K_{CO} = K\exp(Q/RT) \quad (5)$$

The parameters k_{CO} and K_{CO} in equation (3) can be taken as the surface reaction rate constant and CO adsorption equilibrium constant, respectively. The Arrhenius plots of k_{CO} and K_{CO} are shown in Figure 6.9 from which the reaction activation energy and heat of adsorption were obtained.

The experimental data for the $Cu_{0.01}[Ce(La)]_{0.99}O_x$ catalysts were also best regressed by equation (3). The Arrhenius plots of the resulting constants are shown in Figure 6.10. The values of those parameters in equations (4) and (5) for all the Cu-Ce(La)-O catalysts are listed in Table 6.2. The reaction orders in P_O, n, are small numbers close to zero. The activation energy is in the range of 73 to 94kJ/mol while the heat of CO adsorption is in the range of 28 to 61kJ/mol. Some interesting results were observed with the $Cu_{0.01}[Ce(La)]_{0.99}O_x$ catalyst. Heating this catalyst at 860°C in air changed the negative reaction order of P_O to positive and increased the pre-exponential factor of the reaction constant k_{CO} and the heat of adsorption. This increase corresponds to the increase in copper cluster population and Cu^{+1} fraction as we found from the STEM and XPS analyses. The last column in Table 6.2 shows the apparent activation energy when $K_{CO}P_{CO} << 1$. Under this condition, the reaction rate becomes first order in P_{CO} and the apparent activation energy is Ea-Q. Table 6.2 also includes kinetic data for other copper catalysts from the literature for comparison. The $CuO\text{-}Cr_2O_3/\gamma\text{-}Al_2O_3$ catalyst, pre-calcined in air at 500°C *(26)*, gave an pre-exponential factor of the constant k_{CO} four orders of magnitude lower than those of the Cu-Ce(La)-O catalysts and also low heat of adsorption(5 kJ/mol). High heat of adsorption (30 kJ/mol) was reported for the $Cu/\delta\text{-}Al_2O_3$ catalyst pre-reduced by H_2 at 300°C *(27)*. It is noted that we calculated the data in Table 6.2 for the $CuO\text{-}Cr_2O_3/\gamma\text{-}Al_2O_3$ catalyst based on reported rate equation in the literature *(26)*.

Because of the variations in both the pre-exponential factor and activation energy of the rate constant in Table 6.2, it is difficult to evaluate the effect of the copper content on the reaction kinetics. In Figure 6.11, the rate constant k_{CO} normalized by the BET surface area is plotted versus the surface copper content(at.%) as measured by XPS. One can see that the rate constant k_{CO} steeply increases with the surface copper content. The plots for three different reaction temperatures are well regressed by the same power order equation:

$$k_{CO}/S_g \propto S_{Cu}^{3.4} \quad (6)$$

where Sg is the catalyst surface area, m^2/g, and S_{Cu} is the surface copper content. Although we cannot find a mechanistic explanation for such a relationship at the present time, the high nonlinear correlation suggests a complex interaction of copper and cerium oxide. The high catalytic activity did not result from copper dispersion alone. One can extrapolate that k_{CO} will increase by an order of magnitude if the surface copper content is further increased from 25 % to 40 %. However, we could not achieve a surface copper level higher than ca. 25 at.% in this work. Figure 6.12 shows that the catalyst surface was enriched in copper for low bulk copper content and reached a plateau for high bulk copper

content. The 24.8 at.% for the $Cu_{0.15}[Ce(La)]_{0.85}O_x$ is the largest surface copper content reached by a series of Cu-Ce-O catalysts prepared by 4 h calcination at 650°C. The surface copper level of the $Cu_{0.15}[Ce(La)]_{0.85}O_x$ was not increased by reduction in 25% H_2/He or heating in air. The impregnation method did not increase the copper level either. The main reason, based on the catalyst characterization results, is that excess amount of copper over a certain value favored the agglomeration of copper in bulk CuO form. Bulk CuO particles were then covered by fine cerium oxide particles and could not be detected by XPS.

6.3.2.3 Methane Oxidation

Figures 6.13 and 6.14 show the variation of the methane oxidation rate over the $Cu_{0.15}[Ce(La)]_{0.85}O_x$ catalyst with the partial pressure of methane and oxygen, respectively. The reaction kinetics were similar to the CO oxidation. Thus, the experimental data were best fitted by equation (7). The Arrhenius plots of the constants k_m and K_m in this equation are shown in Figure 6.15, from which equations (8) and (9) were derived.

$$R_m = \frac{k_m K_m P_m P_O^{0.18\pm0.04}}{1 + K_m P_m} \tag{7}$$

$$k_m = 7.84 \times 10^1 \exp(-93.4 \times 10^3 / RT) \tag{8}$$

$$K_m = 3.46 \exp(-14.2 \times 10^3 / RT) \tag{9}$$

The plot of K_m data versus 1/T in Figure 6.15 shows an abrupt change between 1.37 x 10^{-3} and 1.32 x10^{-3} in 1/T axes (corresponding to 455°C and 483°C) resulting in a low correlation coefficient. We could have divided the data into two regions to achieve better curve-fitting. Considering, however, the overall small variation in K_m, we preferred to use the single Arrhenius equation as a crude approximation.

6.3.2.4 Verification of Kinetic Equations

Since the above kinetic models for both the CO and methane oxidation were obtained with experimental data measured in a differential reactor mode, the question whether the rate equations are valid at high conversions was considered next. We calculated the light-off curves for the simultaneous oxidation of CO and methane over the $Cu_{0.15}[Ce(La)]_{0.85}O_x$ catalyst for a gas mixture of 0.1% CO, 0.228 % CH_4, and 1% O_2 at a contact time of 0.09 s·g/cc. We did not detect any axial temperature gradient under these reaction conditions because of the small reactor diameter and shallow packed catalyst bed. Therefore, CO conversion at each temperature was calculated by integrating the following equation:

$$\frac{N_t \cdot dP_{CO2}}{P \cdot dW_{Cat}} = \frac{k_{CO} K_{CO} P_{CO} P_O^{0.08}}{1 + K_{CO} P_{CO}} \tag{10}$$

$$P_{CO2} = (P_{CO})_{inlet} - P_{CO} \tag{11}$$

Where N_t is the total gas flowrate; P is the total pressure and is assumed to be constant when a dilute reacting gas is used; W_{cat} is the catalyst weight. Methane conversion was calculated in exactly the same manner. The calculated light-off curves in Figure 6.16 are in

excellent agreement with experimental data. It is noteworthy that kinetic model was developed based on individual reaction data while the experimental data were for the simultaneous oxidation of CO and methane. This indicates that oxidation of CO and methane are independent reactions.

6.4 Discussion

6.4.1 CO Oxidation over the $Au_{0.05}[Ce(La)]_{0.95}O_x$ Catalyst

The $Au_{0.05}[Ce(La)]_{0.95}O_x$ catalyst characterization revealed that gold was distributed in the cerium oxide matrix as distinct metallic particles. There was no evidence of "strong interaction" between the gold particles and cerium oxide. It is known that neither cerium oxide nor gold alone is an active CO oxidation catalyst. The enhanced activity was solely due to the synergistic effect of the two kinds of materials. Extensive studies of the gold/oxide catalysts were reported by Haruta et al. *(14)*. The Au-Ce-O is a new catalyst system, but we propose a reaction mechanism similar to that for other gold/oxide catalysts *(14)* as illustrated by the following Figure.

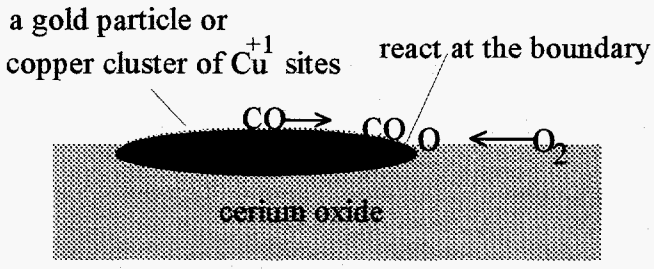

Figure 6.17 Synergistic Reaction Model for CO Oxidation over the Au-Ce-O and Cu-Ce-O Catalysts.

In this model, CO molecules adsorb on the gold particle surface, while oxygen molecules adsorb on the metal oxide surface. Then, the two adsorbed species react at the boundary of the gold and metal oxide. The highly active sites created at the boundary provides quick turnover of reacting species and high reaction activity. The adsorbed CO on the gold particle and the surface oxygen on the metal oxide may move to the boundary area by surface diffusion. Apparently, decreasing gold particle size will increase the boundary area and thus, the catalytic activity. The kinetic results in Table 6.1 show that the rate on the $Au_{0.05}[Ce(La)]_{0.95}O_x$ catalyst had stronger dependence on the partial pressure of the reacting species and higher activation energy than those on the other gold/oxide catalysts *(14)*. The present catalyst, prepared by air calcination for 1 h at 500°C+1 h at 650°C, comprised bigger gold particles (8 nm). The bigger gold particles resulted in lower interface and slower diffusion of the reacting species on the surface.

The high activity of the $Au_{0.05}[Ce(La)]_{0.95}O_x$ catalyst clearly demonstrated the synergistic effect of dual function materials in the CO oxidation. It is known that water vapor inhibits CO adsorption on cerium oxide. CO oxidation on the $Au_{0.05}[Ce(La)]_{0.95}O_x$ catalyst was not affected by water vapor further suggests the role which gold plays in

providing CO adsorption sites. The role of cerium oxide in supplying oxygen will be discussed next together with the CO oxidation on the Cu-Ce-O catalyst.

6.4.2 CO Oxidation over the Cu-Ce(La)-O Catalyst

On base metal oxide catalysts *(26-28)*, the CO oxidation rate generally has a weak dependence on P_O and has a positive order from 0 to 1 in P_{CO}. The kinetic behavior of the Cu-Ce(La)-O catalyst is overall similar to that of the base metal oxide catalysts. Both the Eley-Rideal and Langmuir-Hinshelwood models have been proposed for CO oxidation on the copper-based catalysts. Dekker et al. *(26)* developed a comprehensive kinetic model for CO oxidation over the $CuO\text{-}Cr_2O_3/\gamma\text{-}Al_2O_3$ catalyst based on a Eley-Rideal model consisting of several elementary steps. With in situ IR measurements of CO oxidation on the $Cu/\delta\text{-}Al_2O_3$ catalyst, Choi and Vannice *(27)* revealed a clear first-order dependence of the reaction on chemisorbed CO and the absence of activity when no adsorbed CO was detected. The different conclusion was underlined by the difference in catalyst pretreatment and reaction conditions. Copper was in a partially oxidized state in the $Cu/\delta\text{-}Al_2O_3$ catalyst but likely in fully oxidized state in the $CuO\text{-}Cr_2O_3/\gamma\text{-}Al_2O_3$. Jernigan and Somorjai *(18)* recently compared the CO oxidation over three different oxidation states of copper: Cu, Cu_2O, and CuO, and found that the apparent activation energy increases with increasing copper oxidation state ($Cu(37.6)<Cu_2O(58.5)<CuO(71.1)$). The apparent activation energy listed in Table 6.2 for the Cu-Ce(La)-O catalysts is in the range of 26 to 50kJ/mol, similar to the reduced copper oxide.

The unique information conveyed by Table 6.2 is the high heat of CO adsorption over the Cu-Ce(La)-O derived from the kinetic measurements, which is comparable to that of CO adsorption on metallic copper, 30 to 68kJ/mol as reported in the literature *(29,30)*. Notice that heat of CO adsorption over the pre-calcined $CuO\text{-}Cr_2O_3/\gamma\text{-}Al_2O_3$ catalyst is indeed a small number. This may be the reason that CO has been assumed not to adsorb on the CuO surface. Recall that the Cu^{+1} species for the Cu-Ce(La)-O catalyst was observed by XPS. We believe that the Cu^{+1} surface species provide strong CO adsorption sites and CO oxidation over the Cu-Ce(La)-O catalyst proceeds via the Langmuir-Hinshelwood mechanism.

6.4.3 Strong Interaction of Copper with Cerium Oxide and Synergism

Given the fact that the present Cu-Ce(La)-O catalyst was typically prepared by a few hour-long calcination at temperatures of or over 650°C in air and used for kinetic studies without any pre-reduction treatment, how are the Cu^{+1} species stabilized? We propose that the copper ions at the interfacial area of a copper cluster and cerium oxide can penetrate into the cerium oxide lattice by occupying the vacant sites of cerium ions as illustrated by Figure 6.18. The copper ionic size found in the literature varies among different sources. However, it is agreed that Cu^{+1} ion size is bigger than the Cu^{+2}. The Cu^{+1} species is more compatible in cerium oxide lattice in terms of the size. Thus, Cu^{+1} is stabilized by the cerium oxide lattice and transferred to the outer surface by a copper oxide chain, Cu^{+1} -O-Cu- ••• -O-Cu^{+1}. The reducibility of Ce^{+4} to Ce^{+3} enhances the flexibility for a copper ion

to adapt to different oxidation state by maintaining the electronic neutrality of the lattice. The existence of isolated Cu^{+2} ions and ion pairs in the cerium oxide lattice was studied with the electron paramagnetic resonance technique *(23-25)*, but this technique cannot detect the Cu^{+1} species. The formation of chemical bonding between the copper clusters and cerium oxide explains the strong association of copper with cerium oxide as found in catalyst preparation and activity tests.

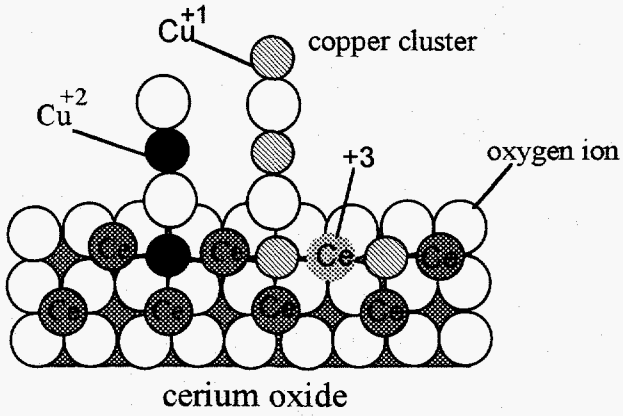

Figure 6.18 Interaction Model of Copper with Cerium Oxide(cross section of ceria showing a [001] plane of oxygen ions and adjacent cerium cations).

In addition to the strong CO adsorption, the reaction rate on the Cu-Ce(La)-O catalysts was several orders of magnitude higher than that either on the oxidized CuO-Cr_2O_3/γ-Al_2O_3 or the reduced Cu/δ-Al_2O_3 catalyst. We propose a reaction model for CO oxidation over the Cu-Ce(La)-O catalyst similar to the Au/metal oxide system with the Cu^{+1} species of the copper cluster replacing gold particles and providing surface sites for CO adsorption. Given the catalyst configuration in Figure 6.17, a minute Schottky junction can form at the interface between metals and oxides and affect the electronic properties of metal oxides *(31)*. However, it has always been difficult to relate the catalyst electronic property to catalytic activity. We rather attribute the enhanced catalytic activity to the concerted effect of CO adsorption and oxygen activation. Cerium oxide can provide various active surface oxygen species for oxidation reactions. The surface oxygen species on cerium oxide were studied by TPR *(32)*, FT-IR *(33, 34)*, and EPR *(35)*. The possible oxygen species are shown in equation *(12)*. Generally, increasing the catalyst treatment temperature shifts the equilibrium to the right, that is, the lattice oxygen will be a major component if heated at high temperatures.

$$O_2 \overset{e}{\longleftrightarrow} O_2^- \overset{e}{\longleftrightarrow} O_2^{2-} \longleftrightarrow O^- \overset{e}{\longleftrightarrow} O_{lattice}^{2-} \qquad (12)$$

Superoxide species (O_2^-) forms from the adsorption of an oxygen molecule on a single unsaturated surface cerium ion ($Ce^{+4}\cdots O_2^-$). Formation of peroxide species(O_2^{-2}) increases with the reduction extent of the cerium oxide surface. The peroxide species is probably associated with a pair of reduced cerium ions or one oxygen vacancy. The superoxide species has very quick exchange rate with gaseous oxygen at low temperatures (below 100°C) according to Li et al. *(34,36)*. It is labile on cerium oxide surface and its surface

diffusion is much faster than on SiO_2 or Al_2O_3 *(37)*. Therefore, we propose the superoxide species as the active surface oxygen species in CO oxidation over both the Au-Ce(La)-O and Cu-Ce(La)-O catalysts according to the reaction model in Figure 6.17. In fact, oxygen spill-over and reaction with CO at the interface were demonstrated by Metcalfe and Sundaresan with the Pt/YSZ catalyst *(10)*. Tarasov et al. *(38)* proposed that the junction effect between the precious metals and cerium oxide facilitates the formation of superoxide species. This argument is applicable to the Au-Ce(La)-O catalyst where distinctive metallic gold particles were identified. In the Cu-Ce-O system, however, we do not regard the copper cluster as distinct fine metallic copper or Cu_2O particles but rather as a group of copper atoms. We postulate that the presence of copper ions in the Cu-Ce(La)-O systems may increase the concentration of unsaturated cerium ion(Ce^{+3}) and the concentration of superoxide species.

Most of experimental observations in this work can be explained with this reaction model. First of all, based on the model, only a small amount of copper or gold is needed to form an active catalyst. Bulk CuO oxide does not contribute to the observed CO oxidation activity. Isolated copper ions as found in the $Cu_{0.01}[Ce(La)]_{0.99}O_x$ catalyst prepared by calcination in nitrogen are not active because they can be capped by oxygen and water molecules so that CO adsorption sites are greatly suppressed. In the Cu-Zr-O system, copper clusters may be stabilized by zirconia through the interstitial interaction model in Figure 6.18. But, the high stability of Zr^{+4} ion would not favor the formation of superoxide species(O_2^-) and the Cu^{+1} species. This may be the reason why the Cu-Zr-O catalyst showed greatly improved resistance to water vapor poisoning but only a small enhancement in catalytic activity compared to bulk CuO catalyst as reported in the preceding paper *(1)*.

6.4.4 Methane Oxidation Kinetics

A variety of kinetic models for methane combustion on metal oxides have been reported *(39,40)*. The activation energy for methane oxidation over the $Cu_{0.15}[Ce(La)]_{0.85}O_x$ catalyst is comparable to the literature data. In general, the rates on base metal oxides such as perovskite-type mixed oxides are first order in methane, while the order in oxygen may vary from zero to approximately 0.5. A non-competitive Langmuir-Hinshelwood kinetic model was proposed by Otsuka et al. *(41)* for oxidative coupling of methane over a Ba-doped CeO_2 catalyst. However, all previous kinetic studies used a narrower window of partial pressure of methane(P_m) than the present work. The Langmuir adsorption type dependence on P_m in the kinetic expression (Equation 6) for methane oxidation over the $Cu_{0.15}[Ce(La)]_{0.85}O_x$ catalyst suggests that the rate-determining step involves the adsorbed methane. The power order dependence on the partial pressure of oxygen (P_O) suggests complex oxygen sources for the reaction. The following reaction mechanism is proposed based on the present kinetic results.

$$CH_{4,cat} + O^-_{cat} \xrightarrow{slow} CH^-_{3,cat} + HO_{cat} \quad (13)$$

$$CH^-_{3,cat} + O_{cat} \xrightarrow{fast} O^-_{cat} + CH^{\cdot}_{3,cat} \xrightarrow{O} CO_2 + H_2O \quad (14)$$

In the above equations, cat denotes catalyst surface. Gas phase oxygen can quickly reach equilibrium with the various surface oxygen species as described by equation (2). The rate-limiting step involves the reaction of adsorbed methane with the surface basic groups(oxygen ions). The negative charge on the resulting methyl group can transfer to the surface oxygen through the electronic band or a metal ion intermediate(e.g., $M^{+n} + e \rightarrow M^{+(n-1)} + O_{cat} \rightarrow M^{+n} + O^{-}_{cat}$). The methyl radical is rapidly and completely oxidized into carbon dioxide and water over the present catalyst. This mechanism is overall similar to the ones proposed in the literature for methane oxidation over base metal oxide catalysts. But, some of previous kinetic studies of methane combustion suggested the direct reaction of gaseous methane with the catalyst surface. Here, we would like to emphasize that methane adsorption on the catalyst surface is necessary to activate the methane at low temperatures, because the hydrogen abstraction process is a complex step as we stated in the preceding paper *(1)*.

Although it has a similar rate expression to CO oxidation, the methane oxidation process may be intrinsically different from CO oxidation. The pre-exponential factor of the methane oxidation rate constant in equation (8) is about five orders of magnitude smaller than that of the CO oxidation rate constant in Table 6.2. The heat of methane adsorption on the $Cu_{0.15}[Ce(La)]_{0.85}O_x$ catalyst is only about 14.2kJ/mol. The Cu^{+1} species provide sites for strong CO adsorption but not for methane. Van Kooten et al. *(42)* found no measurable interaction of methane with metallic and oxidized copper over the temperature range of 300 to 750K. At the present time, we do not know what are the specific surface sites for methane adsorption on the Cu-Ce(La)-O catalyst. Regarding the oxygen source, Li et al. *(43)* observed that methane oxidation on cerium oxide occurred in the absence of gaseous oxygen and superoxide species, which were considered to be active for CO oxidation. Our fixed-bed, steady-state measurements of CO and methane oxidation found that the two reactions were virtually independent of each other. Methane oxidation over the Cu-Ce(La)-O catalyst occurred at higher temperatures(>300°C). Although such temperatures may not be high enough to cause significant bulk oxygen mobility, the participation of surface capping(O_2^{-2}, O^- or O^{-2}) and lattice oxygen is very likely since surface species on the CeO_2 surface are more active than the bulk *(33,44)*. In conclusion, methane oxidation is a more complicated process than CO oxidation and a detailed adsorption/desorption study is necessary to elucidate the reaction mechanism.

6.5 Summary

Gold in the $Au_{0.05}Ce(La)_{0.95}O_X$ catalyst exists in fine metallic particles in contact with the cerium oxide. The CO oxidation kinetics over the $Au_{0.05}Ce(La)_{0.95}O_X$ catalyst were described by a rate equation such as $kP_{CO}^{0.30}P_O^{0.18}$.

Copper in small amounts showed strong tendency to attach to cerium oxide surface irrespective of catalyst preparation. Copper in the Cu-Ce-O composite existed in the form of isolated ions, clusters, and bulk CuO particles. Isolated ions aggregated into clusters after heating at high temperatures (≥650°C) in air. When the cerium oxide surface was saturated by copper clusters, excess copper formed bulk CuO particles which were

typically covered by the fine cerium oxide particles. Cu^{+1} species was observed with all the Cu-Ce-O catalysts in the XPS studies and its formation is considered to originate from the interaction of copper clusters with cerium oxide.

The oxidation rates of CO and methane over the Cu-Ce(La)-O catalysts were expressed as $kK_R P_R P_O^n/(1+K_R P_R)$, where P_R denotes the partial pressure of CO or methane and P_O is the partial pressure of oxygen. The activation energies of the surface reactions were 78-94kJ/mol for CO oxidation and 79kJ/mol for methane oxidation, respectively. The heat of adsorption on the Cu-Ce-O catalyst was in the range of 28 to 62kJ/mol for CO adsorption and 14kJ/mol for methane adsorption, respectively.

The Langmuir-Hinshelwood mechanism and synergistic reaction model was proposed for CO oxidation over the Cu-Ce-O and Au-Ce-O catalysts. In this model, the Cu^{+1} species of a copper cluster or fine gold particles provide sites for CO adsorption, cerium oxide provides the oxygen source, and the reaction proceeds at the boundary of the two kinds of materials. The Langmuir-Hinshelwood mechanism was also proposed for methane oxidation over the Cu-Ce-O catalyst.

6.6 Notation

Ea = activation energy, kJ/mol.
E_{app} = apparent activation energy, kJ/mol.
k = reaction constant, mol/(g·s·bar^{m+n})
k_{CO} = reaction constant of CO oxidation, mol/(g·s·bar^n).
k_m = reaction constant of methane oxidation, mol/(g·s·bar^n).
K_{CO} = CO adsorption equilibrium constant, 1/bar.
K_m = methane adsorption equilibrium constant, 1/bar.
K_O = adsorption equilibrium constant of reacting species, 1/bar.
m, n = reaction orders.
N_t = total gas flow rate, mol/s.
P = total pressure of reacting gases mixture, bar.
P_{CO} = partial pressure of CO, bar.
P_{CO2} = partial pressure of CO_2, bar.
P_m = partial pressure of methane, bar.
P_O = partial pressure of oxygen, bar.
P_R = partial pressure of reacting species, bar
Q = heat of adsorption, kJ/mol.
R = gas constant, J/mol·K.
R_{CO} = reaction rate of CO oxidation, mol/g·s.
R_m = reaction rate of methane oxidation, mol/g·s.
T = reaction temperature, K.
W_{Cat} = weight of catalyst loading, g.
X_{CO2} = conversion to CO_2.

6.7 Literature Cited

1. Liu, W., and Flytzani-Stephanopoulos, M., *J. Catal.*,Vol. 153, No. 2, May 1995 .
2. Tauster, S.J., Fung, S.C., Baker, R.T.K., and Horsley, J.A,.*Science* **211**, 1121-1125 (1981).
3. Baker, R.T.K., Tauster, S.J., and Dumesic, J.A., (Editors), "Strong Support Interactions", American Chemical Society, Washington, DC, 1986.
4. Stevenson, S.A., Dumesic, J.A., Baker, R.T.K., and Ruckenstein, E., (Editors), "Metal-Support Interactions in Catalysis, Sintering, and Redispersion", Van Nostrand Reinhold Company Inc., 1987.
5. Narayanan, S., *J. of Sci. and Ind. Res.* **44**, 580-587 (1985).
6. Burch, B., and Flambard, A.R., *J. Catal.* **78,** 389-405 (1982).
7. Bell, A.T., in Hegedus, L.L., et al. (Editors), "Catalyst Design, Process and Perspectives", Wiley, New York, p103, 1987.
8. Frost, J.C, *Nature* **334**, 577-580 (1988).
9. Crucq, A., (editor), "Catalysis and Automotive Pollution Control II", Elsevier Science Publishers B.V., Amsterdam, 1991.
10. Metcalfe, I.S., and Sundaresan, S., *AIChE J.* **34**, 195-208 (1988).
11. Schryer, D.R., Upchurch, B.T., Sidney, B.D., Hoflund, G.B., and Herz, R.K., *J. Catal.* **130**, 314 (1991).
12. Boulahouache, A., Kous, G., Lintz, H.-G., and Schulz, P., *Appl. Catal.* A: General **9**, 115-123 (1990).
13. Sheintuch, M., Schmidt, J., Lecthman, Y., and Yahav, G., *Appl. Catal.* **49**, 55 (1989).
14. Haruta, M., Tsubota, S., Kobayashi, T., Kageyma, H., Genet, M.J., and Delmon, B., *J. Catal.* **144**, 175-192 (1993).
15. Dow, W.P., and Huang, T.J., *J. Catal.* **147**, 322-332 (1994).
16. Wagner, C.D., Riggs, W.M., Davis, L.E., Moulder, J.F., and Muilenberg, G.E., (Editors), "Handbook of X-ray Photoelectron Spectroscopy", Perkin-Elmer Corporation, 1978.
17. Agudo, A.L., Palacios, J.M., Fierro, J.L.G., Laine, J., Severio, F., *Appl. Catal.* A: General **91**, 43-55 (1992).
18. Jernigan, G.G., and Somorjai, G.A., *J. Catal.* **147,** 567-577 (1994).
19. Siriwardane, R.V., and Poston, J.A., *Appl. Surf. Sci.* **68**, 65-80 (1993).
20. Shpiro, E.S., Grunert, W., Joyner, R.W., and Baeva, G.N., *Catal. Lett.* **24**, 159-169 (1994).
21. Jin, T., Zhou, Y., Mains, G.J., and White, H.M., *J. Phys.Chem.* **91**, 5931-5937 (1987).
22. Arai, T., Maruya, K., Domen, K., and Onishi, T., *J. Catal.* **141**, 533-539 (1993).
23. Abou kais, A., Bennani, A., Aissi, C.F., Guelton, M., and Vedrine, J., *Chem. Mater.* **4**, 977-979 (1992).
24. Abou kais, A., Bennani, A., Aissi, C.F., Wrobel, G., and Guelton, M., *J. Chem. Soc. Faraday Trans.* **89(9)**, 1321-1325 (1992).

25. Soria, J., Conesa, J.C., Martinez-Arias, A., and Coronado, J.M., Bechara, *Solid State Ionics* **63-65**, 755-761 (1993).
26. Dekker, N.J.J., Hoorn, J.A.A., Stegenga, S., Kapteijn, F., and Moulijn, J.A., *AIChE J.* **38**, 385-396 (1992).
27. Choi, K.I., and Vannice, M.A., *J. Catal.* **131**, 22-35 (1991).
28. Klimisch, R.L., and Taylor, K.C., *Science* **179**, 798-799 (1973).
29. Clarke, D.B., Suzuki, I., and Bell, A.T., *J. Catal.* **142**, 27-36 (1993).
30. Sandval, M.J., and Bell, A.T., *J. Catal.* **144**, 227-237 (1993).
31. Sze, S.M., Physics of Semiconductor Devices, 2nd edition, Wiley, New York, 1981.
32. Yao, H.C., and Yao, Y.F.Y., J. Catal. **86**, 254-265 (1984).
33. Li, C., Domen, K., Maruya, K.I., and Onishi, T., *J. Am. Chem. Soc.* **111**, 7683-7687 (1989).
34. Li, C., Domen, K., Maruya, K.I., and Onishi, T., *J. Catal.* **123**, 436-442 (1990).
35. Zhang, X., and Klabunde, K.J., *Inorg. Chem.* **31**, 1706-1709 (1992).
36. Li, C., Chen, Y., Li, W., and Xin, Q., in Inui, T., et al. (Editors), New Aspects of Spillover in Catalysis, Elsevier Science Publishers B.V., pp217-220, 1993.
37. Martin, D., and Duprez, D., in Inui, T., et al. (Editors), New Aspects of Spillover in Catalysis, Elsevier Science Publishers B.V., pp201-206, 1993.
38. Tarasov, A.L., Przheval'skaya, L. K., Shvets, V.A., and Kazanskii, V.B., *Kinet. i Katal.* **29**, 1181-1188 (1988).
39. Seiyama, T., *Catal. Rev.-Sci. Eng.* **34**, 281-300 (1992).
40. Zwinkels, M.F.M., Jaras, S. G., and Menon, P. G., *Catal. Rev.-Sci. Eng.* **35**, 319-358 (1993).
41. Otsuka, K., Komatsu, T., and Shimizu, Y., in Inui, T., (Editor), Successful Design of Catalysts, Elsevier Science Publishers B.V., Amsterdam, PP43-50, 1988.
42. van Kooten, W.E.J., Kragten, D.D., Gijzeman, O.L.J., and Geus, J.W., *Surf. Sci.* **290**, 302-308 (1993).
43. Li, C., Xin, Q., Guo, X., and Onishi, T., in Guczi, L., et al.(Editors), New Frontiers in Catalysis, Proceedings of the 10th International Conference on Catalysis, 19-24 July, Budapest, Hungary, 1993 Elsevier Science Publishers B.V., pp1955-1958M, 1992.
44. Sayle, T. X.T., Parker, S.C., and Catlow, C.R.A., *J. Chem. Soc., Chem. Commun.* 977-978 (1992).

Table 6.1 CO Oxidation Kinetics over the Au-Oxide Catalysts.

Catalysts	Au size (nm)	m	n	E_{app} (kJ/mol)
$Au_{0.05}[Ce(La)]_{0.95}O_x$*	8.0	0.30	0.18	53.7
Au-Fe_2O_3 *(14)*	4.0	0.00	0.05	35.0
Au-TiO_2 *(14)*	2.0	0.05	0.24	34.2

*catalyst was prepared by air calcination: 1 h at 500°C + 1 h at 600°C.

Table 6.2 CO Oxidation Kinetics over the Cu-Ce(La)-O and Other Copper Catalysts.

Catalyst	n	A	E	K	Q	E^{d}_{app}
		(mol/g·s·bar^{n})	(kJ/mol)	(1/bar)	(kJ/mol)	(kJ/mol)
$Cu_{0.15}[Ce(La)]_{0.85}O_x$[a]	0.08±0.03	5.91×10^{6}	78.0	6.47×10^{-3}	27.9	50.1
$Cu_{0.01}[Ce(La)]_{0.99}O_x$						
fresh[b]	-0.09±0.02	9.82×10^{3}	72.7	6.82×10^{-4}	36.8	35.9
+ 3 h in air at 660°C[c]	0.0±0.07	3.23×10^{7}	93.9	2.49×10^{-5}	45.6	48.3
+ 3 h in air at 860°C[c]	0.12±0.02	1.78×10^{7}	87.3	2.50×10^{-7}	61.2	26.1
$CuO\text{-}Cr_2O_3/\gamma\text{-}Al_2O_3$ *(26)* (Cu:Cr=1:1)10 wt.%	0.0	2.96×10^{2}	91.0	7.4×10^{-2}	5.0	86
12 wt.% $Cu/\delta\text{-}Al_2O_3$ *(27)*	—	—	90-110	—	~30.1	—

a. calcined in air for 4 h at 650°C.

b. calcined in N_2 for 4 h at 600°C.

c. calcined in flowing air.

d. E_{app} = Ea-Q, corresponding to the kinetic equation $kK_{CO}P_{CO}P_{O}^{n}$ when $K_{CO}P_{CO}<<1$.

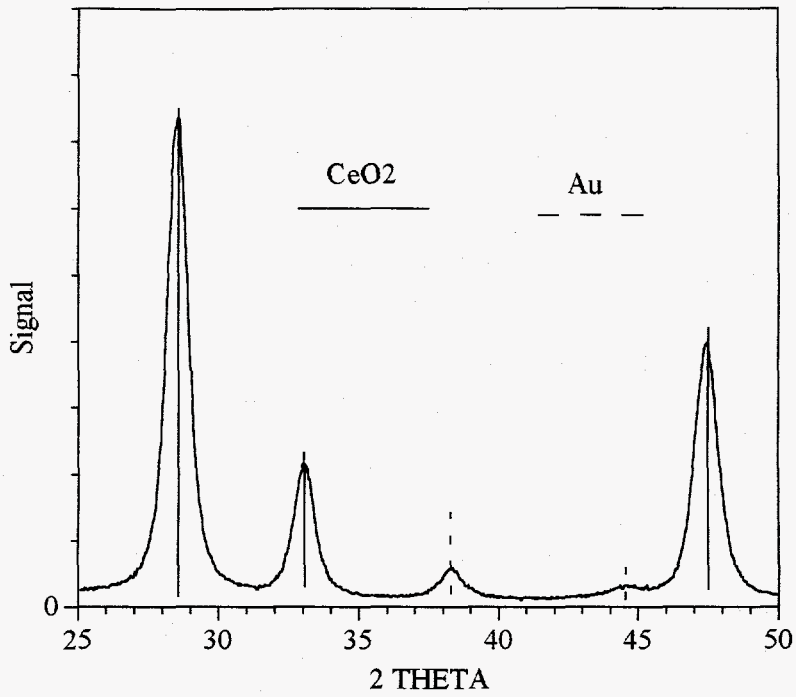

Figure 6.1a XRD Pattern of the $Au_{0.05}[Ce(La)]_{0.95}O_x$ Catalyst.

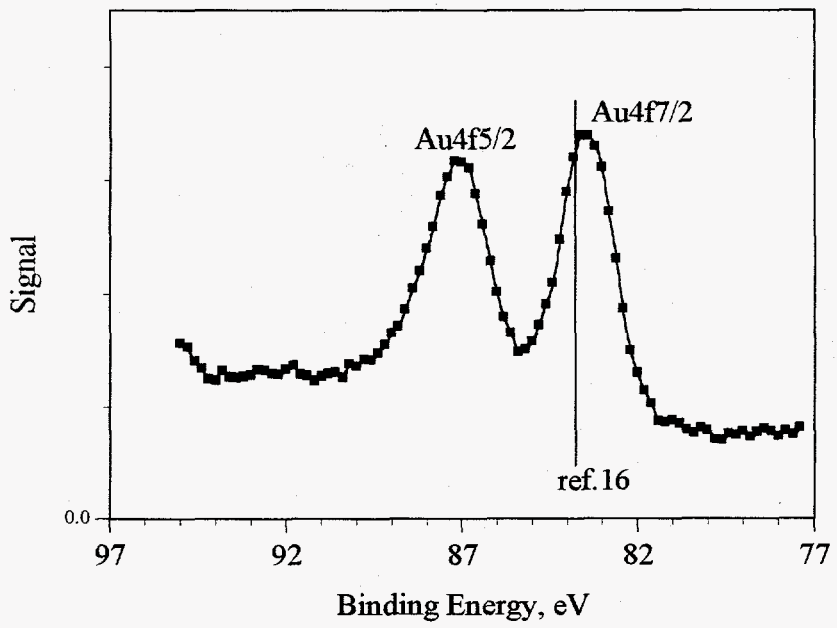

Figure 6.1b XP Spectra of Au4f in the $Au_{0.05}[Ce(La)]_{0.95}O_x$ Catalyst.

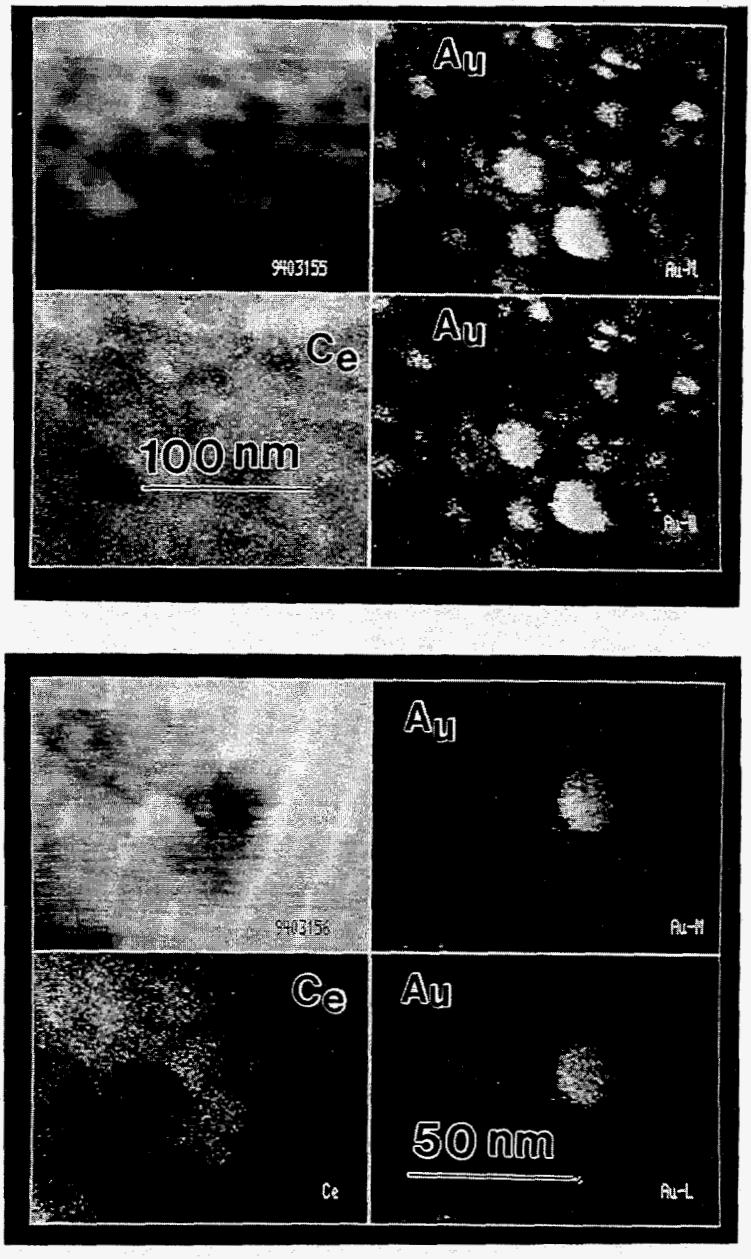

Figure 6.1c STEM/EDX Elemental Maps of the $Au_{0.05}[Ce(La)]_{0.95}O_x$ Catalyst.

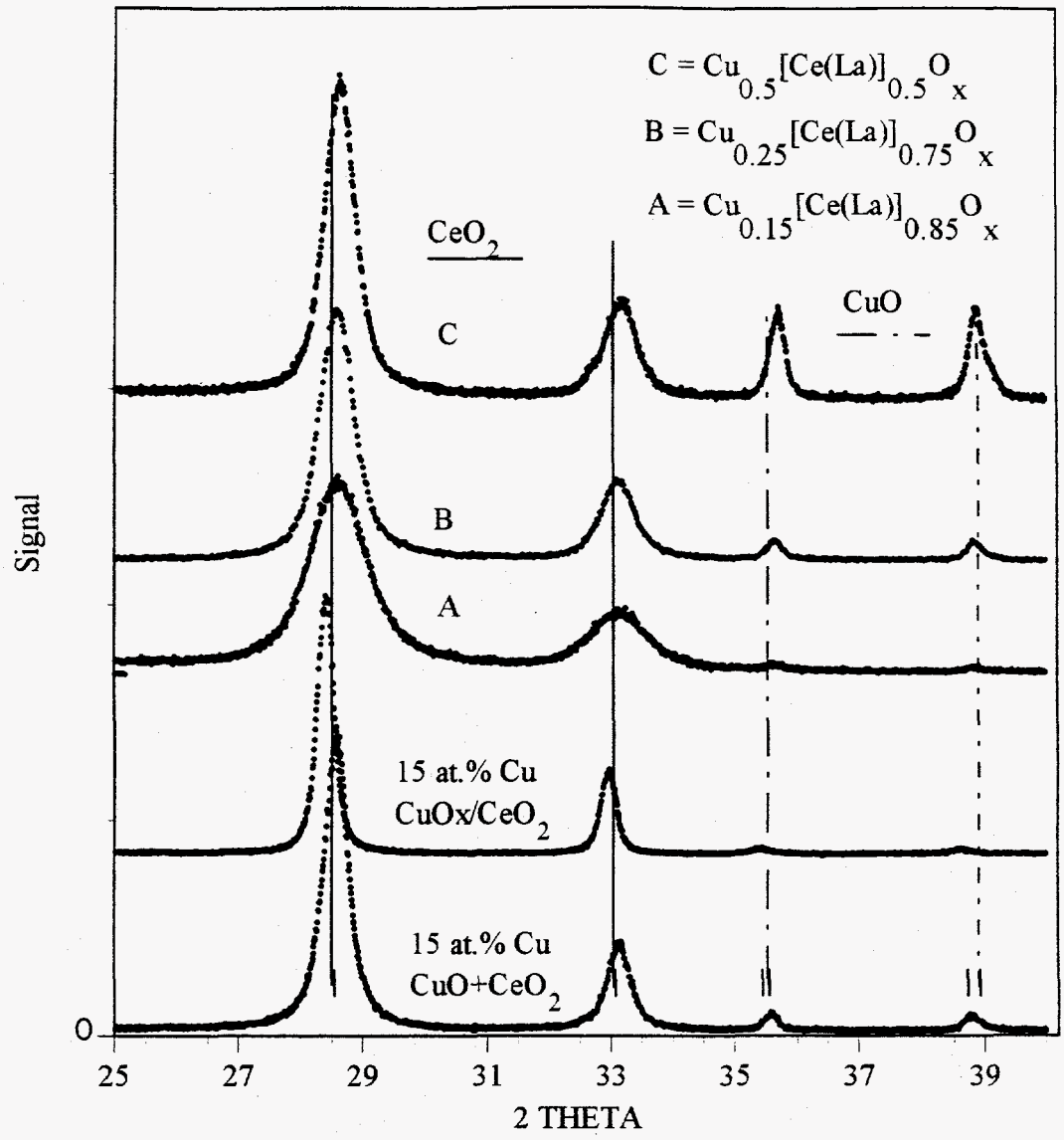

Figure 6.2 XRD Patterns of Various Cu-Ce-O Catalysts (wet mixture of CuO+CeO2 was dried for 1 h at 300°C and all the others were prepared by 4-h calcination at 650°C in air).

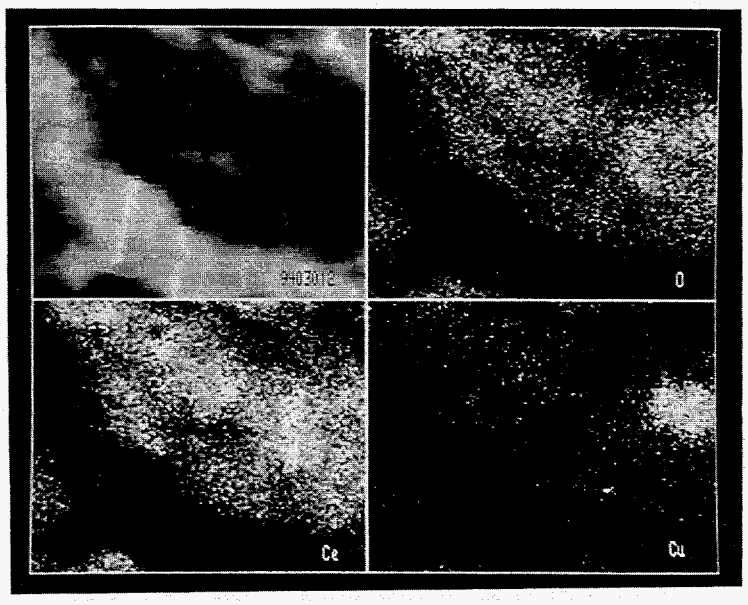

(a) $Cu_{0.15}[Ce(La)]_{0.85}O_x$ 40nm

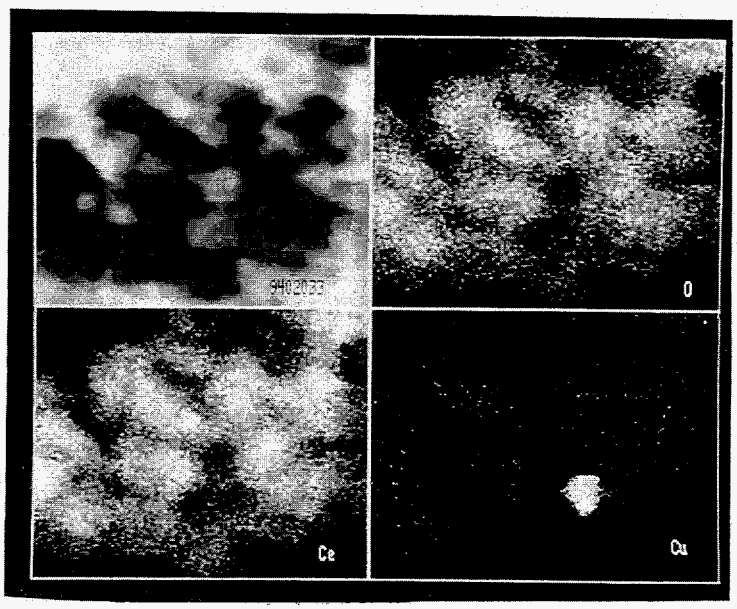

(b) 15 at.% $CuOx/CeO_2$ 40nm

Figure 6.3 Elemental Mapps of Cu-Ce-O Catalysts by STEM/EDX.

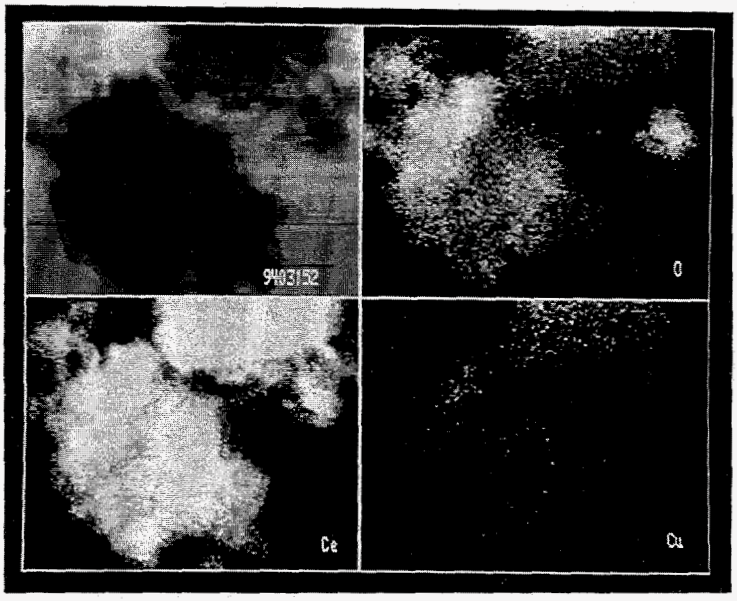

(c) 15 at.% $CuO+CeO_2$ 200 nm

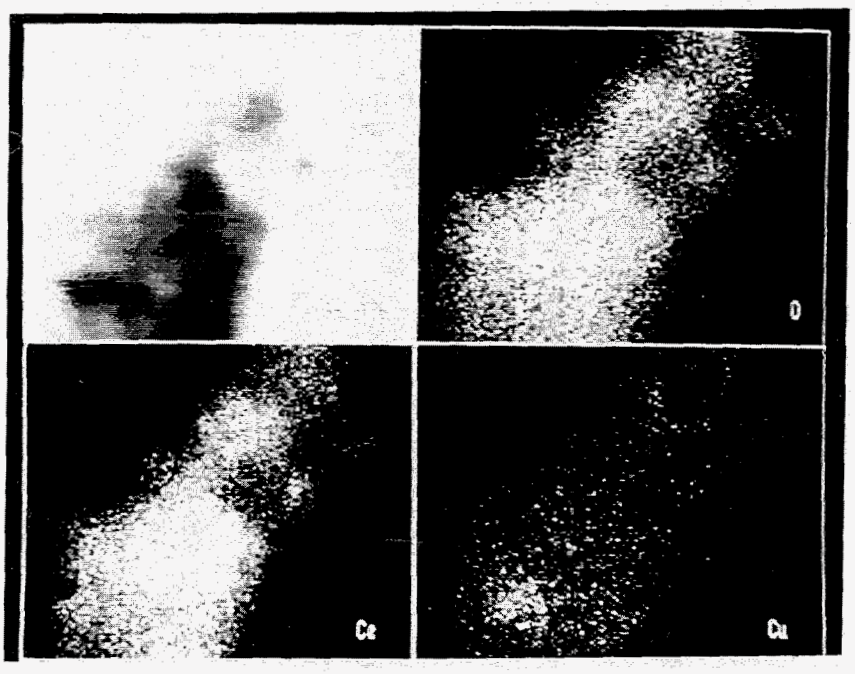

(d) $Cu_{0.15}[Ce(La)]_{0.85}O_x$ leached by nitric acid 40nm

Figure 6.3—contd.

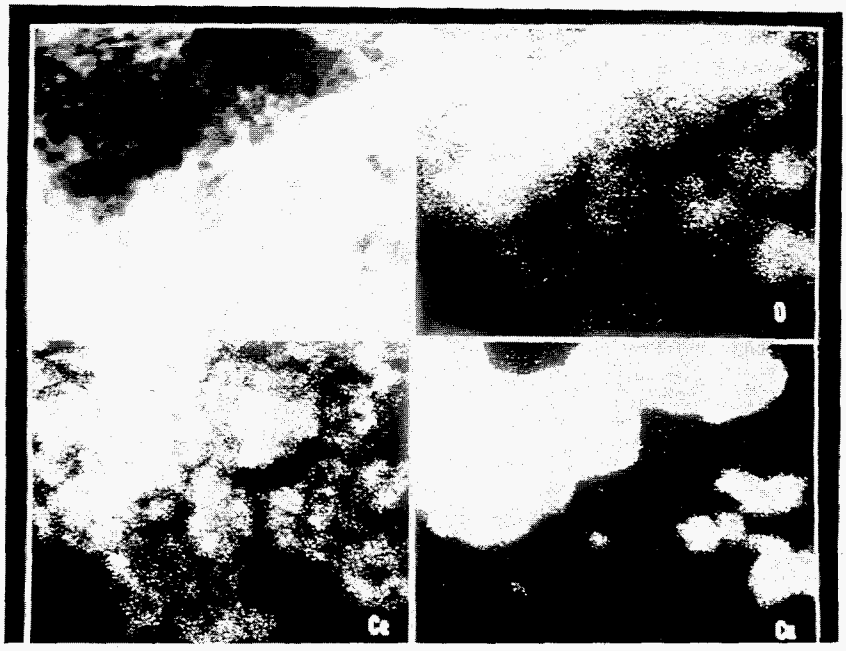

200 nm

(e) $Cu_{0.5}[Ce(La)]_{0.5}O_x$

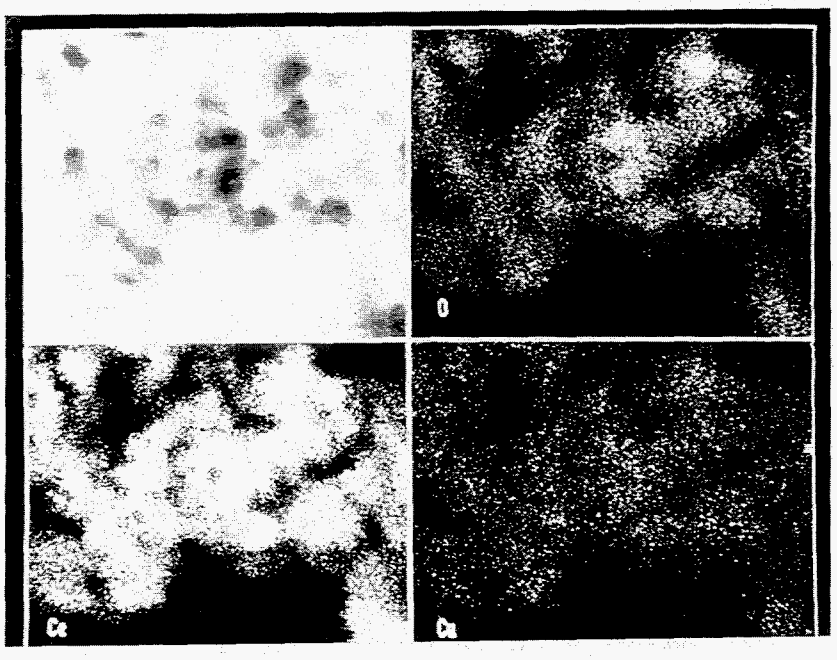

40nm

(f) $Cu_{0.5}[Ce(La)]_{0.5}O_x$

Figure 6.3—contd.

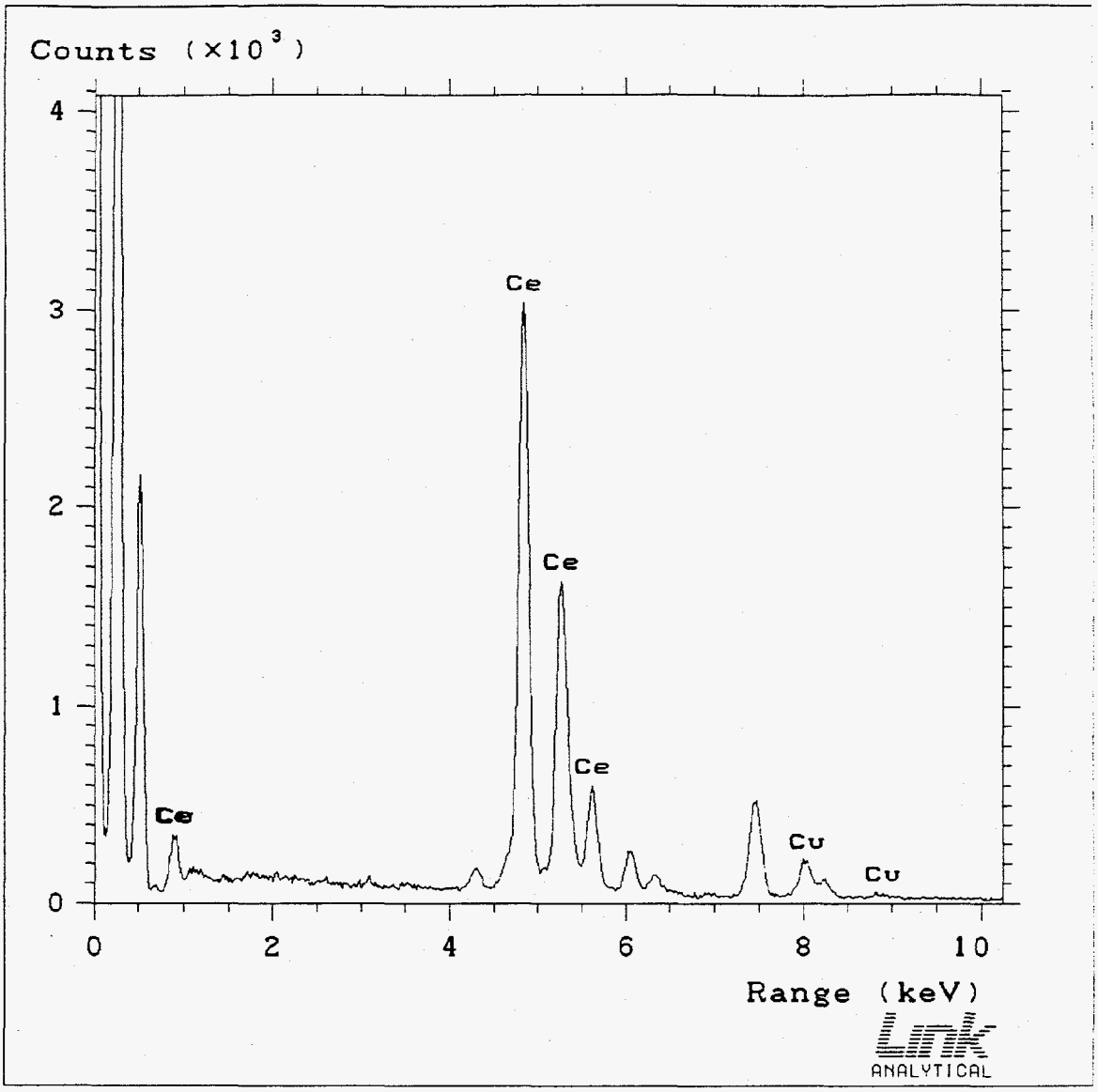

(g) X-ray Energy Dispersive Spectra of An Area Shown in Figure 7.3f.

Figure 6.3—contd.

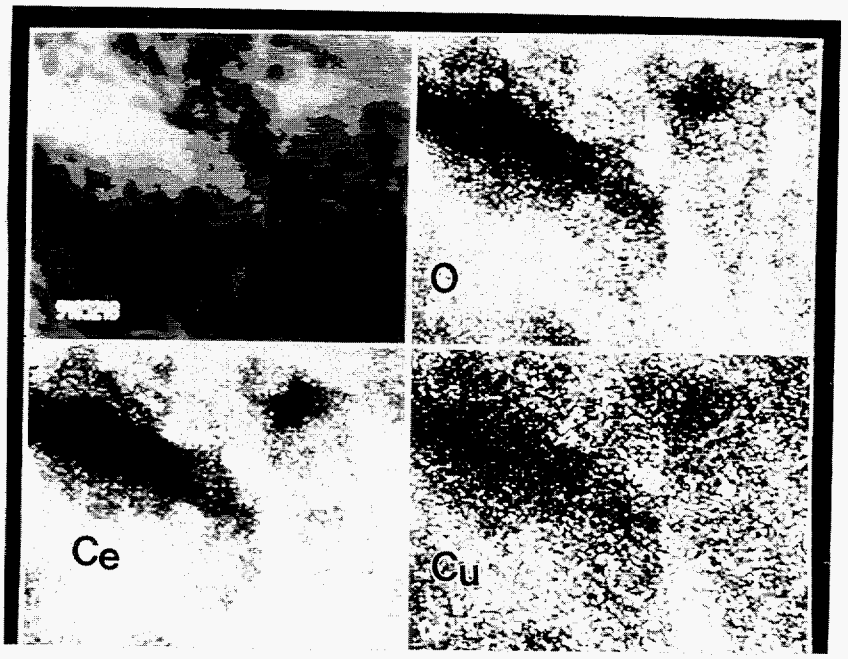

40 nm

(h) $Cu_{0.01}[Ce(La)]_{0.99}O_x$

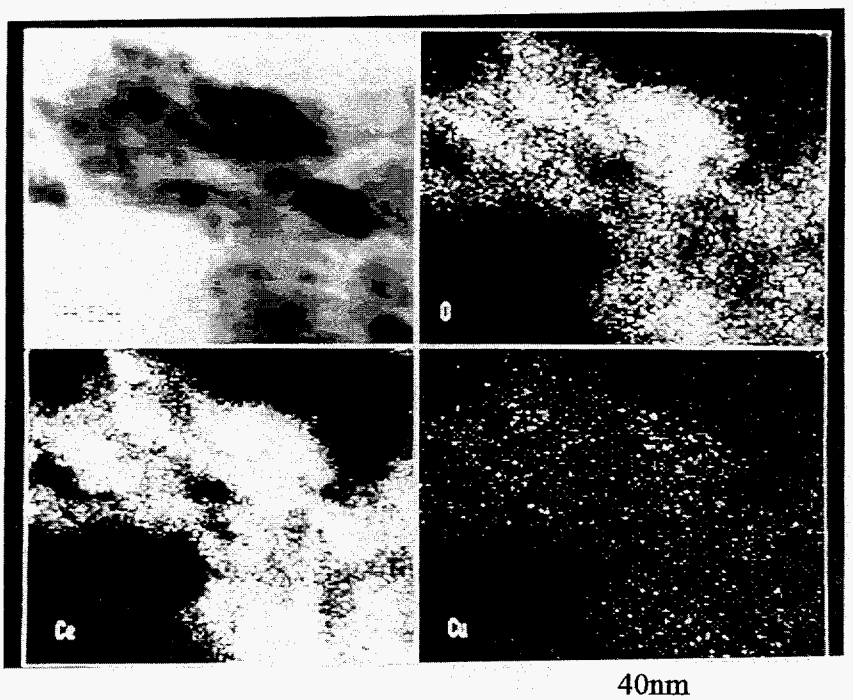

40nm

(i) $Cu_{0.01}[Ce(La)]_{0.99}O_x$ + 3 h in air at 860°C

Figure 6.3—contd.

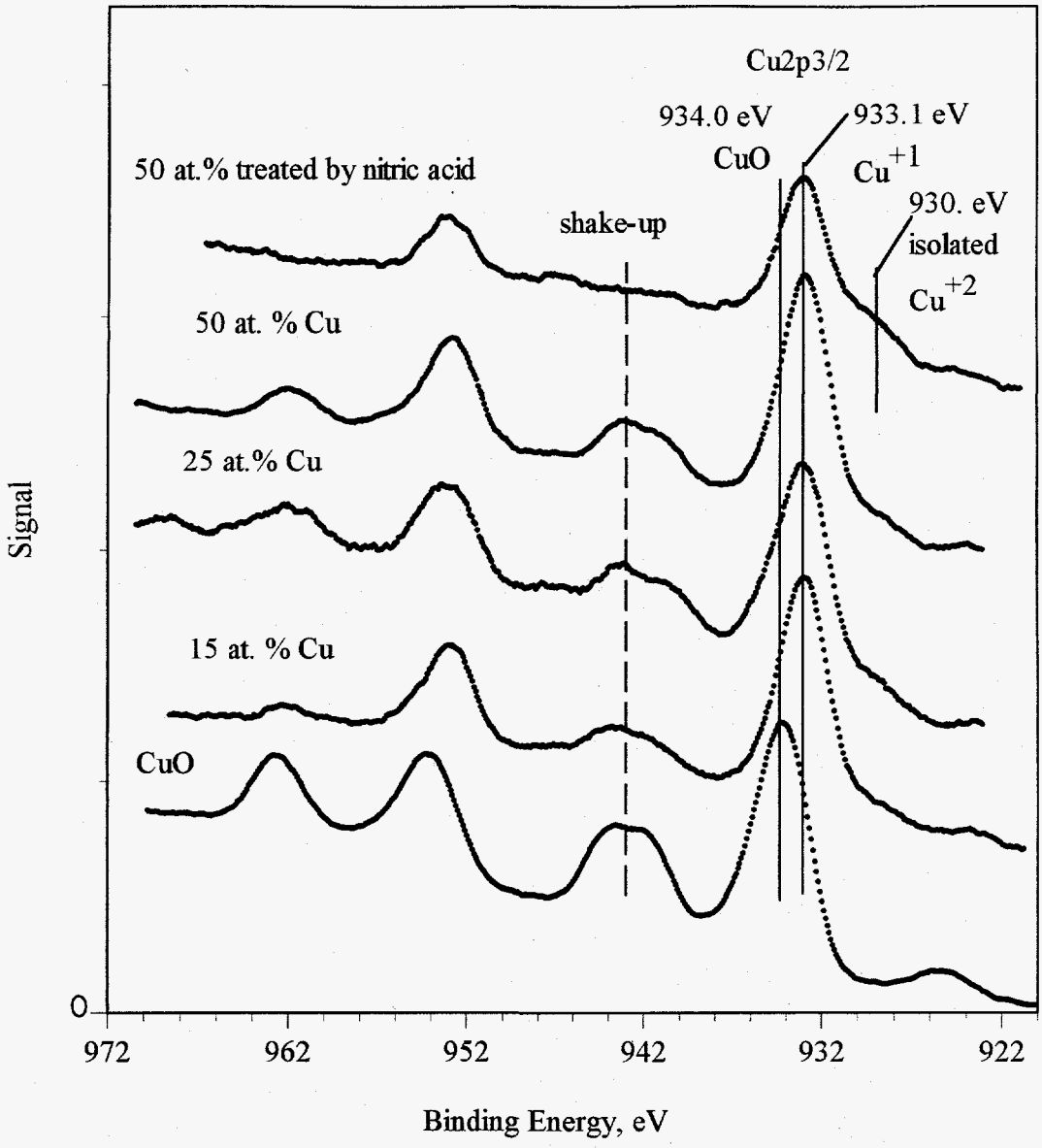

Figure 6.4a Cu2p XP Spectra of Cu-Ce(La)-O Catalysts of High Copper Content (prepared by coprecipitation).

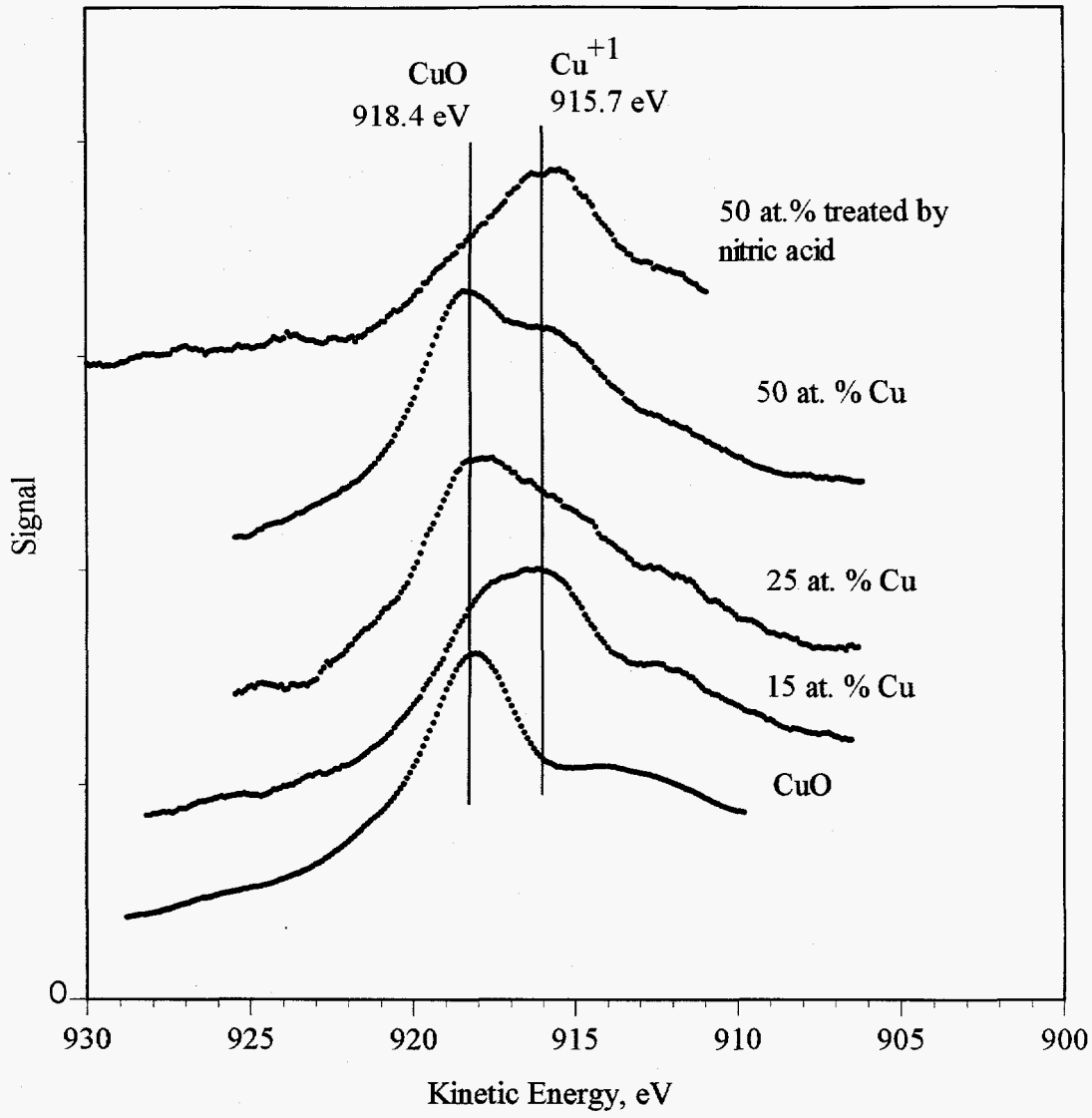

Figure 6.4b Kinetic Energy Spectra of the Auger L_3VV Electron of the Cu-Ce(La)-O Catalysts.

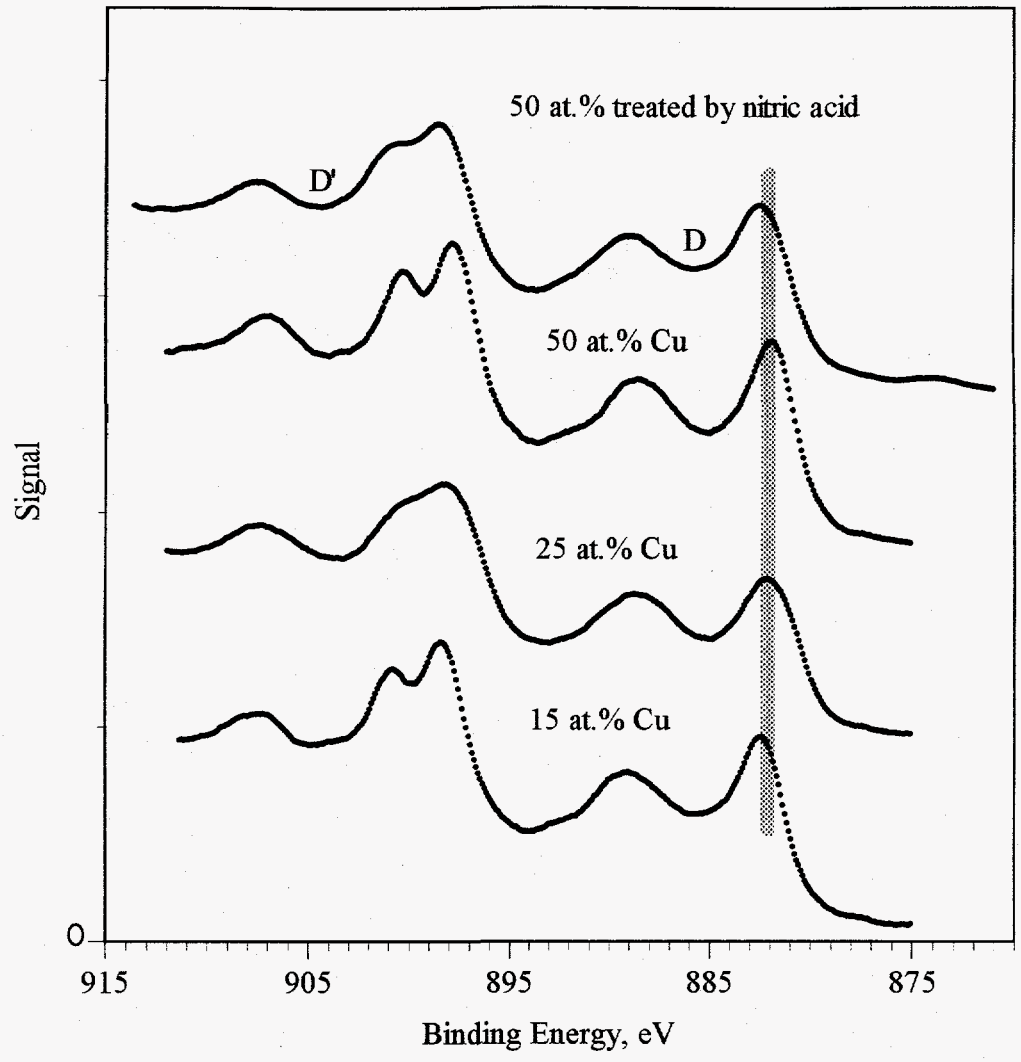

Figure 6.4c Ce3d XP Spectra of the Cu-Ce(La)-O Catalysts.

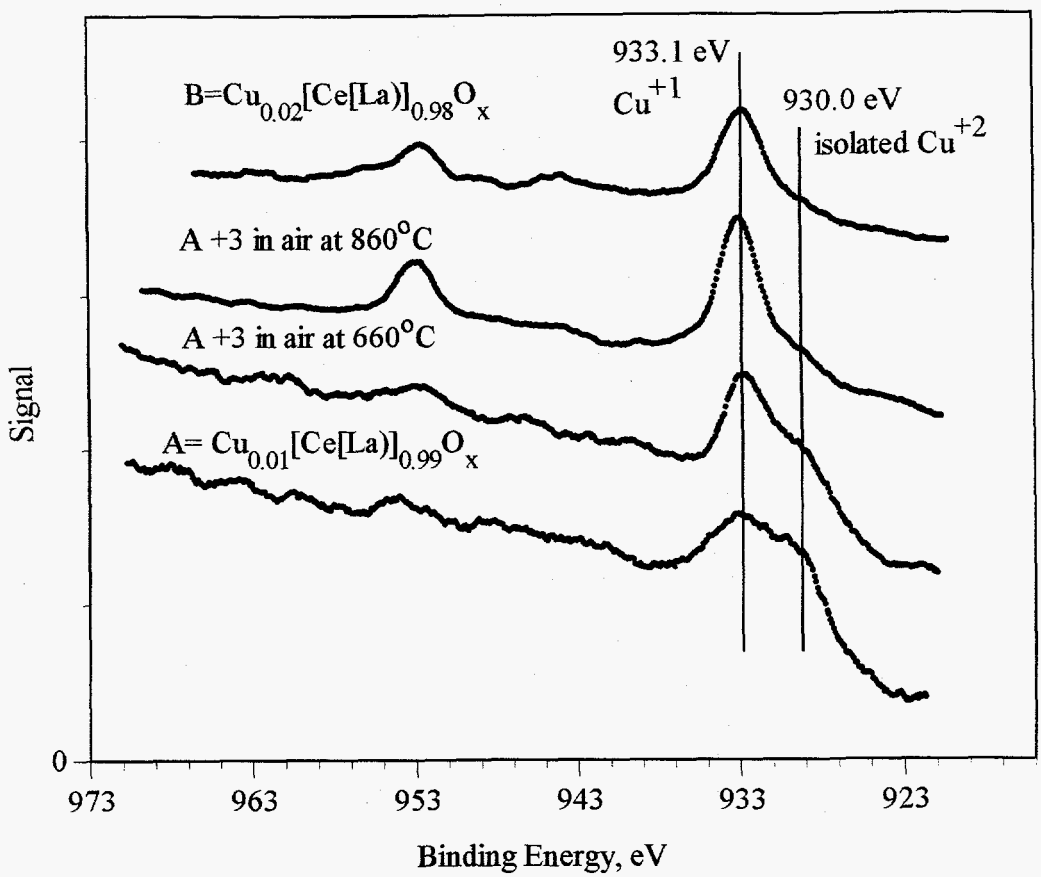

Figure 6.5a Cu2p XP Spectra of $Cu_{0.01}[Ce(La)]_{0.99}O_x$ and $Cu_{0.02}[Ce(La)]_{0.98}O_x$ Catalysts ($Cu_{0.01}[Ce(La)]_{0.99}O_x$ prepared by 4 h calcination in N_2 at 600°C; $Cu_{0.02}[Ce(La)]_{0.98}O_x$ prepared by 4-h calcination at 650°C and 3-h calcination at 860°C both in air).

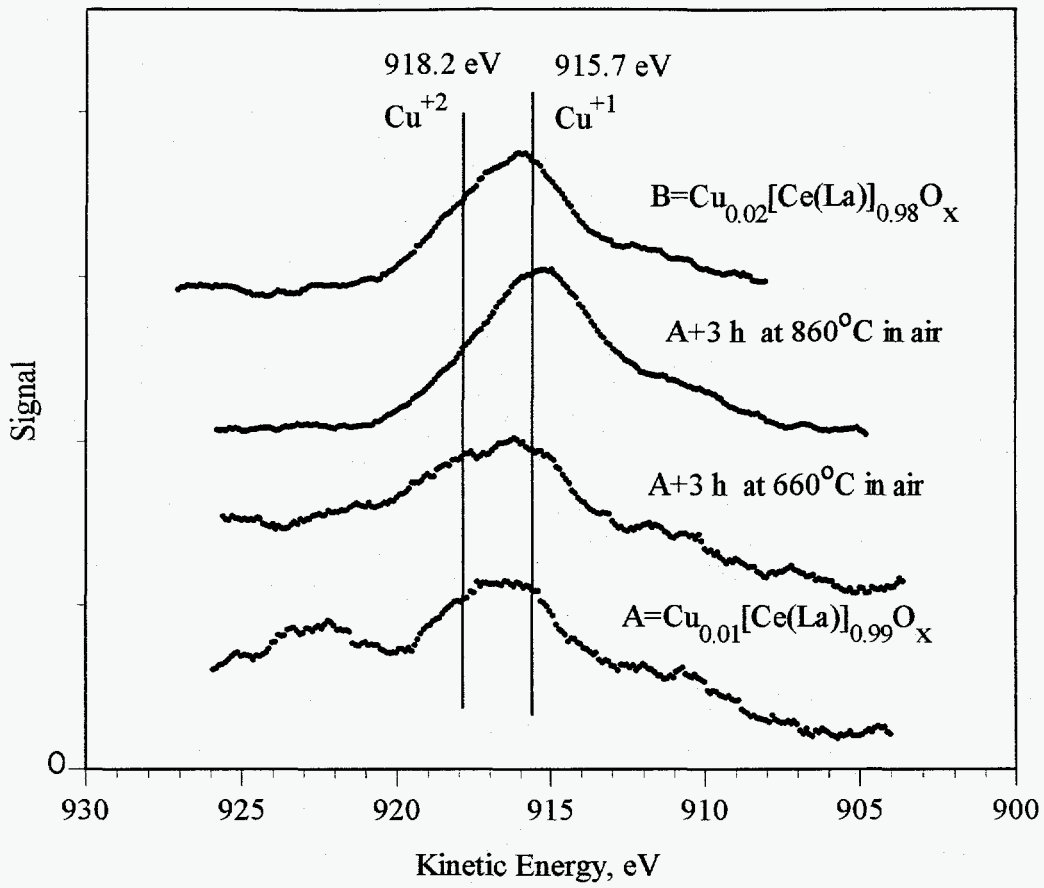

Figure 6.5b Kinetic Energy Spectra of the Auger L_3VV Electron of the $Cu_{0.01}[Ce(La)]_{0.99}O_x$ $Cu_{0.02}[Ce(La)]_{0.98}O_x$ Catalysts.

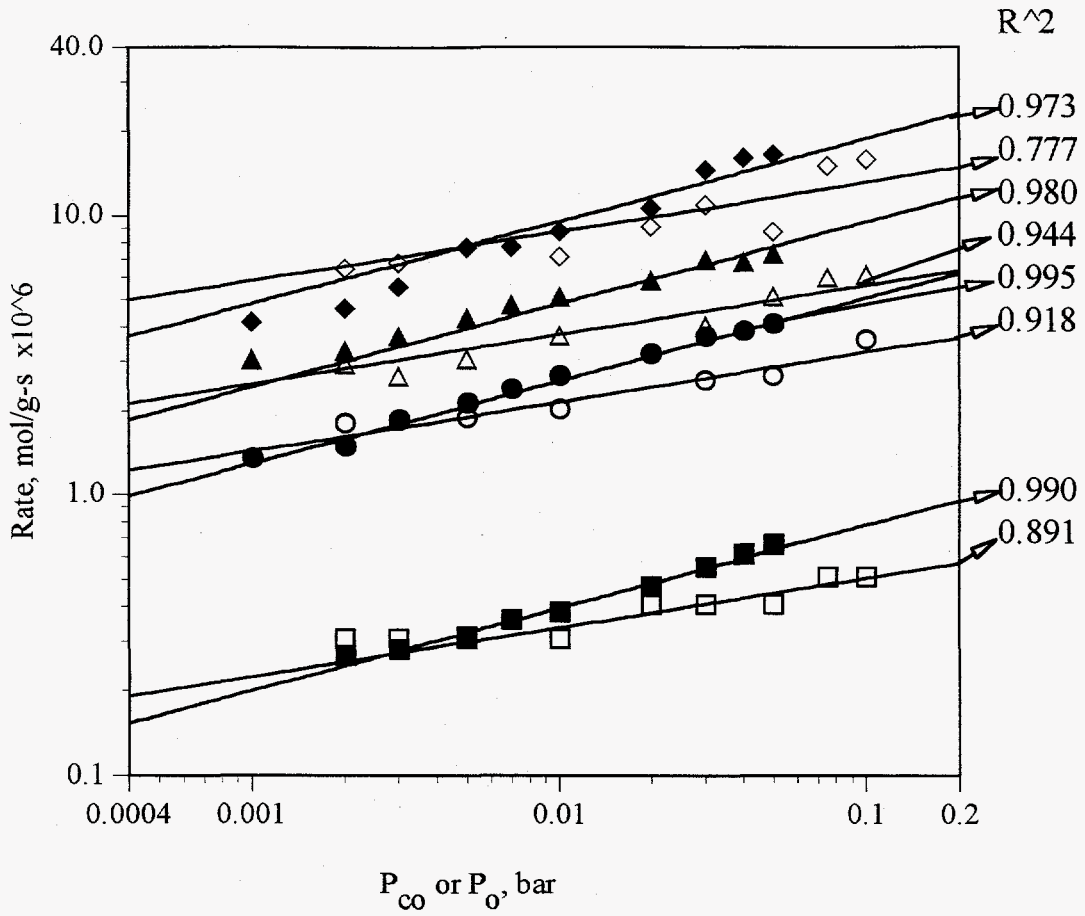

Figure 6.6 Variation of CO Oxidation Rate over the $Au_{0.05}[Ce(La)]_{0.95}O_x$ Catalyst with Partial Pressure of Oxygen and CO. Filled symbols for P_{CO} under P_O=0.05 and the open ones for P_O under P_{CO}=0.01. ■ 10°C ● 25°C ▲ 43°C ◆ 54°C.

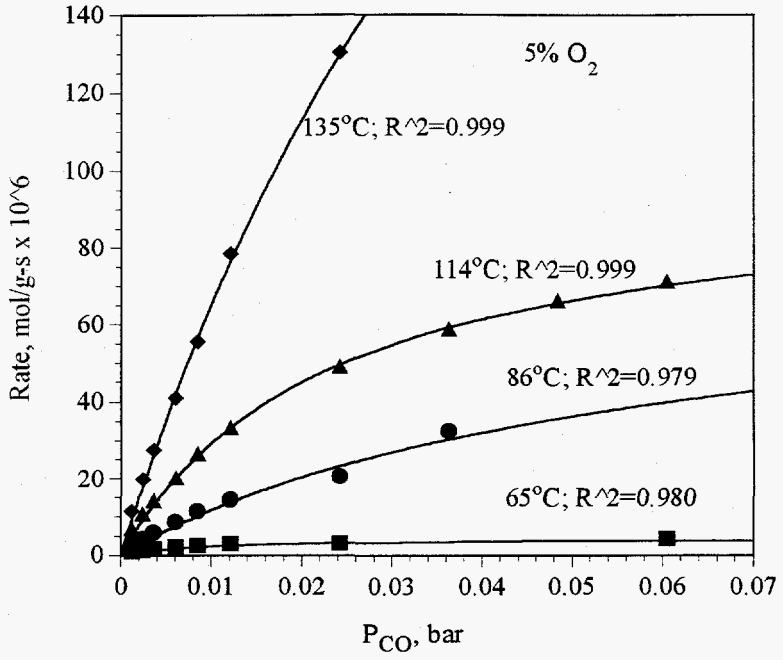

Figure 6.7 Variation of CO Oxidation Rate over the $Cu_{0.15}[Ce(La)]_{0.85}O_x$ Catalyst with Partial Pressure of CO under Constant P_O.

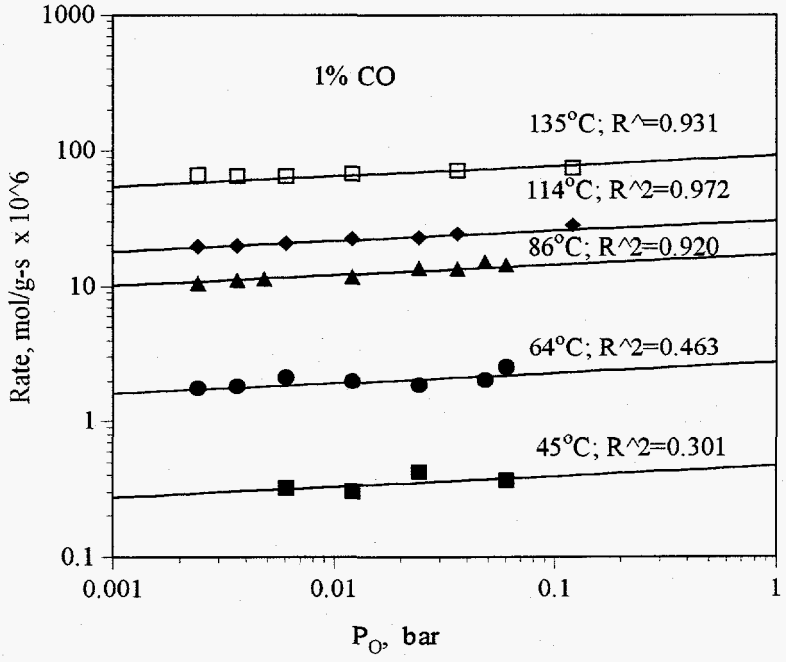

Figure 6.8 Variation of CO Oxidation Rate over the $Cu_{0.15}[Ce(La)]_{0.85}O_x$ Catalyst with Partial Pressure of Oxygen under Constant P_{CO}.

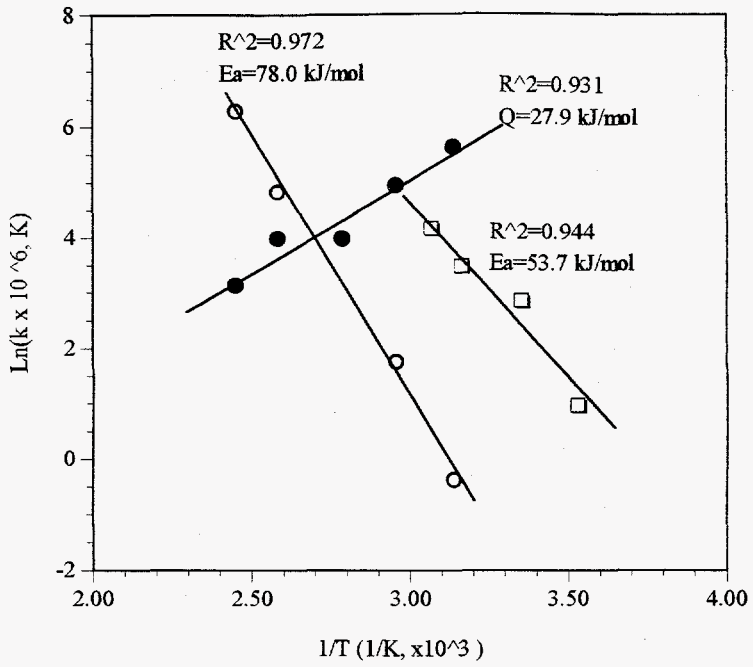

Figure 6.9 Arrhenius Plots of Constants k and K for CO Oxidation over $Au_{0.05}[Ce(La)]_{0.95}O_x$ and $Cu_{0.15}[Ce(La)]_{0.85}O_x$ Catalysts. □ k for $Au_{0.05}[Ce(La)]_{0.95}O_x$, ○ k_{CO} for $Cu_{0.15}[Ce(La)]_{0.85}O_x$, ● K_{CO} for $Cu_{0.15}[Ce(La)]_{0.85}O_x$.

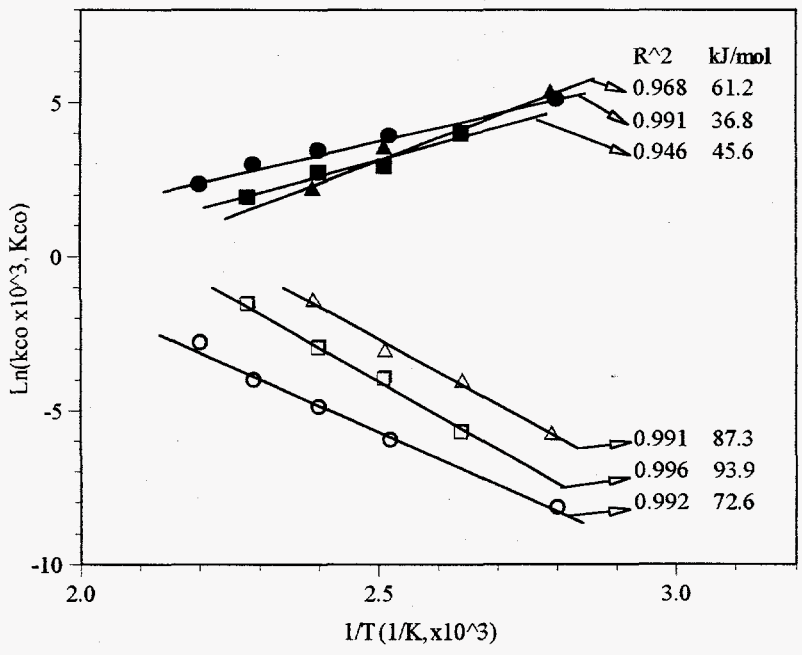

Figure 6.10 Arrhenius Plots of Constants k_{CO} and K_{CO} for CO Oxidation over $Cu_{0.01}[Ce(La)]_{0.99}O_x$ Catalysts. Open symbols for k_{CO} and the filled ones for K_{CO}: ○ fresh □ +3 h at 650°C, △ +3 h at 860°C.

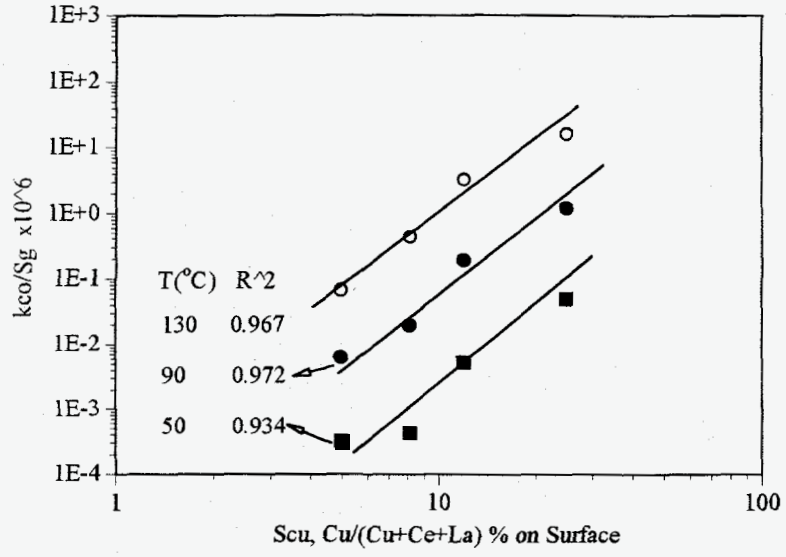

Figure 6.11 Variation of Normalized Reaction Rate Constant (k_{CO}/Sg) for CO Oxidation over the Cu-Ce(La)-O Catalysts with the Surface Copper Fraction.

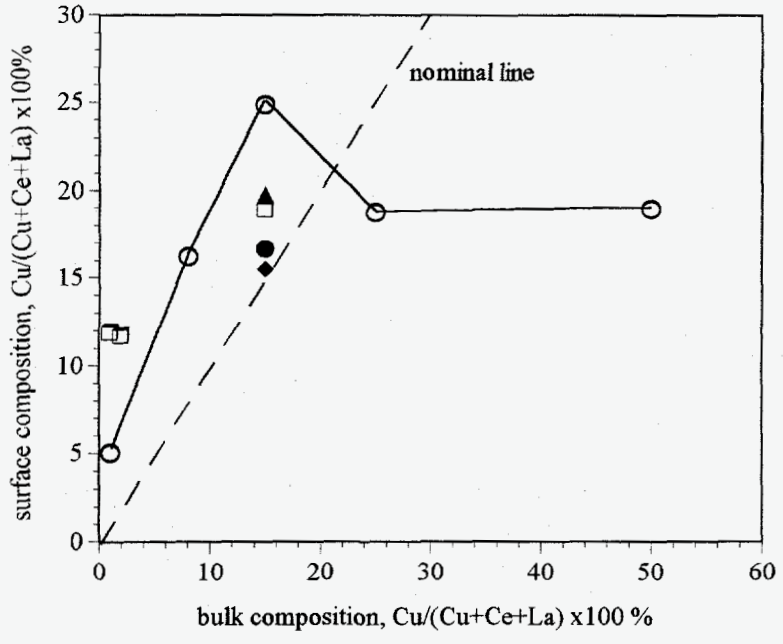

Figure 6.12 Variation of the Surface Copper Fraction of the Cu-Ce(La)-O Catalyst with Bulk Composition and Thermal Treatment. ○ as prepared by 4-h calcination at 650°C in air, □ further heated for 3 h in flowing air at 860°C, ▲ reduced by 25% H_2/He for 2 h at 300°C, ◆ reduced by 25% H_2/He for 1 h at 600°C, ● prepared by impregnation.

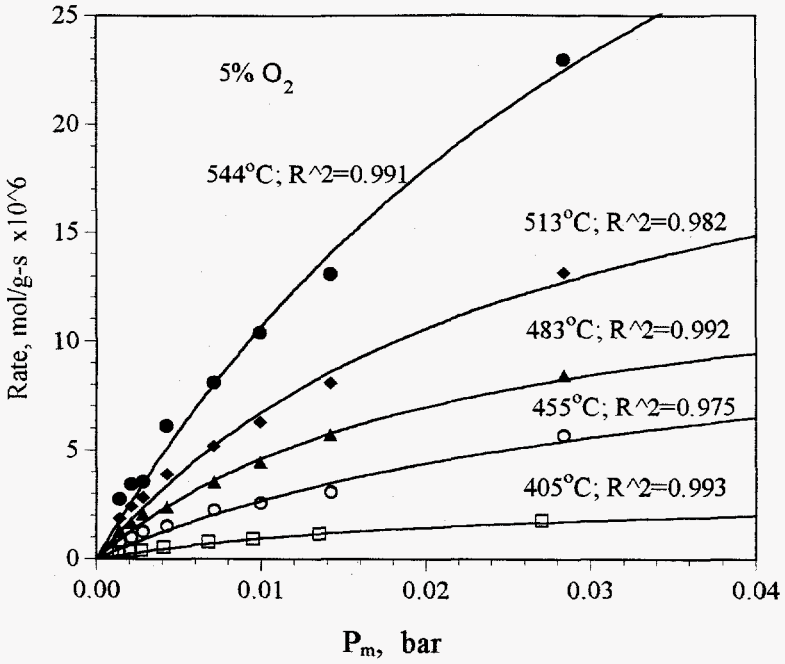

Figure 6.13 Variation of Methane Oxidation Rate over the $Cu_{0.15}[Ce(La)]_{0.85}O_x$ Catalyst with Partial Pressure of Methane under Constant P_O.

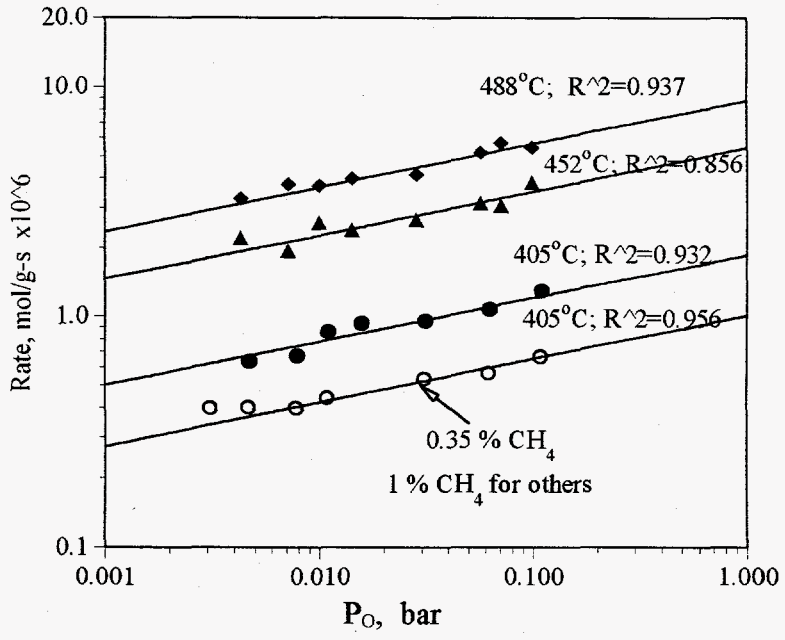

Figure 6.14 Variation of Methane Oxidation Rate over the $Cu_{0.15}[Ce(La)]_{0.85}O_x$ Catalyst with Partial Pressure of Oxygen under Constant P_m

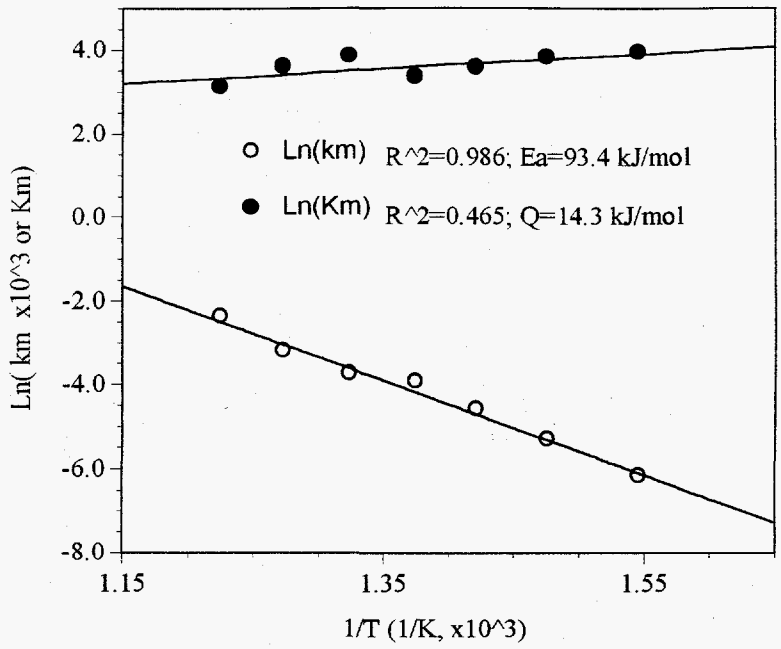

Figure 6.15 Arrhenius Plots of Constants k_m and K_m for Methane Oxidation over $Cu_{0.15}[Ce(La)]_{0.85}O_x$ Catalyst.

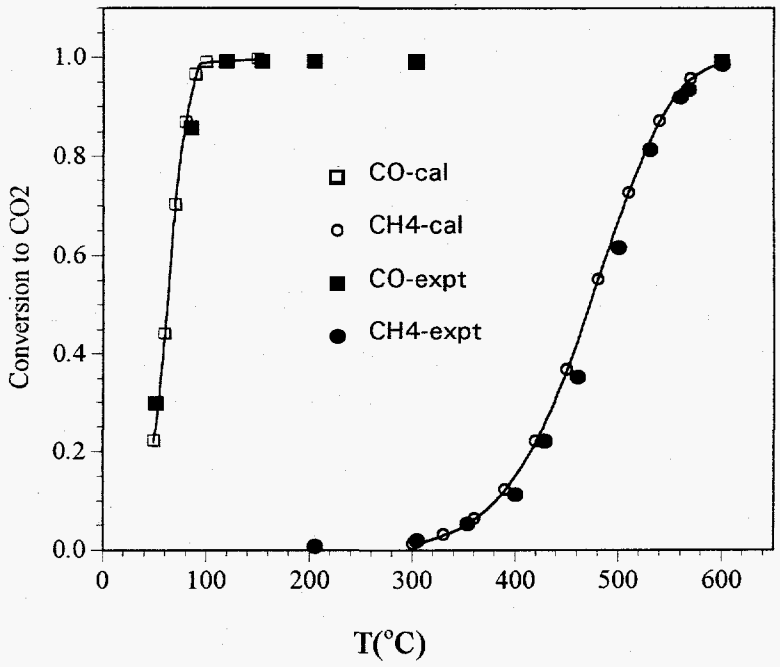

Figure 6.16 Comparison of Calculated Light-off Curves with Experimental Data ($Cu_{0.15}[Ce(La)]_{0.85}O_x$ catalyst; 0.09 g·s/cc; 0.228% CH_4, 0.1% CO, 1% O_2).

Chapter 7

Conclusions and Recommendations

7.1 Reduction of SO_2 by CO to Elemental Sulfur

Fluorite oxides, CeO_2 and ZrO_2, and rare earth zirconates such as $Gd_2Zr_2O_7$ are active catalysts for reduction of SO_2 by CO. More than 95% sulfur yield was achieved at reaction temperatures about 500°C or higher with the feed gas of stoichiometric composition. These catalysts were stable and did not lose their structure after the reaction. Detailed studies of CeO_2 catalyst found that the catalytic activity can be enhanced by rare earth dopants (La, Gd, etc). Fluorite oxides and rare earth zirconates are known oxygen ion conducting materials of high oxygen mobility and/or vacancy concentration. Reaction of SO_2 and CO over these catalysts demonstrated a strong correlation of catalytic activity with the catalyst oxygen mobility.

However, the above catalysts showed strong hysteresis effect and propensity to H_2O and CO_2 poisoning. These catalysts need to be activated either by pre-reduction with CO or by starting the reaction at high temperatures. With the stoichiometric feed gas, the fluorite oxide catalysts lighted off at temperatures above 600°C, while the zirconates lighted off above 650°C. To avoid H_2O and CO_2 poisoning, reaction temperatures higher than 550°C were required for these catalysts. Addition of active transition metals, such as Cu, Ni, Co, etc., to the fluorite oxide lowered the light-off temperature to about 500°C and significantly enhanced the catalyst resistance toward H_2O and CO_2 poisoning. Among various composite catalysts the Cu-Ce-O system was chosen for extensive studies.

An active Cu-Ce-O catalyst can be prepared by either coprecipitation or impregnation. XRD, XPS, and STEM analyses of the used Cu-Ce-O catalyst found that the fluorite crystal structure of ceria was stable at the present reaction conditions, a small amount of copper was dispersed and stabilized on the ceria matrix, and excess copper oxide particles formed copper sulfide crystals of little contribution to catalytic activity. Kinetic studies were carried out with the $Cu_{0.02}[Ce(La)]_{0.98}O_x$ and $Cu_{0.15}[Ce(La)]_{0.85}O_x$ catalysts. The conversion-contact time profiles were approximately represented by the following first order equation:

$$-\frac{dP_{SO2}}{d\tau} = k \cdot P_{SO2}$$

The reaction mechanism was discussed within the following redox framework:

Initiation step: $CO_{ads} + O_{cat} \rightarrow CO_{2,gas} + V_{O,cat}$

Follow-up step: $SO_2 + 2V_{O,cat} \rightarrow S_{cat} + 2O_{cat}$

SO_2 inhibition effect: $SO_2 + 2O_{cat} \xrightarrow{fast} SO_{4,cat} + 2CO \xrightarrow{slow} SO_2 + 2CO_2 + 2V_{O,cat}$

Surface capping oxygen has to be scavenged by CO to create oxygen vacancies. SO_2 molecule then fills the vacancy. But, SO_2 can also react with the surface oxygen to form strongly-bonded sulfate species. Thus, a working catalyst consisted of partially sulfated cerium oxide surface and partially sulfided copper. Copper and cerium oxide in the composite catalyst play different roles: copper provides CO adsorption sites and cerium oxide provides oxygen vacancy sites. Thus, a synergism is realized. In the presence of water vapor, H_2O molecule competes with SO_2 to donate oxygen to the vacancy site that the water-gas-shift(WGS) reaction proceeds. Hydrogen produced from the WGS reaction promoted H_2S production. The sulfur yield in the presence of water vapor could not be optimized by changing the reactor operation conditions. However, the strong redox property of the Cu-Ce-O catalyst always made complete conversion of CO.

7.2 Total Oxidation of CO and Methane

Transition metal-fluorite oxide composite catalysts were studied in this work for the complete oxidation of carbon monoxide and methane. A variety of highly active oxidation catalysts can be prepared from this family of catalysts. The Cu-Ce-O composite showed higher CO oxidation activity than any other base metal oxide catalysts reported in the literature. The catalytic activity was not affected by small amounts of alkaline earth and rare earth dopants or impurities(ca. 1 at.%). Only a small amount of copper(ca. 2 at.% or 0.7 wt.%) was needed to promote the catalytic activity of CeO_2, while excess copper formed bulk CuO particles of little contribution to the catalyst activity. These catalysts showed excellent resistance to water vapor poisoning. The Au-Ce-O was identified as an active and stable catalyst for low temperature CO oxidation. Complete CO conversion at room temperature over $Au_{0.05}[Ce(La)]_{0.95}O_x$ catalyst was achieved at a space velocity of 45,000 v/v/h. This catalyst also exhibited remarkable resistance to water vapor poisoning and thermal sintering. The activity of the Cu-Ce-O system was superior to Co-Ce-O and Cu-Zr-O, but all these catalyst systems showed significantly improved resistance to water vapor poisoning.

The Cu-Ce-O and Cu-Zr-O composites are also active catalysts for complete oxidation of methane. The Cu-Ce-O catalyst activity can be tuned by using alkaline earth and rare earth oxide dopants in suitable amounts. Both La and Sr dopants provided significant promotion effect. No partial oxidation products, such as CO, H_2, etc., were observed during methane oxidation over the Cu-Ce(La)-O and Cu-Zr-O catalysts, even under reducing reaction conditions.

Au in the $Au_{0.05}Ce(La)_{0.95}O_X$ catalyst exists as fine metallic particles in intimate contact with the cerium oxide. This is a model catalyst system demonstrating synergism in CO oxidation. Copper in the Cu-Ce-O composite existed in the forms of isolated ions, clusters, and bulk CuO particles. Isolated ions and clusters were strongly bonded to cerium oxide matrix, while bulk CuO particles were segregated and physically covered by the fine cerium oxide particles. Cu^{+1} species was observed with all the Cu-Ce-O catalysts in the XPS studies and its formation is considered to originate from the interaction of

copper clusters with cerium oxide. The oxidation rates of CO and methane over the Cu-Ce(La)-O catalysts were expressed by the following equation:

$$\frac{dP_{CO2}}{dt} = \frac{kK_R P_R P_O^n}{1 + K_R P_R}$$

where P_R denotes the partial pressure of CO or methane and P_O is the partial pressure of oxygen, and n is a small number close to zero. The activation energies of the surface reactions were 78-94 kJ/mol for CO oxidation and 79 kJ/mol for methane oxidation, respectively. The heat of adsorption derived from the kinetics is in the range of 28 to 62 kJ/mol for CO and 14 kJ/mol for methane, respectively. The Langmuir-Hinshelwood mechanism and synergistic reaction model were proposed for CO oxidation over the Cu-Ce-O and Au-Ce-O catalysts. In this model, copper clusters of Cu^{+1} species or fine gold particles provide sites for CO adsorption, cerium oxide provides the oxygen source, and the reaction proceeds at the interface of the two kinds of materials. The Langmuir-Hinshelwood mechanism was also proposed for methane oxidation over the Cu-Ce-O catalyst.

Effect of thermal treatment on the Cu-Ce-O catalyst activity was studied with CO oxidation as a model reaction. Heating the Cu-Ce-O catalyst induced the following processes: copper diffusion from bulk to surface, clustering of isolated copper ions, aggregation of copper clusters, strengthening interaction of copper and cerium oxide, crystal growth of cerium oxide, and decreasing active oxygen species on cerium oxide. The catalytic activity is determined by the sum of these effects. Formation of copper clusters and strong interaction of copper with cerium oxide are desirable to obtain high activity. One salient conclusion drawn from this study is that a small amount of copper (e.g.<2 at.%) is preferred for a catalyst to have good resistance to thermal sintering, while excess amount of copper has detrimental effect on catalytic activity.

7.3 Oxidation Activity of Non-stoichiometric Cerium Oxide

For SO_2 reduction by CO over non-stoichiometric cerium oxide, the light-off temperature was decreased by about 100°C and hysteresis effect was almost eliminated. This result confirmed the proposed redox reaction mechanism in which the active catalyst comprises a partially reduced surface. Also, light-off temperatures of CO oxidation and methane oxidation over the non-stoichiometric cerium oxide were decreased by ca. 175°C and 60°C, respectively. Pronounced activity enhancement with the non-stoichiometric cerium oxide catalyst for the above three reactions suggests that structural defects of metal oxide are important for oxidation reactions.

7.4 Recommendations

Direct reduction of SO_2 to elemental sulfur is a promising technology for the treatment of SO_2-containing industrial streams. To make this process scheme more viable for practical applications, other reducing gases in addition to CO may need to be considered.

Consequently, the composite catalysts need to be optimized in basic and acidic properties, as opposed to the redox property.

Cu-Ce(D)-O (D=dopant) appears to be a strong oxidation catalyst. Application to catalytic combustion of volatile organic compounds merits to be explored. Cu-Ce(La)-O catalysts may be used in the fluid catalytic cracking unit as a CO oxidation promoter replacing the Pt/alumina catalyst and/or SO_2 transfer agent, and also for the low-temperature light-off application in the automobile catalytic converter. Life time test and parametric studies of Au-CeO_2 catalyst need to be further studied for its application as low temperature CO oxidation catalyst for indoor air filter, sensors, etc. The Au-CeO_2 catalyst has intrinsic superiority to the other Au-based and (Pt, Pd)-based low temperature CO oxidation catalyst.

In this project, only alkaline earth and rare earth elements were considered as dopants to the composite catalysts. Ceria can be made electronically conductive by doping with pentavalent or hexavalent cations. From a fundamental point of view, it is worthwhile to try such dopants as Nb, Ta, W, etc.